Structural and Functional Characterization of TMEM16 Family Members

Dissertation

zur Erlangung der naturwissenschaftlichen Doktorwürde

(Dr. sc. nat.)

vorgelegt der

Mathematisch-naturwissenschaftlichen Fakultät der

Universität Zürich

von

Novandy Karunia Lim

aus

Indonesien

Promotionskomitee

Prof. Dr. Raimund Dutzler (Vorsitz)

Prof. Dr. Markus Seeger

Prof. Dr. Martin Jinek

Zürich, 2016

Acknowledgements

I would like to take this opportunity to thank all the people who have supported and helped me throughout my stay and project in the lab.

Firstly, I would like to thank Prof. Raimund Dutzler for the opportunity to work on this highly exciting project. I am sincerely grateful for his constant support and his faith in me throughout my time in his group.

I would like to thank Prof. Martin Jinek and Prof. Markus Seeger for being part of my thesis committee.

I would like to thank Janine Brunner and Stephan Schenck for the helpful discussion on TMEM16 project. A big thank you to Alessia Dürst too for helping us with the homologue screen during her Masters thesis.

I am grateful to all the past and present members of the Dutzler for their friendship, support and scientific discussions. In particular to Yvonne, I can't thank you enough for the support and for always looking out for me. Thank you for bearing the brunt of the lab to make our lives here as pleasant as it could be.

I would also like to thank the infrastructure team in Department of Biochemistry. Special thanks to: Beat Blattmann and Celine Stutz-Ducommun from the protein crystallization facility for their help with crystallization trials. IT department and Workshop: for their fast troubleshooting with the frequent spontaneous problems in the lab. Sascha Weidner: for taking the initiative to invent the ultimate cell lyser, HPL6, and taking care of its maintenance.

I want to thank my friends outside the lab environment. The Thursday Frisbee ASVZ group always ensured that I had a little weekly workout to clear the mind.

Last but not least, thank you to my family for their constant support despite being half the world away.

Contents

List of Figures

List of Tables

List of Abbreviations

aa	Amino acid
BLAST	Basic local alignment search tool
$[Ca^{2+}]_i$	Intracellular Ca^{2+} concentration
CaCC	Ca^{2+}-activated chloride channel
CaM	Calmodulin
cER	Cortical endoplasmic reticulum
CFTR	Cystic fibrosis transmembrane conductance regulator
DDM	N-Dodecyl-β-D-Maltopyranoside
EC_{50}	Half maximal effective concentration
EDTA	Ethylenediaminetetraacetic acid
EGTA	Ethylene glycol tetraacetic acid
EGFP	Enhanced GFP
ER	Endoplasmic reticulum
Erev	Reversal potential
FSEC	Fluorescent size exclusion chromatography
FX	Fragment-exchange
GFP	Green fluorescent protein
HEK	Human embryonal kidney
HPLC	High performance liquid chromatography
HRP	Horseradish peroxidase
IMAC	Immobilized metal affinity chromatography
KCC	K^+-Cl^- cotransporters
LPR	Lipid to protein ratio
NKCC	Na^+-K^+-$2Cl^-$ cotransporter
PBS	Phosphate buffered saline
PC	Phosphatidylcholine
PE	Phosphatidylethanolamine
PG	Phosphatidylglycerol
PM	Plasma Membrane
PEG	Polyethylene glycol
PI(4,5)P2	Phosphatidylinositol-4,5-bisphosphate
PS	Phosphatidylserine
SBP	Streptavidin binding peptide
SDS-PAGE	Sodium dodecyl sulfate polyacrylamide gel electrophoresis
SEC	Size exclusion chromatography
STIC	Spontaneous Transient Inward Current
TM	Transmembrane
TMEM16	Transmembrane protein of unknown function 16
UDM	N-Undecyl-α-D-Maltopyranoside
vYFP	Venus yellow fluorescent protein
YPL	Yeast polar lipids

Abstract

Calcium-activated chloride channels (CaCC) play an important role in cellular physiology ranging from fluid secretion in epithelia to the regulation of excitability in muscle and neurons. Their importance and widespread expression has put them into the focus of ion channel research for more than three decades and their functional properties have been well characterized by electrophysiology in their native tissues. CaCCs forms anion-selective channels that are activated by Ca^{2+}-binding from the intracellular side. Channel activation by Ca^{2+} was shown to be voltage-dependent with an increase of the EC_{50} at negative potentials. However, very little is known about the molecular mechanism behind these processes due to the uncertainty of their molecular identity. The main breakthrough came in 2008 when CaCC activity was shown to be conferred by one of the ten members of TMEM16 protein family. It was soon established that only two of the members, TMEM16A and TMEM16B, function as CaCCs while the roles of many other TMEM16 proteins were controversial. TMEM16F, in particular, has not only been described as ion channels, but has also been attributed to Ca^{2+}-dependent scrambling of the phospholipid in the plasma membrane and the exposure of phosphotidylserine to the outer leaflet in platelets. The ability of the TMEM16 family protein to carry out these two very different physiological functions remained puzzling due the lack of structural information of this family.

The aim of the thesis was to determine the first high-resolution structure of a TMEM16 family member and to apply the structural information to understand how TMEM16A functions as a Ca^{2+}-activated chloride channel. To increase the likelihood of obtaining a crystal structure, a broad homologue expression screen was performed. Over the course of the screen, 65 homologues from different branches of eukaryotes were chosen and expressed in *S. cerevisiae*. The use of a GFP fusion tag on the homologues allowed rapid identification of well-behaving homologues from crude lysate of 50 ml cultures by fluorescence size-exclusion chromatography (FSEC). From the small-scale expression screen, ten promising homologues were selected, scaled-up to 5-10 liter cultures and tested in protein purification. One of the proteins, nfTMEM16, could be purified with good yield and was successfully crystallised in one condition. To increase the number of crystallization hits and to improve crystal diffraction, nfTMEM16 was truncated systematically in attempt to remove unstructured regions that may interfere with the formation of crystal contacts. A stable truncated construct, C-661, with 74 amino acids removed at the C-terminal were identified. Although the construct yielded more crystallization hits and improved the resolution of the diffraction data to 7.4 Å, the data quality was still insufficient for structure determination. Another fungal homologue, nhTMEM16, was later identified as a potential candidate and its crystal structure was subsequently determined in our group. The characterization of nhTMEM16 as phospholipid scramblase and its structure determination was described in the thesis of Janine Brunner. In order to investigate its potential role as an ion channel, nhTMEM16 was reconstituted into proteoliposomes and its current properties were studied on a horizontal lipid bilayer system. However, due to the presence of current artifacts, no definitive conclusion could be drawn as there was no convincing evidence for ion conduction of nhTMEM16. As an alternative approach, nhTMEM16 was expressed in HEK cells and studied by patch clamp electrophysiology in both whole cell and excised path configuration. Despite strong overexpression, no currents were observed in the presence of Ca^{2+}.

The crystal structure of nhTMEM16 revealed the novel dimeric architecture of TMEM16 proteins. A notable feature of this structure was the presence of a hydrophilic cavity (termed subunit cavity) facing the hydrophobic bilayer at the lateral side of each subunit. The hydrophilic nature of the groove makes this a suitable path for polar lipid head group of phospholipids and thus a likely path for lipid scrambling. The second notable feature was the presence of a conserved Ca^{2+} binding site within the transmembrane region of each subunit. As mammalian TMEM16s share high sequence identity in the transmembrane region to nhTMEM16, it is highly likely that TMEM16A adopts the same architecture. The relevance of the Ca^{2+} binding site was studied in TMEM16A by patch clamp electrophysiology. Single mutants of corresponding residues shift the EC_{50} of activation to higher Ca^{2+} concentrations, suggesting that the direct binding of Ca^{2+} to the site activates the channel. As the subunit cavities are far apart from one another and the binding site is located adjacent to the cavity, we proposed that these subunit cavities would work as two independent ion conduction pathways. To test this hypothesis, concatenated constructs containing two subunits with different affinities for Ca^{2+} were generated. The oligomeric state of the concatemeric protein were first verified biochemically by showing that the concatemer migrates as dimer in size exclusion chromatography and SDS gel electrophoresis. In patch-clamp electrophysiology, these concatemers show a biphasic activation curve that can be described as a sum of the activation properties of its constituents. The results suggest that TMEM16A contains two ion conduction pores that are independently activated by Ca^{2+}.

The nhTMEM16 structure combined with the structure-function studies on TMEM16A described in this thesis, provide first mechanistic insight into gating and ion conduction of CaCCs. This work serves as basis for further investigation of the dual functionality found within the TMEM16 family, which can act as ion channels as well as lipid scramblases.

Zusammenfassung

Calcium-aktivierte Chloridkanäle (CaCC) spielen eine zentrale Rolle in der zellulären Physiologie und sind unter anderem an der Fluidsekretion in Epithelien und der Regulierung von Muskel- und Nervenzellenanregung beteiligt. Aufgrund ihres weitverbreiteten Vorkommens und ihrer physiologischen Relevanz sind sie seit mehr als drei Jahrzehnten, in den Fokus der Ionenkanal-Forschung geraten, wo ihre funktionellen Eigenschaften durch Elektrophysiologie in nativen Geweben untersucht werden. CaCCs bilden anionselektive Kanäle, welche durch die Bindung von Ca^{2+}-Ionen an der intrazellulären Seite reguliert werden. Weitere Studien zeigten, dass die Aktivierung und das damit verbundene Öffnen des Kanals spannungsabhängig ist, mit einer Erhöhung des EC_{50} bei negativen Potentialen. Mangelnde strukturelle Informationen limitieren jedoch das Verständnis über den molekularen Mechanismus dieser Prozesse. Ein großer Durchbruch wurde 2008 erreicht, als für eins der zehn Mitglieder der TMEM16 Proteinfamilie eine CaCC-Aktivität nachgewiesen werden konnte. Folgestudien zeigten schnell, dass nur zwei der Mitglieder, nämlich TMEM16A und TMEM16B, als CaCCs fungieren, während die Funktion der restlichen Mitglieder stark umstritten ist. Insbesondere für TMEM16F konnten sowohl Aktivitäten, die auf einen Ionenkanal als auch auf eine Ca^{2+}-abhängige Skramblase hindeuten, nachgewiesen werden. Letzteres beschreibt den Transport von Phospholipiden von einer Membranseite zu anderen, wie zum Beispiel bei der Exposition von Phophatidylserin nach Außen in Blutplättchen. Wie Mitglieder derselben TMEM16 Proteinfamilie solch unterschiedlichen physiologischen Funktionen ausführen können, bleibt aufgrund der fehlenden strukturellen Informationen rätselhaft.

Das Ziel dieser Arbeit war, die erste hochaufgelöste Struktur eines TMEM16 Familienmitglieds zu bestimmen, um daraus Schlüsse auf die Funktion von TMEM16A als ein Ca^{2+}-aktivierter Chloridkanal zu ziehen. Um die Erfolgschancen einer Kristallstruktur zu erhöhen, wurde eine umfangreiche Homologiestudie herangezogen, um das ideale TMEM16-Model zu finden. Bei dieser Studie wurde die Expression von insgesamt 65 eukaryotischen Homologen im Expressionssytem *S. cerevisiae* getestet. Die Verwendung eines GFP-Fusionsproteins erlaubte eine schnelle Identifizierung der besten Homologe direkt nach Zellaufschluss von 50 ml Kulturen durch Fluoreszenz-Größenausschlusschromatographie (FSEC). Aus dieser Studie wurden zehn Homologe ausgesucht und die Proteinaufreinigung im Großmaßstab von 5-10 L Kulturen getestet und optimiert. Eins dieser Proteine, nfTMEM16, konnte mit guter Ausbeute aufgereinigt und kristallisiert werden. Um die Anzahl der Kristallisationstreffer zu erhöhen und die Kristallbeugung zu verbessern, wurden systematisch unterschiedliche nfTMEM16 Varianten getestet. Hierbei wurden unstrukturierte Bereiche entfernt, die der Bildung von Kristallkontakten stören könnten. Ein stabiles Konstrukt (C-661), wo die letzten 74 Aminosäuren am C-Terminus entfernt wurden, lieferte weitere Kristallisationstreffer. Obwohl die Auflösung der Beugungsdaten bis 7,4 Å verbessert werden konnte, war die Qualität der Daten für eine Strukturbestimmung noch unzureichend. Ein weiteres Homolog aus dem Reich der Pilze, nhTMEM16, wurde im Verlauf dieser Studie als potenzieller Kandidat identifiziert und dessen Kristallstruktur konnte anschließend in unserer Gruppe bestimmt werden. Die Charakterisierung von nhTMEM16 als eine Phospholipid-Skramblase und dessen Strukturbestimmung wurde in der Dissertation von Dr. Janine Brunner beschrieben. Um herauszufinden, ob nhTMEM16 ebenfalls als Ionenkanal fungiert, wurde das Protein in Proteoliposomen rekonstituiert und dessen Permeabilitätseigenschaften mittels

Elektrophysiologie untersucht. In den Studien konnte keine eindeutige Ionenleitfähigkeit von nhTMEM16 gemessen werden, zudem behinderten auftretende Artefakte im experimentellen Aufbau eine endgültige Schlussfolgerung. Daraufhin wurde nhTMEM16 in HEK-Zellen exprimiert und durch *Patch-Clamp*-Elektrophysiologie untersucht. Trotz einer nachweislich starken Überexpression konnten keine Ströme in Gegenwart von Ca^{2+}-Ionen beobachtet werden.

Die Kristallstruktur von nhTMEM16 zeigte die neuartige dimere Architektur von TMEM16 Proteinen. Ein bemerkenswertes Merkmal dieser Struktur ist das Vorhandensein einer hydrophilen Vertiefung an der Peripherie jedes Protomers, welches der Membranseite zugewandt ist. Der hydrophile Charakter dieser Vertiefung macht es zu einem idealen Pfad für den Transport der polaren Kopfgruppen von Phospholipiden. Die Struktur erlaubte zudem die Identifizierung einer konservierten Ca^{2+}-Bindungsstelle innerhalb der Transmembranregion. Da TMEM16 Proteine aus Säugetieren eine hohe Sequenzidentität in der Transmembranregion mit nhTMEM16 teilen, wird angenommen, dass TMEM16A eine ähnliche Architektur aufweist. Die Bedeutung der Ca^{2+}-Bindungsstelle wurde in TMEM16A mit Hilfe von *Patch-Clamp*-Elektrophysiologie untersucht. Punktmutationen an der Ca^{2+}-Bindungsstelle verschieben den EC_{50} Aktivierungswert zu höheren Ca^{2+}-Konzentrationen, was darauf hindeutet, dass das Binden von Ca^{2+}-Ionen den Kanal aktiviert. Da die Vertiefungen und Ca^{2+}-Bindestellen jedes Protomers räumlich voneinander getrennt sind, ist unsere Hypothese, dass beide Protomere als unabhängige Ionenkanäle fungieren. Um diese Hypothese zu testen, wurden zwei Protomere mit unterschiedlicher Ca^{2+}-Affinität als ein Fusionskonstrukt (Konkatemer) generiert. Der oligomere Zustand der Konkatemere wurde durch Größenausschlusschromatographie und SDS-Gelelektrophorese untersucht und die Bildung eines Dimeres nachgewiesen. Elektrophysiologische Studien dieser Konkatamere zeigen eine zweiphasige Aktivierungskurve, die sich aus der Summe der Aktivitätseigenschaften der unterschiedlichen Protomere zusammensetzt. Die Resultate deuten darauf hin, das TMEM16A zwei Ionenleitungsporen besitzt, die unabhängig von einander durch Calcium aktiviert werden.

Die im Rahmen dieser Arbeit durchgeführten strukturellen und funktionellen Studien erlauben einen Einblick in den Mechanismus, welchen die Regulation und die Permeabilität von CaCCs beschreibt. Sie geben eine Basis für weiterführende Studien zum Verständnis der dualen Funktionalität innerhalb der TMEM16 Familie, welche sowohl als Ionenkanäle als auch Lipid-Skramblasen fungiert.

1. Introduction

1.1 Ion transport in cell homeostasis

One of the most basic principle of sustaining life in cellular organisms is the continuous transfer of nutrients and other solutes between the cell and the surrounding. The first requirement to achieving the steady-state is the presence of a physical barrier between the two environments in the form of the plasma membrane. The membrane is composed of amphiphilic lipids that self-assemble to form a bilayer. The hydrophobic tails of the lipids point inward forming a hydrophobic region while the hydrophilic head groups face outward towards the intracellular and extracellular side. This arrangement accounts for the impermeability of the membrane to charged solutes and provides the necessary separation of the cytoplasm from the environment. In eukaryotes, the role of bilayer membranes are further extended to forming additional compartmentalization within the cell in the form of organelles. The isolation of nucleus, lysosomes or mitochondria from the cytoplasm allow highly specialized roles of these organelles.

The steady-state maintenance of highly asymmetric concentrations of inorganic cations and anions is made possible by the presence of intrinsic membrane transport proteins. Depending on the underlying mechanism, the transport proteins can be classified into two major classes: active transporters/carriers and passive channels. Active transporters facilitate the transport of substrates whereby one of the substrate is transported across the membrane against its concentration gradient. As the process is energetically unfavorable, the transporter would require an input of energy. Depending on whether it is a primary or secondary active transporter, this energy is derived from either the hydrolysis of ATP or the transport of another substrate down the electrochemical gradient respectively. In contrast to active transporters, channel proteins facilitate the passive diffusion of substrate down the electrochemical gradient of the substrate. Many of these proteins specifically transport inorganic ions and are thus referred to as ion channels. Unlike transporter proteins, ion channels form hydrophilic pores across the membrane. The pore is usually selective for the conducted ion. The ion conduction is regulated either by the binding of a specific ligand or a change in membrane potential, resulting in a transition between close and open pore state.

From the point of view of transport efficiency, ion channels have an advantage over carrier proteins as they allow ions to pass through the protein at a rate up to 10^5 times faster than the highest efficient carrier protein could do. This efficiency has made ion channels important in cellular functions, which involve rapid changes in cells such as the generation of action potentials, muscle contraction and the propagation of nerve impulses. The primary ion channels responsible in cell regulation are sodium, potassium, calcium and chloride channels.

1.2 Chloride channels: Overview

Chloride channels have not been as extensively studied as cation channels despite the large diversity of chloride channel families. The equilibrium potential of Cl^- has been assumed to be to close to the resting potential in all cells, hence Cl^- was thought to cross the membrane in both directions without affecting its electrical properties. The misconception was due to most of the initial studies on Cl^- being conducted on skeletal muscles and erythrocytes where there is high resting permeability of Cl^-. Nowadays it is accepted that Cl^- is actively maintained to be out of electrochemical equilibrium and it is therefore capable of performing work (Figure 1). Cl^- is the most abundant anion in physiological conditions and its resting concentration is highly variable. Many transporters move Cl^- against its electrochemical gradient utilizing the energy provided by the electrochemical gradients of K^+ and Na^+, which is maintained by the activity of the Na^+–K^+ ATPase. In epithelial cells and immature sensory neurons, Cl^- loaders such as Na^+-K^+-$2Cl^-$ cotransporter (NKCC), Na^+-Cl^- cotransporter (NCC) and Na-independent Cl^--HCO_3^- exchangers actively pump Cl- into the cell. In epithelial cells, the resulting high intracellular Cl^- concentration provides the drive for fluid secretion on the apical surface whereby Cl- passively exits the cell through Cl^- channels followed by diffusion of water and Na^+. In immature neurons, the Cl^- gradient is used by ligand gated ion channel GABA receptors for the depolarizing post-synaptic potentials important in stabilizing neonatal synapses (1). On the contrary, mature neurons actively maintain low intracellulars Cl- concentration through the expression of Cl- extruders such as K^+-Cl^- cotransporters (KCC) and Na^+-dependent Cl^--HCO_3^- exchangers (NDCBE). In these cells, GABA receptors facilitate the membrane hyperpolarization (2).

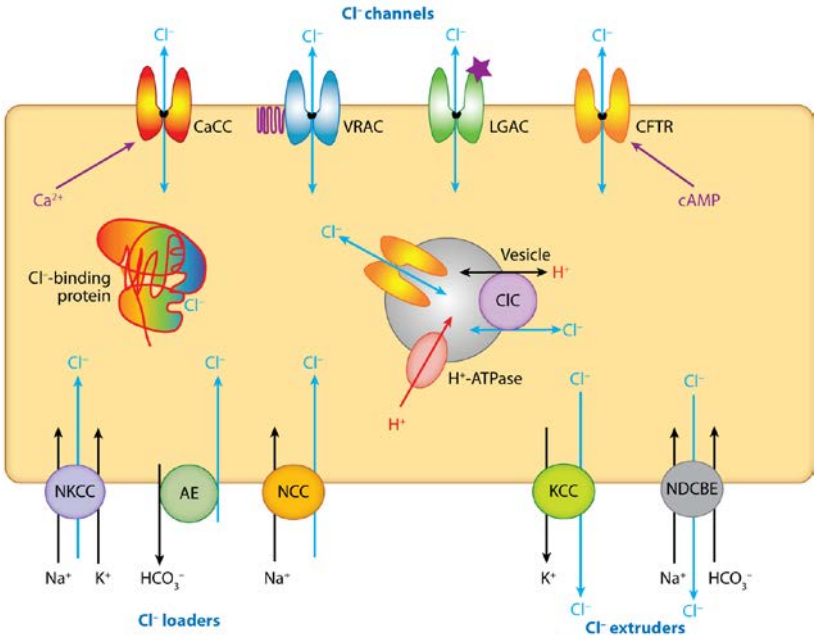

Figure 1 Cl^- signaling.

Cells actively regulate Cl^- concentration across the plasma membrane through membrane proteins functioning as Cl^- loaders (including the Na^+-K^+-Cl^- cotransporter NKCC, the Cl^--HCO_3^- exchanger AE, and the Na^+-Cl^- cotransporter NCC) or Cl^- extruders (including the K^+-Cl–cotransporter KCC and the Na^+-dependent Cl^--HCO3$^-$ exchanger NDCBE). With the Cl^- gradient established, Cl- flow is facilitated by various Cl^- channels in the plasma membrane, including Ca^{2+}-activated Cl^- channels (CaCC), cAMP-

activated Cl^- channels (CFTR), cell volume–regulated anion channels (VRAC), and ligand-gated anion channels (LGAC). The regulation of Cl- inside the cell is important for various intracellular Cl- binding proteins. Cl^- channels and transporters are also found in intracellular membranes. Picture is taken from Duran et al. (3).

Cl^- channels are important for large variety of physiological functions**.** In epithelium, Cl^- channels facilitates the transport of ions and water. As seen in salivary acinar cell, the transport of Cl- drives the fluid secretion into the mouth cavity (4). An increase in intracellular [Ca^{2+}] activates Cl^- and K^+ channels, resulting in the simultaneous efflux of Cl^- across the apical membrane, and K^+ across the basolateral membrane into the interstitial fluid. The opposing movement of Cl^- and K^+ creates a transepithelial electrical difference which drives Na^+ ions across the tight junctions into the lumen. The build-up of Na^+ and Cl^- creates a transepithelial osmotic gradient which propels the movement of water to generate saliva (5). Cl^- channels play similar roles in the secretory epithelia of kidneys, airways and pancreas (6-8). Misfunctioning of the key Cl^- channel Cystic Fibrosis Transmembrane Regulator (CFTR) in carrying out the efflux of Cl^- leads to cystic fibrosis, resulting in thickened mucus in the lungs with frequent respiratory infections. Apart from secretion, Cl^- channels are also important in regulating the membrane potentials. For example, mutations in ClC-1 lead to the skeletal muscle disorder myotonia congenital. The impairment of the channel causes the muscle fiber membrane to hyper-excitable upon the efflux of K^+ during muscle, resulting in prolonged muscle contraction (9).

Compared to cation channels, which are relatively selective for a certain cation, Cl^- channels usually exhibit a low selectivity among anions. They are permeant to a range of anions to varying extents but with Cl^- being the most abundant anion, they mostly conduct Cl^- and hence are termed chloride channels. The structure of a bacterial ClC protein identified the Cl^- conduction pathway in the ClC protein family (10). Despite the protein being the Cl^-/H^+ antiporter member instead of a channel, the structure showed that the fundamentals defining the anion permeation and selectivity may differ significantly from those of cation channels. Most cation channels form oligomers whereby the ion permeation pathway is made of homologous regions within each subunit. In the tetrameric K^+ channels, two transmembrane helices and a 'P-Loop' within each subunit contribute to the ion pathway and gating (11). In contrast, ClC channels forms a dimer in which each pore is formed by a single subunit with several non-homologous regions within the same protein contributing the ion pathway (10).

The small number of known Cl^- channel genes does not reflect the large variety of biophysically identified Cl^- channels. There were mainly three well-established gene families of chloride channels. The cystic fibrosis transmembrane conductance regulator (CFTR), which is the only member in a large gene family of ABC transporters known to function as an ion channel, is controlled by intracellular ATP and through phosphorylation by cAMP or cGMP-dependent kinases. The ClC channels, with 9 family members in mammals, function on both the plasma membrane and the membranes of intracellular organelles. However, only four members (ClC1, 2, Ka, Kb) are channels while the remaining members (ClC 3-7) are Cl^-/H+ antiporters (12). The ligand-gated chloride channels, GABA- and glycine-receptors, represent the largest known family of Cl^- channels (13).

On top of these well-studied Cl^- channel families, there are proteins whose role as Cl^- channel still remains tentative or has just been characterised. Identification of Cl^- channels through sequence

homology has proven to be challenging due to absence of characteristic sequences that are conserved across the known Cl^- channel families. While the Cl^- currents have been characterized mostly by electrophysiology, the molecular identities of the channels remained unknown or controversial for a long time. The lack of knowledge limited the studies on these channels to native cells and research stagnated for long time. One of the classes of unknown channel proteins was the Volume Regulated Anion Channel (VRAC) important for controlling the cell volume by dissipating osmotic gradients that drive water in and out of cells. It has been characterized for over a decade but its underlying molecular identity as members of the LRRC8 protein family has only been identified recently (14, 15). Similarly, the molecular identity of outwardly rectifying Ca^{2+}-activated chloride channels (CaCCs) had also been contentious. Several molecular candidates had been proposed for CaCCs, including members of the bestrophin family (16). While bestrophins could function as CaCCs, they are unlikely to code for the classical outwardly rectifying CaCC observed in various epithelia. Unlike endogenous CaCCs, bestrophins have a very limited expression profile and display biophysical properties that differ from native CaCCs. In 2008, it was discovered that members of TMEM16 family of transmembrane proteins mediate endogenous CaCC function (17-19). With the identification of TMEM16 as a new family of Cl^- channels, it was possible to perform structure function studies that may help uncover underlying principles regarding anion channel function.

Cl^- channels can be classified according to their gating mechanism. The gating mechanism of chloride channels can be dependent on a variety of factors including membrane voltage, protein kinase activity, cell swelling, and intracellular Ca^{2+} (13). Activation of some cation channels utilized certain common principles regarding channel gating, such as the positively charged S4 segment in voltage-gated sodium channel (VGSC) required for voltage-sensing (20). In contrast, the voltage dependent gating in anion channel seems to differ in that the gating is affected by the permeant anions themselves binding to specific sites within the channel. For example, the voltage sensitivity of some chloride channels of the ClC family is exhibited not by voltage sensing regions, but by the voltage dependence of Cl^- binding to sites within the channel (21, 22). In ClC channels, pH also strongly modulates gating (23). This feature may be the reminiscence of the ClC channels evolving from ancestral transporters. In CFTR, which is functioning more similar to a transporter, the gating mechanism is highly complex involving the phosphorylation of serine in the regulatory domain and ATP hydrolysis (24). CaCCs also possess unique gating properties as they exhibit strongly coupled voltage-dependence and ligand-dependent gating (25). It remains unknown how voltage-dependent and Ca^{2+}-dependent gating comes about at the molecular level. The following chapter addresses how the discovery of TMEM16 as the molecular correlate of CaCC paved the path for structure-function studies.

1.3. Ca^{2+}-activated chloride channel (CaCC): Role in Physiology

The Ca^{2+}-activated chloride channel (CaCC) being addressed here refers specifically to the class of chloride channels attributed to the phenotype first described in the early 1980s in Xenopus oocytes (26, 27).The molecular identity of CaCCs had been controversial prior to the discovery of TMEM16, in part due to the diversity of CaCC currents. At the macroscopic level, CaCCs share similar features in whole-cell recordings from a variety of cell types. They are Ca^{2+} sensitive, activate slowly upon depolarization, and display an outwardly rectifying I-V curve at steady state. In addition, CaCCs are more sensitive to Ca^{2+} at positive voltages than at negative voltages and the rectification is abolished at high [Ca^{2+}]. While CaCCs across various cell types display some similarities, the understanding of CaCC physiology has been confounded by the fact that they display heterogeneity in their biophysical properties and regulatory mechanisms. CaCCs have been observed in many different cell types and tissues, such as neurons, epithelial and smooth muscles cells, where they play a role in controlling excitability, contractility and secretion.

Smooth Muscle Cells

CaCCs were well characterized pharmacologically in smooth muscle cells from a variety of tissues including portal vein, pulmonary artery, lymphatic vessels and trachea (28-32). The classical CaCC inhibitors such as niflumic acid (NFA), Anthracene-9-carboxylic acid (A9C) and 5-nitro-2-(3-phenylpropylalanine) benzoate (NPPB) decreases the intensity and frequency of smooth muscle cells contraction from portal vein, suggesting that CaCCs are involved in regulation of muscle rhythmicity and contraction.

In general, CaCCs plays a role in myogenic tone and contraction stimulated by agonists. CaCC is activated in smooth muscle cells by the release of Ca^{2+} from intracellular stores by Inositol 1,4-5-triphosphate (IP_3) or through activation of VGCC resulting in Ca^{2+} influx (29, 33). In vascular smooth muscle, Cl^- accumulation by co-transporter NKCC1, maintain a positive E_{Cl^-} compared to the cell resting potential. Activation of CaCC by Ca therefore results in flow of Cl^- out of the cell, causing membrane depolarization and opening of voltage-gated calcium channel (VGCC) to further raise $[Ca^{2+}]_i$.

It has also been proposed that CaCC might play a role in facilitating the spontaneous depolarisation in the form of spontaneous transient inward current (STIC) resulting from localized rapid Ca^{2+} release from the internal ryanodine-sensitive Ca^{2+} store, known as Ca^{2+} sparks (34). These depolarisations could influence pulmonary artery membrane potential and alter the smooth muscle tone but the precise physiological significance and contribution by CaCC remain unclear (35).

Neurons

CaCC plays a role in controlling the excitability of neurons. The type of neuronal cells would determine whether activation of CaCC is inhibitory or excitatory. In mature neurons of the central nervous system (CNS), the relatively low $[Cl^-]_i$ causes the E_{Cl} to be more negative than the resting membrane potential (36), hence activation of CaCC result in action potential inhibition. On the other hand, in peripheral

somatosensory neurons and immature CNS neurons, Cl^- is significantly accumulated so that activation of a CaCC depolarizes the membrane and triggers an action potential (37-39). The difference in $[Cl^-]i$ could be explained by the interaction between Cl^- uptake and release pathways. In neurons, the transporter NKCC1 facilitates the main Cl^- uptake, while the K^+-Cl^- cotransporter 2 (KCC2) facilaites the main Cl^- extrusion. In the rat central nervous system (CNS) cells, expression of NKCC1 is high during the first week of postnatal development but decreases during postnatal development to a stable low level in adult phase. On the contrary, the expression of KCC2 in rat brain cells starts low after birth but increases rapidly during growth (2, 40, 41). This interplay during development results in shift of E_{Cl-} from approximately -40 mV to -80 mV and lower. Thus, CaCC activation leads to Cl^- extrusion, membrane depolarization and excitation in the immature CNS, but Cl^- influx, hyperpolarization, and an inhibitory effect in the mature CNS. On the other hand, NKCC1 expression level in peripheral somatosensory system remains high throughout development, thus CaCC activation results in Cl^- efflux and depolarization (42-44). CaCCs were also recorded in single cilia of olfactory receptor neurons (45), photoreceptors in retina (46, 47) and sensory neurons in the mouse vomeronasal organ. Odorants open cyclic nucleotide gated channels by binding to G-protein coupled olfactory receptors that elevate cAMP (48, 49). In the classical signal transduction pathway, Ca^{2+} influx through the cyclic nucleotide gated channels activates CaCCs, hence enhancing depolarisation.

Epithelial cells

CaCCs play important roles in transepithelial transport, particularly in chloride and fluid secretion triggered by calcium-mobilising agonists. The function of CaCCs has been well characterised in the fluid and secretory processes of glandular tissues such as the salivary gland and the pancreas. The acinar and duct cells of these tissues secrete plasma-like primary fluid rich in NaCl. The fluid secretion is Ca^{2+} dependent and triggered by acetylcholine (50). The rise in $[Ca^{2+}]_i$ is triggered by the muscarinic receptor-induced production of IP_3 leading to Ca^{2+} release from internal stores. The elevation of $[Ca^{2+}]_i$ activates CaCCs and subsequently Cl^- efflux through the apical membrane.

In the airways, CaCCs are localized to the surface epithelium (51, 52). Cl^- conductance is strongly increased when bronchial epithelial cells are treated with Interleukin-4 (17). The elevation of cytosolic Ca^{2+} triggers mucus secretion. Apart from Cl^-, HCO_3^-, which is important for mucus expansion and fluidification, is also secreted by CaCCs. The selectivity of these channels in airway epithelia mimics that of CFTR, making it therapeutically interesting as a treatment for cystic fibrosis. In cystic fibrosis, impairment of CFTR results in immobilized mucus and dehydration of the airway surface (53). The upregulation and activation of CaCC in CF airways could thus provide a route for chloride and bicarbonate secretion to compensate for the inactivity of CFTR. Clinical trials using CaCC as therapeutic target has been carried out but, despite intial promising results, no significant improvement of respiratory function was observed (54).

1.4. Members of the TMEM16 protein family mediate are CaCCs

Despite extensive biophysical and physiological studies of calcium-activated chloride currents since their first discovery over two decades ago, the molecular identity of CaCCs had been elusive for a long time. In 2008, three groups independently proposed TMEM16A to be the protein responsible for the observed CaCC currents (17, 18, 55). Caputo et al. recognized that Axolotl oocytes do not express CaCCs and thus utitilised them as the expression system to perform expression cloning of transcripts from Xenopus oocytes. Yang et al. identified TMEM16A through a bioinformatic analysis of putative membrane proteins with more than two transmembrane domains containing multiple paralogs. Schroeder et al. performed a microarray analysis of genes whose products are upregulated by interleukin-4 and narrowed the number of candidates down to TMEM16A by a siRNA gene-silencing study. All the three groups then confirmed TMEM16A to be responsible for the phenotype of CaCCs through various heterologous expression and patch-clamp experiments. This discovery provides new avenues to explore and study CaCCs at a molecular level.

TMEM16A belongs to the protein family of Transmembrane Proteins with Unknown Function number 16 (TMEM16). TMEM16 proteins do not share significant sequence homology with other known ion channel families. Although TMEM16s are found in all eukaryotic kingdoms, they are best represented in higher vertebrates. Mammals have 10 TMEM16s paralogs, termed A-K (omitting I), that are well conserved across species and are predicted to have similar topologies. When compared to TMEM16A, the sequence identity ranges from 61% in TMEM16B to 23% in TMEM16K. Within each paralog, there are possibly multiple splice variants, hence contributing to further functional complexity (56). After the discovery of TMEM16A as a CaCC, a large effort had been spent on discovering the physiological role of the remaining family members and whether they also function as channels. It was soon discovered that TMEM16 proteins exhibit diverse functions and are involved in several diseases (Table 1). Out of the 10 members, only TMEM16A and B recapitulate the properties of native CaCCs and are thus accepted to constitute CaCCc subunits in mammals. The other family members are poorly understood or and their function remains controversial. Some were reported to be phospholipid scramblases, ion channels, or both while some were reported to be the regulatory subunits of other channels. The following sub-chapters will focus on the various roles of TMEM16 proteins.

	Roles	Relationship with Diseases
TMEM16A	CaCC	Upregulated in gastrointestinal stromal tumors, breast cancer and asthma (57-59)
TMEM16B	CaCC	
TMEM16C	Regulator of Slack Channel (60)	Mutated in neurological disorder craniocervical dystonia (61)
TMEM16D		Upregulated in aldosterone-producing adenoma (62)
TMEM16E		Mutated in Limb-girdle muscular dystrophy (LGMD2L), Miyoshi myopathy (MMD3), Gnathodyaphyseal dysplasia (GDD). (63-66)
TMEM16F	Channel, Lipid scramblase	Mutated in Scott Syndrome (19, 67)
TMEM16G		Upregulated in prostate cancer (68)
TMEM16H		?
TMEM16J		?
TMEM16K		Mutated in autosomal-recessive cerebellar ataxias (69)

Table 1 Physiological implication of TMEM16 family.

TMEM16 protein family is implicated in variety of physiological disorders although the involvement of TMEM16H and TMEM16J remain unclear. In terms of molecular role, only TMEM16A and TMEM16B have been identified as constituents of CaCC while the role of TMEM16F have been disputed to be channel and/or lipid scramblase.

Hydropathy analysis suggests that all TMEM16 proteins have eight transmembrane helices with cytosolic N- and C-termini. This prediction together with the fact that TMEM16A is a chloride channel, gave rise to the alternative family name anoctamin ('An' for anion, 'Oct' for eight TMHs). The proposed topology was initially verified experimentally for TMEM16G using hemagglutinin epitope tag accessibility methodology before a similar approach was applied to TMEM16A (70, 71). The proposed topology also suggests that there might be a re-entrant loop between transmembrane helix 6 and 7 (TM6 and TM7). Due to the limitation of the technique in verifying location and actual numbers of TMHs, closer investigations are still required to further investigate the topology of TMEM16 proteins. Nevertheless, the predicted topology has provided the template for many studies on structure-function relationships. Four splice variants have been identified for TMEM16A (56) and two splice variants have been found for TMEM16G (68). Human TMEM16A has 4 different alternatively-spliced segments termed as *a*, *b*, *c*, and *d* corresponding to alternative initiation site in exon-6b, exon-13, and exon-15 respectively (56). TMEM16s form dimers and dimerization was proposed to be mediated by intermolecular contacts of the N-termini prior to the incorporation of the protein into plasma membrane (72-74). Most TMEM16s form homodimers but TMEM16A and B were shown to be able to

form heterodimers too. Currently it is still unclear whether the C-termini contribute to the formation and stabilization of the dimer.

1.4.1. TMEM16A and B: Ca^{2+}-activated Cl channels

Heterologous expression of TMEM16A and TMEM16B in various cells evokes Cl^- currents with biophysical properties similar to native CaCCs. The Ca^{2+} sensitivity and voltage dependence of TMEM16A are similar to those of endogenous CaCCs, with an EC_{50} of 0.4 µM at +60 mV in HEK cells (55) compared to 280 nM in calf endothelial cells at + 100 mV (75) and 0.9 µM in Xenopus oocyte at 120 mV (76). The Ca^{2+} sensitivity increases with depolarization, much like endogenous CaCC currents in *Xenopus* oocytes (76). Furthermore, the current is strongly outwardly rectifying at Ca^{2+} concentrations lower than 1µM (18, 55). At Ca^{2+} concentrations higher than 5 µM, the rectification is abolished, which is also consistent with native CaCCs (55, 77). *Xenopus* TMEM16A behaves similarly to native *Xenopus* oocyte CaCCs, as it exhibits an outwardly rectifying current at low and a linear current-voltage relationship at higher intracellular Ca^{2+} (18). TMEM16B is also outwardly rectifying but activates more quickly at positive voltages than TMEM16A with a significantly lower apparent Ca^{2+} affinity (78, 79). The CaCC activity observed in olfactory sensory neurons and photoreceptor terminals are now accepted to be contributed by TMEM16B (79, 80).

TMEM16A and TMEM16B have anion selectivity of $NO_3^- > I^- > Br^- > Cl^- > F^-$, which is similar to those of native CaCCs (17, 55, 81, 82). They are also blocked by traditional Cl− channel blockers, including 4,4’-diisothiocyanatostilbene-2,2’-disulfonic acid (DIDS), 5-nitro-2-(3-phenylpropylamino)benzoic acid (NPPB), tamoxifen, and niflumic acid (NFA) (55, 83). TMEM16A and B are the first CaCC candidates shown to be activated by physiological Ca^{2+} signals provided by G protein–coupled receptor (GPCR) stimulation. When mTMEM16A or TMEM16B are cotransfected with GPCRs that raise intracellular Ca^{2+}, such as endothelin, angiotensin II, muscarinic, histamine, and purinergic receptors, GPCR activation induces TMEM16A currents (17).

TMEM16A is gated by both Ca^{2+} and voltage. In the absence of Ca^{2+} or other divalent cations, TMEM16A could be partially activated by strong depolarization. At 200 mV, the magnitude of the Ca-independent current is less than 10% of current activated by maximum $[Ca^{2+}]_i$ (25). The TMEM16A primary structure did not reveal clear sites that sense voltage or bind to Ca^{2+}. Unlike voltage-gated cation channels which possess amphipathic transmembrane helices (TMH) with charged amino acids to sense voltage, TMEM16A lacks such sequences. There are also no canonical Ca^{2+} binding sites. Reminiscent of the Ca^{2+} sensor of bestrophin channel, the first intracellular loop of TMEM16A between TMH2 and TMH3 has a stretch of 5 consecutive glutamates, 444EEEEE448, resembles a potential Ca^{2+} binding site (25). However, it was shown that this sequence is not the main Ca^{2+} sensor (25). The last glutamate in the sequence is the first residue of a 4-amino acid alternatively-spliced segment *c* (448EAVK451). Neutralization of the glutamates do not significantly alter the Ca^{2+} sensitivity, although deletion of the alternatively-spliced segment (ΔEAVK) alters both voltage-dependent gating and Ca^{2+} sensitivity (25, 56). Similar studies in TMEM16B, where 444EEEEE448 was deleted, show that this region has little

effect on Ca^{2+} sensitivity, but it does affect voltage-dependent gating (84). Taken together, although the loop plays an important role in coupling of voltage sensing and Ca^{2+} binding to channel activation, it is unlikely the main binding site for Ca^{2+}. On the other hand, two residues, E702 and E705, on the intracellular loop between the predicted TMH5 and TMH6 have been identified to be involved in channel activation of TMEM16A by Ca^{2+} since the mutation of both residues to asparagine resulted in a decrease in the EC_{50} of channel activation (71).

The mode of activation of TMEM16A by Ca^{2+} either via an accessory subunit such as calmodulin (CaM), or by binding directly to the channel has been discussed controversially. In a study, CaM reportedly binds to a 22-amino acid region that coincides with the *b splice variant* segment in the N-terminus which is essential for gating of TMEM16A (85). This putative CaM binding site is not canonical, although it resembles some CaM binding sites. However, only the TMEM16A splice variants containing the *b* segment seem to require CaM. TMEM16Aac, which lacks this segment, does not require CaM and is activated directly by Ca^{2+}. On the other hand, some endogenous CaCCs have been described to be regulated directly by Ca^{2+} and others by CaM-dependent pathways (16, 86, 87). Recently, it was shown that reconstituted TMEM16A could be activated by Ca^{2+} alone, without addition of calmodulin (88, 89). This may be explained by expression of different splice variants, isoforms, or even different channel subunits. Understanding how TMEM16A is regulated by Ca^{2+} is essential to understand the involvement of the protein in various signaling pathways.

1.4.2. TMEM16F: A Ca^{2+} activated channel and lipid scramblase

The function of TMEM16F has been controversially discussed during the recent years. In 2010, TMEM16F was reported to be a Ca^{2+} dependent lipid scramblase, a protein required for lipid scrambling in platelets during blood coagulation. In healthy cells, the asymmetric distribution of different lipids is established and maintained by the coordinated activities of lipid flippase and floppase. For example, phosphatidylserine (PS) is actively transported by a flippase from the outer into the inner leaflet of the plasma membrane. The activation of the TMEM16F scramblase by Ca^{2+} during tissue damage triggers the transport of PS in both directions. The exposure of PS to the outer leaflet triggers signaling cascades eventually leading to blood coagulation. Missense mutations of the TMEM16F gene give rise to Scott syndrome, a rare congenital bleeding disorder.

However, amidst this discovery, there were many other reports claiming TMEM16F to be functioning as various ion types of channels, as non-selective cation channel (19, 90), outwardly rectifying Cl^- channel (91) and CaCC (92-94). When considering the functional behavior of TMEM16F, it is highly unlikely that a single protein could account for such a wide e range of different ion selectivity. Whitlock and Hartzell noted that TMEM16F was shown to be partially permeable to $NMDG^+$ and MES^- and estimated that the pore diameter to be greater than 6 Å (95). A possible explanation would be that TMEM16F possess a large non-selective pore which might exist in multiple open conformations including a restricted and a dilated conformation. They thus proposed that the ionic current mediated by TMEM16 might be a leak current that occurs while lipids are transported (95).

1.4.3. Other mammalian TMEM16s

Following the discovery that TMEM16A and B are CaCCs, there was a great interest in defining the roles of the remaining eight TMEM16 members in mammals. To this end, several groups have carried out comparative functional studies of all family members simultaneously. In a study by Schreiber et al. (96), it was concluded that in addition to TMEM16A and TMEM16B, TMEM16F, G and K were chloride channels. However, in iodide flux assays, ionomycin or ATP stimulated flux reported for TMEM16F, G, and K were less than 10% of the response by TMEM16A. Furthermore, the short splice variant of TMEM16H, with no predicted transmembrane domains and thus unlikely to be a channel, exhibited approximately the same flux as the full length TMEM16H. Overexpression of TMEM16K produced a Cl− current that was evoked slowly over a time range of 10 minutes. In another study, Suzuki et al. (67) established a mouse lymphocyte *TMEM16F*$^{-/-}$ cell line, which is incapable of exposing PS in response to a Ca^{2+} ionophore. By expressing all the TMEM16 members separately in this cell line, it was discovered that TMEM16C, D, F, G, and J could recover the scramblase activity although with different preference for lipid substrates. Furthermore, patch clamp analysis in HEK293T cells showed that only TMEM16A and B evoked CaCC currents in response to a Ca^{2+} concentration of 500 nM.

TMEM16C was recently to shown to be a regulator of pain processing by modulating the activity of the Slack channel, a Na^{+}-activated K^{+} channel in the central and peripheral nervous system of human, mouse, and rat (60, 61). In TMEM16C knockout rats, behavioral tests showed they were hypersensitive to temperatures higher than 50 °C. It was discovered that the expression and activity of Slack in TMEM16C knockout rat was strongly reduced and on the other hand, the coexpression of TMEM16C with Slack in HEK293 cells resulted in increase of Slack currents. Immunostaining revealed that the two proteins colocalize in a subset of puncta on the plasma membrane. However, it remains unclear how TMEM16C modulates the activity of the channel. It was also noted that the expression of TMEM16C alone did not result in any currents.

1.4.4. Fungal TMEM16s

In *Saccharomyces cerevisiae*, the TMEM16 homologue, Ist2, is important for the recruitment and tethering of cortical endoplasmic reticulum (cER) to the plasma membrane (PM) (97). The membrane junction is important for sterol lipid transfer, Ca^{2+} transport, phosphoinositide signaling and intracellular signaling (98, 99). Ist2 together with two other protein families, tricalbin and vesicle-associated membrane protein-associated protein (VAP), are anchored on the cER membrane and forms interactions with the plasma membrane to maintain an average spacing of 30 nm needed for membrane to membrane interaction (97, 100). Ist2p forms contact with plasma membrane by binding phosphatidylinositol-4,5-bisphosphate (PI(4,5)P2) via the lysine/histidine-rich polybasic domain in its C-terminus (101, 102). Apart from its role in membrane tethering, no other function of Ist2 is known. It was also shown that reconstituted Ist2 does not mediate any lipid scrambling (103).

Recently, the molecular function of a TMEM16 family member of the fungus *Aspergillus fumigatus* (afTMEM16), was studied (103). The protein was heterologously expressed, purified and reconstituted into liposomes. In artificial planar lipid bilayers, afTMEM16 mediates a single channel conductance of ~300pS with low ion-selectivity of P_K:P_{Cl} = 1.5. Similar currents were also observed in a chloride flux assay. Interestingly, currents were only observed in complex lipid mixtures containing *Escherichia coli* polar lipids and none were observed in mixture containing POPE/POPG at 3:1 ratio. Furthermore, reconstituted afTMEM16 also displayed a Ca^{2+}-dependent lipid scrambling activity. It could transport a wide range of NBD-labelled phospholipids such PS, PE, PC and glucosylceramide. Combining all the findings, Malvezzi et al. proposed that afTMEM16 contains separate pathways for ions and lipids as the two functions show two differential patterns of lipid requirement. This study reinforce the idea proposed by TMEM16F studies that some TMEM16 proteins might indeed exist as both lipid scramblase and ion channels.

1.5. Aim and Outline of Thesis

Calcium-activated chloride channels play an important role in cellular physiology ranging from epithelial secretion to the regulation of neuronal and cardiac excitability. Their importance and abundant expression has put them into the focus of ion channel research for more than three decades. However, the uncertainty of their molecular identity has limited their studies to native tissues, which poses its own set of limitations. The discovery in 2008 that TMEM16A underlines the observed CaCC activity in several tissues has opened up new avenues of research. To date there is still little known about the molecular mechanisms underlying channel function. Furthermore, it was reported over the years that other TMEM16 members are not ion channels and that they might be lipid scramblases or may contain both functions. The contradicting reports highlight the diverse functions of TMEM16 proteins and underline how little is known about their architecture and structure function relationships.

The aim of my thesis was to gain insight into the structural properties of the TMEM16 family by X-ray crystallography and subsequently apply the structural information to understand how TMEM16A functions as a Ca-activated chloride channel. In this context the molecular structure of a TMEM16 protein would provide a framework to reveal the mechanism of ion transport and channel activation in TMEM16A and provide explanation behind the diverse molecular functions of TMEM16 family members.

The first part of the thesis describes the expression screening for TMEM16 homologues suitable for structure determination by X-ray crystallography. After several iteration of expression and purification screening, nfiTMEM16 was identified as a suitable candidate for crystallization trials and subsequently obtain diffracting crystals. Although the diffraction resolution was too low for structural determination, the search for more closely related fungal genes using nfiTMEM16 sequence led to the discovery of nhTMEM16. The crystal structure determination of nhTMEM16, was described in the thesis of Janine Brunner. The structure revealed the architectural framework for the TMEM16 family and provided insight into potential scrambling mechanisms in and ion conduction in TMEM16 proteins. The second part of the project focused on applying the newly gained structural knowledge to study the molecular mechanism of channel activation in TMEM16A. We showed the role of the conserved Ca^{2+} binding site of TMEM16A in channel activation by Ca and proved that TMEM16A contains two independent ion conduction pores.

2. Result

2.1 Selection of TMEM16 homologues for structural studies

Members of TMEM16 family are found throughout eukaryotes with a high degree of conservation. Fungal and protista homologues share 20-30% sequence identity to mouse TMEM16A while the homologues from the animalia and plantae kingdom share 40-90% sequence identity. There are up to ten paralogs in mammals and up to two members in fungi and protista. As mouse TMEM16A was functionally characterized as a CaCC, it was used as the initial query in BLAST (basic local alignment search tool) search. Pairwise sequence alignments were scored based on the Blosum62 block substitution matrix using NCBI BLASTp (104, 105)according to their degree of sequence conservation.

A large number of positive hits were obtained from the search. In order to narrow them down to a manageable number of genes for expression screening, few criteria were imposed. Firstly, compact proteins with short termini and loops were given priority since flexible and potentially unstructured loops might be disadvantageous for crystallization. Secondly, as the primary choice of host for expression screening is *Saccharomyces cerevisiae*, homologues from funghi were given priority due to their closer relationship to the expression host, hence increasing the chance of the protein for being folded correctly and expressed well. Additionally, in the case of multiple paralogs within a species, up to two proteins per species were chosen to allow for a diverse gene pool to be tested. With that in consideration, a total of 65 homologues were initially selected and screened (Table 2).

The expression screens were performed in multiple rounds. In each round, a pool of approximately 20 genes were selected and characterized biochemically. From the outcome of the preceding rounds, proteins which showed superior biochemical or crystallization properties were used as the sequence query for the subsequent BLAST searches. This would allow the identification of homologues with high sequence identity to the query, hence potentially increasing the chance of identifying new homologues which perform similarly well or better with respect to their biochemical properties.

No.	Species	Origin	Shortname	NCBI or Uniprot accession no.	aa length	Identity (%)
1	**Ajelomyces capsulatus**	fungi	acaTMEM16	XM_001537152.1	743	25.1
2	**Arthroderma benhamiae**	fungi	abeTMEM16	XM_003015597	784	24.4
3	**Arthroderma otae**	fungi	aotTMEM16	XP_002849760.1	745	26.1
4	**Aspergillus clavatus**	fungi	acl1TMEM16	XP_001274896.1	725	23.1
5	**Aspergillus clavatus**	fungi	acl2TMEM16	XP_001274970.1	738	25.7
6	**Aspergillus flavus**	fungi	afl1TMEM16	B8N5V7	823	27.4
7	**Aspergillus flavus**	fungi	afl2TMEM16	XP_002377441.1	763	24.1
8	**Aspergillus fumigatus**	fungi	Af2TMEM16	XP_746520.1	729	22.1
9	**Aspergillus fumigatus**	fungi	Af1TMEM16	XP_746483.1	735	26.6
10	**Ashbya gossypii**	fungi	agoTMEM16	Q75B72	926	23.3
11	**Aspergillus nidulans**	fungi	aniTMEM16	CBF78946.1	715	24.7
12	**Aspergillus niger**	fungi	anig1TMEM16	XP_001400927.1	734	27.1
13	**Aspergillus niger**	fungi	anig2TMEM16	XM_001400785	734	22.2
14	**Aspergillus terreus**	fungi	ate1TMEM16	XP_001213993.1	741	25.5
15	**Aspergillus terreus**	fungi	ate2TMEM16	XP_001211316.1	728	23.1
16	**Bortryotinia fuckeliana**	fungi	bfuTMEM16	CCD55619.1	739	29.5
17	**Candida albicans**	fungi	calTMEM16	XP_711758.1	952	23.4
18	**Candida glabrata**	fungi	cglTMEM16	Q6FUD4	929	22.9
19	**Chaetomium thermophilum**	fungi	cthTMEM16	G0S5G1	743	24.5
20	**Coccidioides immitis**	fungi	cimTMEM16	XP_001241728.1	771	25.1
21	**Cordiceps militaris**	fungi	cmiTMEM16	EGX94757.1	751	23.6
22	**Exophiala dermatitis**	fungi	edeTMEM16	EHY59986.1	739	24.1
23	**Fusarium oxysporum**	fungi	foxTMEM16	EGU84773.1	732	25.2
24	**Glomerella graminicola**	fungi	ggrTMEM16	EFQ27658.1	732	24.5
25	**Giberella zeae**	fungi	gzeTMEM16	XP_389929.1	737	24.7
26	**Kluyveromyces lactis**	fungi	klaTMEM16	Q6CVG2	857	20.6
27	**Lachancea thermotolerans**	fungi	lthTMEM16	C5DIR7	890	22.5
28	**Leptosphaeria maculans**	fungi	lmaTMEM16	CBX99755.1	646	23
29	**Magnaporthae oryzae**	fungi	morTMEM16	XP_003714771.1	825	22.8

30	**Metharhizium acridum**	fungi	macTMEM16	EFY92738.1	665	25.1
31	**Nectria haematococca**	fungi	nhTMEM16	XM003045982.1	735	24.8
32	**Neurospora crassa**	fungi	ncaTMEM16	Q7S8J4	738	27.2
33	**Neosartorya fischerii**	fungi	nfiTMEM16	XP_001262513.1	735	26.4
34	**Penicillium chrysogenum**	fungi	pchTMEM16	XP_002558196.1	736	26.7
35	**Penicillium marneffei**	fungi	pmaTMEM16	B6QU56	730	24.3
36	**Phytophthora infestans**	fungi	pinTMEM16	D0MXY8	765	24.1
37	**Pichia pastoris**	fungi	ppaTMEM16	XP_002491412.1	888	20.4
38	**Pyrenophora teres**	fungi	pteTMEM16	XM_003305265.1	721	24.12
39	**Saccharomyces cerevisiae**	fungi	sceTMEM16	P38250	946	23
40	**Scheffersomyces stipitis**	fungi	sstTMEM16	A3LWT2	887	20.7
41	**Schizosaccharomyces pombe**	fungi	spoTMEM16	O13621	668	22.5
42	**Sclerotinia sclerotiorum**	fungi	ssclTMEM16	XM_001585956.1	750	23.5
43	**Sporotrychum thermophile**	fungi	sth1TMEM16	G2Q4S1	731	25.5
44	**Sporotrychum thermophile**	fungi	sth2TMEM16	G2QG98	718	24.3
45	**Talaromyces stipitatus**	fungi	tstTMEM16	B8MP59	730	25.1
46	**Trichoderma virens**	fungi	tviTMEM16	EHK43266.1	720	23.5
47	**Uncinocarpus reesii**	fungi	ureTMEM16	C4JI53	733	25.9
48	**Ustilago maydis**	fungi	umaTMEM16	Q4P618	951	24.2
49	**Verticillum albo-atrum**	fungi	valTMEM16	XM_003003988.1	741	24.6
50	**Xenopus laevis**	amphibia	xlaTMEM16A	B5SVV6	979	77.1
51	**Taeniopygia guttata**	bird	tguTMEM16A	H0Z4V6	952	86.1
52	**Danio rerio**	fish	dreTMEM16A	NP_001155062.1	925	64
53	**Acyrthosiphon pisum**	insect	apiTMEM16	XP_001944325	892	39.8
54	**Bos taurus**	mammalian	btaTMEM16A	NP001179646.1	985	92.3
55	**Homo sapiens**	mammalian	hsaTMEM16Aa,ac,abcd	Q5XXA6	956,960,1008	~92
56	**Mus musculus**	mammalian	mTMEM16A	Q8BHY3	960	100
57	**Mus musculus**	mammalian	mTMEM16B	Q8CFW1	1002	59.1
58	**Sus scrofa**	mammalian	sscTMEM16A		885	82.1

59	**Arabidopsis thaliana**	plant	athTMEM16	NP_177445.2	665	27.4
60	**Physcomitrella patens**	plant	phpaTMEM16	A9RCS9	627	26.2
61	**Sorghum bicolor**	plant	sbiTMEM16	SB03G032470	657	29.1
62	**Vitis vinifera**	plant	vviTMEM16	D7U040	951	26.4
63	**Phaeodactylum tricornutum**	protista	ptrTMEM16	B7G411	731	23.4
64	**Tetrahymena thermophila**	protista	tthTMEM16	TTHERM_0010718	847	22.2
65	**Thalassiosira pseudonana**	protista	tpsTMEM16	XP_002291773.1	724	24.4

Table 2 List of TMEM16 proteins investigated in the expression screen in Saccharomyces cerevisiae.

The table shows a summary of TMEM16 proteins chosen for the expression screen. The shortname identifier will be used throughout this thesis. Either the NCBI accession number or the UniProt code of the protein is specified. The sequence length of each homologue is indicated as number of amino acids (aa), the sequence identity between mTMEM16A and the homologues was derived from Clustal Omega.

2.2 Expression, Purification and Crystallisation Screening towards a Structural Characterisation

2.2.1 General Strategy using GFP-based expression and purification pipeline

Protein crystallography has high requirements with respect to the biochemical stability of the target protein. Preferably milligram amounts of well-folded protein is need to be produced per production round and purified to homogeneity before setting up crystallization trials. Additionally, membrane proteins have to be extractable by detergents and ideally remain stable at protein concentrations of several milligrams per milliliter. These considerations should to be taken into account when choosing the expression and purification pipeline.

To facilitate the identification of well-expressing and stable homologues for crystallization trials from a large starting pool of homologues, we adopted a GFP-based expression screening in *Saccharomyces cerevisiae* and a purification pipeline from Drew et al. (106). As TMEM16 proteins are only found in eukaryotes and a majority of the cloned homologues originated from fungi, the use of *Saccharomyces cerevisiae* as eukaryotic overexpression host would improve the chance of the homologues being folded properly, hence increasing the yield of well-folded proteins. *S. cerevisiae* was chosen over the methylotrophic yeast *Pichia pastoris* due to the much shorter cloning and selection procedure. In *P. pastoris*, genes must be first cloned into vectors in bacteria before genomic integration and multiple clones have to be tested in terms of their expression properties to find highly expressing ones for each gene. The use of enhanced green fluorescence protein (eGFP) fusion tag enables a quick quantitative assessment of the protein yield and stability at any stage of the screening process. It allowed to identify the stages of the pipeline that would need further optimization. Each gene is expressed as construct with either N-terminal or C-terminal tags bearing 3C-cleavage site, eGFP and 6xHis (Figure 2).

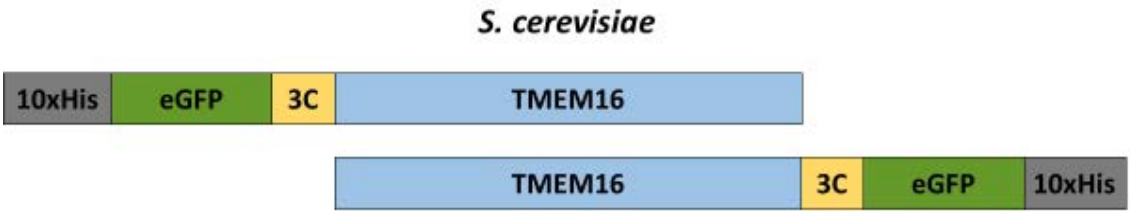

Figure 2 Scheme of construct Design for homologue expression screening in *S. cerevisiae*.

Scheme of N-terminally tagged or C-terminally tagged construct coded by pYES2CT vector. 10xHis = 10 His residues, eGFP = enhanced green fluorescent protein, 3C = 3C protease cleavage site.

The screening process was carried out in three stages. In the first stage, a small-scale expression screen was performed in 20 ml cultures per construct to assess the expression level of each homologue. This is achieved by measuring the whole-cell fluorescence post induction during the harvest step and Western Blot analysis of detergent-solubilized membrane extract. Quick assessment of the protein quality could be gained by subjecting detergent-solubilized membrane extract of each construct to size exclusion chromatography. By detecting the fluorescence of the GFP tag, the 'monodispersity' of the protein peak could be investigated without the need of any protein purification step. This provides an indication of which homologues are behaving well biochemically. Well behaved proteins were scaled up to 1-5 liter of culture. The medium scale

assessment stage comprised the investigation of the scalability of protein expression, purification of the protein with Nickel immobilized metal affinity chromatography (IMAC) via the 6xHis tag of the construct, the removal of the eGFP-His tag by limited proteolysis and further purification using size exclusion chromatography. The protein is assessed in terms of its yield and stability post purification. In case of a favorable behavior, the protein production is scaled up to 20-40 liter of culture. At this large-scale stage, the main aim is to establish a reproducible and optimized pipeline to repeatedly produce protein of sufficient quantity and quality for broad crystallization screening.

2.2.2 Small scale expression screening of homologues in S. cerevisiae

In the small scale expression screening, a total of 65 homologues were expressed with either N-terminal and/or C-terminal yEGFP tag in 50 ml culture. Expression was under the control of the GAL1 promoter and induced by addition of 2% galactose and usually proceeded for 40 hours at 30 °C in a shaker incubator. During harvest, the cultures were diluted to the same cell density (judged by measurement of the OD_{600}) and their fluorescence signal were quantified to obtain a relative measure of the whole-cell expression yield of the protein. For analysis, all cultures were pelleted and resuspended to an OD_{600} of 60, before being lysed by a bead-beater homogenizer. Cell debris and unlysed cells were removed by low speed centrifugation. The membrane fraction was pelleted by ultracentrifugation, resuspended in one fifth the volume of buffer used during the lysis step and extracted with 1% n-Dodecyl β-D-maltoside (DDM). After solubilization, the insoluble components are pelleted by ultracentrifugation to obtain the solubilized membrane fraction. The fluorescence of the total membrane extract and the solubilized membrane fraction were measured to estimate the solubilization efficiency. To verify the estimation, SDS-PAGE of the samples were performed followed by in-gel fluorescence detection and Western blot using anti-His antibody.

The expression behavior of a representative selection of the homologues is summarized in (Table 3) and discussed below. The fluorescence measurement throughout the small-scale screening allowed an approximate quantification of the GFP-tagged constructs. The whole-cell fluorescence provided a first criteria for selection. Only constructs which gave fluorescence reading higher than 5000 RFU were lysed and further analyzed. Overall, the N-terminal GFP-tagged constructs expressed better than their C-terminal GFP tagged counterparts. Remarkably, the whole-cell fluorescence did not correlate well with the fluorescence of the total membrane fraction during extraction. This could be due to a varying percentage of misfolded proteins with correctly folded GFP which were removed during low speed centrifugation speed prior to pelleting of the membrane fraction by ultracentrifugation. The membrane protein extraction with DDM was a bottleneck in the screening procedure resulting in significant drop in the protein yield. The solubilization efficiency of the homologues, as calculated from the fluorescence reading of the detergent-extracted sample before and after ultracentrifugation, varied between 20 to 50%. The solubilization efficiency of C-terminally tagged constructs were consistently lower than that of N-terminally tagged constructs thus indicating a potential misfolding of the protein.

Construct		Wholecell fluorescence (RFU)	Total membrane fluorescence (RFU)	Solubilized membrane fluorescence (RFU)	Solubilisation efficiency (%)
ncrTMEM16	N-GFP	19900	48300	22000	46
	C-GFP	17700	30200	10700	35
nfiTMEM16	N-GFP	24000	9300	4700	**51**
	C-GFP	20100	7300	3200	44
gzeTMEM16	N-GFP	36900	14900	7600	**51**
	C-GFP	44700	20100	6100	30
klaTMEM16	N-GFP	23800	35500	10100	28
	C-GFP	15500	20400	5300	26
calTMEM16	N-GFP	33000	14100	4800	34
	C-GFP	22300	3400	1000	29
afu1TMEM16	N-GFP	17300	3000	1000	33
	C-GFP	13700	1800	400	22
-ve		700	500	600	-

Table 3 Fluorescent measurement of selected homologues during small-scale screening.

Whole cell fluorescence was measured after normalization to the same cell density. Total membrane fluorescence and solubilized membrane fluorescence was measured after the membrane fraction had been solubilized with DDM before and after high speed ultracentrifugation respectively. Solubilization efficiency indicates the percentage of remaining fluorescence after the high speed ultracentrifugation.

Following solubilization, the samples were loaded onto a SEC column for FSEC analysis. The size exclusion profile of each homologue was recorded with a fluorescence detector monitoring the fluorescence of the GFP tag. For this selection, most homologues exhibited a monodispersed peak at an elution volume around 10 ml corresponding to approximately twice of the respective molecular weights of a single subunit (Figure 3a-e, g-i). The N-GFP construct of one homologue, klaTMEM16 (Figure 3d), despite showing a fluorescent signal similar to nfiTMEM16 (Figure 3b), did not produce any peak significantly above background on SEC. In another case, af2TMEM16 (Figure 3f), the lack of a peak in the FSEC profile above background level was attributed to a low amount of protein present even before solubilization (Table 3). The general trend was that if N-GFP tagged homologues yielded clear monodispersed peak (eg. ncrTMEM16 and nfiTEM16, Figure 3a,b), the C-GFP tagged constructs would also yield monodispersed peak albeit with a lower fluorescence signal. In some cases, the C-GFP tagged construct (klaTMEM16, Figure 3d) would yield peak at higher elution volume, indicative of protein degradation. Secondly, there was no observed case where C–terminally tagged homologue would perform better than N-terminally tagged variant. For these reasons, the fourth expression screening round only focused on N-terminally tagged fungal homologues (eg. tviTMEM16, anig1TMEM16, nhTMEM16, Figure 3g-i).

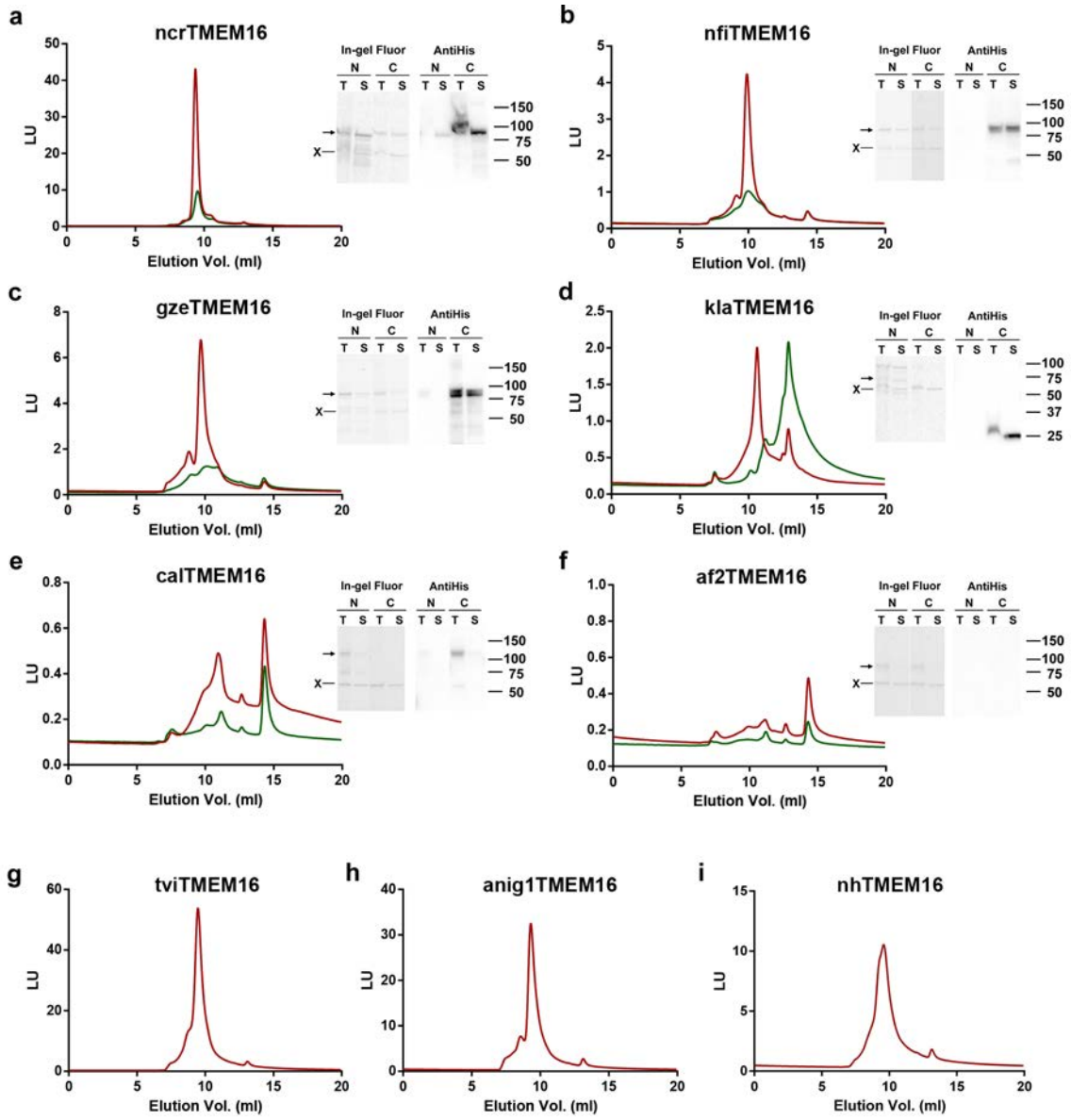

Figure 3 FSEC profiles of selected TMEM16 family members.

TMEM16 proteins fused to EGFP were extracted from membranes of *Saccharomyces cerevisiae* and the cleared supernatant was subsequently subjected to fluorescence size exclusion chromatography (FSEC). The profile of N-terminal and C-terminal GFP tagged constructs are shown in red and green respectively. Samples were run on a GF-450 column, fluorescence was excited at 480 nm and emission detected at 515 nm. A peak around 9.5 min corresponds to stable and intact protein. In-gel fluorescence image and Western Blot with an AntiHis antibody are shown to the right of each FSEC profile. Mw in kDa is shown on the right. The arrow indicates the position of homologues. X indicates fluorescent band present in non-induced cell extract. N = N-terminal GFP tag, C = C-terminal GFP tag, T = Total membrane extract, S = Soluble membrane extract.

To verify the molecular weight of the constructs, samples of the total and solubilized extract were run on SDS-PAGE and analyzed by in-gel fluorescence and Western Blot using an antiHis antibody. FSEC profiles of selected TMEM16 family members.). With the exception of klaTMEM16, all homologues migrated at the expected molecular weight. The low Mw band of klaTMEM16 on the Western blot confirmed that the protein was degraded. In general, there is a variable discrepancy between in-gel fluorescence and Western Blot. While In-gel fluorescence always revealed the protein band when there is measurable fluorescent signal in the sample, the corresponding band might occasionally be omitted on Western Blot. This could be due to the occasional inefficient transfer of the respective protein from the whole-cell extract onto the blot. The relative intensity of the bands on the in-gel fluorescence image also does not correlate well with those of Western Blots. Overall, these two methods should be used mainly for a qualitative check of the protein integrity rather than quantification.

2.2.3 Scale-up and purification of positive hits from the expression screen

The small-scale screening of homologues from 50ml cultures has identified 10 promising homologues, which expressed well and behaved well biochemically. To further investigate the stability of these constructs and to estimate the protein yield, a medium scale purification was carried out. 5-7 liter of culture were grown either in shake flasks or a fermenter and the expressed proteins in the isolated membrane fraction were extracted with DDM and affinity purified by IMAC. The eluted purified protein was incubated with 3C protease to cleave off the GFP-His fusion tag. The digested fractions were subsequently dialyzed to remove imidazole, subjected to a second IMAC step to remove the cleaved fusion tag, and further purified by size exclusion chromatography to investigate the dispersity and the yield of fusion tag-free proteins.

In general, all 10 homologues could be scaled up successfully and purified by IMAC. The yield of the purified tagged protein ranged between 0.2 to 2mg per liter of expression culture. Several homologues, such as ncrTMEM16 (Figure 4a) were only stable with GFP tag. Cleavage of the fusion tag by 3C protease in this case resulted in aggregation of the majority of the protein. When the remaining non-aggregated protein fraction was injected onto a size-exclusion column, wide dispersed peaks were observed. The results suggest that ncrTMEM16 is stabilized by the GFP tag and is not stable on its own. Apart from this case, the majority of the homologues tolerated the cleavage by 3C protease. Significant precipitation was observed during the protein concentration step of all homologues prior to SEC analysis. Nonetheless, the homologues exhibited a peak corresponding to the column void volume and another peak corresponding to the estimated elution volume of dimeric constructs. Reinjection of the fraction from the main peak yielded variable result. With stable homologues such as nfiTMEM16 (Figure 4b), a single monodispersed peak was observed, indicating that the purified protein was stable and did not form aggregates spontaneously. While with other homologue such as anig1TMEM16 (Figure 4c), an additional peak at the column void volume was observed, suggesting that the purified protein was less stable.

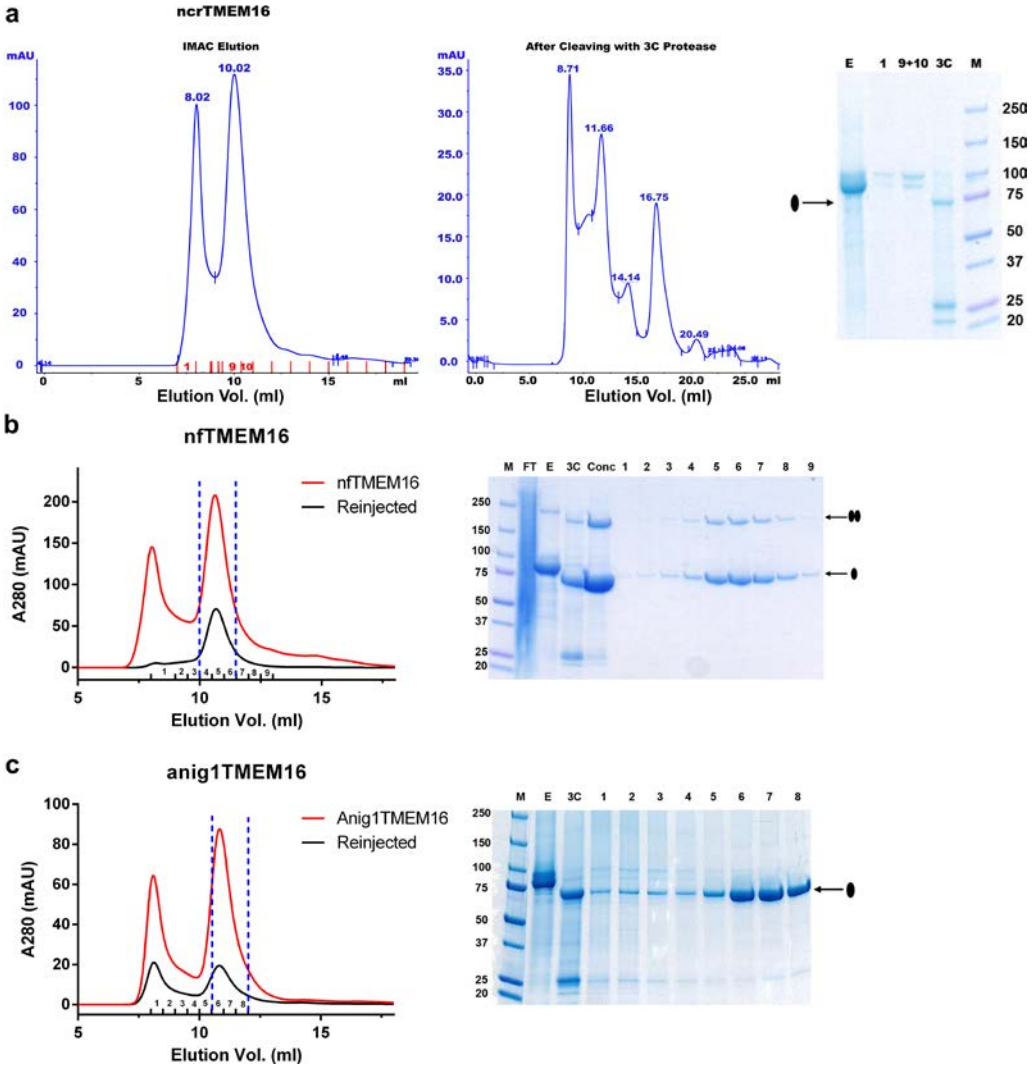

Figure 4 Protein purification of selected homologues.

a, SEC profile of ncrTMEM16-NGFP after IMAC and ncrTMEM16 after cleavage of the GFP tag respectively. **b**, SEC profile of nfiTMEM16. **c**, SEC profile of anig1TMEM16. In **b** and **c**, the black trace shows a SEC profile of the reinjected main peak fraction outlined by the dotted blue line. Right, SDS PAGE gel of samples from IMAC and gel filtration. M = Marker, FT = flowthrough after binding with Ni-NTA resin, E = Elution with high concentration of imidazole, 3C = fraction after incubation with 3C protease, conc = concentrated sample prior to injection onto gel filtration column. Arrow indicates the protein band at as monomer or dimer.

2.2.4 Optimisation of nfTMEM16

In order to increase the stability of the protein and to improve the likelihood of crystal formation, nfTMEM16 was systematically truncated at its termini (Figure 5). Disordered region prediction using the Disopred server (http://bioinf.cs.ucl.ac.uk/index.php?id=806) suggested a 10 amino acid unstructured region at the N-terminus and approximately 80 amino acid unstructured region at the C-terminus. In order to obtain a stable minimal construct for crystallization, the protein was truncated on each terminus in steps of 10 amino acids up to the predicted transmembrane region. As the truncation approached the transmembrane region predicted by TMHMM server (http://www.cbs.dtu.dk/services/TMHMM/), the

truncation was done in smaller increments as a precaution to avoid cutting into the transmembrane region. Overall, 18 N-terminal and 10 C-terminal truncations were selected. The sequences encoding for truncated proteins were created by PCR and cloned as GFP fusion construct. In order to minimize the effect of the GFP fusion on the stability of the modified protein, the N-terminally truncated protein was fused to GFP at the C-terminal end and vice-versa.

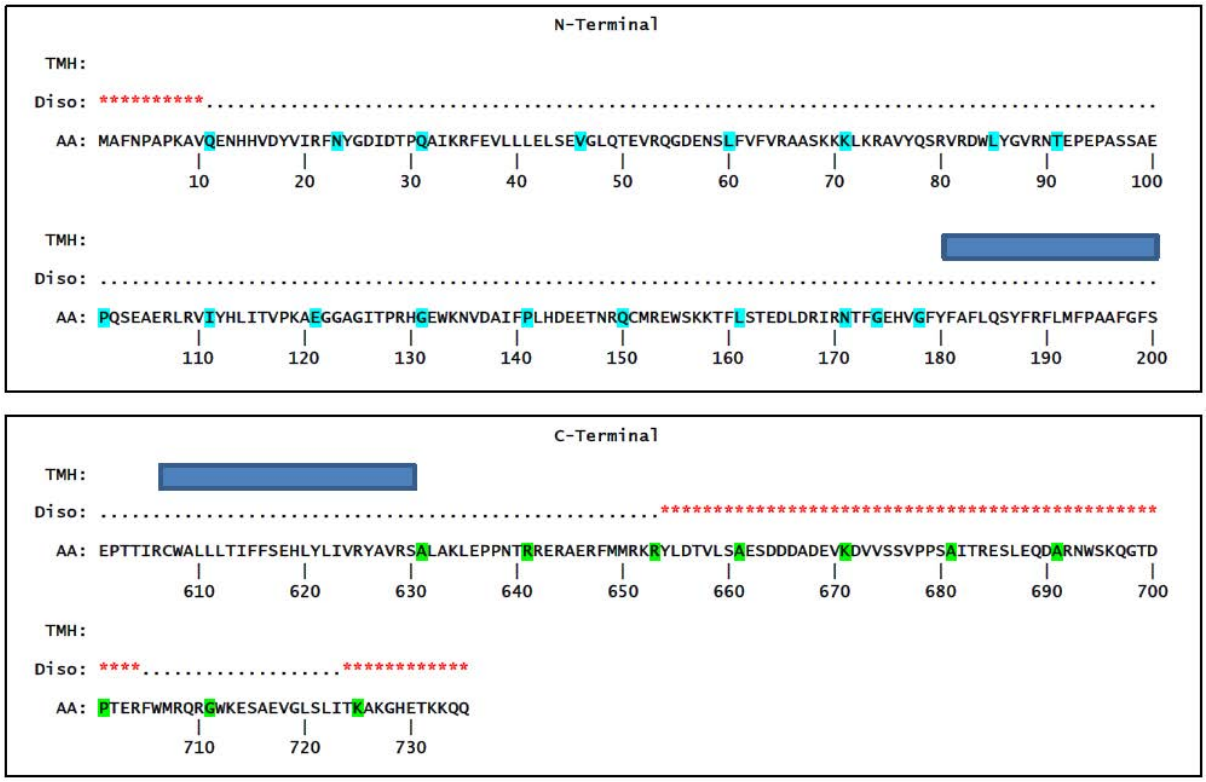

Figure 5 Truncation of nfTMEM16 terminal domains.

Blue rectangles represent the first or last predicted transmembrane helix after and before the two terminal domains. Truncations were introduced at the highlighted residues. Disorder prediction was performed on the Disopred server and transmembrane helix prediction was performed with TMHMM. Potentially disordered regions are indicated by *.

To assess their biochemical properties, the eGFP-fusion truncation constructs were expressed in *S. cerevisiae* as 50 ml cultures. The cells were lysed and the DDM-solubilized membrane fraction was applied to a size-exclusion column for FSEC analysis (Figure 6). The expression of C-terminal GFP fusions constructs of nfTMEM16 was significantly lower than the N-terminal GFP variant, which is consistent with the results from the wide homologue screen described in 2.3.2. Of the 18 N-terminal truncation mutants tested, only the construct with the first 10 aa truncated (N-11) exhibit a peak at the expected volume, albeit with low signal (Figure 6a). The results suggested that only the first 10 amino acids, which were predicted to be disordered, could be truncated without affecting the N-terminal domain adversely. The remaining N-terminal truncations might disrupt the secondary structure of the N-terminal domain and consequently affect the folding of the protein.

As ‘N-terminal GFP-fusions’, the C-terminal truncation mutants generally performed better with respect to their biochemical behavior (Figure 6b). Apart from the first 3 truncations, all mutants eluted as a monodispersed peak in FSEC analysis. 661-C mutant (without residue 663 and higher) gave the highest signal and further truncations towards the C-terminus gradually decreased the intensity of the peak. The result suggested that truncation at Ala661 generated the shortest construct at the C-terminus that still results in a stable core protein. Further truncations were tolerated but affected either the total expression or the stability of the constructs.

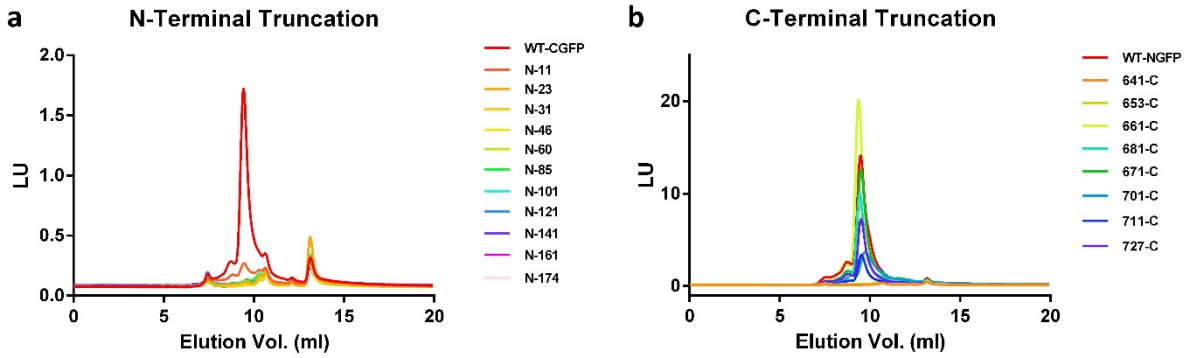

Figure 6 FSEC of N-terminal and C-terminal truncated nfTMEM16.

FSEC profile of whole cell lysate containing **a,** N-terminally truncated nfTMEM16 constructs with C-terminal GFP fusion or **b,** C-terminally truncated nfTMEM16 construct with N-terminal GFP fusion.

As 661-C construct behaved biochemically very similar to the WT nfTMEM16 and its expression level was high, the expression culture was scaled up to 20 liter for crystallization trial. The purification of 661-C-nf yielded a protein with a monodisperse peak on SEC and high purity as confirmed by SDS PAGE (Figure 7a). In an attempt to improve the crystallization properties of the 661-C construct, the protein was purified with the shorter detergent UDM. The smaller detergent micelle could potentially expose more of the protein surfaces that may provide additional crystallization contacts. However, as direct solubilization of membrane vesicles bearing 661-C with UDM resulted in aggregation, the protein was instead solubilized and purified with DDM before exchanging the detergent by applying it to a second gel filtration step in a column incubated with 0.3% UDM (Figure 7b). The partial exchange into UDM yielded a main peak corresponding to the protein at right Mw preceded by a ‘shoulder’ and a void peak. The construct is less stable in UDM than in DDM but it was stable enough to be used for crystallization screening.

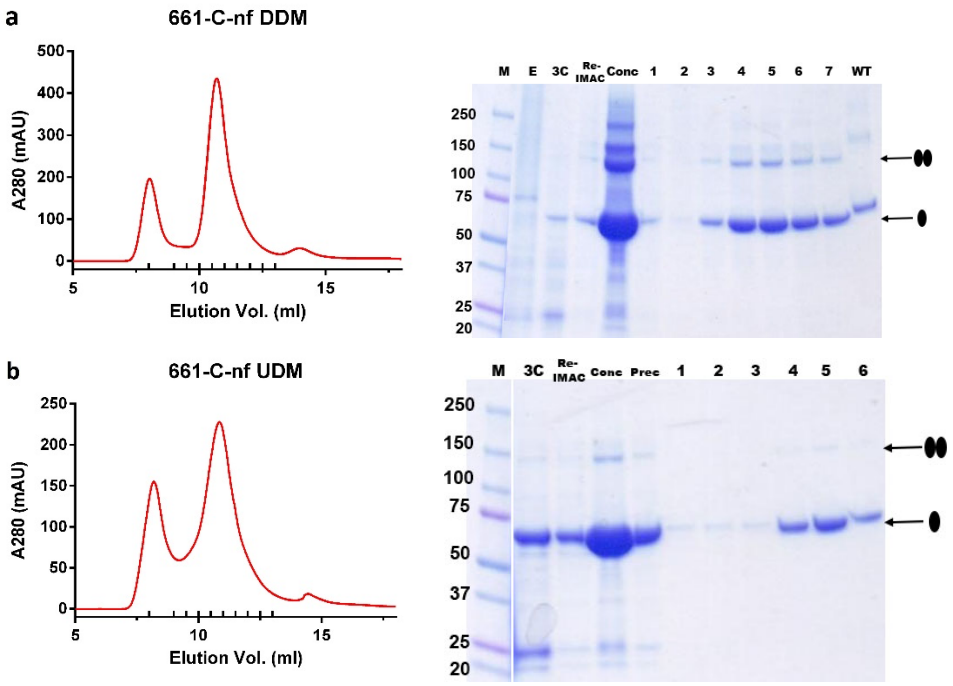

Figure 7 Protein purification of 661-C-nf

a, Size exclusion chromatography of the truncated construct 661-C-nf in 0.03% DDM buffer after cleavage of the tag by 3C protease. **b,** Size exclusion chromatography of truncated construct in 0.3% UDM 661-C-nf after cleavage of the tag by 3C protease. Buffer exchange from DDM to UDM was performed on size exclusion column. right, SDS PAGE gel of a sample from IMAC and gel filtration. M = Marker, E = Elution with high concentration of imidazole, 3C = fraction after incubation with 3C protease, re-IMAC = after second IMAC step to remove cleaved tag and 3C protease, conc = concentrated sample prior to injection onto gel filtration column. Arrow indicates the protein band at as monomer or dimer.

2.2.5. Crystallization of nfTMEM16

Crystallization of nfTMEM16 was broadly screened in 100 nl volume by vapor diffusion in sitting drops. Over 2000 conditions were screened through a combination of commercially available sparse matrix screens and an in-house systematic grid screen. Despite its purity nfTMEM16 only crystallized in one condition: 50 mM Glycine pH 9.4, 100mM NaCl, 1 mM $CaCl_2$, 25% PEG400. The diffraction properties of crystals was investigated at the X06SA (PXI) beamline at the Swiss Light Source after cryoprotection in 35% PEG400 and flash-freezing in liquid propane. Initial crystals diffracted up to 10 Å. Despite extensive refinement of crystallization conditions such as fine-tuning around the initial crystallization conditions and inclusion of crystallization additives, the diffraction did not improve significantly.

Crystallization trials with the truncated construct, 661-C-nf, purified in DDM yielded crystals in 5 conditions. When the protein buffer was exchanged into UDM buffer via size-exclusion chromatography, the number of crystallization hits increased to approximately 50 conditions. Crystallization with lipid and detergent additives did not further increase the number of hits but improved the size and appearance of the crystals. Ultimately, the condition giving the best diffracting crystal was obtained from 50 mM Glycine pH 9.2, 150 mM Mg-Acetate, 1 mM $CaCl_2$, 0.3 mM Sucrose monolaurate, 0.1 mM yeast polar lipid (Avanti) (Figure 8a).

The crystal diffracted to ~7.4 Å (Figure 8b, Table 4) and is of space group of $P2_12_12$ with the cell dimension of a=148.8 Å, b= 275.8 Å, c= 277.6 Å, α=β= γ =90°. The Matthews parameter was calculated to estimate the number of protein molecules per asymmetric unit (107). 8 molecules per asymmetric unit were estimated with solvent-content of 71%.

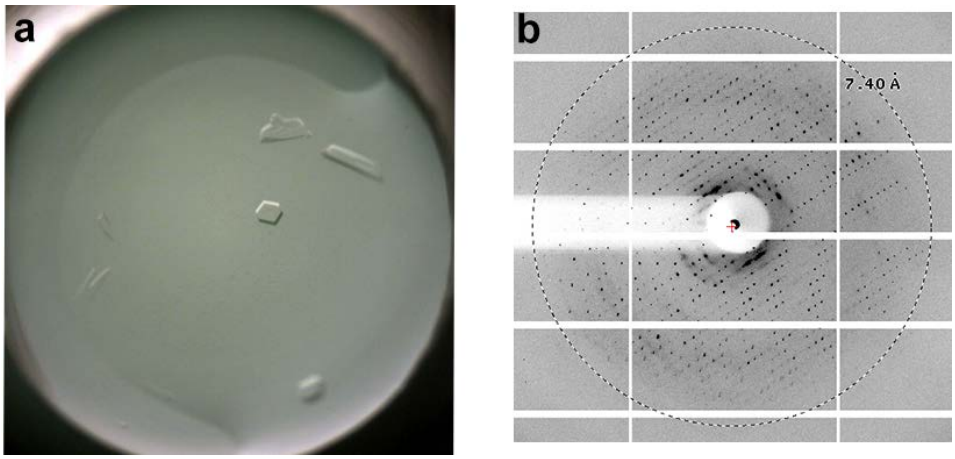

Figure 8 Best diffracting crystal of truncated nfTMEM16 construct 661-C-nf

a, Initial crystal hit. **b,** Diffraction pattern collected at PXI. Resolution limit is at 7.4 Å.

SUBSET OF INTENSITY DATA WITH SIGNAL/NOISE >= -3.0 AS FUNCTION OF RESOLUTION

RESOLUTION LIMIT	NUMBER OF REFLECTIONS OBSERVED	UNIQUE	POSSIBLE	COMPLETENESS OF DATA	R-FACTOR observed	R-FACTOR COMPARED expected		I/SIGMA	R-meas	CC(1/2)
15.00	7540	1829	2026	90.3%	2.4%	2.7%	7425	37.76	2.8%	99.9*
10.00	18787	4317	4548	94.9%	6.4%	5.9%	18523	21.84	7.3%	99.6*
9.00	10766	2261	2364	95.6%	13.2%	12.6%	10651	12.26	14.7%	98.9*
8.00	15842	3533	3672	96.2%	31.8%	32.2%	15627	5.26	35.8%	94.1*
7.50	10696	2505	2601	96.3%	91.4%	93.2%	10502	1.94	103.7%	61.3*
7.40	2672	592	622	95.2%	114.5%	120.2%	2636	1.53	128.9%	55.4*
7.30	2916	624	650	96.0%	188.8%	203.6%	2880	1.06	211.5%	37.9*
7.20	3044	662	689	96.1%	163.3%	173.7%	2996	1.09	183.4%	30.9*
7.10	3119	670	701	95.6%	182.1%	197.3%	3077	1.00	204.2%	36.0*
7.00	3425	734	761	96.5%	248.8%	263.1%	3376	0.75	279.1%	21.9*
6.90	3778	786	818	96.1%	274.9%	310.1%	3739	0.69	307.7%	28.1*
6.80	3898	806	846	95.3%	280.7%	310.4%	3849	0.63	313.3%	22.3*
total	86483	19319	20298	95.2%	7.2%	7.4%	85281	11.34	8.2%	99.9*

Table 4 Data collection statistics of 661-C-nf crystal

Table of a dataset collected from a dataset of the 661-C-NF mutant with the program XDS. The number of reflections, the completeness of the data set, its calculated R-factor and the intensity over background are displayed for different resolution shells.

Despite all attempts to improve the resolution, the diffraction of truncated nfTMEM16 was not sufficient for structural determination. Nevertheless, the finding that nfTMEM16 was crystallizable lead to the use of nfTMEM16 as Blastp search query, which allowed the discovery of the fungal homologue nhTMEM16. nhTMEM16 was successfully crystallized and optimized by Janine Brunner, up to 3.3 Å resolution for structure determination (108).

2.2.6 Summary of Screening

In summary, a total of 65 homologues were screened for expression in *Saccharomyces cerevisiae* (Table 5). Approximately half of the homologues could be expressed as fusion to GFP to varying degree as quantified by the total whole-cell fluorescence reading. Low extraction efficiency by the mild detergent DDM appeared to be a big bottleneck in the pipeline as the best extraction efficiency was only up to 50% as judged by in-gel fluorescence measurement and the Western blot signal of total and solubilized membrane extract. Only half of the expressing homologues could be extracted at an efficiency above 10%. Out of these 24 homologues, 10 had a polydisperse behavior or weak signal in FSEC analysis while another 10 produced a single monodispersed peaks. It is worth noting that the positive hits with good FSEC profile were all fungal homologues, suggesting that the fungal proteins might be biochemically more stable and are thus likely more compatible with the transcription and translation machinery of *Saccharomyces cerevisiae*. The lack of expression of higher eukaryotic homologues might be due to incompatible codon usage.

From the initial expression screen, 10 homologues were scaled up to large scale expression and tested for purification. 8 of the homologues could be successfully purified. As nfiTMEM16 gave the best yield, it was the main construct used for construct optimization and crystallization. The remaining 7 homologues were also subjected to crystallization but did not yield any crystals.

	N-GFP				C-GFP			
	exp	ext	FSEC	SEC	exp	ext	FSEC	SEC
acaTMEM16	++	+	+					
abeTMEM16	++	++	+					
aotTMEM16	+	-						
acl1TMEM16	++	++	++	+				
acl2TMEM16	++	++	++					
afl1TMEM16	+	-			-			
afl2TMEM16	+	-			-			
afu1TMEM16	-				-			
afu2TMEM16	++	++	+	+	+	+	+	
agoTMEM16	-				-			
aniTMEM16	++	++	-		++	-		
anig1TMEM16	++	++	++	+				
anig2TMEM16	++	++	++					
ate1TMEM16	++	++	++	+				
ate2TMEM16	-							
bfuTMEM16	+	+	+					
calTMEM16	++	-			+	-		
cglTMEM16	++	-			+	-		
cthTMEM16	+	-			-			
cimTMEM16	+	+	+		+	-		
cmiTMEM16	-							
edeTMEM16	+	+	+	+				
foxTMEM16	-							
pchTMEM16	++	++	++	+				
pmaTMEM16	++	-			+	-		
pinTMEM16	+	-			-			
ppaTMEM16	++	-			+	-		
pteTMEM16	-							
sceTMEM16	++	-			++	-		
sstTMEM16	-				-			
spoTMEM16	++	++	++	-	+	+	+	
ssclTMEM16	-							
sth1TMEM16	+	-			-			
sth2TMEM16	-				-			
tstTMEM16	+	-			-			
tviTMEM16	++	++	++	+				
ureTMEM16	-				-			
umaTMEM16	+	-			-			
valTMEM16	-				-			
ptrTMEM16	-							
tthTMEM16	+	-			-	-		
tpsTMEM16	-							
xlaTMEM16A	-				-			
tguTMEM16A	-				-			
dreTMEM16A	-				-			
apiTMEM16	-				-			

ggrTMEM16	-							
gzeTMEM16	++	++	+	+	+	+	+	
klaTMEM16	++	++	+	-	+	+	+	
lthTMEM16	++	-			+	-		
lmaTMEM16	-							
morTMEM16	-							
macTMEM16	-							
nhTMEM16	++	++	++	+				
ncrTMEM16	++	++	++	-	+	+	+	-
nfiTMEM16	++	++	+	+	++	+	+	

btaTMEM16A	-		-	
hsaTMEM16Aa	-		-	
mTMEM16A	-		-	
mTMEM16B	-		-	
sscTMEM16A	-		-	
athTMEM16	++	-	+	-
phpaTMEM16	+	-	+	-
sbiTMEM16	-		-	
vviTMEM16	-		-	

Table 5 Overview of the 65 homologues in expression screen.

Homologues that could not be amplified are marked in grey. Minus (-) indicates that the sample was either not expressed (exp.), or extracted (ext.). Expression, extraction and stability properties on FSEC/SEC were ranked between medium (+) to good (++). Extraction was rated as -, +, or ++ when extraction efficiency is at 0-10%, 10-20% or 20-40% respectively. FSEC profile was rated as + when a peak could be resolved around elution volume of 9.5 ml and rated as ++ when a monodisperse peak with fluorescence signal higher than 5 LU was observed. SEC profile is rated as + when the scaled up purification would yield a monodisperse peak and stable protein after GFP tag cleavage by 3C protease. Grey background indicates homologues for which only N-terminally GFP-tagged constructs were tested.

2.3 Functional study of TMEM16

2.3.1 Learning from Structure of nhTMEM16

From the homologue screen, we identified nhTMEM16 as a promising candidate for structural determination. nhTMEM16 was crystallized in two different crystal forms (CF1 and CF2), for which data up to 3.3 and 3.4 Å resolution were collected respectively. Both crystal forms adopt space group $P2_12_12_1$. CF1 was obtained in crystallization condition 100 mM CAPSO pH 9.4, 100 mM $MgCl_2$, 100 mM NaCl, 21–23% PEG400 while CF2 was obtained in 50 mM HEPES pH 7.4, 100 mM ammonium sulphate, 21–23% PEG400. Both crystal forms are of space group $P2_12_12_1$. The protein buffer is 5 mM HEPES pH 7.6, 150 mM NaCl, 3 mM $CaCl_2$, 0.025% DDM. Prior to crystallization, 0.2% αUDM, 50 µg ml^{-1} yeast polar lipid extract and 2% 1,2,3-heptanetriol were added to the protein.

The crystal structure revealed a dimeric arrangement of nhTMEM16 (Figure 9a). Each subunit consists of a transmembrane domain and N-terminus and C-terminus on the cytoplasmic side. Contrary to the hydropathy analysis, the transmembrane domain is made up of ten helices preceded by two short helices (Figure 9c). The N-terminal domain adopts a ferredoxin fold while the C-terminus is mainly unstructured apart from the three helices which wraps around the N-terminus of the other subunit. The majority of the intersubunit interface was imparted by helix 10 in the transmembrane domain. The structure revealed two type of cavities. The first cavity is found close to the dimer interface, hence termed as the dimer cavity. The arrangement of the helices and relatively minimum intersubunit contacts results in a large pore-like structure which contains two separate 15 Å wide entrances at the extracellular side and which merges to one big, about 30 Å wide vestibule, at the intracellular half of the membrane. The vestibule is predominantly composed of hydrophobic and aromatic residues, which are conserved within the protein family. In the density map of the structure, the vestibule is filled with unresolved electron density which might been attributed to detergent or lipid. The second cavity is found at the surface away from the dimer interface, termed as the subunit cavity (Figure 9b). It is made up of 6 helices forming semitubular pore that is exposed to the lipid bilayer. Despite being juxtaposed to the membrane, the surface lining the cavity is hydrophilic. For TMEM16 scramblase such as nhTMEM16, this cavity is the potential site of catalysis by providing favorable path for the polar head group of the phospholipid being transported.

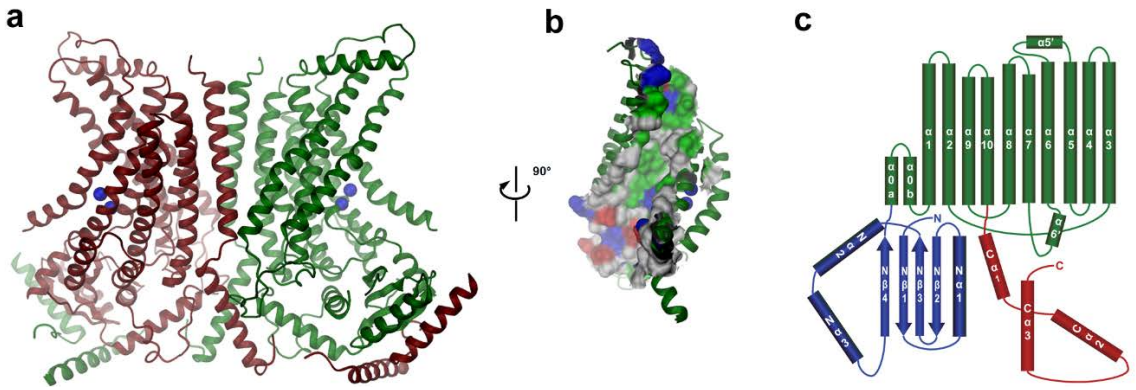

Figure 9 Structure of nhTMEM16

a, structure of nhTMEM16 viewed from within the membrane. Bound Ca^{2+} ions are displayed as blue spheres. **b,** surface of the subunit cavity. Residues are colored according to their properties (red acidic, blue

basic, green polar). **c,** Topology of the nhTMEM16 subunit. The transmembrane domain is colored in green, the N- and C-terminal domains in blue and red, respectively.

The structure also revealed a Ca^{2+} binding site embedded between TM helices 6, 7 and 8 in each subunit of the dimer (Figure 10a). The binding site consists of five acidic residues and one asparagine. Sequence alignment with TMEM16 members in mammal showed the residues are highly conserved despite wide functional divergence in TMEM16 family (Figure 10b). On the anomalous difference density map, two strong peaks corresponding to Calcium anomalous scattering were observed within the binding site, implying that there are two Ca^{2+} ions present. Although the occupancy could not be determined with certainty from the crystallographic data, simultaneous occupation of two Ca^{2+} ions appeared highly plausible judging from spatial availability and the presence of the 5 acidic residues for coordination.

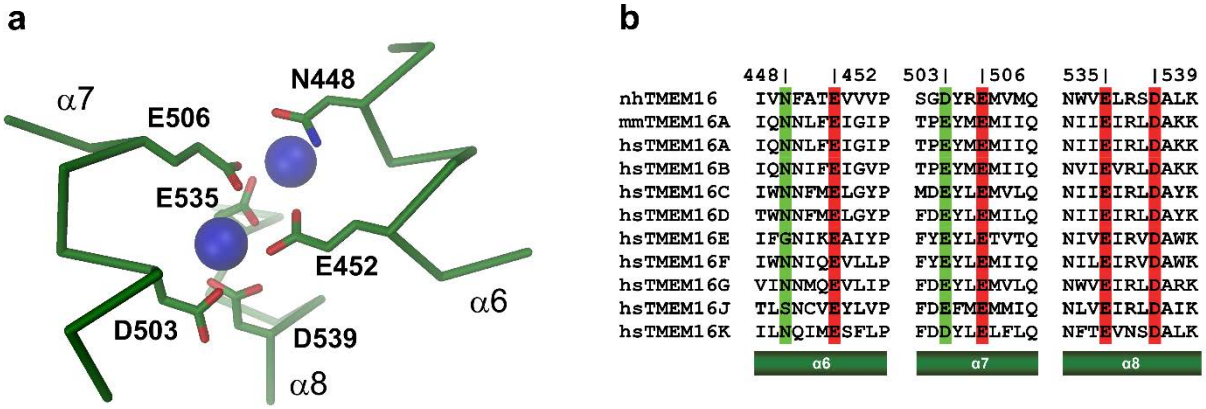

Figure 10 Ca^{2+}-binding site in nhTMEM16.

a, model of Ca-binding site in nhTMEM16. **b,** Sequence alignment of the mammalian TMEM16 members with nhTMEM16. The residue numbering is based on nhTMEM16.

In the following sub-chapter 2.4.2, I show that nhTMEM16 is most likely not functioning as an ion channel. However, due to high sequence identity between the homologues, the general architecture must be conserved among protein family and therefore applicable to members performing as CaCC, such as TMEM16A. The crystal structure of nhTMEM16 provided a wealth of information which explain the gating mechanisms of CaCC and also raised several questions about the architecture of CaCC. The sub-chapter 2.4.3 will focus on addressing these aspects.

2.3.2. Investigating nhTMEM16 potential role as an ion channel

Reconstitution of nhTMEM16 and planar lipid bilayer recording

nhTMEM16 was shown by Janine Brunner (108)in our lab to function as a lipid scramblase. The previous study by Malvezzi et. al. (103) on the TMEM16 protein from *A. fumigatus*, afTMEM16, had proposed that afTMEM16 functions as an ion channel on top of functioning as a lipid scramblase. The recordings of reconstituted afTMEM16 in planar lipid bilayers demonstrated large non-selective conductance. The channel activity was also described to have a low probability of activation (as judged by the low macroscopic currents that only show a small number of open channels) with a weak Ca^{2+} dependence and to be highly

dependent on the composition of the lipids in the liposome. In an attempt to investigate whether a similar behavior would also be observed for nhTMEM16, the protein is expressed, reconstituted into liposome and characterized in planar lipid bilayers. As nhTMEM16 shares 48% sequence identity with afTMEM16, we decided to test whether nhTMEM16 also functions as a channel on planar lipid bilayer. Prior to that, we want to elucidate the oligomeric state of nhTMEM16 in the preparative detergent-containing buffer using multi-angle light scattering.

nhTMEM16 was expressed in S. cerevisiae in a 20 liter fermenter batch as N-terminal GFP tagged construct. The protein was extracted with DDM, purified using Nickel-NTA IMAC and size-exclusion chromatography. The protein eluted as a monodisperse peak and appeared relatively pure when ran on SDS-PAGE (Figure 11a,b). The fractions corresponding to the peak were pooled and subjected to MALS analysis (Figure11). The protein-detergent complex ran at apparent Mw of 295 kDa, of which 150 kDa was contributed by detergent DDM micelle. The theoretical Mw of nhTMEM16 is 83kDa. The experimental protein molecular weight of 145 kDa thus fit the hypothesis that nhTEM16 is a dimer in the detergent solution.

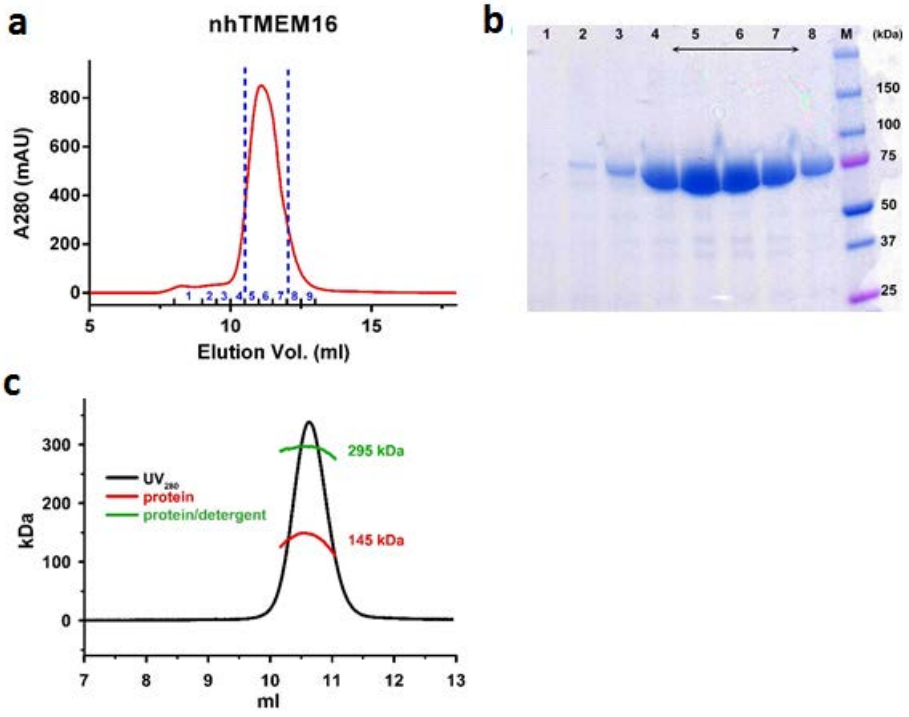

Figure 11 Purification and MALS analysis of nhTMEM16.

a, Size-exclusion profile of nhTMEM16. Fractions between the dotted line were pooled for reconstitution. **b,** SDS-PAGE of size-exclusion fractions. **c**, Gel filtration and light scattering results for nhTMEM16 in the detergent DDM. The black trace corresponds to the absorption at 280 nm. Molecular weights of the protein and the protein-detergent complex are shown in red and green, respectively.

To investigate on the potential channel property, nhTMEM16 was expressed in *S. cerevisiae*, purified and reconstituted into proteoliposome post size-exclusion. For reconstitution, *E. coli* polar lipid extract was mixed with L-α phosphatidylcholine at a ratio of 3:1 (w/w). The concentrated protein was incubated Triton-

destabilized liposomes at a protein-to-lipid ratio of 1:100 or 1:200 (w:w). Detergent was removed by addition of Bio-Beads and the resulting proteoliposomes were stored in liquid nitrogen. The incorporation of the protein was confirmed by viewing the surface of the proteoliposome replica using freeze-fracture electron microscopy. Liposomes of approximately 150-300 nm in diameter were observed on the replica with approximately 5% exhibiting protein reconstituted proteins. Number of proteins observed on the proteoliposome range between 3 to 9 (Figure 12a). Despite the low incorporation rate, the proteoliposome were suitable for electrophysiology recording on lipid planar bilayer as the single channel recordings could provide insight on the channel conductance, if any.

Recording chamber was prepared by painting a horizontal bilayer using a 3:1 (w/w) mixture of POPE/POPG. The two chambers were filled with either 10 mM HEPES pH 7.4, 0.3 mM $CaCl_2$, 150 mM NaCl on both sides for symmetrical condition or 150 mM NaCl on one side and 30 mM NaCl on the other side to set up a 5x NaCl gradient across the bilayer. 1-10 µl of 4mg/ml proteoliposome aliquots were added directly above the bilayer to initiate the fusion of the proteoliposome on to the bilayer. The recordings were carried out with an Axopatch 200B amplifier. Currents indicating single ion channel activity were frequently observed after addition of high concentrations of proteoliposomes after long incubation (*i.e.* 10-20 minutes) at 100 or -100 mV. The recorded activity was compatible with the presence of high conducting non-selective ion channels that did not show any pronounced Ca^{2+} dependence (Figure 12b-c). To rule out that the currents observed was due to contaminating channels from expression host S. cerevisiae, nhTMEM16 was expressed in HEK cells and reconstituted in the same manner. Similar currents were still observed on the bilayer (Figure 12d). We usually observed currents corresponding to 1-3 putative channels and never found more than 10 channels in the bilayer. Similar single channel activity was also found in liposomes of the same lipid composition not containing any protein (Figure 12e). Several attempts in removing the artifact conductance included obtaining new batch of lipid from several manufacturers, varying the ratio of POPE/POPG of the bilayer and using liposomes made of POPE/POPC, However, the artifact still remained to varying effect. As we were unable to distinguish the conductance observed from proteoliposomes containing nhTMEM16 to the similar currents observed in empty liposomes, we could not draw definite conclusions on ion channel activity mediated by reconstituted nhTMEM16.

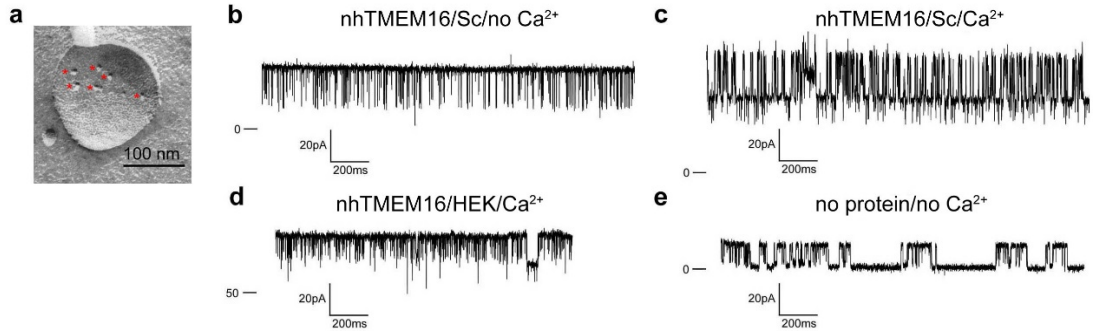

Figure 12 Planar-lipid bilayer experiments.

a, Freeze fracture electron microscopy image of a proteoliposome containing nhTMEM16 formed from a 3:1 mixture of *E. coli* polar lipids/egg PC. Reconstituted proteins are labeled with a red asterisk. **b,** Currents recorded after fusion of proteoliposomes containing nhTMEM16 expressed and purified from *S. cerevisiae*. **c,** Currents recorded from the same proteoliposomes as in b, except that 300 µM Ca^{2+} was added on both sides of the bilayer. **d,** Currents recorded after fusion of proteoliposomes containing nhTMEM16 expressed and purified from HEK tsA201 cells in the presence of 300 µM Ca^{2+} added on both sides of the bilayer. **e,** Currents recorded after fusion of liposomes of the same lipid composition not containing any protein

recorded without addition of Ca^{2+}. Displayed traces were recorded at a holding potential of 100 mV in symmetric solutions containing 150 mM NaCl, 10 mM HEPES pH 7.4. Selected current levels (in pA) are indicated on the left.

Patch clamp experiments

As lipid bilayer recording with the reconstituted protein was not conclusive, we decided to access its function as ion channel by patch-clamp electrophysiology as an alternative method. nhTMEM16 was expressed as fusion protein bearing C-terminal vYFP tag in HEK293T cells. Similar fusion construct of mTMEM16A was expressed in HEK293T cells to be used as direct comparison. Transfected cells were identified by the fluorescence of YFP after 24 hours. As viewed by confocal fluorescence microscopy, whereas the majority of the fluorescence of mTMEM16A was observed at the boundaries of the cell, which denotes localization of the protein on the plasma membrane, cells expressing nhTMEM16 showed a broad distribution of the protein inside the cell and beneath the cell boundary (Figure 17a,b). Although this suggests that a large part of nhTMEM16 were translocated in intracellular compartments, at least a fraction of the protein could be presumed to have been targeted to the plasma membrane due to overexpression. When recording the excised patches in the inside-out configuration, while mTMEM16A displayed robust currents in response to the application of Ca^{2+}, no current response in patches from cells expressing nhTMEM16 was observed in any of the 40 independent patches recorded (Figure 17c,d). The localization of both proteins on the recorded cells were illustrated in Figure 17c,d and were in agreement with the fluorescence confocal images.

2.4 Functional investigations of TMEM16 proteins

2.4.1 Learning from the Structure of nhTMEM16

From the homologue screen, we identified nhTMEM16 as a promising candidate for structure determination. nhTMEM16 was crystallized in two different crystal forms (CF1 and CF2), for which data up to 3.3 and 3.4 Å resolution were collected respectively. Both crystal forms are of space group $P2_12_12_1$. CF1 was obtained was crystallized at pH 9.5 from a solution containing 100 mM $MgCl_2$, and 21–23% PEG400, CF2 at pH 7.6 from a solution containing 100 mM ammonium sulphate and 21–23% PEG400. The protein was purified in the Detergent DDM. The addition of αUDM, yeast polar lipid extract and 1,2,3-heptanetriol to the protein solution proved to be essential to improve the diffraction quality.

The crystal structure revealed a dimeric arrangement of nhTMEM16 (Figure 13a). Each subunit consists of a transmembrane domain and soluble N-terminal and C-terminal domains both on the cytoplasmic side. Contrary to the hydropathy analysis, the transmembrane domain is made up of ten membrane spanning helices preceded by two short amphipathic helices that are peripherally interacting with the membrane (Figure 13c). The N-terminal domain adopts a ferredoxin-like fold while the three helices of the C-terminus wrap around the N-terminus of the other subunit. Within the membrane, the majority of the intersubunit interactions are mediated by helix 10 of the transmembrane domain. The structure revealed two types of cavities. The first cavity is found close to the dimer interface, hence termed dimer cavity. The arrangement of the helices and relatively few intersubunit contacts results in a large pore-like structure which contains two separate 15 Å wide entrances at the extracellular side and which merge to one big, about 30 Å wide vestibule, at the intracellular half of the membrane. The subunit cavity is predominantly composed of hydrophobic and aromatic residues, which are conserved within the protein family. In a 2Fo-Fc map, the vestibule is filled with residual density, which could been attributed to either detergent or lipid. The second cavity is found at the surface away from the dimer interface, termed as the subunit cavity (Figure 13b). It is made up of 6 helices forming semitubular pore that is exposed to the lipid bilayer. Despite being exposed to the membrane, the surface lining of the cavity is hydrophilic. For TMEM16 scramblases such as nhTMEM16, this cavity is the potential site of catalysis by providing a favourable path for the polar headgroups of the transported phospholipids.

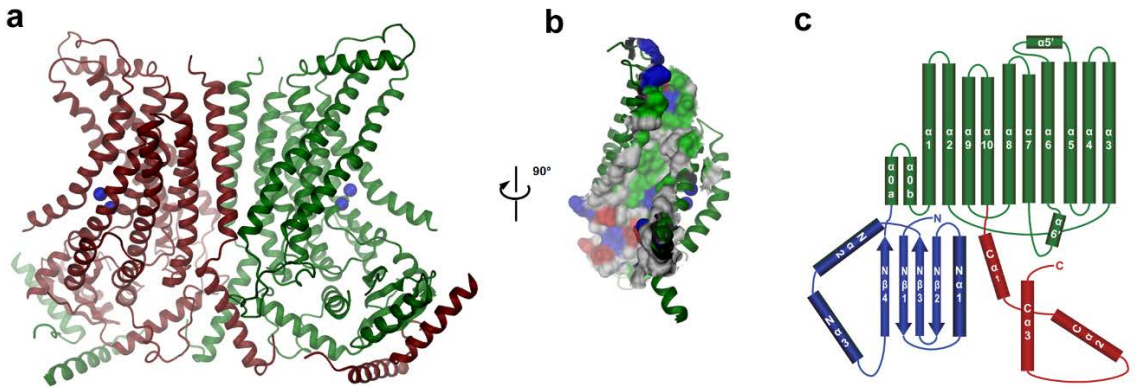

Figure 13 Structure of nhTMEM16

a, structure of nhTMEM16 viewed from within the membrane. Bound Ca^{2+} ions are displayed as blue spheres. **b,** surface of the subunit cavity. Residues are coloured according to their properties (red acidic,

blue basic, green polar). **c,** Topology of the nhTMEM16 subunit. The transmembrane domain is coloured in green, the N- and C-terminal domains in blue and red, respectively.

The structure also revealed a Ca^{2+} binding site embedded between transmembrane helices 6, 7 and 8 of each subunit of the dimer (Figure 14a). The binding site consists of five acidic residues and one asparagine. A sequence alignment of nhTMEM16 with mammalian TMEM16 members showed that these residues are highly conserved, despite the functional divergence in TMEM16 family (Figure 14b). In the anomalous difference density map, two strong peaks corresponding to Calcium were observed within the binding site, implying that there are two Ca^{2+} ions present. Although the occupancy could not be determined with certainty from the crystallographic data, simultaneous occupation of two Ca^{2+} ions appears plausible judging from geometric considerations and the presence of 5 acidic residues coordinating the ions.

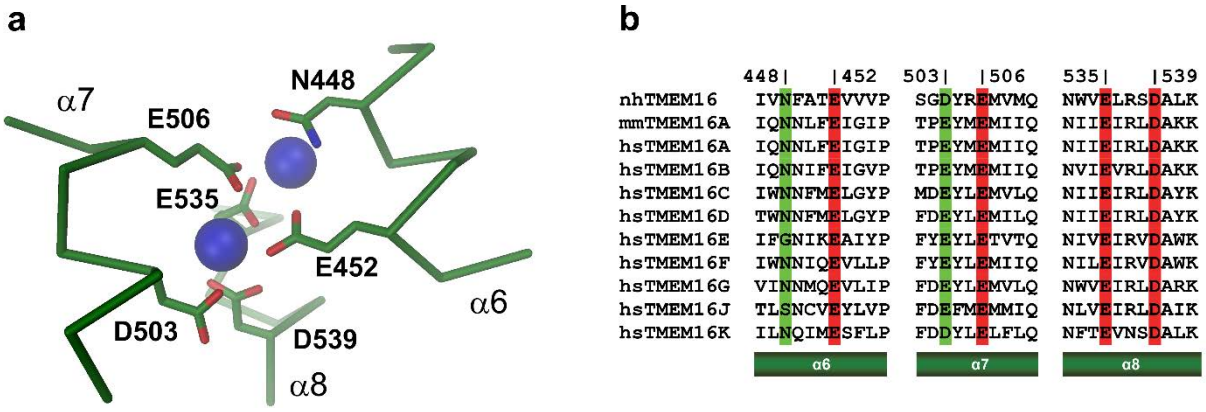

Figure 14 Ca^{2+}-binding site in nhTMEM16.

a, model of Ca-binding site in nhTMEM16. **b,** Sequence alignment of the mammalian TMEM16 members with nhTMEM16. The residue numbering corresponds to nhTMEM16.

In the following sub-chapter 2.4.2, I show that nhTMEM16 is most likely not functioning as an ion channel. However, due to high sequence identity between the homologues, the general architecture is likely conserved among the protein family and therefore also valid for members functioning as CaCCs, such as TMEM16A. The crystal structure of nhTMEM16 provided a wealth of information, which provides insight into the gating mechanisms of CaCC but it also raised several questions concerning the architecture of a CaCC. The sub-chapter 2.4.3.3 will focus on addressing these aspects.

2.4.2. Investigating a potential role of nhTMEM16 as ion channel

Reconstitution of nhTMEM16 and planar lipid bilayer recording

nhTMEM16 was shown by Janine Brunner to function as lipid scramblase. A previous study by Malvezzi et. al. (103) on the homologous TMEM16 protein from *A. fumigatus* (afTMEM16) has proposed that afTMEM16 functions as an ion channel on top of functioning as a lipid scramblase. This was suggested based on recordings of reconstituted afTMEM16 in planar lipid bilayers, which showed large non-selective

conductance steps attributed to single ion channels. The channel activity was also described to have a low probability of activation (judged by the absence of large macroscopic currents since recordings only showed a small number of open channels) with a weak Ca^{2+} dependence and to be highly dependent on the lipid composition of the liposome. In an attempt to investigate whether a similar behaviour would also be observed for nhTMEM16, the protein was expressed, reconstituted into liposome and characterized in planar lipid bilayers. As nhTMEM16 shares 48% of sequence identity with afTMEM16, we anticipated a similar functional behaviour. Prior to the electrophysiological investigations, I elucidated the oligomeric state of nhTMEM16 in detergent buffer using multi-angle light scattering.

nhTMEM16 was expressed in *S. cerevisiae* in a 20 litre fermenter batch as N-terminally GFP tagged construct. The protein was extracted with DDM, purified using Nickel-NTA and size-exclusion chromatography. The protein eluted as a monodisperse peak and was pure when applied on SDS-PAGE (Figure 15a,b). The fractions corresponding to the peak were pooled and subjected to MALS analysis (Figure 15c). The protein-detergent complex ran at an apparent Mw of 295 kDa, of which 150 kDa was contributed by the DDM micelle. The theoretical Mw of nhTMEM16 is 83kDa. The experimental protein molecular weight of 145 kDa thus support the hypothesis that nhTEM16 is a dimer in the detergent solution.

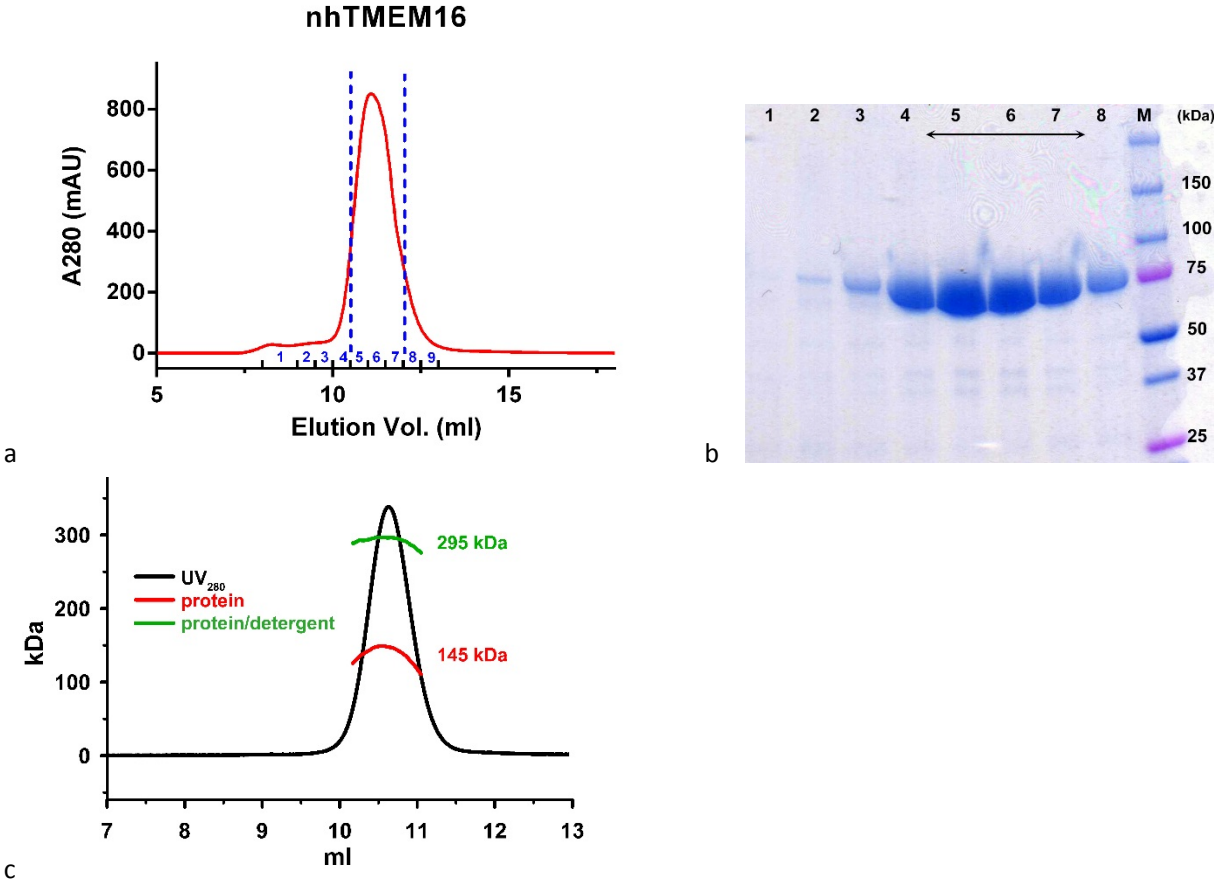

Figure 15 Purification and MALS analysis of nhTMEM16.

a, Size-exclusion profile of nhTMEM16. Fractions between the dotted line were pooled for reconstitution. **b,** SDS-PAGE of size-exclusion fractions. **c**, Gel filtration and light scattering results for nhTMEM16 in the detergent DDM. The black trace corresponds to the absorption at 280 nm. Molecular weights of the protein and the protein-detergent complex are shown in red and green, respectively.

To investigate a potential function as ion channel, purified nhTMEM16 was reconstituted into proteoliposomes. For reconstitution, *E. coli* polar lipid extract was mixed with L-α phosphatidylcholine at a ratio of 3:1 (w/w). The concentrated protein was incubated with Triton-destabilized liposomes at a protein-to-lipid ratio of 1:100 or 1:200 (w:w). Detergent was removed by addition of Bio-Beads and the resulting proteoliposomes were stored in liquid nitrogen. The incorporation of the protein was confirmed by viewing the surface of the proteoliposome replica using freeze-fracture electron microscopy. Liposomes of approximately 150-300 nm in diameter were observed on the replica with approximately 5% exhibiting reconstituted proteins. The number of proteins observed on the proteoliposome range between 3 to 9 (Figure 16a). Despite the low incorporation rate, the proteoliposome were suitable for electrophysiology recording on planar lipid bilayers. Any currents obtained in such recordings would provide insight into a potential channel function.

The recording chamber was prepared by painting a horizontal bilayer using a 3:1 (w/w) mixture of POPE/POPG. The two chambers were filled with either 10 mM HEPES pH 7.4, 0.3 mM $CaCl_2$, 150 mM NaCl on both sides for recordings in symmetrical conditions or 150 mM NaCl on one side and 30 mM NaCl on the other side to set up a 5-fold NaCl gradient across the bilayer for investigations of selectivity properties. 0.5-10 µl of 4mg/ml proteoliposome aliquots were applied directly above the bilayer to initiate the fusion of proteoliposomes with the bilayer. Currents were amplified and recorded with an Axopatch 200B amplifier. Currents resembling single ion channel activity were frequently observed after addition of high concentrations of proteoliposomes after long incubations (*i.e.* 10-20 min) at 100 or -100 mV. The recorded activity was compatible with the presence of high conducting non-selective ion channels that did not show any pronounced Ca^{2+} dependence (Figure 16b-c). To rule out that the observed currents were due to contaminating channels from the expression host *S. cerevisiae*, nhTMEM16 was also expressed in HEK cells and reconstituted in the same manner. Also in this case similar currents were observed (Figure 16d). We usually observed currents corresponding to 1-3 putative channels and never found more than 10 channels in the bilayer. Similar single channel activity was occasionally also found in liposomes of the same lipid composition not containing any protein (Figure 16e). Several attempts to remove endogenous artefacts included the use of lipids from different manufacturers, a variation of the POPE/POPG ratio of the painted planar bilayer and the use of proteoliposomes prepared from synthetic lipids. However, the artefact still were still observed at varying degrees. As we were unable to distinguish the conductance observed from proteoliposomes containing nhTMEM16 from the similar currents observed in empty liposomes, we could not draw definite conclusions on ion channel activity mediated by reconstituted nhTMEM16.

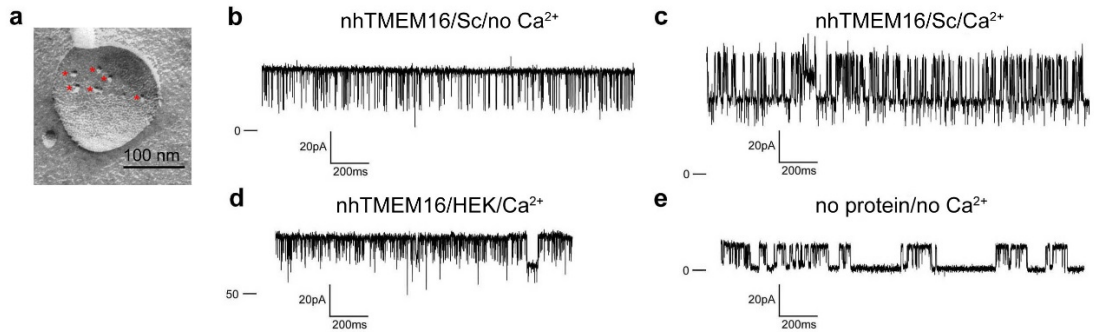

Figure 16 Planar-lipid bilayer experiments.

a, Freeze fracture electron microscopy image of a proteoliposome containing nhTMEM16 formed from a 3:1 mixture of *E. coli* polar lipids/egg PC. Reconstituted proteins are labelled with a red asterisk. **b,** Currents recorded after fusion of proteoliposomes containing nhTMEM16 expressed and purified from *S. cerevisiae*. **c,** Currents recorded from the same proteoliposomes as in b, except that 300 µM Ca^{2+} was added on both sides of the bilayer. **d,** Currents recorded after fusion of proteoliposomes containing nhTMEM16 expressed and purified from HEK tsA201 cells in the presence of 300 µM Ca^{2+} added on both sides of the bilayer. **e,** Currents recorded after fusion of liposomes of the same lipid composition not containing any protein recorded without addition of Ca^{2+}. Displayed traces were recorded at a holding potential of 100 mV in symmetric solutions containing 150 mM NaCl and 10 mM HEPES pH 7.4. Selected current levels (in pA) are indicated on the left.

Patch clamp experiments

As lipid bilayer recording with the reconstituted nhTMEM16 was not conclusive, I decided to access its function as ion channel by patch-clamp electrophysiology as an alternative method. nhTMEM16 was expressed as fusion protein bearing C-terminal vYFP tag in HEK293T cells. A similar fusion construct of mouse TMEM16A (mTMEM16A) was expressed in the same cells to be used as direct comparison. Transfected cells were identified by the fluorescence of YFP after 24 hours. Confocal fluorescence microscopy showed that, whereas the majority of the fluorescence of mTMEM16A was observed at the boundaries of the cell, indicating the localisation of the protein on the plasma membrane, cells expressing nhTMEM16 showed a broad distribution of the protein inside and beneath the cell boundary (Figure 17a,b). Although this suggests that a large part of nhTMEM16 were located in intracellular compartments, at least a fraction of the protein could be presumed to have been targeted to the plasma membrane due to overexpression. When recording the excised patches in the inside-out configuration, TMEM16A displayed robust currents in response to the application of Ca^{2+}, but no current response in patches from cells expressing nhTMEM16 was observed in any of 40 independent patches recorded (Figure 17c,d). The localization of both proteins in cells used for recording is illustrated in Figure 17c,d. In both cases the proteins showed a similar distribution as in the fluorescence confocal images.

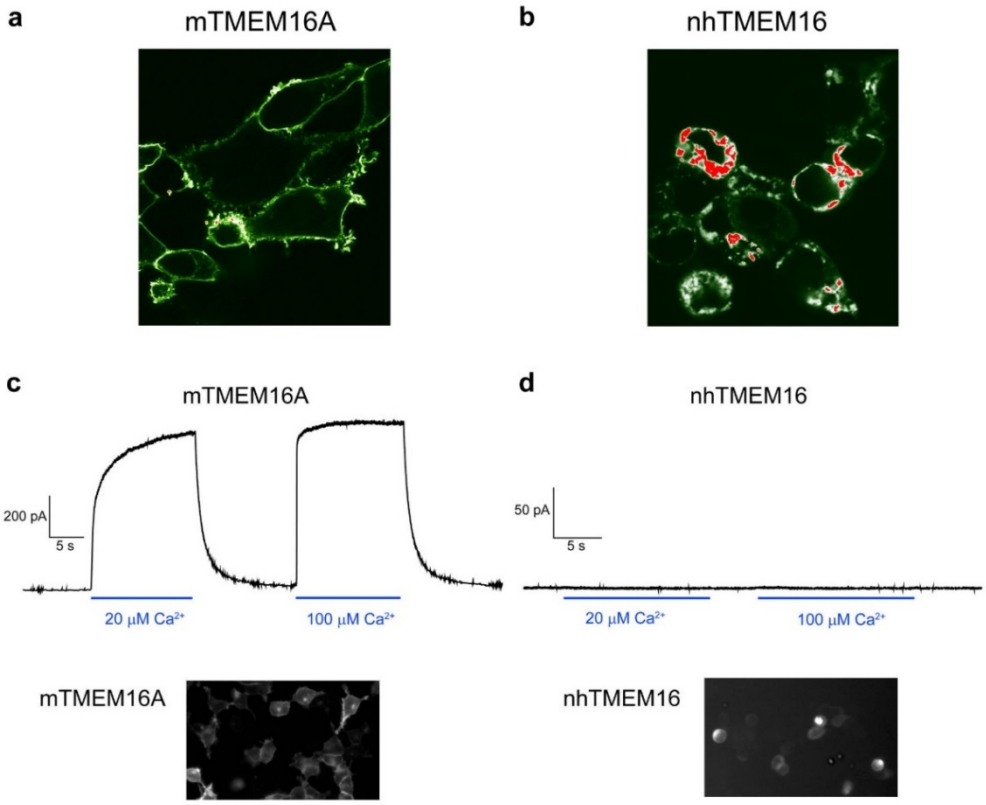

Figure 17 Recording from excised inside-out patches.

a, Fluorescence confocal microscopy image of a HEK293T cell expressing a mTMEM16A-YFP fusion construct. **b**, Fluorescence confocal microscopy image of a HEK tsA201 cell expressing a nhTMEM16-YFP fusion construct. **c**, Representative current response in a membrane patch excised from cells expressing a mTMEM16A-YFP fusion construct (top) upon rapid exchange into solutions containing the indicated amount of Ca^{2+}. The voltage was clamped at 80 mV. The fluorescence of transfected cells expressing mTMEM16A-YFP used for recording is shown below. **d**, Equivalent recordings from patches that were excised from cells expressing a nhTMEM16-YFP fusion protein. The fluorescence of transfected cells expressing nhTMEM16-YFP used for recording is shown below.

To increase the likelihood to record from nhTMEM16 on the plasma membrane, we switched to patch-clamp experiments in the whole-cell configuration. Under the assumption that a fraction of nhTMEM16 would be translocated to the plasma membrane, the number of nhTMEM16 recorded from the surface of the entire cell should be significantly higher than on a single membrane patch. Robust current response were observed for cells expressing mTMEM16A-YFP in solutions containing either 0.1 or 20 µM Ca^{2+} in the patch pipette (Figure 18a,b), whereas only a very small response (typically about 40 pA at 80 mV) was observed in cells expressing nhTMEM16 (Figure 18c). These low currents were not increased by Ca^{2+} and they were in a similar range as observed for mock-transfected cells (Figure 18d) thus suggesting that the small response is due to ion flow mediated by nhTMEM16.

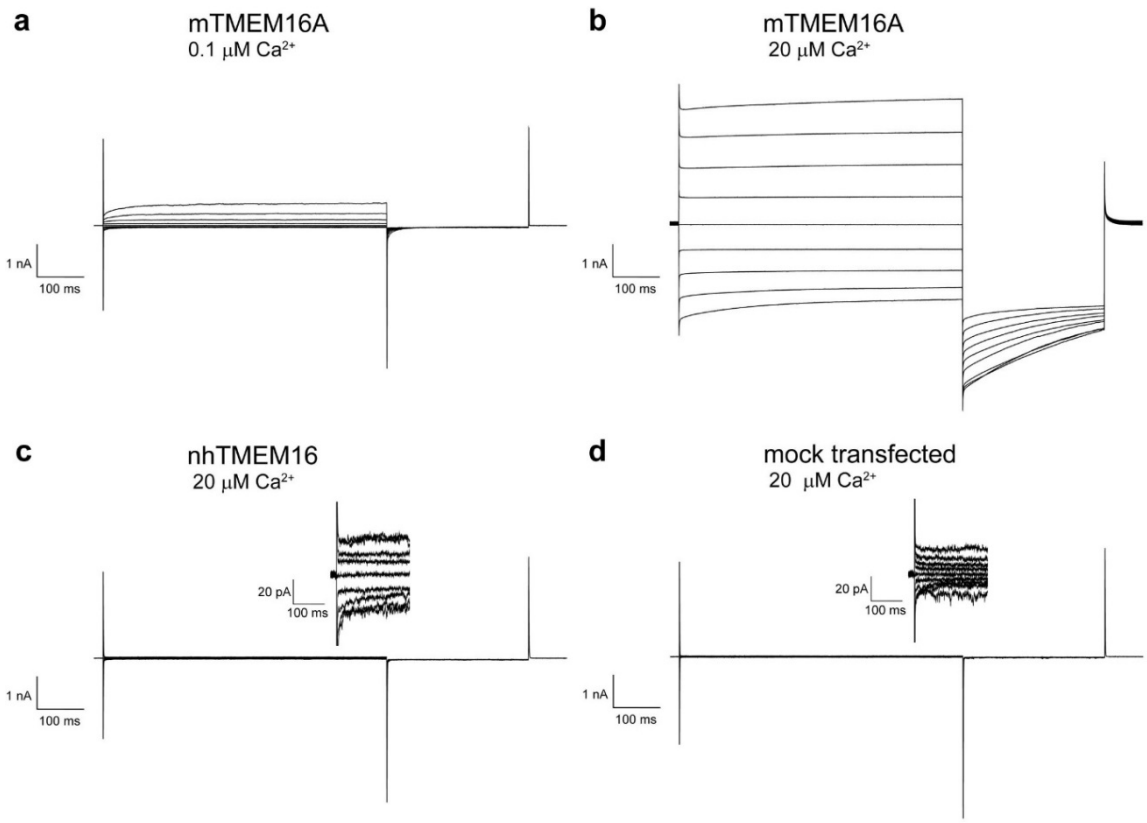

Figure 18 Patch-clamp recording in the whole-cell configuration.

a, Currents from a HEK293T cell expressing a mTMEM16A-YFP construct recorded from a solution, containing 0.1 µM free Ca^{2+} in the patch pipette. **b**, Currents from a cell expressing a mTMEM16A-YFP construct. **c**, Representative currents from a cell expressing a nhTMEM16-YFP fusion protein recorded from a solution. **d**, Current response from mock transfected cells. Recordings shown in b-d contained 20 µM of free Ca^{2+} in the patch pipette. Insets in c and d show part of the traces with different current scale.

In summary, we were not able to find any convincing evidence for ion conduction mediated by nhTMEM16 despite addressing this question with different approaches. Although, I also do not want to exclude the possibility that nhTMEM16 would conduct ions, it appears unlikely that it does this with large conductance observed in the bilayer experiments of afTMEM16 (103).

2.4.3 Structure-function relationships of the mouse CaCC mTMEM16A

2.4.3.1 Characterisation of mTMEM16A by electrophysiology

mTMEM16 is activated by Ca^{2+}

To establish the methods for studies on structure-function relationships of mTMEM16A, I first characterised the functional property of mTMEM16A by patch clamp electrophysiology. The a,c splice-variant of mTMEM16A was cloned into pCDNA3.1 vector bearing a C-terminal YFP tag. HEK293T cells were transfected with the plasmid using Fugene transfection reagent for 36-48 hours prior to recording. After 24 hours, transfected cells that express mTMEM16A on the plasma membrane were identified under the microscope via the fluorescence properties of attached YFP.

TMEM16A is activated by the increase of intracellular Ca^{2+} concentration. In order to study the effect of varying Ca^{2+} on the channel, TMEM16A was investigated by patch-clamp in an inside-out configuration. This is achieved by first forming GigaOhm seal with the patch pipette on the cell membrane and then withdrawing the pipette rapidly to obtain a membrane patch with the intracellular side facing the bath solution. This setup thus allows rapid addition and removal of Ca^{2+} by perfusing the patch with solutions containing different concentrations of Ca^{2+}.

Upon clamping the voltage at +80 mV and application of low concentrations of Ca^{2+}, a steady-state current was evoked. As higher Ca^{2+} concentrations are applied, the evoked current increases until a maximum is reached. The currents were normalised to the maximum current and plotted against the applied Ca^{2+} concentration. The plot exhibited the expected sigmoidal curve. EC_{50} values were obtained by fitting concentration-response data to the Hill equation:

$$I/I_{max} = \frac{1}{1 + \left(\frac{EC_{50}}{[Ca^{2+}]}\right)^{n_H}}$$

where EC_{50} is the concentration where the activation is half of the maximum and n_H is the Hill coefficient. The equation also constrains the minima and maxima of the fit to 0 and 1 respectively.

The resulting dose-response curves showed that Ca^{2+} activates channel with EC_{50} of 360 nM and n_H of 2.0 (Figure 19). The Hill coefficient greater than 1 suggests that multiple Ca^{2+} ions are required to activate the channel and it implies that there is positive cooperativity in Ca^{2+} binding. Overall, the result showed that mTMEM16A is gated by Ca^{2+} as in agreement with previous studies (18, 55, 76).

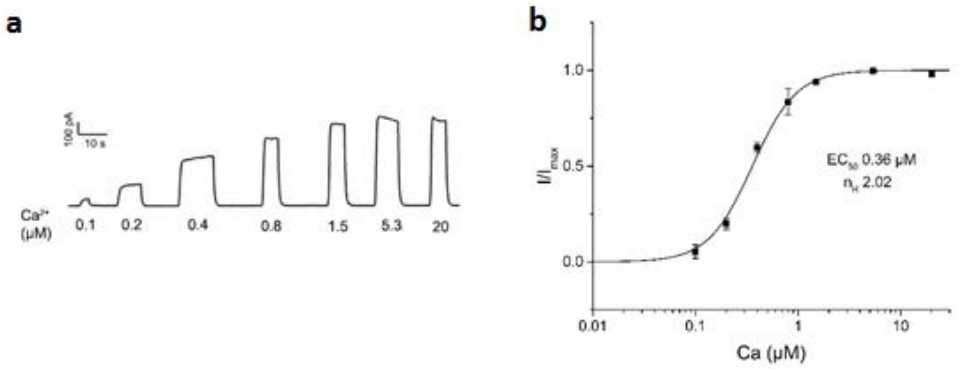

Figure 19 Activation of mTMEM16A by Ca^{2+}.

a, Representative current trace of the mTMEM16A in response to different intracellular Ca^{2+} solutions recorded at +80 mV. Numbers indicate the Ca^{2+} concentration in µM. **b,** Ca^{2+} dose-response relationships of mTMEM16A at +80 mV

It was noted that the inside-out patch-clamp recordings of mTMEM16A were susceptible to irreversible rundown (109). Rundown is the reduction of channel current, which is often associated with the loss of an important co-factor over time. I commonly observed that the current at highest recorded Ca^{2+} concentration was lower than of the preceding data point. Although it is still not clear what causes rundown in TMEM16A however, the process is dependent on the Ca^{2+} concentration and is getting more pronounced after perfusing with a Ca^{2+} concentration higher than 1 µM. The degree of rundown was variable from patches to patches. To reduce the effect of rundown affecting the patches, measurements usually started by applying lower concentrations first. The total time of exposure to Ca^{2+} was kept to the minimum required to reach steady state.

Voltage-dependence of channel activation

Ca^{2+} activation in CaCCs was previously shown to be voltage dependent (76). To investigate the voltage-dependence of channel activation, the patch was perfused at different Ca^{2+} concentrations and sweeps were recorded at different voltages ranging from +100 mV to -100 mV in 20 mV steps (Figure 20a). The currents were subsequently plotted against the holding potential to show the current-voltage relationships (Figure 20b). At sub-micromolar concentration, the resulting non-linear curve showed that the channel is more sensitive to Ca at positive voltage. This rectification property was diminished when the same patch was perfused at higher Ca concentration and it was subsequently abolished as maximum activating Ca concentration was reached. The plotted dose-response curves at different voltages maintained similar Hill coefficient (n = 2.0) at all voltages while the EC_{50} of channel activation gradually increased as the voltage was decreased (Figure 20c).

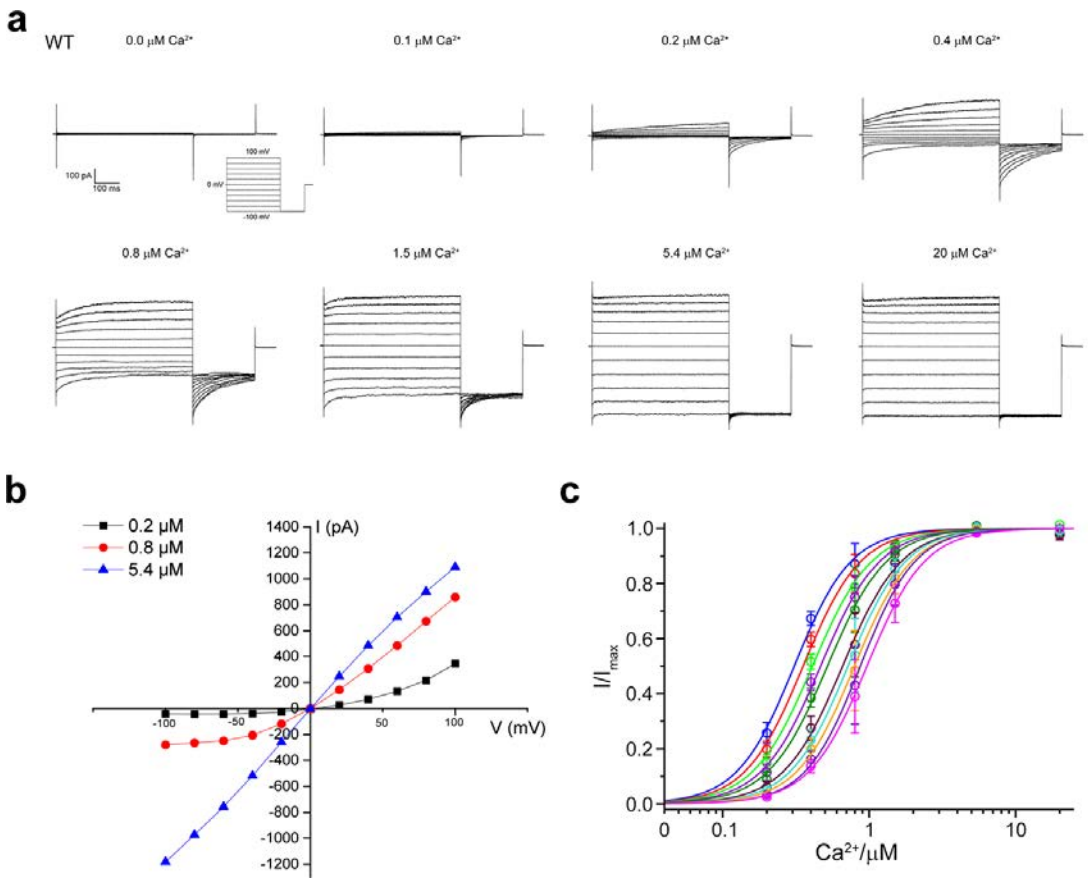

Figure 20 Voltage-dependence of mTMEM16A.

a, Representative steady-state currents of mTMEM16A at various Ca^{2+} concentrations. Voltage ramp protocol is shown as inset. **b,** Current voltage relationships at different Ca^{2+} concentrations. **c,** Ca^{2+} dose response relationships at different voltages.

The crystal structure of nhTMEM16 revealed that the conserved Ca^{2+}-binding site is located within the membrane inserted region of the protein. This raised the question whether the characteristic voltage dependence of channel activation might be contributed by Ca^{2+} ions crossing the membrane electric field to reach the binding site. Depending on the polarity of the membrane potential, the entry of Ca^{2+} into the binding site might be hindered or facilitated by the electric field which would also affect the energy of binding.

To quantify the voltage dependence of TMEM16A activation, the Woodhull equation was used by plotting the logarithm of the EC_{50} of Ca^{2+} activation against the holding potential (Figure 21). The equation allows to calculate the fraction of the electrical field an ion has to cross to reach its binding site.

$$Ln(\mathrm{EC_{50}})_{\mathrm{E}_m} = Ln(\mathrm{EC_{50}})_{0\ \mathrm{mV}} - \frac{\mathrm{z}\ \delta\ \mathrm{FV}}{\mathrm{RT}}$$

Where $(\mathrm{EC_{50}})_{\mathrm{E}_m}$ is the EC_{50} value at a given holding potential, $(\mathrm{EC_{50}})_{0\ \mathrm{mV}}$ is EC50 value at holding potential of 0 mV. z, F, R, T are the valency of Ca^{2+} ions, the Faraday constant, the gas constant and the absolute temperature, respectively. δ denotes the fraction of the membrane potential acting on the binding site. The EC50 describes the apparent affinity of the binding side for Ca^{2+}.

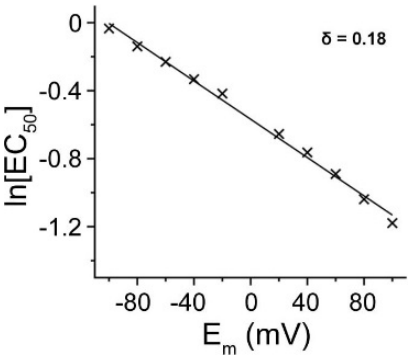

Figure 21 Voltage dependence of Ca^{2+}-binding in TMEM16A activation.

Plot of the EC_{50} of Ca^{2+} binding against the holding potential.

The slope of the linear fit yielded a δ value of 0.18, implying that Ca^{2+} ions cross approximately 18% of the membrane to reach the binding site. The results are generally consistent with the hypothesis that the voltage-dependence of TMEM16 activation was due to the voltage dependence of Ca^{2+} binding within the transmembrane region. Still, the structure suggests a deeper location of the binding site of about 34 % from the intracellular membrane boundary. This might either be due to a distortion of the membrane or due to other factors also contributing to the voltage-dependence of CaCCs.

2.4.3.2 Role of the conserved Ca^{2+}-binding site in the activation of ion conduction

The crystal structure of nhTMEM16A revealed a Ca^{2+} binding site embedded in each subunit of the dimer between TM helices 6, 7 and 8. In this site two ions are coordinated by six residues, five of which carry a negative charge. Despite the functional divergence within the family, the six residues are highly conserved among TMEM16 proteins including CaCCs such as mTMEM16A and B. This conservation gave rise to the hypothesis that CaCCs are activated by the binding of Ca^{2+} ions to this site.

To test this hypothesis, single binding residue mutants of mTMEM16A were generated in a construct containing a C-terminal YFP tag. Conservative mutants were introduced in case of the acidic residues while the asparagine was mutated to a non-polar Ala. The mutants were expressed in HEK293T cells with a similar procedure as WT and expression of the fluorescence tag was monitored under a fluorescence microscope. After 36 hours of expression, the steady-state currents of mutated constructs were studied by patch clamp electrophysiology of excised patches in inside-out configuration. The dose-response curves were plotted from averaged data of 3 to 5 patches for each mutant.

E702Q

The E702Q mutant was well expressed and localised on the cell membrane. The mutant displayed the characteristic rectification property of TMEM16A at low Ca^{2+} concentration and its macroscopic currents were similar to that of WT, reaching up to 1 nA at 80 mV in excised patches (Figure 22a). The EC50 of channel activation was reduced by approximately 25 fold compared to WT (Figure 22b). The Hill coefficient of Ca^{2+} activation of 2.1 was is comparable to WT, indicating a similar cooperativity of activation.

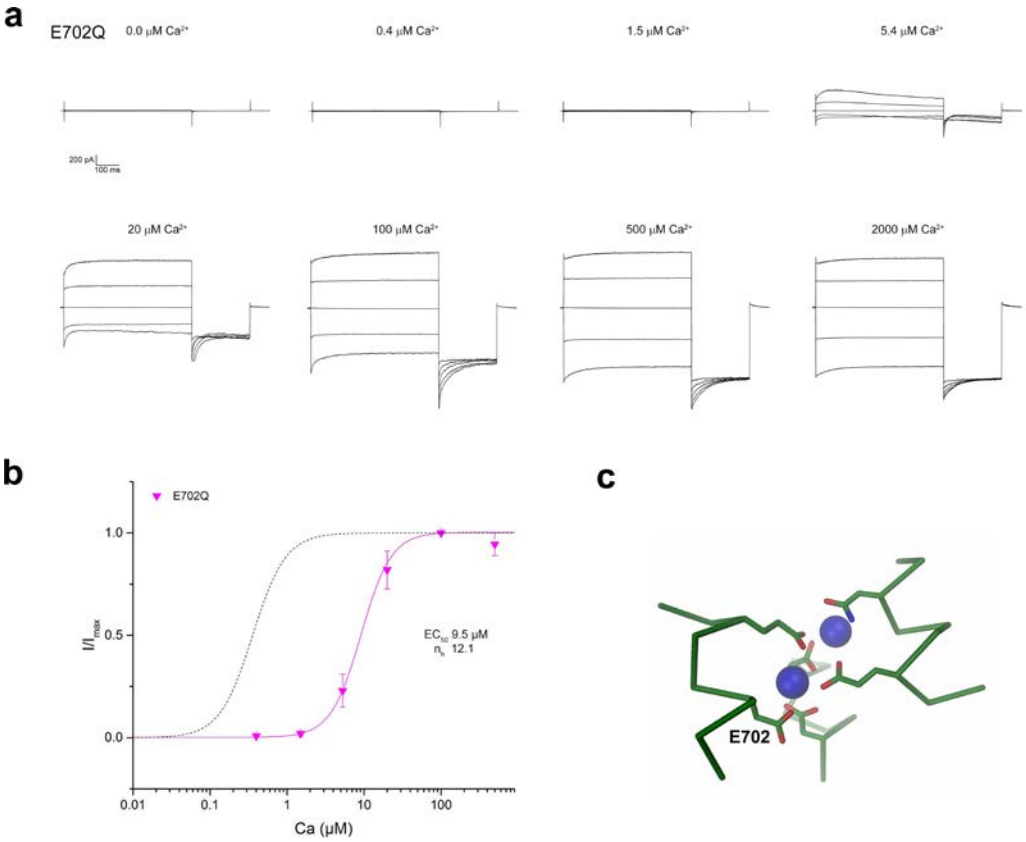

Figure 22 Characterisation of the Ca^{2+}-binding Mutant E702Q.

a, Representative steady-state currents at different Ca^{2+} concentration. **b,** Ca^{2+} dose-response relationships of the mutant. WT is shown as dotted line for comparison. **c,** shows position of the mutated residue within the Ca^{2+}-binding site.

E705Q

Similar to E702Q, the mutant E705Q was well expressed on the plasma membrane and exhibited robust currents. Also this mutation caused a strong reduction in apparent affinity of Ca^{2+} (Figure 23a). In order to reach the maximal steady-state currents, a Ca^{2+} concentration as high as 10 mM was required. Unfortunately, the exposure to high Ca^{2+} concentrations reuted in severe rundown. This is reflected in the the relatively high standard deviation of the measurements at concentrations higher than 500 uM. Compared to WT, the EC_{50} is E705Q is shifted by a factor of 600 towards higher Ca^{2+} concentrations (Figure 23b). E705Q also gave the lowest Hill coefficient of 1.0 among all investigated mutants.

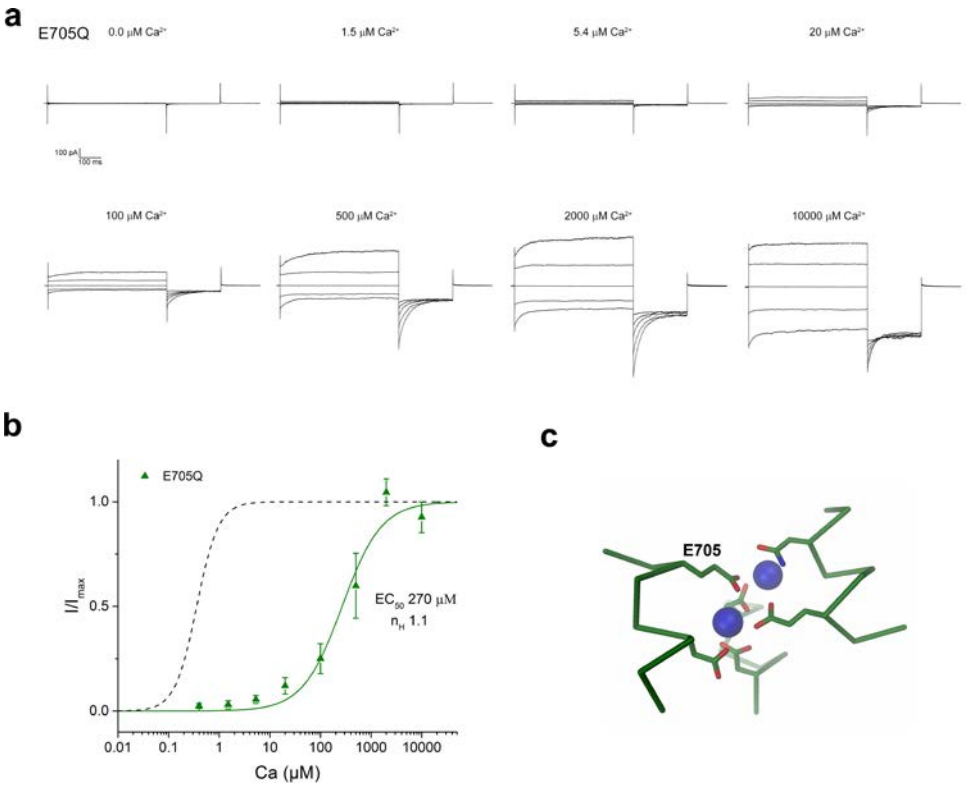

Figure 23 Characterisation of the Ca^{2+}-binding Mutant E705Q.

a, Representative steady-state currents at different Ca^{2+} concentrations. **b,** Ca^{2+} dose-response relationships of the mutant. WT is shown as dotted line for comparison. **c,** Position of the residue within the Ca^{2+}-binding site.

N650A

N650A showed a similar profile as WT in terms of rectification at low Ca^{2+} concentrations while the observed maximal currents in excised patches were approximately half of WT (Figure 24a). In terms of the effect on channel activation, the EC_{50} was reduced approximately 5 fold while the Hill coefficient of activation remained similar to the WT (Figure 24b).

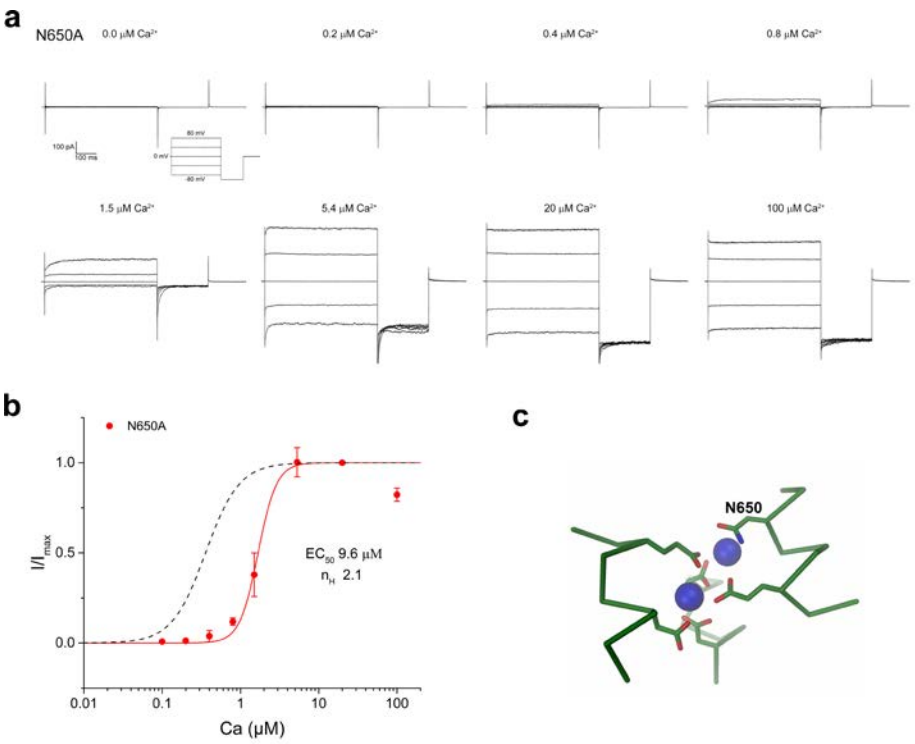

Figure 24 Characterisation of the Ca^{2+}-binding Mutant N650A.

a, Representative steady-state currents at different Ca^{2+} concentrations. **b,** Ca^{2+} dose response relationships of the mutant. WT is shown as dotted line for comparison. **c,** Position of the mutated residue within the Ca^{2+}-binding site.

E654A

The mutation of Glu654 caused the strongest effect on Ca^{2+} activation among all residues of the binding site. The conservative mutation of the residues to Gln was initially tested but no current higher than 10 pA above background were observed even at 10 mM Ca^{2+} when recorded at 80 mV. The E654A mutation partially rescued the current, although no saturation was achieved even if increasing the Ca^{2+} concentration to 10 mM (Figure 25a,b). The measurement was greatly hampered by low current and rundown due to the high Ca^{2+} concentration applied. The weak current observed was likely not due to poor expression of the mutants as both E654A and E654Q constructs were well expressed and localised at the plasma membrane.

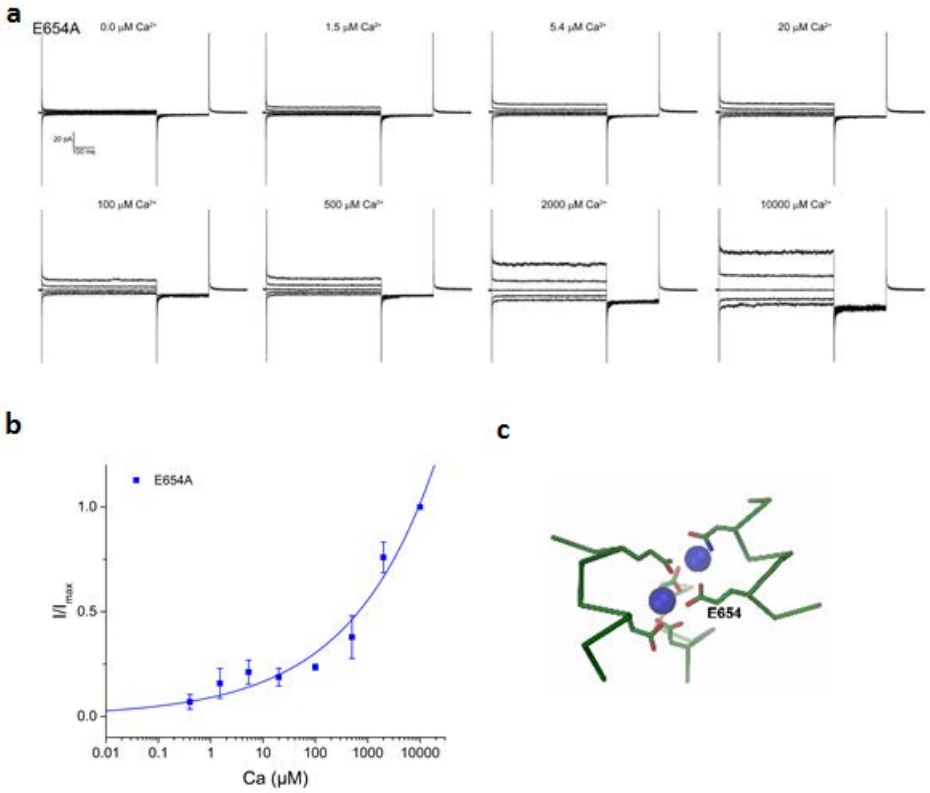

Figure 25 Characterisation of the Ca^{2+} Binding Mutant E654A.

a, Representative steady-state currents at different Ca^{2+} concentrations. **b,** Ca^{2+} dose-response relationships of the mutant. **c,** Position of the residue within the Ca^{2+}-binding site.

E734Q

Judged by the fluorescence, the expression of the mutant E734Q was the weakest among binding site mutants with a large fraction of the protein localized in intracellular compartments. This was also reflected in the low current measured from individual patches. At maximum Ca^{2+} concentration, the highest recorded steady state current at 80 mV was less than 100 pA compared to 800 pA on average for WT (Figure 26a). Interestingly, the mutation also appeared to abolish the current rectification which is usually observed at sub-maximal Ca^{2+} concentration. The low currents combined with rundown and a high variability between the patches caused a big standard deviation in the plot of normalised current. Compared to WT, the EC_{50} of E734Q was increased approximately 10 fold (Figure 26b).

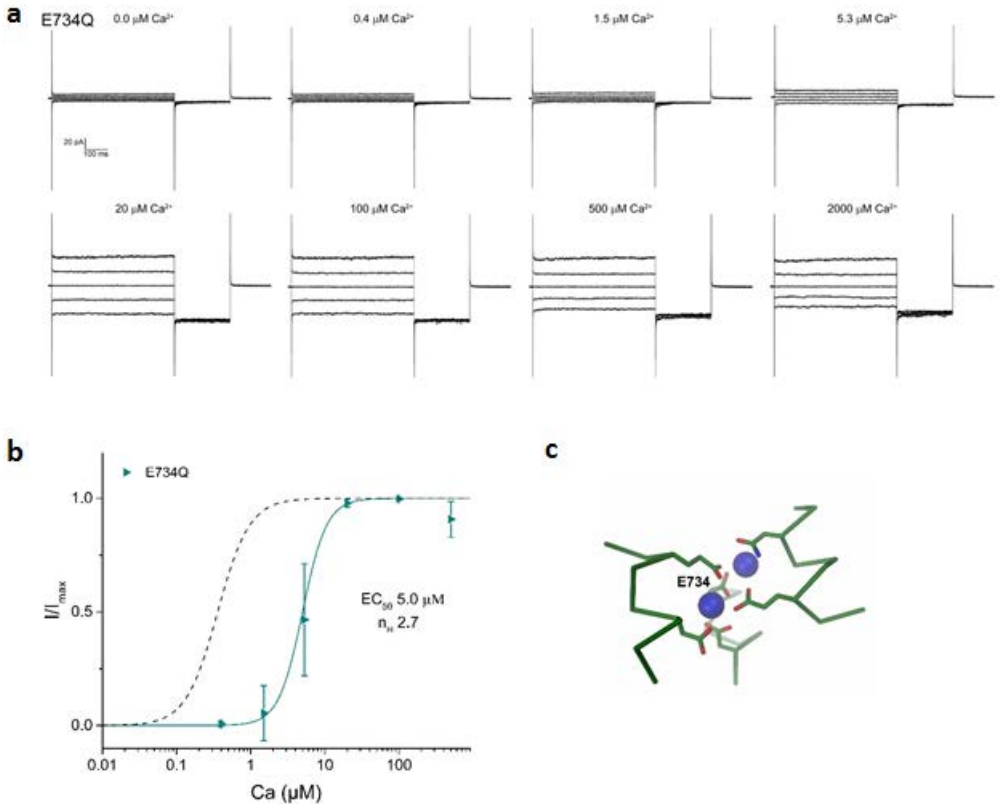

Figure 26 Characterisation of the Ca^{2+}-binding mutant E734Q.

a, Representative steady-state currents at different Ca^{2+} concentrations. **b,** Ca^{2+} dose response relationships of the mutant. WT is shown as dotted line for comparison. **c,** the position of the residue within the Ca^{2+}-binding site.

D738N

The mutation of Asp738 to Asn did not affect the relative expression and localisation of the channel. The mutation had a strong effect on the apparent affinity for Ca^{2+}. Similar to E654A, the maximum current was not reached at 10 mM Ca^{2+} (Figure 27a). However, unlike other mutations, the Ca^{2+} dose response curve in this case was biphasic containing an additional activation step at high Ca^{2+} concentrations. The EC_{50} values and the relative magnitude of each activation step were obtained by fitting the concentration-response data to a biphasic Hill equation:

$$I/I_{max} = (Frac)\frac{1}{1+\left(\frac{EC_{50(1)}}{[Ca^{2+}]}\right)^{n_{H1}}} + (1-Frac)\frac{1}{1+\left(\frac{EC_{50(2)}}{[Ca^{2+}]}\right)^{n_{H2}}}$$

where Frac is the relative magnitude of the first activation step. $EC_{50(1)}$ and n_{H1} are the parameters of the first activation and $EC_{50(2)}$ and n_{H2} the parameters of the second activation.

The fitted curve clearly shows two distinct steps with an $EC_{50(1)}$ and an EC50(2) of 3.5 mM respectively (Figure 27b). The mutation has thus split the activation by Ca^{2+} into two distinct events. The Hill coefficient of the first sigmoid was decreased to 1.4 while the second n_H remain similar to WT above 2. Potentially the

mutation altered the binding affinity of Ca^{2+} ions to the two binding sites significantly so that there are now two distinct affinities.

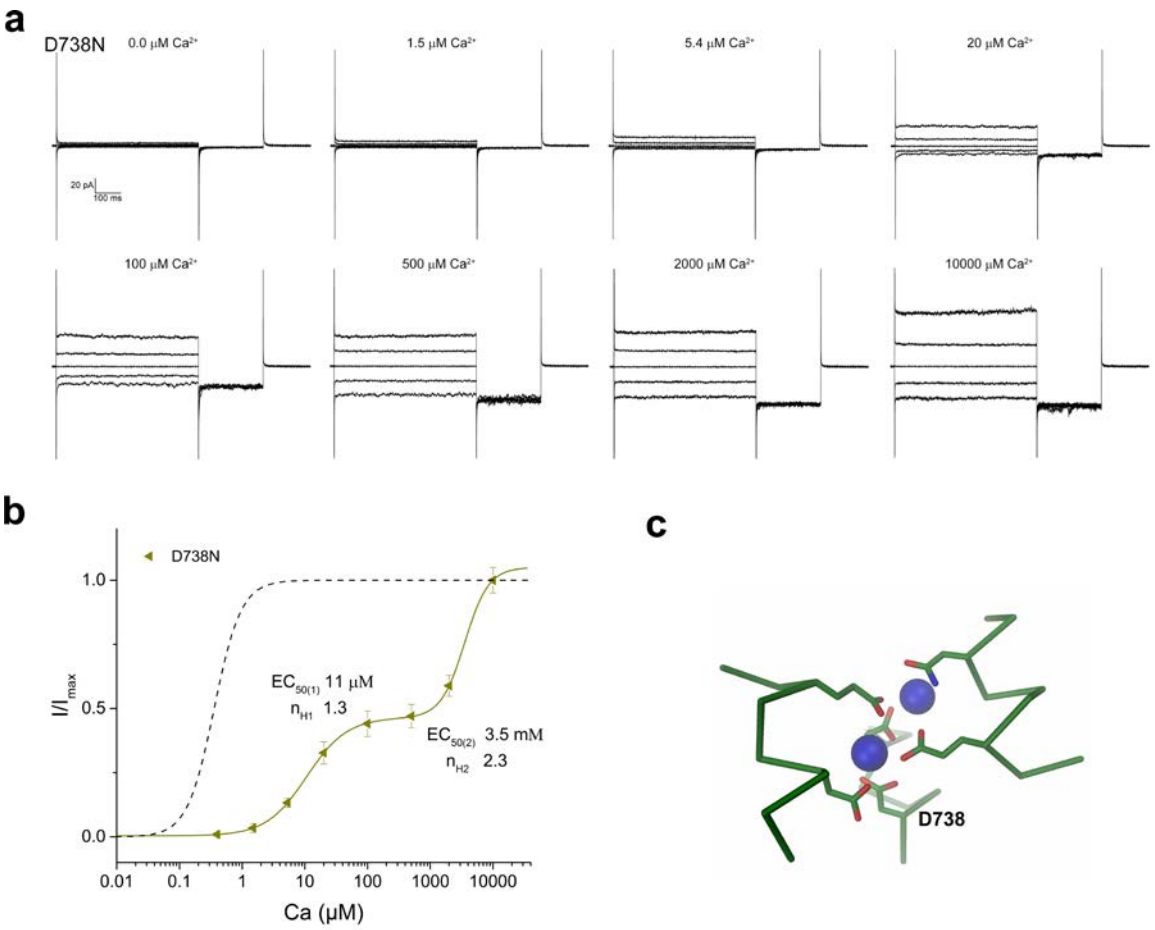

Figure 27 Characterisation of the Ca^{2+}-binding mutant D738N.

a, Representative steady-state currents at different Ca^{2+} concentrations. **b,** Ca^{2+} dose response relationships of the mutant. WT is shown as dotted line for comparison. **c,** position of the residue within the Ca^{2+}-binding site.

Conclusion

The six residues in mTMEM16A corresponding to the Ca^{2+} coordinating residues observed in the crystal structure of nhTMEM16 were mutated and studied with patch clamp electrophysiology. Each single mutation shifts the EC_{50} of activation to higher Ca^{2+} concentrations, suggesting that the direct binding of Ca^{2+} to the site activates the channel. In the attached paper on which I was a co-author, it was shown that mutations of the binding site residues in nhTMEM16 also affect the scrambling activity. These two results strongly imply that the highly conserved Ca^{2+} binding site is important for both activation of ion conduction in CaCC and lipid flipping in lipid scramblase members.

2.4.3.3 Investigations on the ion conduction pathway

Probing the number of independent pores in mTMEM16A with a concatemeric construct

The distinct architecture of the subunit cavity forming a half-channel gave rise to the theory of a potential alternative arrangement of the subunits in the ion channels (108). The two exposed half-channel subunits might adopt laterally inverted arrangement to form a single enclosed aqueous pore that would be completely surrounded by protein residues. The Ca^{2+}-binding site and the residues lining the ion conduction path would be in close proximity, and therefore, any change in the pore or the Ca^{2+}-binding site in one of the subunits may affect the activation and conduction properties of the entire protein. In contrast, in the case of CaCC maintaining similar architecture as nhTMEM16 with two separated ion conduction paths, a mutation in one subunit might only affect the activation and the conduction in one of the two pores.

To address the hypothesis that TMEM16A contains two ion conduction pores that are independently activated by Ca^{2+}, I have generated concatemeric constructs and added mutations to only one subunit. If the channels are comprised of two independent pores, a mutation affecting channel function, e.g. a mutation in the Ca^{2+}-binding site, would result in two distinct phenotypes, one for each channel. On the other hand, a modification in a single subunit on a channel only containing one common pore would result in a single current phenotype with altered properties.

The constructs used in this study was comprised of two subunits conjoined by a flexible linker (Figure 28). In order to accommodate any potential alternative arrangements of subunits, the linker was designed to be long and flexible. In the extreme case, the distance between the N-terminal domain of the first subunit and the C-terminal domain of the second subunit would be approximately 100 Å. By assuming a length of a residue to be 3.8 Å, an unstructured Gly linker of around 30 amino-acid would span this distance. Ser was incorporated in the linker after every two or three Gly to improve the solubility of the linker. After adjusting the nucleotide sequence encoding the linker to optimize codon usage, prevent the formation of hairpins and decrease the complementarity of the primers to avoid self-annealing, a 31 amino-acid long linker was designed with the following sequence: GSSGGSGGSGSSGSSGSGSSGGSGGSGSSGS.

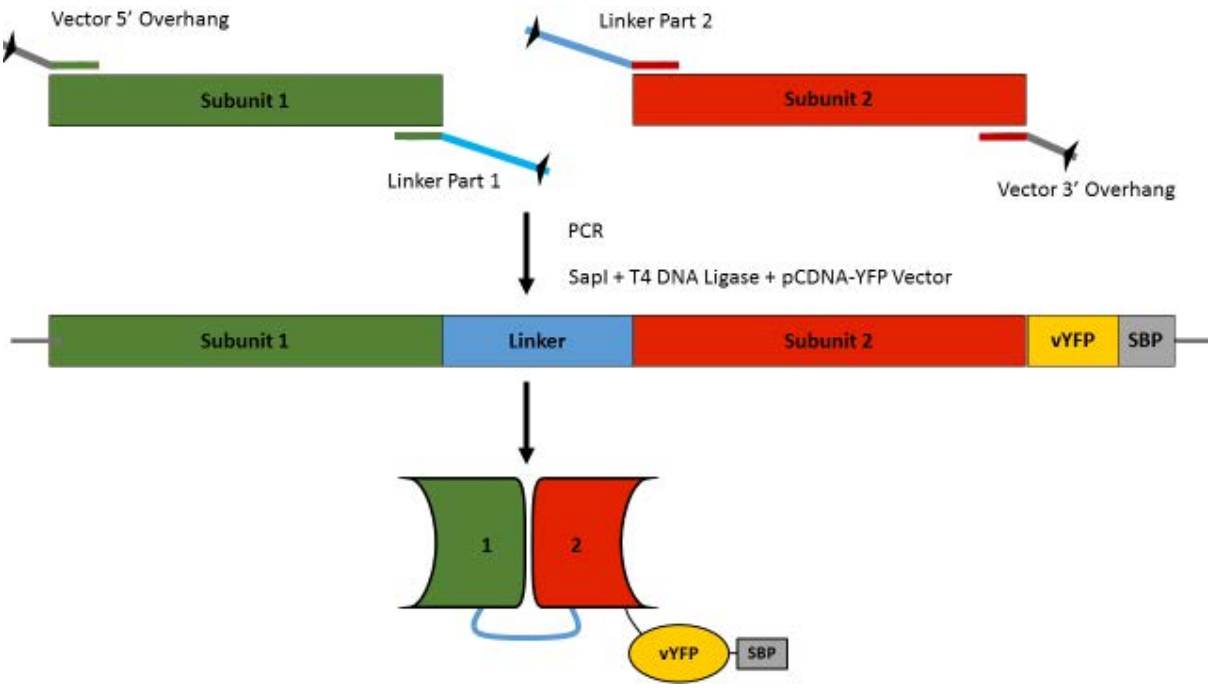

Figure 28 Scheme of concatemeric constructs.

Scheme for the generation of concatemeric constructs. The two subunits were amplified separately while incorporating half of the linker sequence in each subunit. The PCR products were digested by SapI and religated with T4 DNA ligase into a pCDNA vector containing a C-terminal vYFP and an SBP tag for purification.

Biochemical characterization of concatemeric constructs

After generating the concatemeric construct I have first addressed the question whether it would be biochemically stable and resemble the behaviour of WT TMEM16A. An initial characterization was performed by expressing the YFP-tagged protein in HEK cells and applying the extracted lysate onto a SEC column for FSEC analysis.

The concatemeric construct used for biochemical characterization contains a WT subunit linked to an E702Q subunit (WT_E702Q). For expression HEK293T cells were grown in 10 cm petri dishes to 60-80% confluency prior to transfection. For small scale tests, 10 to 20 plates of HEK293T cells were transfected with WT and WT-E702Q respectively. To obtain high transfection efficiency and high protein yield, the cells were transfected with Polyethylimine (PEI) for 36-40 hours. The efficiency of transfection was in the range of 50-80% as compared to 5-25% when transfected with Fugene reagent used for electrophysiological studies. For extraction, the harvested cell pellets were resuspended in buffer containing 1% DDM and solubilized for 2 hours. After extraction, a fraction of the lysate corresponding to the cells of one dish was loaded onto a SEC column and monitored by recording the fluorescence of vYFP. FSEC profiles of both WT and WT-E702Q construct showed a main peak at 8.57 ml, which corresponds to approximated mass of the TMEM16A homodimer, flanked by two smaller peaks (Figure 29a,c). These two smaller peaks were also observed when lysate of untransfected cells were loaded on the column, indicating that they are due to endogenous fluorescent proteins from the host cells. The lack of aggregation and the presence of a monodisperse peak suggested that both proteins are stable and of comparable size. I subsequently proceeded with affinity chromatography purification using Streptavidin coated resin to bind the solubilized proteins via their SBP-tag. After application of biotin, the eluted protein was reloaded onto the SEC column for FSEC. For both protein, in addition to the peak of the dimeric protein an aggregation peak around 7.5 ml and another peak around 11 ml corresponding to molecular weight of YFP were observed (Figure 29b,d). The fractions of the dimer were collected, concentrated and reinjected onto the column. The reinjection of the fraction gave a low-intensity peak at the expected size for both WT and WT-E702Q constructs.

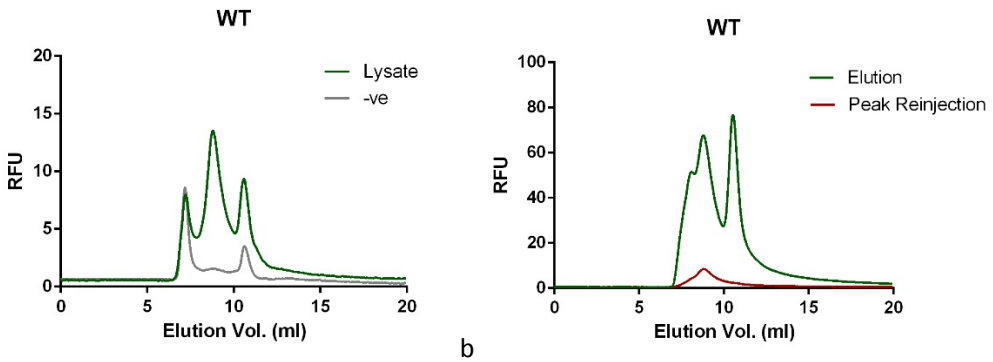

a b

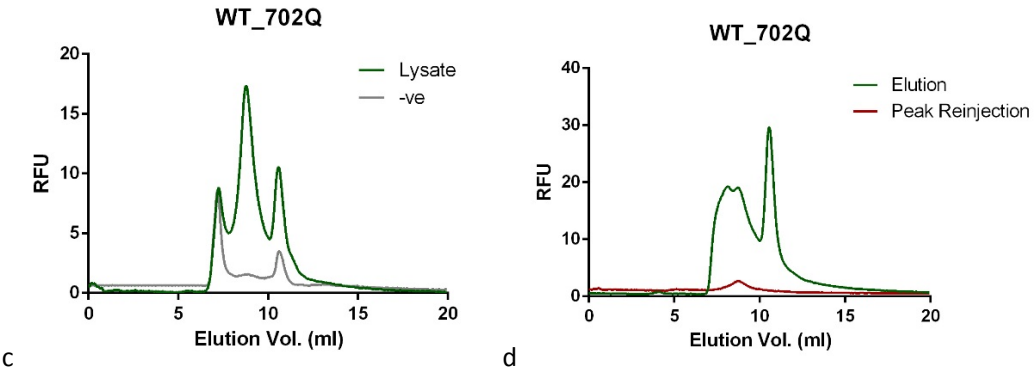

c d

Figure 29 Purification of WT and WT_E702Q extracted in DDM.

a, FSEC profile of WT lysate after extraction in DDM and **b,** FSEC profile of WT after purification with Streptavidin. FSEC profile of purified protein. **c,** FSEC profile of WT_E702Q lysate after extraction and **d,** FSEC profile of WT_E702Q after purification with Streptavidin. SEC was carried out on a Zorbax GF450 column.

Due to the ambiguous results in the small-scale test, expression and purification was repeated several times with both constructs with a culture obtained from 50 dishes. However, the purification attempts have proven to be highly variable and often resulted in aggregation after solubilisation with DDM. To address this, I performed a solubilisation screen for the WT construct with different detergents to improve the stability of the protein. For that purpose the cells from 6 plates were solubilized with 1% (wt/vol) Tridecylmaltoside (TriDM), 1% (wt/vol) Tetradecylmaltoside (TetDM) or 1% (wt/vol) digitonin for 2 hours. The lysates were then applied to a SEC column equilibrated in DDM for FSEC analysis. SEC was performed in DDM buffer instead of in the respective extraction detergent buffer to increase the throughput. I assumed that the protein is at least partially stable in DDM and any exchange of detergent on protein micelle would not rescue any aggregated protein. The analysis in DDM buffer would thus still reflect on the stability in the respective extraction detergent. All the extracts gave similar FSEC profile to the extract by DDM showing a clear main peak at 8.57 ml and the extract by digitonin gave slightly higher signal (Figure 30a). In order to test if the stability has been increased in the new detergents, the proteins were purified in buffer containing the respective detergent used during extraction and subjected to a thermal stability assay. For that purpose aliquots of the eluates were heated to 40 °C for 10 mins. Along with the non-heated samples, they were injected for FSEC analysis (Figure 30b). The retaining amount of non-aggregated protein compared to the non-heated sample is an indicator of the stability of the protein in a certain detergent. Sample extracted in DDM showed a reduction of the main protein peak by 50% and emergence of aggregation peak after being subjected to an incubation step at 40 °C. Samples extracted in TriDM and TetDM retained approximately 90% of the protein in the main peak, indicating that the thermostability has been increased. Sample extracted in digitonin were unaffected by the 40 °C step, and also gave rise to the highest overall signal, which suggests that a larger fraction of the protein could be purified by SBP-affinity chromatography.

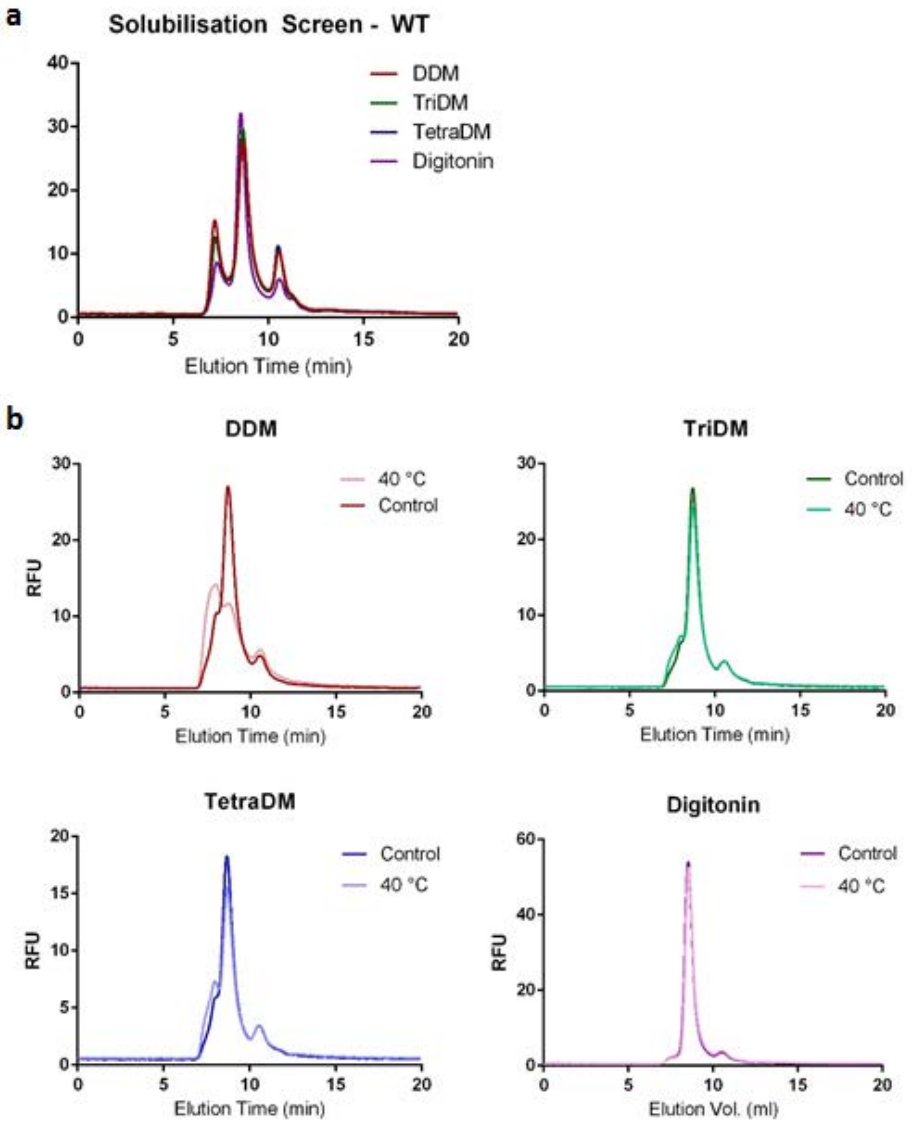

Figure 30 Extraction detergent screen of WT.

a, FSEC profile of lysate extracted in different detergents. **b,** FSEC profile of purified protein in different detergents after a 40 °C incubation step.

Based on the result that digitonin improved the stability of the protein, a scale-up of the purification of both WT and WT_702Q was repeated from 20 plates using 1% digitonin for extraction. For that purpose protein was purified in 0.12% digitonin and subsequently loaded on a SEC column pre-equilibrated in buffer containing 0.12% digitonin. The FSEC analysis showed a sharp monodisperse peak for both WT and WT-702Q (Figure 31a,c). The reinjection of the main peaks again resulted in a clear monodisperse peak without any aggregation or degradation (Figure 31b,d). The peak fractions of both constructs were run on SDS-PAGE (Figure 31e). The concatemer exhibited twice the size of a single subunit and no proteolysis was observed. Taken altogether, these results suggest that the covalent linkage neither affected the stability of the protein nor alter its oligomerization behaviour. This illustrated that the concatemer, even with the addition of a long linker, does not favour intermolecular interactions thereby generating higher molecular weight assemblies.

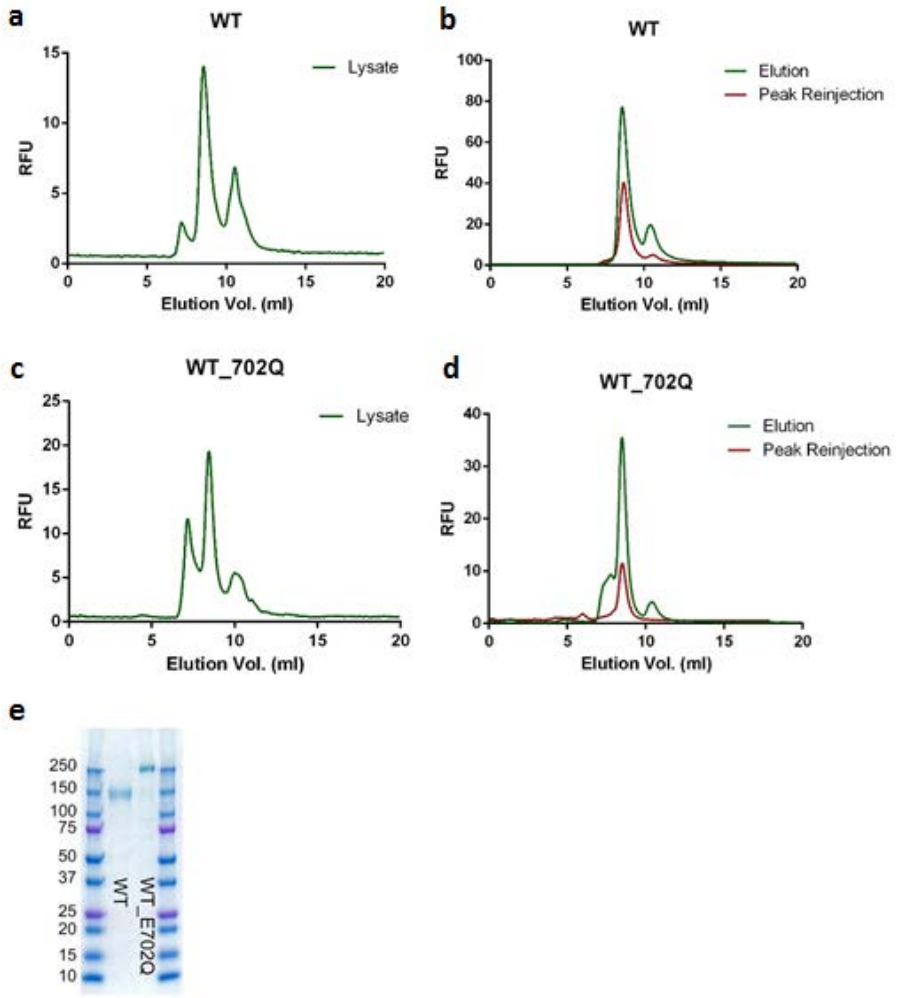

Figure 31 Purification of WT and WT_E702Q in Digitonin.

a, FSEC profile of WT lysate after extraction in digitonin and **b,** FSEC profile of WT after purification with Streptavidin resin. **c,** FSEC profile of WT_E702Q lysate after extraction and **d,** FSEC profile of WT_E702Q after purification with Streptavidin resin. **e,** SDS-PAGE of purified protein. Both proteins (WT and WT_E702Q) run at the expected molecular weight. Molecular weight of markers (kDa) are indicated.

Electrophysiology of concatemeric constructs

WT_WT

After demonstrating that the concatenation of two subunits did not affect the oligomerazation of the protein I have investigated whether it would affect its functional properties. The concatemeric construct WT_WT, containing two WT subunits, was expressed in HEK293T cells and characterised by patch-clamp electrophysiology in inside-out configuration. The Ca dose-response profile of WT_WT could be fitted as single sigmoidal curve with parameters similar to the WT (Figure 32). The EC_{50} value of WT_WT is slightly shifted to 0.39 µM Ca^{2+} while the Hill coefficient of WT_WT of 2.1 is similar to that of WT. This strongly suggests that the WT_WT functions like the WT dimer and that the covalent linker did not significantly affect

ion conduction of the channel. The concatemeric constructs are thus suitable for further functional studies to investigate the questions of independent ion conduction pores in a double-barreled channel.

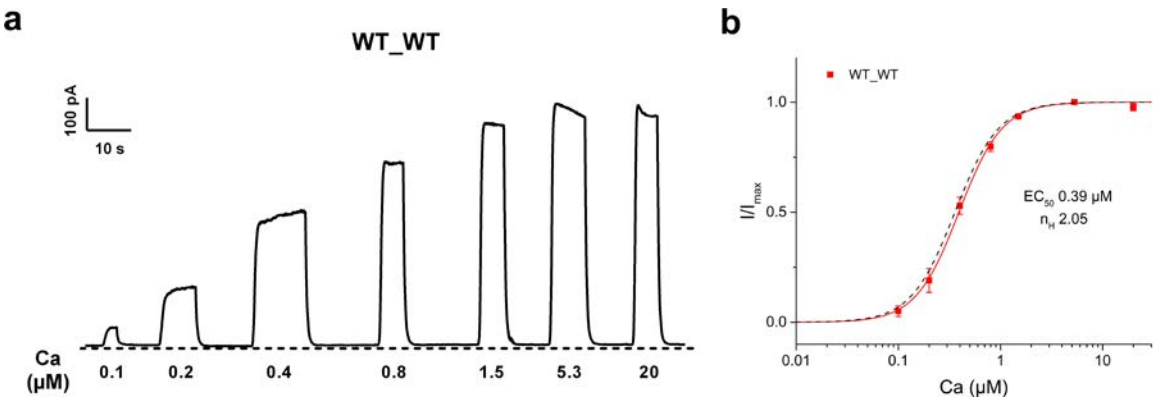

Figure 32 Dose-response relationships of activation by Ca^{2+} of the WT_WT concatemer.

a, Activation of WT_WT by Ca^{2+} recorded at +80 mV. Dotted line represents the baseline at 0 pA. The applied Ca^{2+} concentrations (μM) of each activation step were indicated below the trace. **b,** Dose-response curve of WT_WT. WT is shown as dotted line for comparison.

WT_654Q

As the concatenation of two subunits did not significantly alter the protein function, I was interested whether each subunit would retain its functional phenotype. To test this, I have generated a WT_654Q construct. The E654Q mutation was shown earlier to strongly impair activation by Ca^{2+} and to only exhibit low activation at high Ca^{2+} concentration of around 1 mM. If the protein exhibits functional independence of the two pores, the absence of activation on the second subunit at sub millimolar concentration would result in a channel with the functional phenotype of WT.

WT_E654Q was expressed in HEK293T cells. Inside-out patches were perfused with Ca^{2+} up to 2 mM and channel activation was recorded at 80 mV (Figure 33a). The patches exhibit a WT-like dose-response profile with maximal currents observed at 5 μM Ca^{2+}. At concentrations higher than 5 μM, only sub-maximal currents were observed due to strong rundown effect affecting all the patches. Thus potential low currents from the E654Q subunit could not be detected. The dose-response curve of the concatemer was fitted to a Hill equation with similar parameters as WT (Figure 33b). Both EC_{50} and n_H were slightly lower than WT, which might have been influenced by the rundown effect. Nevertheless, combined with the observation that no current were observed from the inactivated subunit, the results supports the hypothesis that the dimer contains two ion conduction pores that are independently activated by Ca^{2+}.

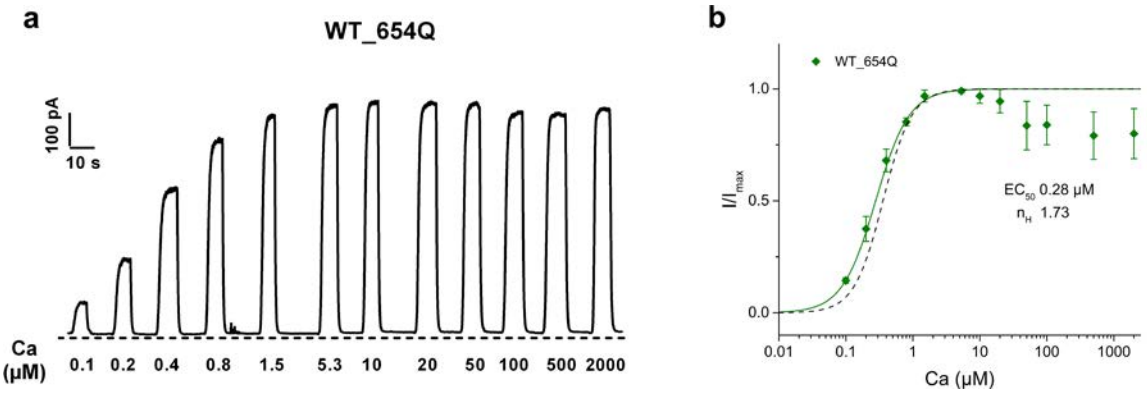

Figure 33 Dose-response relationships of activation by Ca^{2+} of the WT_E654Q concatemer.

a, Activation of WT_654Q by Ca^{2+} at indicated Ca^{2+} concentrations recorded at +80 mV. The dotted line represents baseline at 0 pA. The applied Ca^{2+} concentration (µM) of each activation step is indicated below the trace. **b,** Dose-response curve of WT_654Q. WT is shown as dotted line for comparison.

WT_702Q

To further prove that the two subunits in the dimer are independently activated by Ca^{2+}, I have constructed a concatemer containing two functional subunits that are activated at different Ca^{2+} concentrations. For that purpose I have decided to concatenate WT and the E702Q mutant. This mutant was previously shown to exhibit robust Ca^{2+} dependent currents with similar cooperativity as the WT albeit with EC_{50} of activation that is over 200 times higher than WT. As the range of activating Ca^{2+} concentrations of E702Q is distinctly different to that of WT, I expected WT_E702Q to exhibit a biphasic dose-response behaviour in case two subunits were activated independently.

WT_E702Q was expressed in HEK293T cells and the corresponding inside-out patches were perfused with Ca^{2+} at concentrations up to 2 mM (Figure 34a). An increase number of Ca^{2+} concentrations compared to WT recordings was used to better resolve the activation steps in the dose-response curve. As expected, the curve was biphasic (Figure 34b). When fitted to the biphasic Hill equation, the obtained EC_{50} values were very close to the values of the respective constructs in non-concatenated homomeric proteins. While the Hill coefficient of the second activation was identical to that of E702Q, the Hill coefficient of the first activation was slightly lower than that of WT. The fitting of Frac also suggested that the currents were contributed by WT and E702Q almost equally.

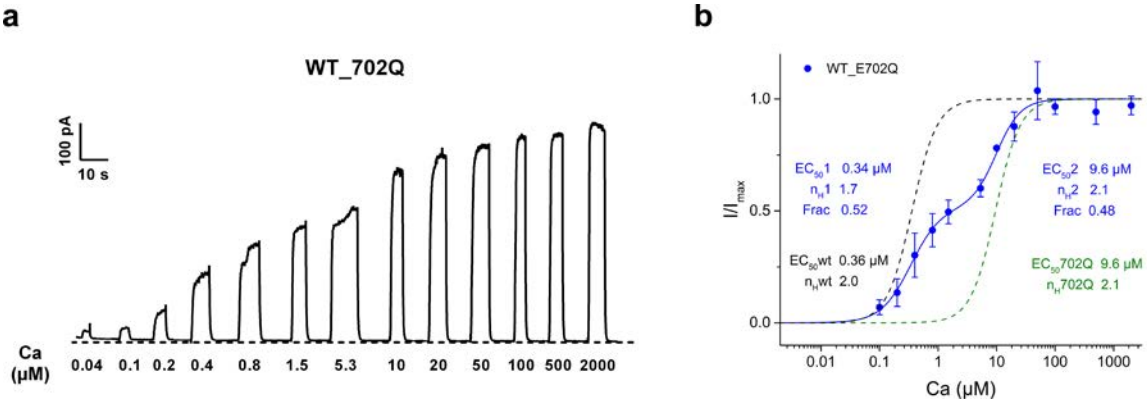

Figure 34 Dose-response of activation by Ca^{2+} of the WT_E702Q concatemer.

a, Activation of WT_702Q by Ca^{2+} recorded at +80 mV. Dotted line represents the current at 0 pA. The applied Ca^{2+} concentrations (μM) of each activation step are indicated below the trace. **b,** Dose-response relationship of WT_702Q. WT and E702Q are showed as dotted lines for comparison.

Conclusion

The work described in this chapter has provided the foundation for the characterization of the functional properties of mTMEM16 that demonstrated that it is acting as a double barreled-channel with two independent pores. This study was expanded and is described in the attached article on which I share first authorship (110). The results shown in this publication differ slightly in terms of the actual values due to difference in the methods employed. In this chapter, the recording of Ca^{2+}-dose response relationships in excised patches was performed in a sequence of rapid application of increasing Ca^{2+} concentrations. In the paper, we have changed the method to correct for the rundown effect. Briefly, a reference Ca^{2+} pulse at a regular time interval was applied before and after the test pulse. The magnitude of the test pulse was then normalized to averaged magnitude of the two reference pulses. The correction for rundown allowed more accurate measurement over a long period time. Despite the small quantitative differences, the conclusions of the experiments shown here are in full agreement with the results shown in the paper.

ARTICLE

doi:10.1038/nature13984

X-ray structure of a calcium-activated TMEM16 lipid scramblase

Janine D. Brunner[1], Novandy K. Lim[1], Stephan Schenck[1], Alessia Duerst[1] & Raimund Dutzler[1]

The TMEM16 family of proteins, also known as anoctamins, features a remarkable functional diversity. This family contains the long sought-after Ca^{2+}-activated chloride channels as well as lipid scramblases and cation channels. Here we present the crystal structure of a TMEM16 family member from the fungus *Nectria haematococca* that operates as a Ca^{2+}-activated lipid scramblase. Each subunit of the homodimeric protein contains ten transmembrane helices and a hydrophilic membrane-traversing cavity that is exposed to the lipid bilayer as a potential site of catalysis. This cavity harbours a conserved Ca^{2+}-binding site located within the hydrophobic core of the membrane. Mutations of residues involved in Ca^{2+} coordination affect both lipid scrambling in *N. haematococca* TMEM16 and ion conduction in the Cl^- channel TMEM16A. The structure reveals the general architecture of the family and its mode of Ca^{2+} activation. It also provides insight into potential scrambling mechanisms and serves as a framework to unravel the conduction of ions in certain TMEM16 proteins.

The TMEM16 or anoctamin family constitutes a class of membrane proteins that is only expressed in eukaryotic organisms. In vertebrates the family encompasses ten members with high sequence conservation[1]. Despite their close relationship these proteins combine different functions as some members are Ca^{2+}-activated ion channels while others work as Ca^{2+}-activated scramblases[2], which catalyse the shuffling of lipids between the inner and outer leaflets of the bilayer in an ATP-independent manner. In 2008 three groups independently identified TMEM16A (or Ano1) as the long sought-after Ca^{2+}-activated chloride channel (CaCC)[3–5]. After this discovery the name anoctamin was coined, synonymous for anion selectivity and the eight transmembrane spanning helices that were predicted by hydropathy analysis[3]. It has been shown that TMEM16A and TMEM16B (Ano2) share similar characteristics, although with different tissue distribution[3,5,6]. Whereas TMEM16A contributes to diverse physiological processes, such as epithelial chloride secretion, electrical signalling in smooth muscles and potentially also nociception[7,8], TMEM16B is expressed in the retina and in olfactory epithelia and might have a role in olfaction[6,9]. In further studies TMEM16F (Ano6) was shown to act as Ca^{2+}-activated small-conductance cation channel[10], possibly also as Cl^- channel[11] and to have a role in Ca^{2+}-activated lipid scrambling by facilitating the exchange of phosphatidylserine from the inner to the outer leaflet of the bilayer in blood platelets[10,12]. Similarly, TMEM16C, D, G and J (Ano3, 4, 7 and 9, respectively) were suggested to work as scramblases, although with variable lipid preference[13]. Recently a fungal TMEM16 homologue from *Aspergillus fumigatus* (afTMEM16) was found to scramble lipids as well after its purification and reconstitution into liposomes[14]. Besides its function as scramblase, afTMEM16 was also proposed to form non-selective ion channels with high conductance[14]. It is still a matter of debate how these closely related proteins can accommodate such a diversity of functional phenotypes[2,15].

Despite the functional breadth, characterized family members appear to share a similar mode of Ca^{2+} activation. This behaviour has been most thoroughly investigated for the chloride channel TMEM16A[3,16,17]. In TMEM16A Ca^{2+} activates the channel from the intracellular side at sub-micromolar concentrations with a half-maximum effective concentration (EC_{50}) that is voltage-dependent and decreases upon depolarization. Two conserved glutamate residues have been discovered to be involved in the Ca^{2+} activation of ion conduction in TMEM16A[18,19] and TMEM16F[10] and scrambling in afTMEM16[14], thus indicating the conservation of this regulatory mechanism within the family.

Although we have by now gained considerable insight into the functional properties of certain family members, their architecture and its relation to mechanisms of action are still unknown. Here we present the X-ray structure of a TMEM16 homologue from *Nectria haematococca* (nhTMEM16). The dimeric protein shows a novel fold with ten membrane-spanning segments per subunit. The transmembrane domain contains a highly conserved region that is embedded within the hydrophobic core of the membrane comprising a Ca^{2+}-binding site. Ca^{2+} binding by six residues, five of which carry a negative charge, controls the activation of scrambling in nhTMEM16 and ion conduction in TMEM16A. Our results thus have revealed a conserved structural framework that supports diverse functional properties within the family.

Functional characterization of nhTMEM16

To gain insight into the architecture of the TMEM16 family we screened 80 members in *Saccharomyces cerevisiae* and HEK tsA201 cells for overexpression and detergent stability, and were able to identify a homologue from the fungus *Nectria haematococca* (nhTMEM16), exhibiting the desired biochemical properties. The protein shares 48% of identical residues with the previously characterized afTMEM16 (with >70% homology within the transmembrane domain) (Extended Data Fig. 1a). Among mammalian proteins the relationship is closest to TMEM16H and K (Ano8 and 10) but it is still close to the more distantly related chloride channel TMEM16A (with homologies in the transmembrane region ranging between 39% and 42%), thus suggesting that all family members share a similar structural organization (Extended Data Fig. 1b,c). Unlike its mammalian counterparts, nhTMEM16 is not glycosylated. The solubilized protein is a dimer, as quantified by multi-angle light scattering, suggesting that the oligomeric organization is preserved in detergent solution (Extended Data Fig. 2a). To characterize its functional properties we have reconstituted the protein into liposomes and found, with respect to its scrambling activity, a very similar behaviour as described for the related afTMEM16. The function as lipid scramblase

[1]Department of Biochemistry, University of Zurich, Winterthurerstrasse 190, CH-8057 Zurich, Switzerland.

©2014 Macmillan Publishers Limited. All rights reserved

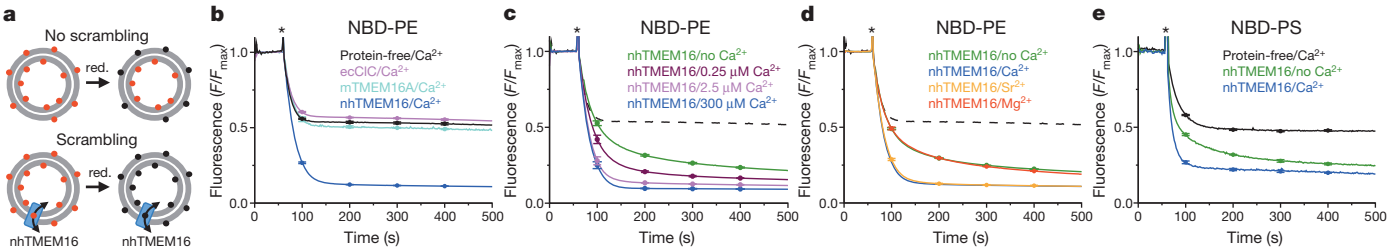

Figure 1 | Phospholipid scrambling by nhTMEM16. **a**, Scheme of the assay depicting the reduction of NBD-labelled phospholipids in the outer leaflet of the bilayer upon addition of dithionite (red.). **b**, Scrambling of NBD-PE. Traces of protein-free liposomes and proteoliposomes containing either nhTMEM16, the *E. coli* ClC transporter (ecClC) or mTMEM16A are shown. Asterisk marks addition of dithionite. **c**, Ca^{2+} dependence of NBD-PE scrambling by nhTMEM16. **d**, Influence of other divalent cations on NBD-PE scrambling by nhTMEM16. In **c** and **d**, protein-free liposomes (dashed lines) are shown for comparison. **e**, Scrambling of liposomes containing NBD-PS. Traces of protein-free liposomes and proteoliposomes containing nhTMEM16 in the absence and presence of Ca^{2+} are shown. **b**–**e**, Traces show averages of 3–4 measurements, standard deviations are included for selected time points. Unless stated otherwise, solutions contain 0.3 mM of the indicated free divalent cations. Scrambling experiments were replicated three times with similar results.

was investigated by an assay that monitors the reduction of fluorescently labelled lipids by sodium dithionite on the outer leaflet of liposomes[14,20] (Fig. 1a, Extended Data Fig. 2b–d). Our results demonstrate that nhTMEM16 catalyses the movement of nitrobenzoxadiazole-phosphatidylethanolamine (NBD-PE) and NBD-phosphatidylserine (NBD-PS) between the two layers of the liposome membrane (Fig. 1b, e). The observed effect is not due to permeation of dithionite through the protein (Extended Data Fig. 2b). Furthermore, we found that this catalytic function is enhanced by Ca^{2+} at submicromolar concentrations (Fig. 1c). Besides Ca^{2+}, we also observed activation for Sr^{2+} but not for Mg^{2+} (Fig. 1d). Scrambling in nhTMEM16 containing proteoliposomes measured under Ca^{2+}-free conditions may either be due to constitutive activity of the ligand-free scramblase or originate from traces of Ca^{2+} still bound to the protein (Supplementary Discussion, Extended Data Fig. 2d). To investigate whether nhTMEM16 would also function as ion channel, we have attempted to study ion conduction from proteoliposomes fused to artificial lipid bilayers and by patch-clamp electrophysiology of HEK293T cells expressing the protein. However, in neither case did we find any convincing evidence for ion channel activity (Extended Data Fig. 3 and Supplementary Discussion).

nhTMEM16 structure

For structure determination, nhTMEM16 was crystallized in two different crystal forms (CF1 and CF2), each containing a dimer in the asymmetric unit, for which we have collected data at 3.3 and 3.4 Å resolution respectively (Extended Data Fig. 4a). Initial phases, obtained by the Se-Met single-wavelength anomalous dispersion method, were improved and extended by non-crystallographic symmetry and cross-crystal averaging. The resulting electron density was of high quality and allowed the unambiguous interpretation by an atomic model (Extended Data Figs 4 and 5). The structure of the dimer is depicted in Fig. 2a. Both subunits are related by twofold symmetry and show very similar conformations. When viewed from the extracellular side the dimer has a rhombus-like shape with about 130 Å in the long and 40 Å in the short dimension (Extended Data Fig. 6). The topology of the nhTMEM16 subunit is shown in Fig. 2b. Both termini are structured and located on the cytoplasmic side of the membrane. The α-helices and β-strands of the amino-terminal domain are organized in a ferredoxin-like fold. The three α-helices of the carboxy terminus are wrapped around the N-terminal domain of the adjacent subunit, thereby constituting a large part of the subunit interface (Fig. 2c). The transmembrane domain starts with two short α-helices (α0a and α0b), followed by ten membrane-spanning segments (α1–α10). The two initial helices form a hairpin with amphiphilic properties, with its hydrophobic side interacting with α-helices 1 and 8. A model of the protein embedded in a lipid bilayer suggests that both helices only peripherally interact with the inner leaflet of the membrane (Extended Data Fig. 7a, b). Helices α1–α10, in contrast, all traverse the entire membrane with some of them being bent and tilted

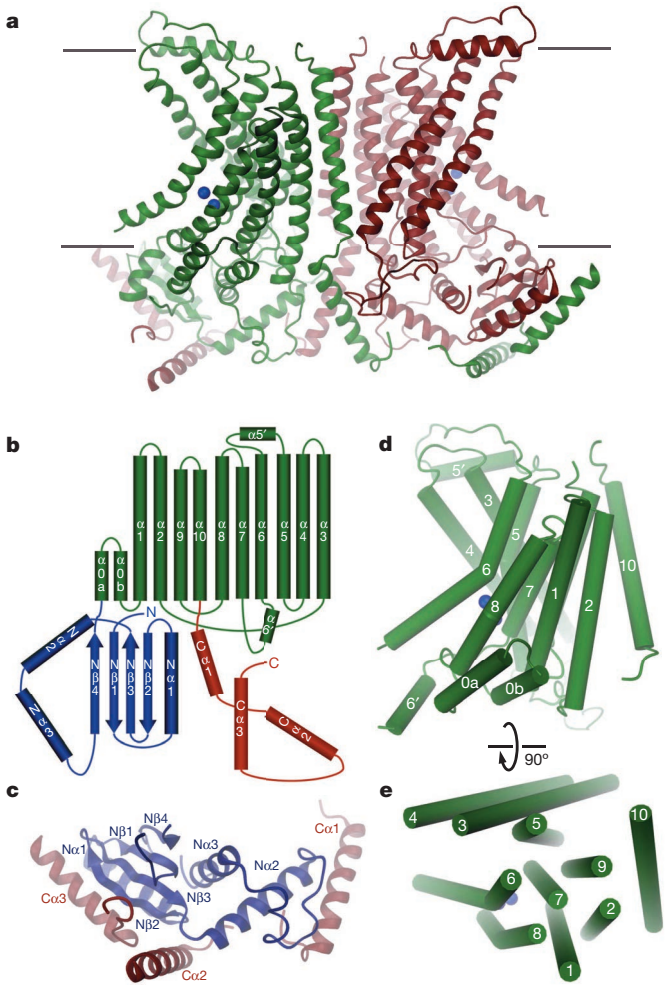

Figure 2 | nhTMEM16 structure. **a**, Ribbon representation of the nhTMEM16 dimer. The view is from within the membrane. Bound calcium ions are shown as blue spheres. The membrane boundary is indicated. **b**, Topology of the nhTMEM16 subunit. The transmembrane domain is coloured in green, the N- and C-terminal domains in blue and red, respectively. **c**, View of the cytoplasmic domains. The interaction of the N-terminal domain with the C-terminal domain of the adjacent subunit is shown. **d**, Transmembrane domain with α-helices shown as cylinders and labelled. The view is as in **a**. **e**, Organization of transmembrane helices. The view is from the extracellular side. Loop regions are omitted for clarity. Figures 2–4 and 6 were prepared with DINO (http://www.dino3d.org/) and show the structure determined in crystal form 1 (CF1) unless stated otherwise.

©2014 Macmillan Publishers Limited. All rights reserved

with respect to its plane (Fig. 2d, e). The transmembrane segments are connected by loop regions of variable length, two of which contain short helical regions (named α5′ and α6′, according to the preceding transmembrane region), on the extracellular and cytoplasmic side, respectively. The arrangement of α-helices does not follow any obvious symmetry or show any relationship to known membrane protein structures.

Dimer interface and dimer cavity

The dimeric organization of nhTMEM16 is reflected in the extended interface between the two subunits, which buries 9,650 Å^2 of the combined molecular surface. The largest part of this interface is contributed by interactions between the N- and C-terminal domains, whereas the contact area of 1,520 Å^2 between the transmembrane domains is comparably small. In the transmembrane region the dimer interface is formed by interactions of residues in the N-terminal part of α-helix 10 at the extracellular side close to the symmetry axis and interactions between α-helices 3 and 10 at their cytoplasmic end (Fig. 3a, b). Mutual interactions between residues of α-helices 10 involve hydrophobic contacts and a pair of salt bridges between a glutamate and a histidine side-chain that are conserved within the family, except for TMEM16A and B (Extended Data Fig. 7c). The arrangement of helices close to the dimer interface generates a large pore-like structure across the transmembrane region, the dimer cavity, which contains two separate 15 Å wide entrances at the extracellular side and which merges to one big, about 30 Å wide vestibule, at the intracellular half of the membrane (Fig. 3b, Extended Data Fig. 7d, e). Although on the inside this large cavity is confined by residues of the cytoplasmic domains, several fenestrations create access to the cytoplasm. In the transmembrane region the dimer cavity is accessible to the outer leaflet of the membrane via two v-shaped gaps framed by α-helices 3 and 10 from adjacent subunits (Fig. 3b, Extended Data Fig. 7e). Within the membrane, the vestibule is predominantly composed of hydrophobic and aromatic residues, which are conserved within the protein family, whereas there are several polar and charged residues found at the intracellular part outside of the predicted membrane region (Extended Data Fig. 7d, e). We thus suppose that the dimer cavity may be packed with lipids. The inside of this large cavity contains excess electron density, which is, however, not sufficiently ordered to be attributed to either solvent, or detergent and lipids (Extended Data Fig. 7f). It is currently not clear whether this region has a critical role for protein function.

Subunit cavity and Ca^{2+}-binding region

With respect to function, the most remarkable feature is found on the surface opposite to the dimer interface. Here a narrow crevice that spans the entire membrane is formed by α-helices 3–7 of the same subunit (Fig. 3c, Extended Data Fig. 8). These α-helices surround an 8–11 Å wide cavity that is twisted like a 'spiral staircase' and on one side is exposed to the membrane. In contrast to the dimer cavity the surface of the subunit cavity is strongly hydrophilic, despite its exposure to the lipid environment (Fig. 3c). Furthermore, it harbours residues for which equivalent positions have previously been shown to be involved in ion conduction in TMEM16A[18] and to influence ion selectivity in TMEM16A and F[10]. These observations make this region a prime candidate for the translocation path in both channels and scramblases. Within the hydrophobic core of the membrane, at a distance corresponding to about one third of its thickness from the intracellular side, the subunit cavity is lined by residues of α-helices 6 and 7, which are part of a conserved Ca^{2+}-binding site (Fig. 4a, b and Extended Data Fig. 8d). In the crystal structure, we have detected bound Ca^{2+} ions by anomalous scattering. Two peaks of strong anomalous difference density were found in each subunit at equivalent places (Fig. 4c, d). These peaks are separated by a distance of 4.2 Å and they are surrounded by three glutamates, two aspartates and an asparagine located on α-helices 6, 7 and 8 (Fig. 4e). Although from our data we cannot tell with certainty whether one or two Ca^{2+} ions are bound at the same time, simultaneous occupancy seems possible owing to the high density of negative charge in this region. All residues involved in Ca^{2+} binding are highly conserved within the TMEM16 family, which strongly supports a common Ca^{2+} binding and activation mode.

Functional investigation of the Ca^{2+}-binding region

Since the nhTMEM16 structure has allowed the identification of a conserved Ca^{2+}-binding site, we were interested to investigate the relevance of these interactions for activation in nhTMEM16 and TMEM16A. The two glutamates located in α-helix 7 have previously been shown to play an important role in the activation of TMEM16A[18], F[10] and afTMEM16[14] by Ca^{2+}. A Ca^{2+}-binding site triple-mutant of nhTMEM16 combining mutations of residues involved in Ca^{2+} coordination identified in this study (that is, E452Q, E535Q and D539N) shows only weak scrambling activity that is not enhanced by Ca^{2+} (Fig. 5a). To probe the importance of the same residues for the activation of ion conduction in murine TMEM16A (mTMEM16A), we have expressed the protein in HEK293T cells and monitored the Ca^{2+}-dependence in binding site mutants by patch-clamp electrophysiology. As previously shown Ca^{2+} activates mTMEM16A in a voltage-dependent manner with an apparent affinity that is higher at positive than at negative potentials[3] (Fig. 5b). At 80 mV Ca^{2+} activates the wild-type protein with an EC_{50} of 0.36 μM and a Hill coefficient of 2.3, which indicates a cooperative process that involves the binding of more than one ion. Single mutants of each residue contributing to the observed interactions in the Ca^{2+}-binding region

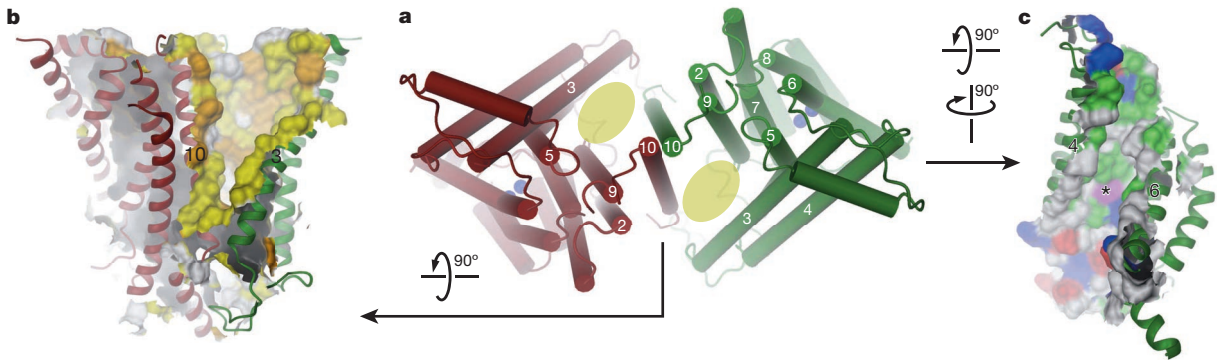

Figure 3 | Dimer interface and subunit cavity. a, Transmembrane domain of the nhTMEM16 dimer viewed from the extracellular side with yellow ovals indicating the location of the dimer cavity. Helices are represented as cylinders. **b**, Dimer cavity viewed from within the membrane. Helices of both subunits lining the cavity are displayed. The solvent-accessible surface of the cavity is shown with locations of hydrophobic and aromatic residues coloured in yellow and orange, respectively. **c**, Subunit cavity viewed from within the membrane. The solvent-accessible surface is coloured according to the properties of contacting residues (red, acidic; blue, basic; green, polar). A position that was shown to influence the ion selectivity in TMEM16A and TMEM16F is coloured in magenta and labelled with an asterisk.

©2014 Macmillan Publishers Limited. All rights reserved

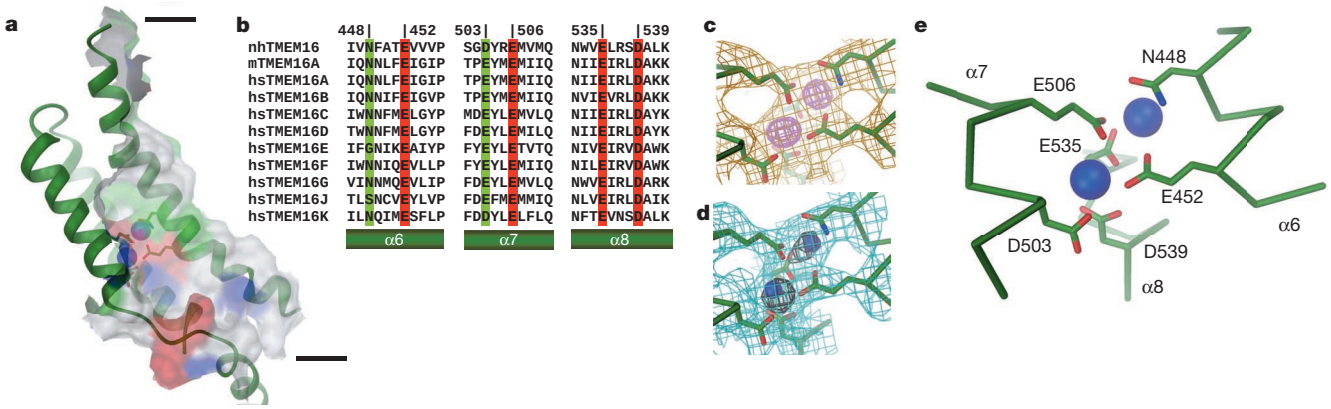

Figure 4 | Ca^{2+}-binding site. **a**, Location of the Ca^{2+}-binding site in relation to the subunit cavity. The view is from within the membrane, the colour coding as in Fig. 3c. **b**, Sequence alignment. Conserved amino acids of the Ca^{2+}-binding site are highlighted in red (identical) and green (homologous). hs, *Homo sapiens*. **c**, View of the Ca^{2+}-binding site in the refined structure of CF2. The $2F_o - F_c$ electron density (at 3.5 Å, contoured at 1σ, orange) is shown superimposed on the model. Anomalous difference electron density (at 3.8 Å, contoured at 5σ) is shown in magenta. **d**, View of the Ca^{2+}-binding site in the refined structure of CF1. The $2F_o - F_c$ electron density (at 3.3 Å, 1σ, cyan, 5σ, black) is shown superimposed on the model containing Ca^{2+} ions (blue spheres). **e**, Model of the Ca^{2+}-binding site.

shift the EC_{50} to higher Ca^{2+} concentrations (Fig. 5c and d, Extended Data Figs 9 and 10). The strongest effect was observed for Glu 654, where we have not observed any activation for E654Q and only low currents at high Ca^{2+} concentration for E654A, despite the strong plasma membrane expression of the channel (Extended Data Fig. 10h). Similar results were reported in a recent study that was based on the mutation of conserved acidic residues[21]. Taken together, our functional experiments on nhTMEM16 and mTMEM16A suggest that Ca^{2+} binding by equivalent residues regulates both functional branches of the family by a common mechanism.

Discussion

The structure of nhTMEM16 has revealed a framework for the TMEM16/anoctamin family. Whereas its homodimeric organization is consistent with previous investigations of TMEM16A, B, F and afTMEM16[14,22–24], a direct interaction between the N termini, which was proposed to be involved in dimerization of TMEM16A, is not observed[24]. In nhTMEM16, each subunit contains ten membrane-spanning helices, which differs from the eight transmembrane segments predicted from hydropathy analysis[3,25] (Extended Data Fig. 1c). It is however noteworthy that a recent study, which has revised the originally proposed topology, has correctly identified residues of the Ca^{2+}-binding site and the extracellular entry to the putative pore region[18]. The structure harbours two regions that are presumably in contact with the membrane; the dimer cavity, a large and predominantly hydrophobic structure at the dimer interface, and the subunit cavity, a hydrophilic membrane-spanning crevice contained within each subunit that resembles a spiral staircase. Whereas the functional relevance of the dimer cavity is currently unclear, the subunit cavity is linked to Ca^{2+} activation and probably also to catalytic properties of the protein (Fig. 3, Extended Data Fig. 8).

As a scramblase nhTMEM16 has provided first structural insight into an important class of transport molecules. These proteins catalyse the passive movement of lipids between the two leaflets of a bilayer, a process that is essential for membrane biogenesis in the endoplasmic reticulum[26] and the shuffling of lipids in several processes, including blood coagulation[10,12], apoptosis[27], glycosylation[28] and the assembly of the bacterial cell wall[29]. To lower the large intrinsic energy barrier associated with lipid flipping, it was proposed that scramblases would provide a hydrophilic path to facilitate the movement of the polar headgroups across the bilayer[26,30]. The subunit cavity of nhTMEM16 would ideally meet these requirements, as it is hydrophilic, accessible to the membrane and of sufficient dimensions to accommodate a phospholipid headgroup (Fig. 6a). These properties would also be consistent with the broad range of lipids that have been shown to be translocated by afTMEM16[14] and other Ca^{2+}-activated lipid scramblases[31]. Proteins with scrambling function belong to various families[13,20,27,29], some of which are still disputed[32] or have not yet been identified on a molecular level. It will thus be interesting to see to which extent structural and mechanistic features proposed in our work are shared by unrelated scramblases and whether still unassigned scrambling processes would be catalysed by TMEM16 proteins.

In TMEM16A, B and F, the subunit cavity may constitute the ion conduction pore, as suggested by the influence of point mutations of

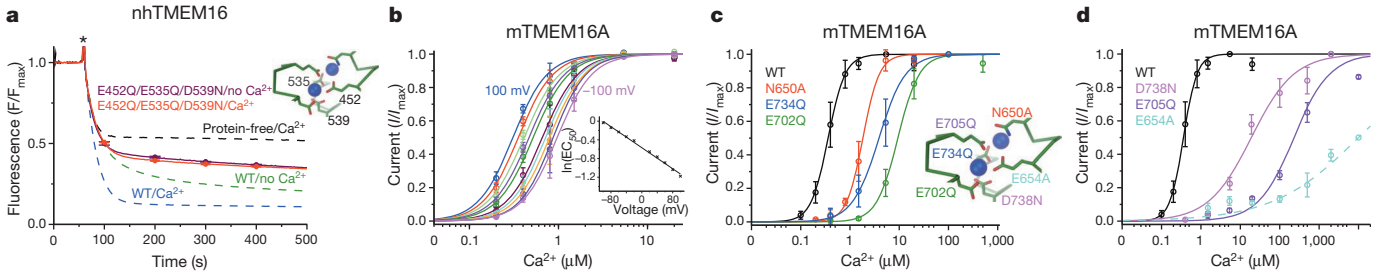

Figure 5 | Functional properties of Ca^{2+}-binding site mutants. **a**, Scrambling of the nhTMEM16 mutant E452Q/E535Q/D539N. Data of proteoliposomes containing NBD-PE and the triple mutant in absence and presence of 0.3 mM free Ca^{2+} are shown. Traces and statistics are as in Fig. 1 with dashed lines shown for comparison. Inset indicates the position of the mutations. WT, wild type. **b**, Voltage dependence of Ca^{2+} activation in mTMEM16A measured from excised inside-out patches. Currents were normalized to the maximum, lines show a fit to a Hill equation. The voltage dependence is shown as inset. **c**, **d**, Activation of Ca^{2+}-binding site mutants. Data were recorded at 80 mV and normalized to the maximum. Lines show a fit to a Hill equation (the fit for E654A was estimated). Numbers in inset correspond to mTMEM16A. Data in **b**–**d** are averages from 3–4 independent measurements, errors are s.d.

©2014 Macmillan Publishers Limited. All rights reserved

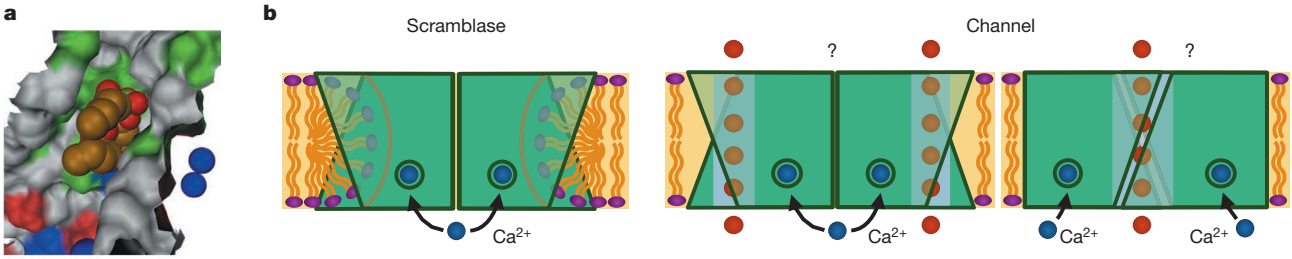

Figure 6 | Mechanism. a, Model of phosphatidylcholine in the subunit cavity. The acyl chains have been truncated for clarity. Bound Ca^{2+} ions are shown as blue spheres. **b**, Scheme illustrating the potential relationship between scramblases and ion channels within the TMEM16 family. Two distinct dimeric arrangements of TMEM16 channels are shown with one resembling the nhTMEM16 structure (centre) and the other formed by monomers that interact via the subunit cavities (right).

residues facing the subunit cavity on ion selectivity and conductance[10,18]. In TMEM16A and B, it is still puzzling how the subunit cavity might provide the aqueous environment required for ion conduction and, conversely, how lipid scrambling would be precluded in these proteins[13,14,33] (Fig. 1b). This distinction could be accomplished by local structural differences in an assembly as observed in nhTMEM16. Alternatively, it is tempting to speculate that in TMEM16 channels, the monomers might be turned by 180° and interact via their subunit cavities to form an enclosed pore. These different dimer assemblies would provide a plausible explanation for the functional dichotomy in TMEM16 proteins and are largely compatible with the structure of the monomer (Fig. 6b). Whereas the arrangement that is similar to nhTMEM16 would contain two potentially independent pores, as seen in the ClC family[34], the latter would probably result in a single ion conduction path.

For scramblases it will be important to investigate whether lipid movement locally distorts the membrane and whether ions can pass through the bilayer by binding to the polar headgroups of lipids that are in the process of being scrambled, which could potentially give rise to the small ion conductance observed in TMEM16F[10]. The large channels observed in afTMEM16[14] may be distinct from the described process and no such property has so far been detected for the closely related homologue investigated in this study. Similarly, a potential chloride-selective ion conductance of TMEM16F[11], which was proposed to be independent of its role in scrambling[35] and a similar function in other TMEM16 proteins[36] still requires closer investigation. The coexistence of ion channels and lipid scramblases in the TMEM16 family is somewhat reminiscent of P-type ATPases[37], which include primary active ion pumps and ATP-driven lipid flippases with similar molecular architecture. Also in this family both transport functions were proposed to localize in the same area. In flippases polar headgroups are thought to interact with a hydrophilic groove during bilayer passage[38], thereby facing a similar environment to that found in the subunit cavity of nhTMEM16.

Despite the breadth of functional behaviours, both branches of the TMEM16 family share the mechanism by which their activity is regulated by Ca^{2+}. The nhTMEM16 structure reveals a conserved Ca^{2+}-binding site contained within each subunit that is positioned within the hydrophobic core of the bilayer in proximity to the subunit cavity. Although this site potentially harbours two Ca^{2+} ions, it is currently not known whether binding of one or two ions is required to activate the protein. The location of this region within the membrane provides an explanation for the voltage-dependence of Ca^{2+} activation observed in TMEM16A[3,5], B[39] and TMEM16F[10]. This effect probably originates from the fact that the ion has to cross a fraction of the transmembrane electric field to reach the binding site[40], a model that was already proposed in an early study on CaCC activation[41]. While in our structure Ca^{2+} ions are buried within the protein, their entry from the cytoplasm via the subunit cavity or another path that becomes accessible in the ligand-free protein appears plausible (Fig. 4a, Extended Data Fig. 8). Ca^{2+} binding may either induce a conformational change in the protein that underlies its activation or modify the electrostatics in the close-by subunit cavity and in that way regulate the conductive properties of this region. Although the mechanism described is probably common for this protein family, there may be additional modes of regulation in certain TMEM16 proteins[42–46]. Our study has shed light on the unique properties of the TMEM16 protein family that does not resemble known classes of membrane proteins with respect to structure nor function. While detailed mechanisms of action are still unknown, the structure of nhTMEM16 has provided a template that will guide the future investigation of structure–function relationships.

Online Content Methods, along with any additional Extended Data display items and Source Data, are available in the online version of the paper; references unique to these sections appear only in the online paper.

Received 3 June; accepted 20 October 2014.
Published online 12 November 2014.

1. Milenkovic, V. M., Brockmann, M., Stohr, H., Weber, B. H. & Strauss, O. Evolution and functional divergence of the anoctamin family of membrane proteins. *BMC Evol. Biol.* **10,** 319 (2010).
2. Pedemonte, N. & Galietta, L. J. Structure and function of TMEM16 proteins (anoctamins). *Physiol. Rev.* **94,** 419–459 (2014).
3. Yang, Y. D. *et al.* TMEM16A confers receptor-activated calcium-dependent chloride conductance. *Nature* **455,** 1210–1215 (2008).
4. Caputo, A. *et al.* TMEM16A, a membrane protein associated with calcium-dependent chloride channel activity. *Science* **322,** 590–594 (2008).
5. Schroeder, B. C., Cheng, T., Jan, Y. N. & Jan, L. Y. Expression cloning of TMEM16A as a calcium-activated chloride channel subunit. *Cell* **134,** 1019–1029 (2008).
6. Pifferi, S., Cenedese, V. & Menini, A. Anoctamin 2/TMEM16B: a calcium-activated chloride channel in olfactory transduction. *Exp. Physiol.* **97,** 193–199 (2012).
7. Ferrera, L., Zegarra-Moran, O. & Galietta, L. J. Ca^{2+}-activated Cl^- channels. *Compr. Physiol.* **1,** 2155–2174 (2011).
8. Huang, F., Wong, X. & Jan, L. Y. International Union of Basic and Clinical Pharmacology. LXXXV: calcium-activated chloride channels. *Pharmacol. Rev.* **64,** 1–15 (2012).
9. Billig, G. M., Pal, B., Fidzinski, P. & Jentsch, T. J. Ca^{2+}-activated Cl^- currents are dispensable for olfaction. *Nature Neurosci.* **14,** 763–769 (2011).
10. Yang, H. *et al.* TMEM16F forms a Ca^{2+}-activated cation channel required for lipid scrambling in platelets during blood coagulation. *Cell* **151,** 111–122 (2012).
11. Martins, J. R. *et al.* Anoctamin 6 is an essential component of the outwardly rectifying chloride channel. *Proc. Natl Acad. Sci. USA* **108,** 18168–18172 (2011).
12. Suzuki, J., Umeda, M., Sims, P. J. & Nagata, S. Calcium-dependent phospholipid scrambling by TMEM16F. *Nature* **468,** 834–838 (2010).
13. Suzuki, J. *et al.* Calcium-dependent phospholipid scramblase activity of TMEM16 protein family members. *J. Biol. Chem.* **288,** 13305–13316 (2013).
14. Malvezzi, M. *et al.* Ca^{2+}-dependent phospholipid scrambling by a reconstituted TMEM16 ion channel. *Nature Commun.* **4,** 2367 (2013).
15. Kunzelmann, K. *et al.* Molecular functions of anoctamin 6 (TMEM16F): a chloride channel, cation channel, or phospholipid scramblase? *Pflugers Arch.* **466,** 407–414 (2014).
16. Kuruma, A. & Hartzell, H. C. Bimodal control of a Ca^{2+}-activated Cl^- channel by different Ca^{2+} signals. *J. Gen. Physiol.* **115,** 59–80 (2000).
17. Ni, Y. L., Kuan, A. S. & Chen, T. Y. Activation and inhibition of TMEM16A calcium-activated chloride channels. *PLoS ONE* **9,** e86734 (2014).
18. Yu, K., Duran, C., Qu, Z., Cui, Y. Y. & Hartzell, H. C. Explaining calcium-dependent gating of anoctamin-1 chloride channels requires a revised topology. *Circ. Res.* **110,** 990–999 (2012).
19. Terashima, H., Picollo, A. & Accardi, A. Purified TMEM16A is sufficient to form Ca^{2+}-activated Cl^- channels. *Proc. Natl Acad. Sci. USA* **110,** 19354–19359 (2013).
20. Menon, I. *et al.* Opsin is a phospholipid flippase. *Curr. Biol.* **21,** 149–153 (2011).
21. Tien, J. *et al.* A comprehensive search for calcium binding sites critical for TMEM16A calcium-activated chloride channel activity. *eLife* **3,** e02772 (2014).
22. Fallah, G. *et al.* TMEM16A(a)/anoctamin-1 shares a homodimeric architecture with CLC chloride channels. *Mol. Cell. Proteomics* **10,** M110.004697 (2011).

©2014 Macmillan Publishers Limited. All rights reserved

23. Sheridan, J. T. *et al.* Characterization of the oligomeric structure of the Ca^{2+}-activated Cl^- channel Ano1/TMEM16A. *J. Biol. Chem.* **286,** 1381–1388 (2011).
24. Tien, J., Lee, H. Y., Minor, D. L. Jr, Jan, Y. N. & Jan, L. Y. Identification of a dimerization domain in the TMEM16A calcium-activated chloride channel (CaCC). *Proc. Natl Acad. Sci. USA* **110,** 6352–6357 (2013).
25. Hartzell, H. C., Yu, K., Xiao, Q., Chien, L. T. & Qu, Z. Anoctamin/TMEM16 family members are Ca^{2+}-activated Cl^- channels. *J. Physiol. (Lond.)* **587,** 2127–2139 (2009).
26. Sanyal, S. & Menon, A. K. Flipping lipids: why an' what's the reason for? *ACS Chem. Biol.* **4,** 895–909 (2009).
27. Suzuki, J., Denning, D. P., Imanishi, E., Horvitz, H. R. & Nagata, S. Xk-related protein 8 and CED-8 promote phosphatidylserine exposure in apoptotic cells. *Science* **341,** 403–406 (2013).
28. Sanyal, S. & Menon, A. K. Stereoselective transbilayer translocation of mannosyl phosphoryl dolichol by an endoplasmic reticulum flippase. *Proc. Natl Acad. Sci. USA* **107,** 11289–11294 (2010).
29. Mohammadi, T. *et al.* Identification of FtsW as a transporter of lipid-linked cell wall precursors across the membrane. *EMBO J.* **30,** 1425–1432 (2011).
30. Zwaal, R. F., Comfurius, P. & Bevers, E. M. Scott syndrome, a bleeding disorder caused by defective scrambling of membrane phospholipids. *Biochim. Biophys. Acta* **1636,** 119–128 (2004).
31. Dekkers, D. W., Comfurius, P., Bevers, E. M. & Zwaal, R. F. Comparison between Ca^{2+}-induced scrambling of various fluorescently labelled lipid analogues in red blood cells. *Biochem. J.* **362,** 741–747 (2002).
32. Sham, L. T. *et al.* Bacterial cell wall. MurJ is the flippase of lipid-linked precursors for peptidoglycan biogenesis. *Science* **345,** 220–222 (2014).
33. Suzuki, T., Suzuki, J. & Nagata, S. Functional swapping between transmembrane proteins TMEM16A and TMEM16F. *J. Biol. Chem.* **289,** 7438–7447 (2014).
34. Miller, C. Open-state substructure of single chloride channels from *Torpedo electroplax*. *Phil. Trans. R. Soc. Lond. B* **299,** 401–411 (1982).
35. Kmit, A. *et al.* Calcium-activated and apoptotic phospholipid scrambling induced by Ano6 can occur independently of Ano6 ion currents. *Cell Death Dis.* **4,** e611 (2013).
36. Tian, Y., Schreiber, R. & Kunzelmann, K. Anoctamins are a family of Ca^{2+}-activated Cl^- channels. *J. Cell Sci.* **125,** 4991–4998 (2012).
37. Baldridge, R. D. & Graham, T. R. Identification of residues defining phospholipid flippase substrate specificity of type IV P-type ATPases. *Proc. Natl Acad. Sci. USA* **109,** E290–E298 (2012).
38. Vestergaard, A. L. *et al.* Critical roles of isoleucine-364 and adjacent residues in a hydrophobic gate control of phospholipid transport by the mammalian P4-ATPase ATP8A2. *Proc. Natl Acad. Sci. USA* **111,** E1334–E1343 (2014).
39. Pifferi, S., Dibattista, M. & Menini, A. TMEM16B induces chloride currents activated by calcium in mammalian cells. *Pflugers Arch.* **458,** 1023–1038 (2009).
40. Woodhull, A. M. Ionic blockage of sodium channels in nerve. *J. Gen. Physiol.* **61,** 687–708 (1973).
41. Arreola, J., Melvin, J. E. & Begenisich, T. Activation of calcium-dependent chloride channels in rat parotid acinar cells. *J. Gen. Physiol.* **108,** 35–47 (1996).
42. Xiao, Q. *et al.* Voltage- and calcium-dependent gating of TMEM16A/Ano1 chloride channels are physically coupled by the first intracellular loop. *Proc. Natl Acad. Sci. USA* **108,** 8891–8896 (2011).
43. Vocke, K. *et al.* Calmodulin-dependent activation and inactivation of anoctamin calcium-gated chloride channels. *J. Gen. Physiol.* **142,** 381–404 (2013).
44. Yu, K., Zhu, J., Qu, Z., Cui, Y. Y. & Hartzell, H. C. Activation of the Ano1 (TMEM16A) chloride channel by calcium is not mediated by calmodulin. *J. Gen. Physiol.* **143,** 253–267 (2014).
45. Tian, Y. *et al.* Calmodulin-dependent activation of the epithelial calcium-dependent chloride channel TMEM16A. *FASEB J.* **25,** 3 1058–1068 (2011).
46. Jung, J. *et al.* Dynamic modulation of ANO1/TMEM16A HCO_3^- permeability by Ca^{2+}/calmodulin. *Proc. Natl Acad. Sci. USA* **110,** 360–365 (2013).

Supplementary Information is available in the online version of the paper.

Acknowledgements This research was supported by a grant from the European Research Council (no. 339116, AnoBest) and by the Swiss National Science Foundation through the National Centre of Competence in Research TransCure. We thank the staff of the X06SA beamline for support during data collection, B. Blattman and C. Stutz-Ducommun of the Protein Crystallization Center at UZH, for their support with crystallization, B. Dreier for help with MALS experiments, A. Szydelko for providing ecClC as negative control in the scramblase assay and D. Drew for the FGY217 yeast strain. All members of the Dutzler laboratory are acknowledged for help in all stages of the project.

Author Contributions J.D.B. screened homologues, purified and crystallized nhTMEM16 and performed scrambling experiments. N.K.L. screened and crystallized homologues, performed electrophysiological recordings and did the MALS measurement. S.S. started the project, made expression vectors and aided in cell culture. A.D. screened homologues. R.D. assisted J.D.B. and N.K.L. during structure determination. J.D.B., N.K.L., S.S. and R.D. jointly planned experiments, analysed data and wrote the manuscript.

Author Information Coordinates and structure factors have been deposited in the Protein Data Bank under accession codes 4WIS (nhTMEM16 CF1) and 4WIT (nhTMEM16 CF2). Reprints and permissions information is available at www.nature.com/reprints. The authors declare no competing financial interests. Readers are welcome to comment on the online version of the paper. Correspondence and requests for materials should be addressed to R.D. (dutzler@bioc.uzh.ch).

©2014 Macmillan Publishers Limited. All rights reserved

METHODS

Cloning. The gene encoding nhTMEM16 from *Nectria haematococca* (PubMed accession number XM_003045982) was synthesized by GenScript and the gene encoding murine TMEM16A (mTMEM16A, isoform a) was obtained from ImaGenes (Clone IRAVp968B10135D). Expression vectors were modified to be compatible with FX-cloning[47]. For expression in *S. cerevisiae* nhTMEM16 was cloned into a modified pYES2/CT plasmid (Life Technologies) as C-terminal fusion to a cassette encoding EGFP, preceded by a His_{10}-tag and followed by a HRV 3C cleavage site (crystallization construct) or as N-terminal fusion to a cassette containing a streptavidin-binding peptide (SBP) tag[48] preceded by a Myc tag and a HRV 3C cleavage site (scramblase assay construct). For expression in tsA201 cells, nhTMEM16 and mTMEM16A were cloned into a modified pcDNA3.1 vector (Invitrogen), bearing a 5′ UTR (untranslated region) of hVEGF (from pcDNA4/HisMax, Invitrogen) upstream of the start codon. nhTMEM16 as well as mTMEM16A (isoform a) contained a C-terminal HRV 3C cleavage site, a Myc- and an SBP tag (scramblase assay constructs). For expression in HEK293T cells mTMEM16A (isoform ac) as well as nhTMEM16 were expressed with a C-terminal fusion encoding a Venus-yellow fluorescent protein (YFP)[49], a Myc- and an SBP tag[50] (defined as mTMEM16A–YFP, nhTMEM16–YFP; used in electrophysiological recordings). The mTMEM16Aac isoform used in patch-clamp experiments was generated by PCR. All point mutations were introduced by site-directed mutagenesis.

Protein expression. For expression of nhTMEM16 and its mutants, the pYES2/CT vectors carrying the respective genes were transformed into *S. cerevisiae* FGY217 cells carrying an *URA* deletion for positive selection as described[51]. Cells were grown at 30 °C in fermentation culture in yeast nitrogen base (without amino acids, Sigma) supplemented with Synthetic Complete drop-out medium without uracil (Formedium) and 0.1% glucose. Protein expression was induced with 2% galactose for 40 h at 25 °C at an OD_{600} of 0.8. For generation of selenomethionine labelled protein, BY4741 cells (*MAT**a** his3Δ1 leu2Δ0 met15Δ0 ura3Δ0*) were grown at 30 °C to an OD_{600} of 2–3, centrifuged and washed to remove residual methionine before induction. The cells were subsequently suspended in yeast nitrogen base without amino acids (Sigma), supplemented with Synthetic Complete drop-out medium without Met/uracil (Formedium), 0.01% raffinose and 100 mg l^{-1} Selenomethionine (Acros Organics), grown for 1 h, induced and expressed as described for wild type (WT). For expression in mammalian cells, tsA201 cells (catalogue no. 96121229, Sigma-Aldrich) with a confluency of 40–60% were transfected with plasmid DNA containing nhTMEM16 or mTMEM16A as described[50], except that the transfection buffer was prepared with 2.8 mM Na_2HPO_4. Expression was carried out in 10-cm dishes (Corning) at 37 °C and 2.2% CO_2 for 1–2 days. For electrophysiology HEK293T cells were transfected with the respective plasmids containing WT or mutant mTMEM16A (isoform ac, 5 μg of DNA per 3.5-cm dish) by similar protocols.

Protein purification. *S. cerevisiae* expressing WT nhTMEM16 was harvested by centrifugation and resuspended in buffer A (50 mM HEPES pH 7.6, 150 mM NaCl) containing 0.5 mM $CaCl_2$, protease inhibitors (Complete, Roche), DNase I, and 1 mM $MgCl_2$ and lysed in a custom-made pressure-based cell disruptor at 40,000 p.s.i. Cell debris was removed by low-spin centrifugation. Membranes were harvested by ultracentrifugation with a 45 TI rotor (Beckmann) at 40,000 r.p.m. for 1.5 h. All steps were carried out on ice or at 4 °C. Protein was extracted in buffer A containing 0.5 mM $CaCl_2$, 1% *n*-dodecyl-β-D-maltopyranoside (DDM, Anatrace) and protease inhibitors (Roche) for 1.5 h. Insoluble parts were removed by centrifugation for 30 min at 40,000 r.p.m. with a 45 TI rotor (Beckmann). After addition of 15 mM imidazole the protein was bound in batch to NiNTA for 1.5 h, washed with buffer B (10 mM HEPES pH 7.6, 150 mM NaCl, 5% glycerol, 0.025% DDM) containing 5 mM $CaCl_2$ and 50 mM imidazole and eluted in buffer B containing 5 mM $CaCl_2$ and 400 mM imidazole. The eluted fraction was cleaved with HRV 3C protease for 2 h and dialysed against buffer B containing 5 mM $CaCl_2$. The GFP–His_{10} fragment was removed by binding to NiNTA resin, the flow-through was concentrated (Amicon) and applied to a Superdex 200 column (GE healthcare) equilibrated in buffer C (5 mM HEPES pH 7.6, 150 mM NaCl, 0.025% DDM) containing 3 mM $CaCl_2$. The peak fraction was concentrated to 8–14 mg ml^{-1}. Prior to crystallization 0.2% *n*-undecyl-α-D-maltopyranoside (Anatrace), 50 μg ml^{-1} yeast polar lipid extract (solubilized in 1% DDM, Avanti Polar Lipids) and 2% 1,2,3-heptanetriol were added to the protein. The addition of additives was essential to remove the anisotropy of diffraction and improve the resolution from 6 to 3.3 Å. A 35 l fermentation culture harvested at an OD_{600} of 4.5 typically yielded about 5 mg of pure protein. Details concerning the purification and crystallization of nhTMEM16 in Ca^{2+}-free conditions are described in the Supplementary Discussion.

For reconstitution into liposomes WT nhTMEM16 and the triple mutant containing an SBP tag were either purified from *S. cerevisiae* or HEK tsA201 cells with similar results. mTMEM16A was expressed in HEK tsA201 cells by the same protocol. HEK tsA201 cells or membranes of *S. cerevisiae* expressing the respective protein were collected and treated with buffer A containing 5 mM EDTA, 5% glycerol, protease inhibitors and 2% DDM. Cell debris was removed by centrifugation. The supernatant was incubated with streptavidin resin (Pierce Streptavidin plus UltraLink) for 1.5 h and washed with buffer B. Protein was eluted with buffer B containing 2 mM biotin. The purity of the protein was confirmed by SDS–PAGE (Extended Data Fig. 2c). Initially, the protein was cleaved to remove the purification tag and subjected to size-exclusion chromatography on a Superdex 200 column before reconstitution. In later stages, the protein was reconstituted after affinity purification at 1 mg ml^{-1} with very similar results. For reconstitution, an 18 l fermentation culture of *S. cerevisiae* typically yielded 400 μg of pure protein. All buffers used during reconstitution were made with Ca^{2+}-free water (Merck Milipore) and chemicals extra low in Ca^{2+}. Multi-angle light scattering (MALS) experiments were carried out at 20 °C on a HPLC (Agilent 1100) connected to an Eclipse 3 system equipped with a miniDAWN TREOS MALS detector and an Optilab T-rEX refractometer (Wyatt Technology). 50 μg of purified nhTMEM16 (1 mg ml^{-1}) were injected onto a Superdex S200 column equilibrated in buffer B and eluted protein was detected online. The molecular weight was calculated at each time point during elution using a combination of ultraviolet absorbance, light scattering and differential refractive index measurements with the Astra software package (Astra 6.0, Wyatt Technology). The determined molecular weight of the protein of about 145 kDa compares well with the predicted 166 kDa of the dimer.

Crystallization and structure determination. WT nhTMEM16 (containing two additional residues on the N terminus remaining from the protease cleavage site) was crystallized in sitting drops at 4 °C. Crystals were prepared by mixing protein at a concentration of 8–14 mg ml^{-1} in a 1:1 ratio with reservoir containing either 100 mM Capso pH 9.4, 100 mM $MgCl_2$, 100 mM NaCl and 21–23% PEG400 (CF1) or 50 mM HEPES pH 7.4, 100 mM ammonium sulphate, 21–23% PEG400 (CF2). Crystals were harvested after 2–3 weeks (CF1) or 1 week (CF2), cryoprotected by increasing the PEG400 concentration to 36% and flash-frozen in liquid propane.

All data sets were collected on frozen crystals on the X06SA beamline at the Swiss Light Source (SLS) of the Paul Scherrer Institut (PSI) on a PILATUS 6M detector (Dectris, Extended Data Fig. 4a). The data were indexed, integrated and scaled with XDS[52] and further processed with CCP4 programs[53]. Both crystal forms are of space group $P2_12_12_1$ and each contains a dimer of the protein in its respective asymmetric unit (Extended Data Fig. 4a). The structure of the nhTMEM16 (CF2) was determined by the single-wavelength anomalous dispersion (SAD) method with data collected from crystals containing selenomethionine-derivatized protein. The Se-sites were identified with SHELX C and D[54,55] and refined in SHARP[56]. Initial phases at low resolution were improved by solvent flattening and twofold NCS averaging in DM[57]. A coarse model was built in O[58] and used as search model for molecular replacement in CF1 with PHASER[59]. Phases were subsequently extended to 3.3 Å by NCS and cross-crystal averaging with DM. Models were built with O and COOT[60]. The correct register of the protein was confirmed with the help of 13 methionine positions defined in the SeMet data set and from sulphur anomalous data collected for mutants F612M and L624M where methionine residues were inserted in regions of the protein that lack this amino acid. The structure was initially refined maintaining strict twofold NCS constraints in CNS[61]. In later stages, the strict constraints were loosened and restraint individual B-factors and TLS parameters were refined in PHENIX[62]. R and R_{free} were monitored throughout. R_{free} was calculated by selecting 5% of the reflection data that were omitted in refinement. The final model (CF1) contains 654 out of 735 residues per subunit, has R/R_{free} values of 23.8% and 28.5%, good geometry and no outliers in the Ramachandran plot (Extended Data Fig. 4a). Regions not defined in the electron density include residues 1–18, 130–140, 465–482, 586–593, 657–659, 685–691 and 720–735. The structure of nhTMEM16 in CF2 was refined in PHENIX as described for CF1. Both structures show very similar conformations. Ca^{2+} positions were identified from data collected at 1.95 Å to improve the anomalous scattering of the bound ions and included in the refinement (Extended Data Fig. 4a).

Liposome preparation and scrambling assay. Liposomes were prepared as 3:1 mixture of *Escherichia coli* polar lipids/egg PC (Avanti Polar Lipids). For scramblase assays lipids were supplemented with either 0.5% 1,2-dimyristoyl-*sn*-glycero-3-phosphoethanolamine-*N*-(NBD) or 1,2-dioleoyl-*sn*-glycero-3-phospho-L-serine-*N*-(NBD) (Avanti Polar Lipids). For control experiments approximately 20 μM NBD-dextran (prepared following manufacturers instruction, Life technologies) was added during liposome preparation instead of NBD-labelled lipids. Liposomes were suspended in buffer D (20 mM HEPES pH 7.4, 300 mM KCl) containing either 2 mM EGTA (for Ca^{2+}-free conditions), or 2 mM EGTA and the concentration of Ca^{2+} or other divalent cations (made from the respective nitrate salts) as calculated by MAXCHELATOR (http://maxchelator.stanford.edu/CaMgATPEGTA-TS.htm) to reach the indicated free divalent ion concentration. Liposomes were prepared as described[63]. Briefly, liposomes were subjected to three freeze-thaw cycles, subsequently extruded through a 400-nm polycarbonate filter (Avestin) and destabilized with Triton-X-100. Purified protein (5 μg per mg lipid) was added and detergent was removed by stepwise addition of SM-2 adsorbent biobeads (Bio-Rad). Proteoliposomes were formed at 4 °C under gentle agitation, incubated for 40 h, collected

©2014 Macmillan Publishers Limited. All rights reserved

by ultracentrifugation, resuspended in buffer D containing the above-mentioned concentrations of EGTA and divalent ions at a lipid concentration of 20 mg ml^{-1}, flash-frozen in liquid N_2 and stored at –80 °C. All buffers were prepared with Ca^{2+}-free water (Merck Millipore) using highly pure chemicals low in Ca^{2+}. The scramblase assay was performed similarly as previously described[14]. After three freeze-thaw cycles and extrusion (400-nm filter), 20 µl of proteoliposome suspension was diluted in 2 ml buffer D (with HEPES pH 7.4 concentration increased to 60 mM) containing either 2 mM EGTA, or 2 mM EGTA and the calculated concentrations of divalent ions, in a stirred cuvette at 23 °C. Sodium dithionite (Sigma) was added after 1 min to a final concentration of 30 mM unless stated otherwise and fluorescence decay was recorded on a Fluoromax-4 spectrofluorometer (Horiba, excitation 470 nm, emission 530 nm). For analysis the fluorescence intensity was normalized to F/F_{max}.

Patch-clamp electrophysiology. For electrophysiology mTMEM16A–YFP and nhTMEM16–YFP were expressed in HEK293T cells. Cells expressing either protein were identified by the fluorescence of the C-terminal Venus–YFP tag and used for patch-clamp experiments within 36 h after transfection. Experiments were conducted at room temperature (20–22 °C) with fire-polished borosilicate glass patch pipettes (4–8 MΩ). Currents were recorded in either whole-cell configuration or from excised patches in the inside-out configuration with an Axopatch 200B amplifier, digitized at 10 kHz, filtered at 1 kHz and analysed using Clampfit (MDS Analytical Technologies). Solutions were prepared as described[16]. Standard external solution contained: 140 mM NaCl, 4 mM KCl, 2 mM $CaCl_2$, 1 mM $MgCl_2$, 10 mM glucose, and 10 mM HEPES (pH 7.4). Ca^{2+}-free intracellular slution contained 146 mM $CsCl_2$, 2 mM $MgCl_2$, 5 mM EGTA, 10 mM sucrose, and 8 mM HEPES (pH 7.4), adjusted with *N*-methyl-D-glucamine. High Ca^{2+} solution contained 5 mM Ca^{2+}-EGTA (resulting in a free Ca^{2+} concentration of 20 µM). Intermediate Ca^{2+} solutions were prepared by mixing Ca^{2+}-free and high-Ca^{2+} solutions in corresponding ratios. Solution containing free Ca^{2+} concentrations higher than 20 µM were prepared by addition of the corresponding amounts of $CaCl_2$. In these cases EGTA was replaced by Br_2-BAPTA (5,5′-dibromo-1,2-bis(2-aminophenoxy)ethane-N,N,N′,N′-tetraacetic acid, 3.5 mM; Invitrogen). Solutions were applied with a double-barrelled theta tubing with a tip diameter of 400 µm attached to a piezo-bimorph (Siskiyou). The Ca^{2+} dependence of mTMEM16A and its mutants was measured in excised inside-out patches. Whereas the observed maximum current was similar to WT in mutants N650A, E702Q and E705Q, it was generally smaller in mutants E734Q, D738N and E654A. Currents generally saturated at high Ca^{2+} concentration except for E654A and D738N, where they continue to increase even at concentrations up to 10 mM Ca^{2+}. Activation in D738N shows a biphasic behaviour with an apparent saturation of currents around 100 µM and a subsequent increase above 500 µM Ca^{2+}. (Extended Data Fig. 9 and 10). A decrease of the response at increasing Ca^{2+} concentrations indicates rundown. For analysis of dose–response relationships, the current-response at different Ca^{2+} concentration recorded at a holding potential of 80 mV, was fitted to a Hill equation. Responses in D738N were only considered up to a Ca^{2+} concentration of 500 µM. The averages in the EC_{50} from 3–4 independent recordings (Extended Data Fig. 9 and 10) show shifts in the EC_{50} towards higher Ca^{2+} concentrations for all investigated mutants (WT, EC_{50} 0.36 µM, n 2.5; N650A, EC_{50} 1.8 µM, n 2.6; E702Q, EC_{50} 9.5 µM, n 2.1; E705Q, EC_{50} 231 µM, n 1.0; E734Q, EC_{50} 4.0 µM, n 1.6; D738N, EC_{50} 20.0 µM, n 0.84, where *n* is the Hill coefficient). To demonstrate the statistical significance of this increase, EC_{50} values were log-transformed for one-way ANOVA and subsequently compared to WT values using Tukey's post-hoc test for significance. Values were considered significantly different if $P < 0.05$. The analysis revealed that all shifts in the EC_{50} of Ca^{2+}-binding site mutants are statistically significant. The voltage dependence of WT suggests that Ca^{2+} crosses about 18% of the transmembrane electric field to reach its binding site (Fig. 5b).

Planar lipid bilayer experiments. For recording in planar lipid bilayers, nhTMEM16 was purified and reconstituted similarly as for the scramblase assay at lipid to protein ratios of 100:1 or 200:1, except that no NBD lipids were added. The incorporation of the protein into liposome was confirmed by freeze-fracture electron microscopy as described[64]. Proteoliposomes containing nhTMEM16 were fused to bilayers formed from 1-palmitoyl-2-oleoyl-*sn*-glycero-3-phosphoethanolamine and 1-palmitoyl-2-oleoyl-*sn*-glycero-3-phospho-(1'-*rac*-glycerol) (in ratio of 1:3 w/w, Avanti) and recorded with a horizontal planar lipid bilayer system as described[65,66]. In recordings under symmetric ion concentrations, both chambers contained 10 mM HEPES pH 7.4, 150 mM NaCl (buffer) and either no or 300 µM $CaCl_2$. In recordings under asymmetric conditions the NaCl concentration in one chamber was reduced to 15 mM. Electrodes were connected to the respective bath solutions via salt bridges. Currents were recorded with an Axopatch 200B amplifier, digitized at 10 kHz, filtered at 1 kHz and analysed using Clampfit.

47. Geertsma, E. R. & Dutzler, R. A versatile and efficient high-throughput cloning tool for structural biology. *Biochemistry* **50,** 3272–3278 (2011).
48. Keefe, A. D., Wilson, D. S., Seelig, B. & Szostak, J. W. One-step purification of recombinant proteins using a nanomolar-affinity streptavidin-binding peptide, the SBP-tag. *Protein Expr. Purif.* **23,** 440–446 (2001).
49. Nagai, T. *et al.* A variant of yellow fluorescent protein with fast and efficient maturation for cell-biological applications. *Nature Biotechnol.* **20,** 87–90 (2002).
50. Schenck, S., Wojcik, S. M., Brose, N. & Takamori, S. A chloride conductance in VGLUT1 underlies maximal glutamate loading into synaptic vesicles. *Nature Neurosci.* **12,** 156–162 (2009).
51. Drew, D. *et al.* GFP-based optimization scheme for the overexpression and purification of eukaryotic membrane proteins in *Saccharomyces cerevisiae*. *Nature Protocols* **3,** 784–798 (2008).
52. Kabsch, W. Automatic processing of rotation diffraction data from crystals of initially unknown symmetry and cell constants. *J. Appl. Crystallogr.* **26,** 795–800 (1993).
53. The Collaborative Computational Project, Number 4. The CCP4 suite: programs for X-ray crystallography. *Acta Crystallogr. D* **50,** 760–763 (1994).
54. Schneider, T. R. & Sheldrick, G. M. Substructure solution with SHELXD. *Acta Crystallogr. D* **58,** 1772–1779 (2002).
55. Pape, T. & Schneider, T. R. HKL2MAP: a graphical user interface for phasing with SHELX programs. *J. Appl. Crystallogr.* **37,** 843–844 (2004).
56. de La Fortelle, E. & Bricogne, G. in *Methods in Enzymology* Vol. 276 (eds Carter, C. W. & Sweet, R. M.) 492–494 (Academic, 1997).
57. Cowtan, K. 'dm': An automated procedure for phase improvement by density modification. *Joint CCP4 and ESF-EACBM Newsletter on Protein Crystallography* **31,** 34–38 (1994).
58. Jones, T. A., Zou, J. Y., Cowan, S. W. & Kjeldgaard, M. Improved methods for building protein models in electron density maps and the location of errors in these models. *Acta Crystallogr. A* **47,** 110–119 (1991).
59. McCoy, A. J. *et al.* Phaser crystallographic software. *J. Appl. Crystallogr.* **40,** 658–674 (2007).
60. Emsley, P. & Cowtan, K. Coot: model-building tools for molecular graphics. *Acta Crystallogr. D* **60,** 2126–2132 (2004).
61. Brünger, A. T. *et al.* Crystallography & NMR system: a new software suite for macromolecular structure determination. *Acta Crystallogr. D* **54,** 905–921 (1998).
62. Adams, P. D. *et al.* PHENIX: building new software for automated crystallographic structure determination. *Acta Crystallogr. D* **58,** 1948–1954 (2002).
63. Geertsma, E. R., Nik Mahmood, N. A., Schuurman-Wolters, G. K. & Poolman, B. Membrane reconstitution of ABC transporters and assays of translocator function. *Nature Protocols* **3,** 256–266 (2008).
64. Garcia-Celma, J., Szydelko, A. & Dutzler, R. Functional characterization of a ClC transporter by solid-supported membrane electrophysiology. *J. Gen. Physiol.* **141,** 479–491 (2013).
65. Accardi, A., Kolmakova-Partensky, L., Williams, C. & Miller, C. Ionic currents mediated by a prokaryotic homologue of CLC Cl^- channels. *J. Gen. Physiol.* **123,** 109–119 (2004).
66. Zimmermann, I. & Dutzler, R. Ligand activation of the prokaryotic pentameric ligand-gated ion channel ELIC. *PLoS Biol.* **9,** e1001101 (2011).
67. Sievers, F. *et al.* Fast, scalable generation of high-quality protein multiple sequence alignments using Clustal Omega. *Mol. Syst. Biol.* **7,** 539 (2011).

©2014 Macmillan Publishers Limited. All rights reserved

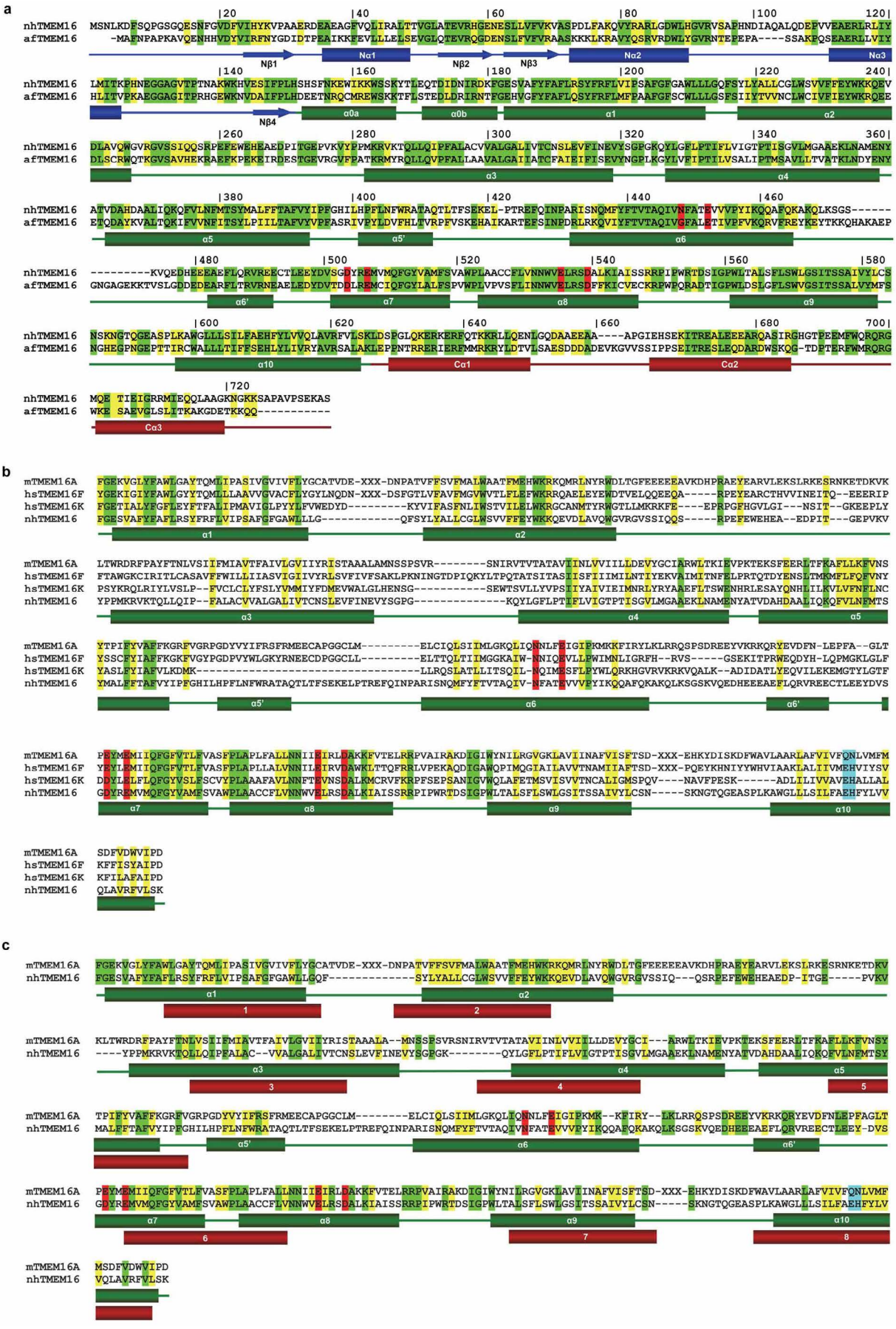

©2014 Macmillan Publishers Limited. All rights reserved

Extended Data Figure 1 | Structure-based sequence alignment. Sequences were aligned with Clustal Omega[67] and edited manually. Identical residues are highlighted in green, homologous residues in yellow and residues of the Ca^{2+}-binding site in red. Secondary structure elements are shown below. **a**, Comparison of nhTMEM16 and afTMEM16. The numbering corresponds to nhTMEM16. **b**, Comparison of the membrane domains of selected TMEM16 proteins, m refers to murine, hs to human proteins. Long insertions in loop regions of mammalian family members (indicated by -xxx-) are not shown in the alignment. The positions of residues in α-helix 10 involved in an inter-subunit salt bridge at the dimer interface are highlighted in cyan. **c**, Comparison of the observed and predicted topology of TMEM16 proteins. Sequence alignment of the membrane spanning regions of mTMEM16A and nhTMEM16 with the observed (green) and predicted topology[25] (red) indicated. Identical residues are highlighted in green, homologous residues in yellow, residues of the Ca^{2+}-binding site in red and the inter-subunit salt bridge at the dimer interface in cyan. The difference between the predicted and observed transmembrane segments is due to the failure of sequence-based approaches to identify the correct boundaries of several helices and to detect α-helix 6 at all and helices 7 and 8 as separate entities.

©2014 Macmillan Publishers Limited. All rights reserved

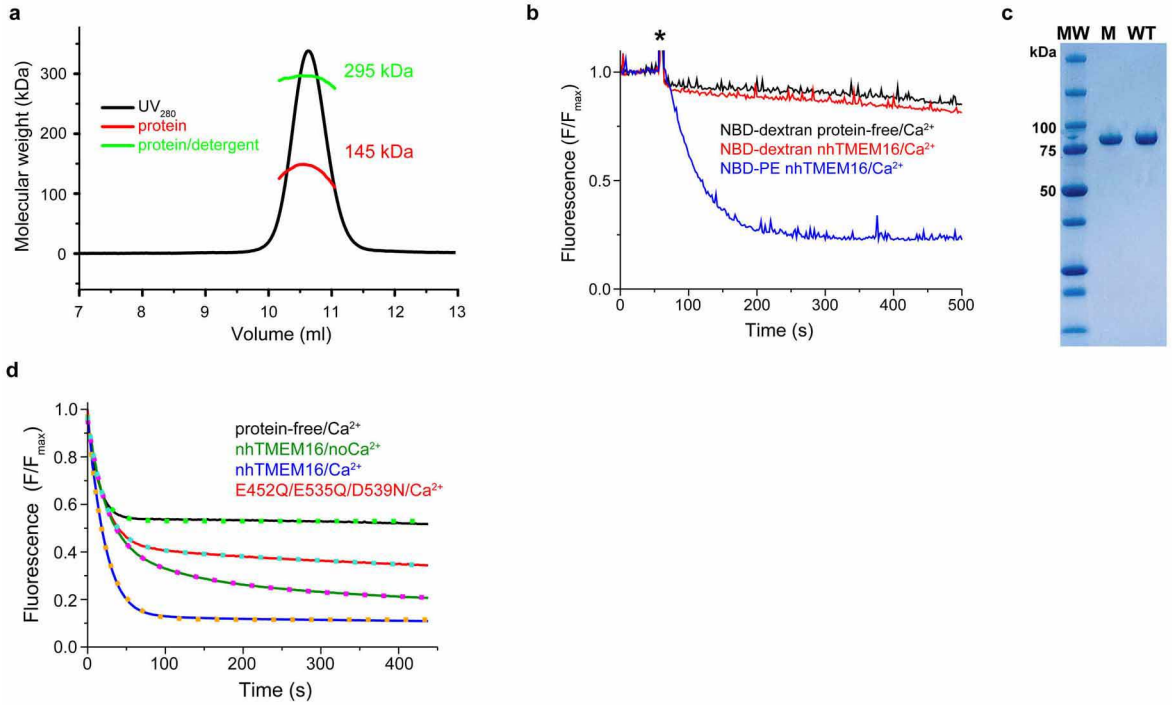

Extended Data Figure 2 | Multi-angle light scattering and lipid scrambling. **a**, Gel filtration and light scattering results for nhTMEM16 in the detergent DDM. The continuous black trace corresponds to the absorption at 280 nm. Molecular weights of the protein and the protein-detergent complex are shown in red and green, respectively. **b**, Inaccessibility of NBD groups trapped within liposomes. Dithionite is incapable of reducing the soluble NBD-dextran trapped in the interior of proteoliposomes containing nhTMEM16. Traces of proteoliposomes containing nhTMEM16 and empty liposomes are shown in red and black respectively. Traces from proteoliposomes of nhTMEM16 containing NBD-PE at equivalent dithionite levels are shown for comparison (blue). Asterisk marks addition of 2.5 mM dithionite. **c**, SDS–PAGE gel of the Ca^{2+}-binding site triple-mutant E452Q/E535Q/D539N (M) and nhTMEM16 (WT) used for reconstitution illustrating the purity of the sample. The molecular weight marker (MW) is shown on the left with selected bands labelled. **d**, Analysis of phospholipid scrambling. Time dependent fluorescence decrease of NBD-PE upon reduction by 30 mM dithionite ($t = 0$). The traces are as in Figs 1b–d and 5a. A fit to a single exponential decay is shown as dotted lines for protein-free/Ca^{2+} and nhTMEM16/Ca^{2+} with time constants of 15 s and 22 s, respectively. A fit to a sum of two exponential functions is shown for nhTMEM16/no Ca^{2+} and E452Q/E535Q/D539N/Ca^{2+} with time constants of 25 and 21 s for the fast component and 175 and 803 s for the slow component, respectively.

©2014 Macmillan Publishers Limited. All rights reserved

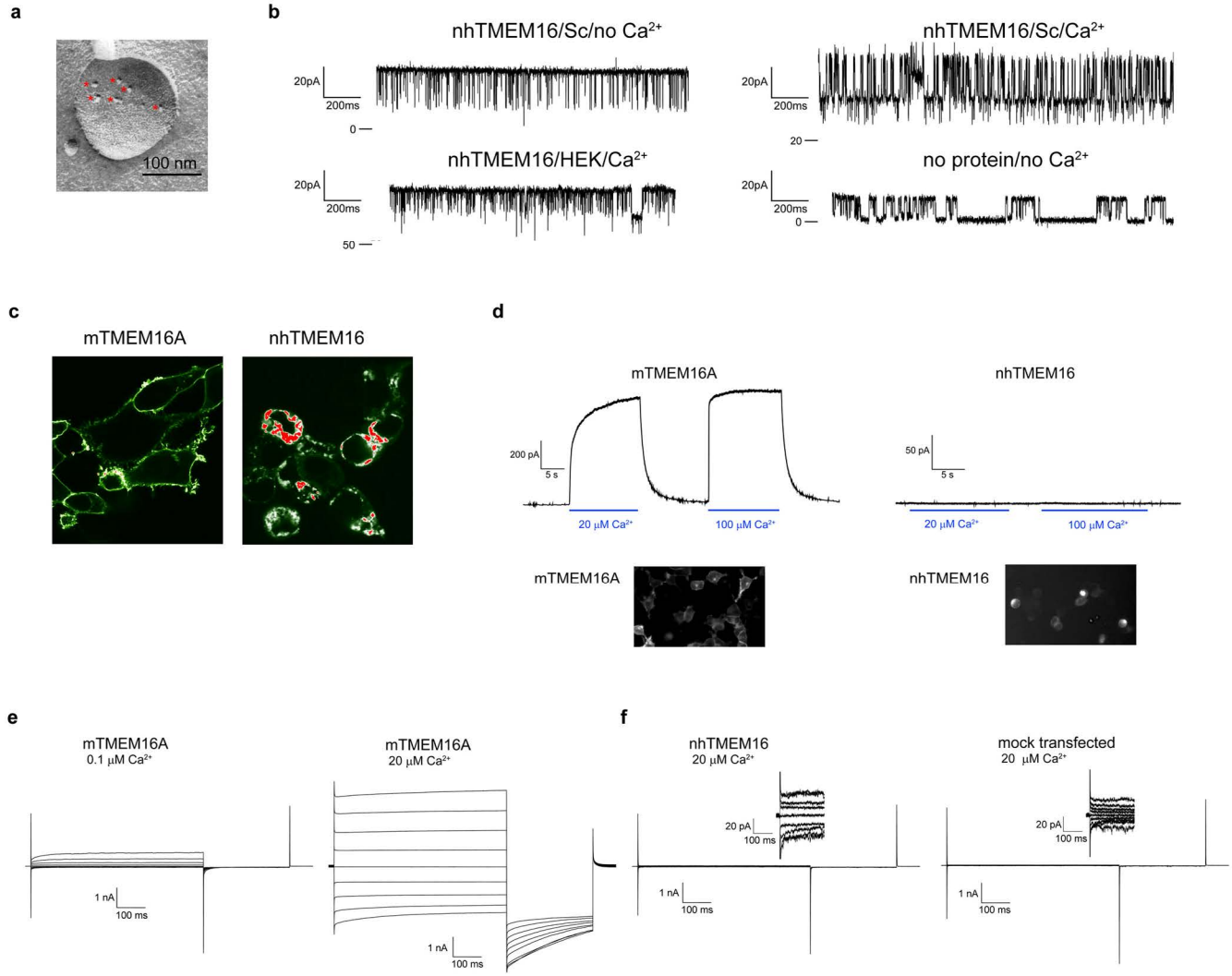

Extended Data Figure 3 | Search for ion channel activity in nhTMEM16. **a**, Freeze-fracture electron microscopy image of a proteoliposome containing nhTMEM16 formed from a 3:1 mixture of *E. coli* polar lipids/egg PC. Reconstituted proteins are labelled with red asterisks. **b**, Planar lipid bilayer experiments. Currents recorded after fusion of proteoliposomes containing nhTMEM16 expressed and purified from *S. cerevisiae* (Sc) in the absence of Ca^{2+} (top, left), with 300 μM Ca^{2+} added on both sides of the bilayer (top right) and of proteoliposomes containing nhTMEM16 expressed and purified from HEK tsA201 cells in the presence of 300 μM Ca^{2+} added on both sides of the bilayer (bottom left). Currents recorded after fusion of liposomes of the same lipid composition not containing any protein are shown for comparison (bottom right). Displayed traces were recorded at a holding potential of 100 mV in symmetric solutions containing 150 mM NaCl and 10 mM HEPES pH 7.4. Selected current levels (in pA) are indicated on the left. **c**, Fluorescence confocal microscopy images of HEK tsA201 cells expressing a mTMEM16A–YFP fusion construct (left) or a nhTMEM16–YFP fusion construct (right). **d**, Recordings from excised inside-out patches. Representative current response in a membrane patch excised from cells expressing a mTMEM16A–YFP fusion construct upon rapid exchange into solutions containing the indicated amount of Ca^{2+} (left) and equivalent recordings from patches that were excised from cells expressing a nhTMEM16–YFP fusion protein (right). The voltage was clamped at 80 mV. The fluorescence of transfected cells expressing mTMEM16A–YFP used for recording is shown below. No activity of nhTMEM16–YFP was observed in any of more than 30 patches. **e**, Patch-clamp recording in the whole-cell configuration. Representative currents from a HEK293T cell expressing a mTMEM16A–YFP construct recorded from a solution containing either 0.1 μM (left) or 20 μM (right) free Ca^{2+} in the patch pipette. **f**, Representative currents from a cell expressing a nhTMEM16–YFP fusion protein recorded from a solution containing 20 μM free Ca^{2+} in the patch pipette (left). Current response from mock-transfected cells recorded under the same conditions is shown for comparison (right). Insets show part of the traces with magnified current scale.

©2014 Macmillan Publishers Limited. All rights reserved

a

Table Data collection and refinement statistics

	nhTMEM16/CF1	nhTMEM16/CF2	nhTMEM16/SeMet	nhTMEM16/anom	nhTMEM16/no Ca^{2+}
Data collection					
Wavelength (Å)	0.9797	1.0	0.9797	1.95	1.95
Space group	$P2_12_12_1$	$P2_12_12_1$	$P2_12_12_1$	$P2_12_12_1$	$P2_12_12_1$
Cell dimensions					
a, *b*, *c* (Å)	96.5, 113.7, 235.7	115.9, 127.2, 180.1	113.7, 124.8, 177.4	115.2, 124.8, 177.4	115.2, 127.1, 179.7
(°)	90, 90, 90	90, 90, 90	90, 90, 90	90, 90, 90	90, 90, 90
Resolution (Å)	50-3.3 (3.4-3.3)*	50-3.4 (3.5-3.4)	50-4.0 (4.1-4.0)	50-3.5 (3.6-3.5)	50-4.2 (4.3-4.2)
R_{merge}	8.3 (123.5)	6.5 (149.3)	11.7 (137.9)	10.2 (116.5)	15.2 (233.7)
$I/\sigma I$	20.1 (2.6)	20.0 (1.7)	18.4 (2.3)	16.5 (1.8)	12.5 (2.0)
Completeness (%)	99.1 (98.8)	98.9 (87.9)	99.0 (100)	99.9 (100.0)	99.9 (100)
Redundancy	12.7 (12.7)	9.6 (8.6)	22.9 (15.9)	12.2 (7.0)	18.8 (17.8)
$CC_{1/2}$ (%)	99.9 (80.3)	99.9 (59.8)	100.0 (71.1)	99.8 (69.5)	99.8 (75.3)
Refinement					
Resolution (Å)	15-3.3	15-3.4		15-3.5	15-4.2
No. reflections	38985	36750		32709	19356
R_{work}/ R_{free}	23.8 (28.5)	24.8 (29.2)		23.7 (28.5)	23.0 (27.2)
No. atoms	10574	10574		10574	10570
Protein	10570	10570		10570	10570
Ligand/ion	4	4		4	0
B-factors					
Protein	137	159		147	199
Ligand/ion	104	146		123	-
R.m.s deviations					
Bond lengths (Å)	0.003	0.002		0.003	0.003
Bond angles (°)	0.74	0.70		0.90	0.78

*Highest resolution shell is shown in parenthesis.

b

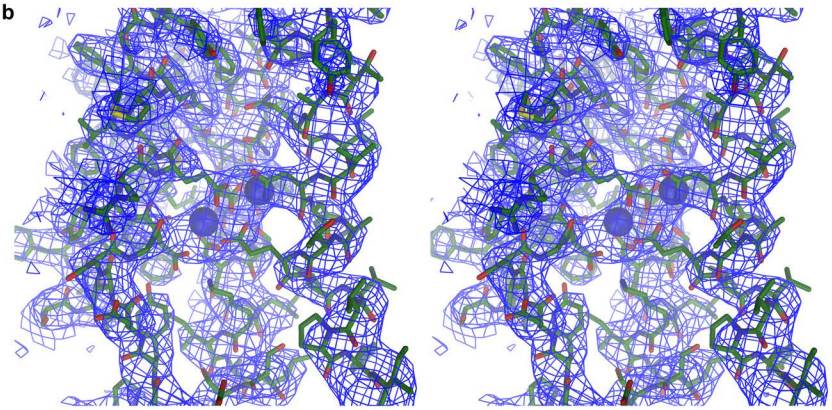

Extended Data Figure 4 | Crystallography. **a**, Table describing data collection and refinement statistics of five data sets presented in this study. nhTMEM16/CF1 and nhTMEM16/CF2 are data sets used for the building and refinement of the crystal structures of CF1 and CF2 respectively that have been deposited in the PDB. nhTMEM16/SeMet, a data set of a selenomethionine derivative collected at the Se anomalous absorption edge, was used for obtaining initial phases of CF2. nhTMEM16/anom is a data set used for the identification of the Ca^{2+}-binding site by anomalous scattering and nhTMEM16/no Ca^{2+} is from a protein purified in the presence of EDTA and crystallized without addition of Ca^{2+}. **b**, Stereo view of the Ca^{2+}-binding region in CF1. The model of the protein displayed as sticks is shown with experimental electron density superimposed. The map was calculated at 3.3 Å with Se-Met SAD phases that were improved by solvent flattening, cyclic twofold NCS and cross-crystal averaging (blue mesh, contoured at 1σ). Ca^{2+} ions are shown as blue spheres.

©2014 Macmillan Publishers Limited. All rights reserved

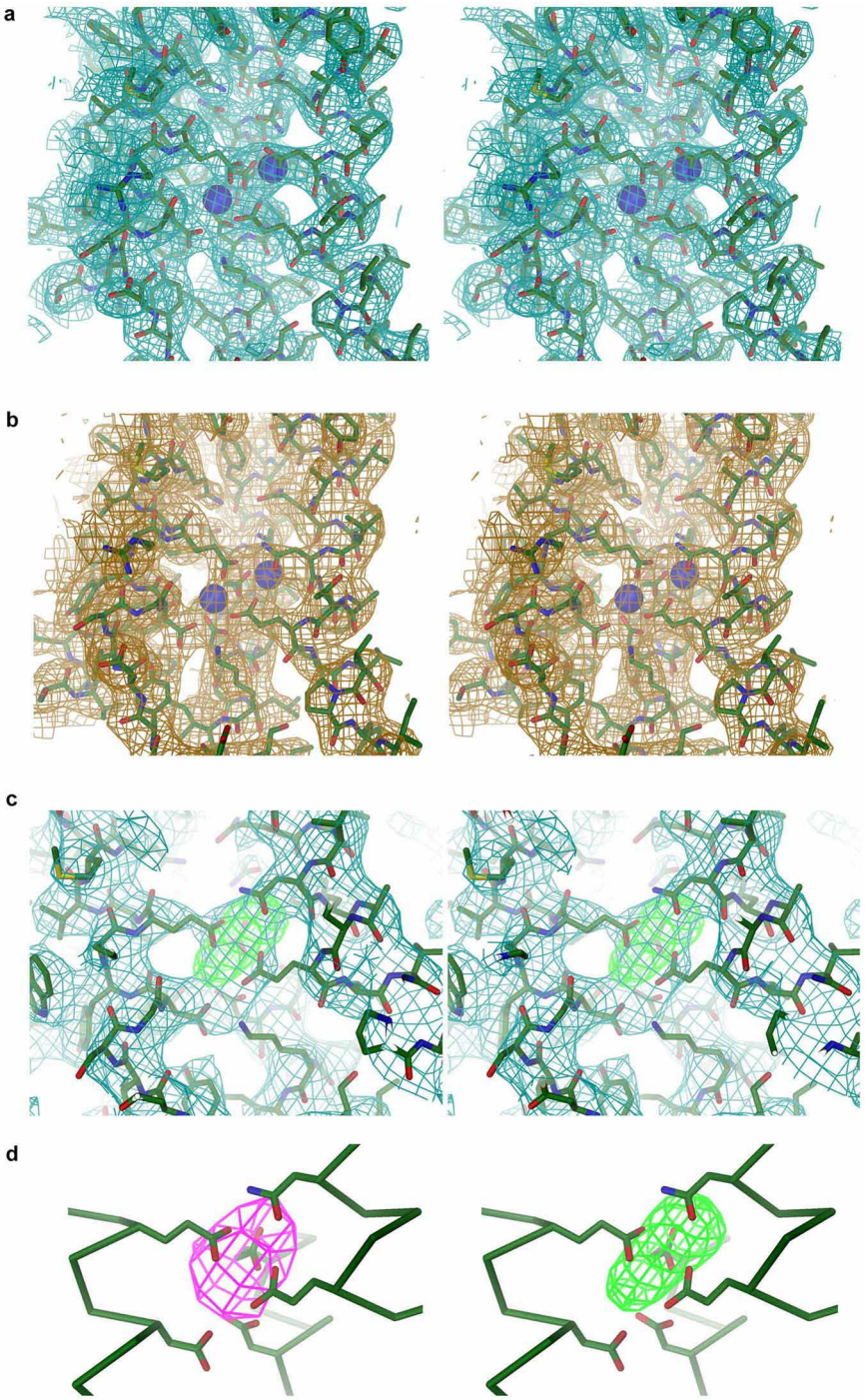

Extended Data Figure 5 | Electron density. **a**, Stereo view of the Ca^{2+}-binding region in CF1. The model of the protein displayed as sticks is shown with $2F_o - F_c$ electron density superimposed (cyan mesh, contoured at 1σ after sharpening with $b = 50$). The density at 3.3 Å was calculated with phases from the refined model. Ca^{2+} ions are shown as blue spheres. **b**, $2F_o - F_c$ electron density of the Ca^{2+}-binding region in CF2 (calculated at 3.4 Å and contoured at 1σ after sharpening with $b = 50$, orange) superimposed on the refined model. **c**, Stereo view of the Ca^{2+}-binding region of a structure obtained from protein purified in the presence of EDTA and crystallized in CF2 without addition of Ca^{2+}. $2F_o - F_c$ electron density (cyan mesh, calculated at 4.2 Å and contoured at 1σ after sharpening with a $b = 50$) and $F_o - F_c$ density (contoured at 3σ, green) is superimposed on the refined model. No ions were included in the refinement. **d**, Close-up of the Ca^{2+}-binding site. Anomalous difference density (left, calculated at 6 Å and contoured at 4σ, magenta) and $F_o - F_c$ density (right, contoured at 3σ, green) indicates the presence of bound Ca^{2+} ions.

©2014 Macmillan Publishers Limited. All rights reserved

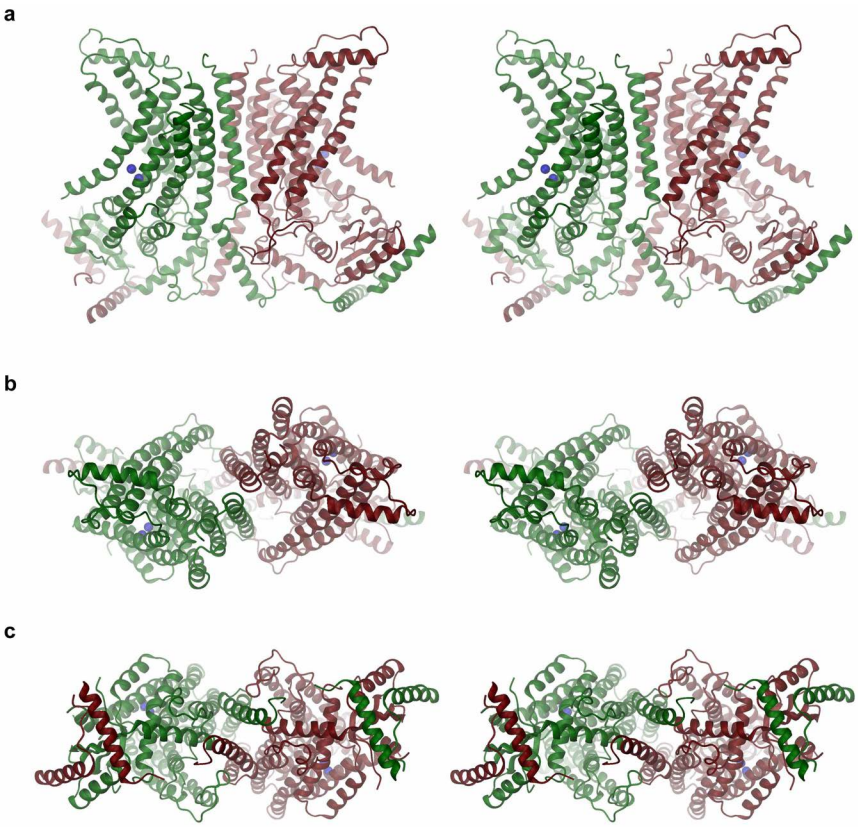

Extended Data Figure 6 | nhTMEM16 dimer. Stereo views of a ribbon representation of the dimeric protein. Bound Ca^{2+} ions are shown as blue spheres. **a**, View from within the membrane; **b**, view from the extracellular side; **c**, view from the cytoplasm.

©2014 Macmillan Publishers Limited. All rights reserved

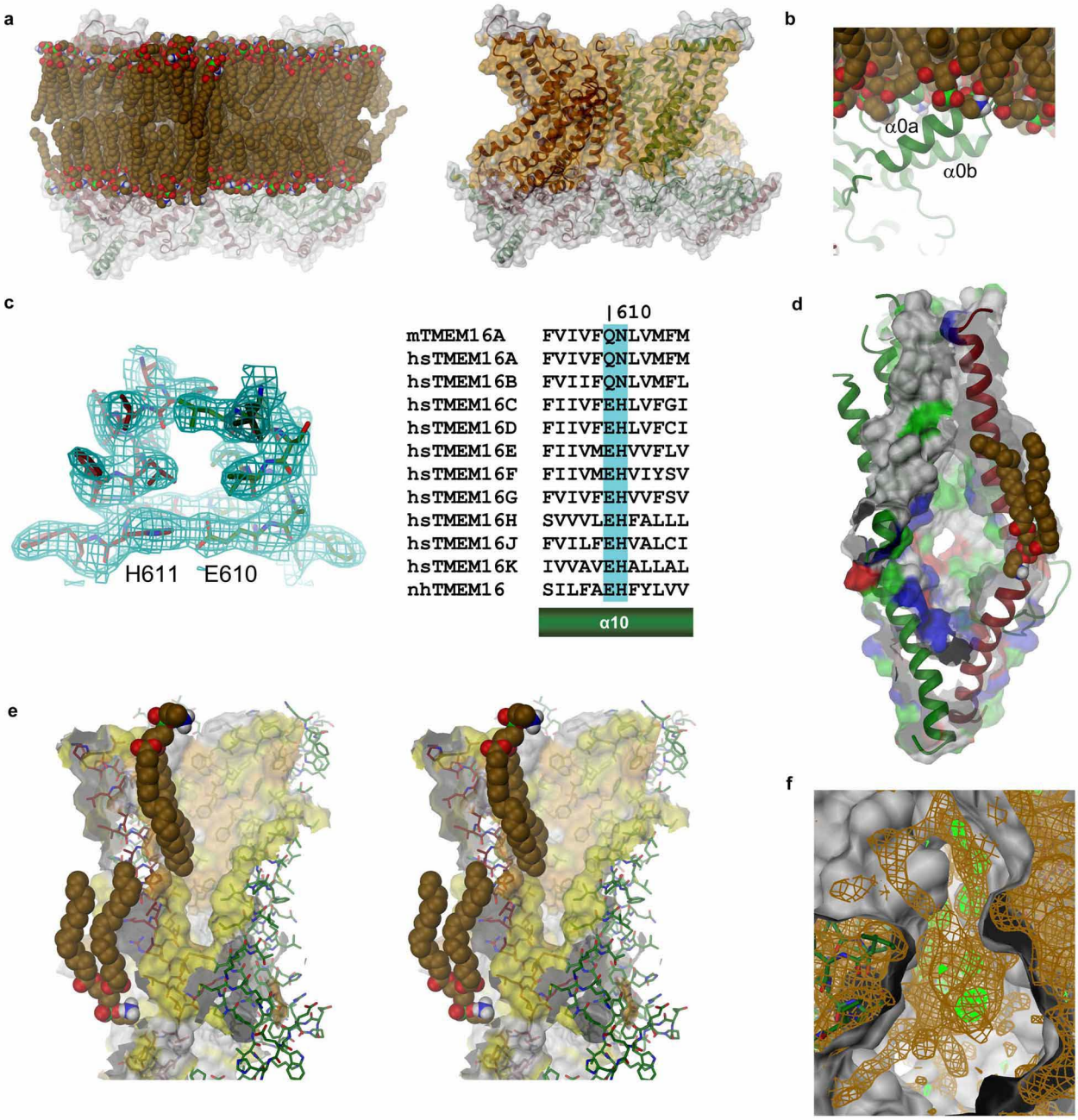

Extended Data Figure 7 | Model of lipid interactions and dimer cavity. **a**, Model of nhTMEM16 embedded in a lipid membrane (left). The protein was positioned within the model of a PC bilayer (obtained from http://www.lobos.nih.gov/mbs/coords.shtml). A ribbon representation of the protein and the molecular surface are shown. Lipids are displayed as CPK models. Same view of the protein with regions on the surface presumably in contact with the membrane coloured in orange (right). **b**, Putative location of α-helices 0a and 0b relative to the lipid bilayer. **c**, Inter-subunit interactions between residues of α-helix 10. The protein is shown as sticks with $2F_o - F_c$ density (CF1, calculated at 3.3 Å and contoured at 1σ after sharpening with $b = 50$, cyan mesh) superimposed (left). A sequence alignment of the corresponding region underlines the conservation of interacting residues. Amino acids of the salt bridge in nhTMEM16 are highlighted in cyan, the numbering corresponds to nhTMEM16. **d**, View on the dimer cavity from the dimer interface. The molecular surface is coloured according to the properties of contacting residues (red, acidic; blue, basic; green, polar). A modelled lipid indicates the boundary of the inner leaflet of the bilayer. **e**, Stereo view of the cleft between α-helices 3 and 10. The protein is shown as stick model. The molecular surface is coloured according to the properties of contacting residues (yellow, hydrophobic; orange, aromatic). Lipids indicate the membrane boundary. **f**, Residual density in the dimer cavity. The molecular surface is coloured in white. $2F_o - F_c$ density (CF2, contoured at 1σ after sharpening with $b = 50$, orange) and $F_o - F_c$ density (contoured at 3σ, green) are shown. The view is as in **d**.

©2014 Macmillan Publishers Limited. All rights reserved

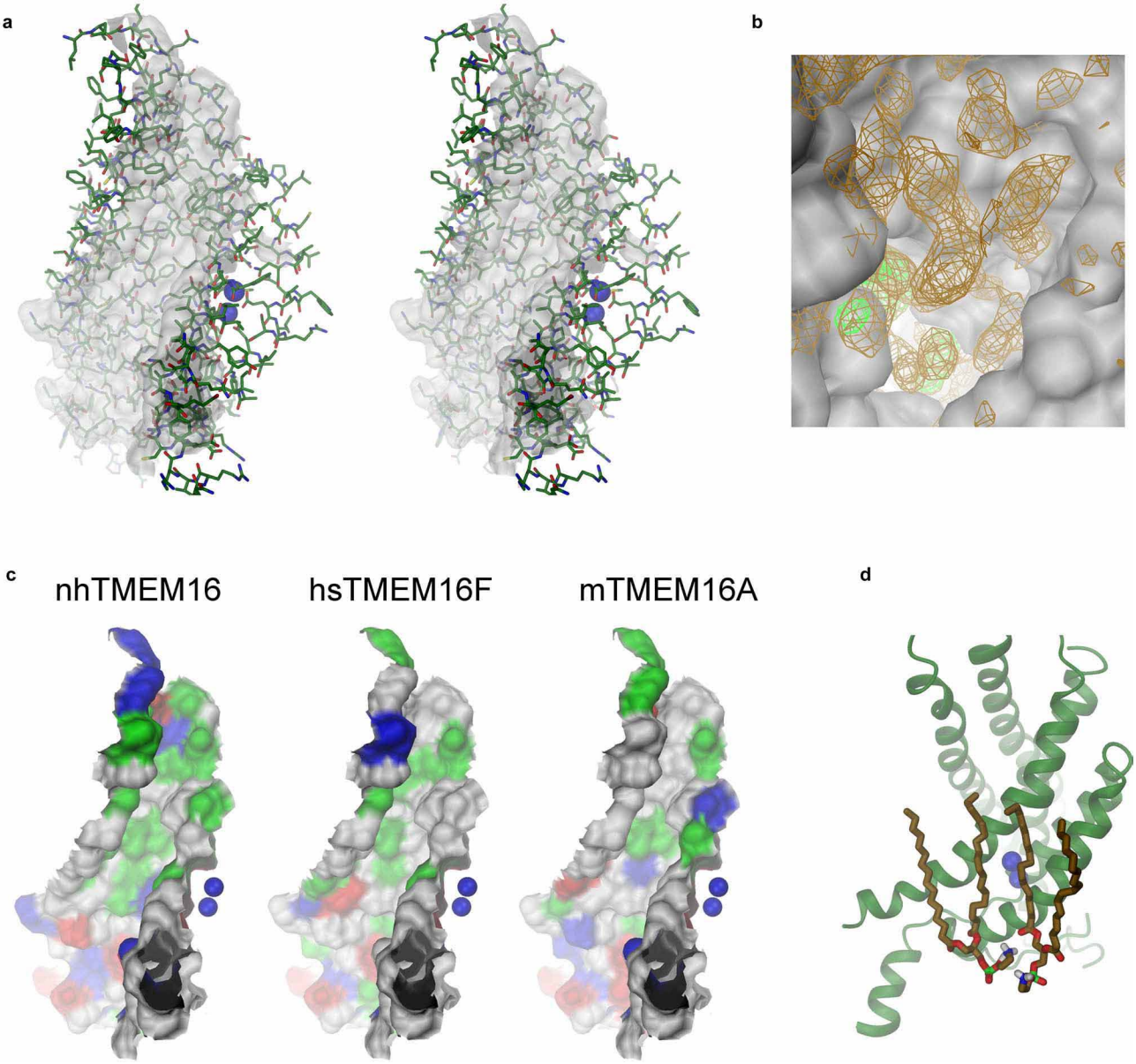

Extended Data Figure 8 | Subunit cavity and Ca^{2+}-binding site. **a**, Stereo view of the subunit cavity viewed from within the membrane. Protein residues and the molecular surface are shown. **b**, Residual density in the subunit cavity. The molecular surface of the protein is shown. $2F_o - F_c$ density (CF2, contoured at 1σ after sharpening with $b = 50$, orange) and $F_o - F_c$ density (contoured at 3σ, green) are displayed. **c**, Model of the subunit cavity in different TMEM16 proteins. The molecular surface is coloured according to the properties of contacting residues (red, acidic; blue, basic; green, polar). Putative surface-exposed residues were obtained from a sequence alignment with nhTMEM16. **d**, Location of the Ca^{2+}-binding site in relation to the lipid bilayer. Modelled lipids of the inner leaflet of the bilayer are shown as sticks.

©2014 Macmillan Publishers Limited. All rights reserved

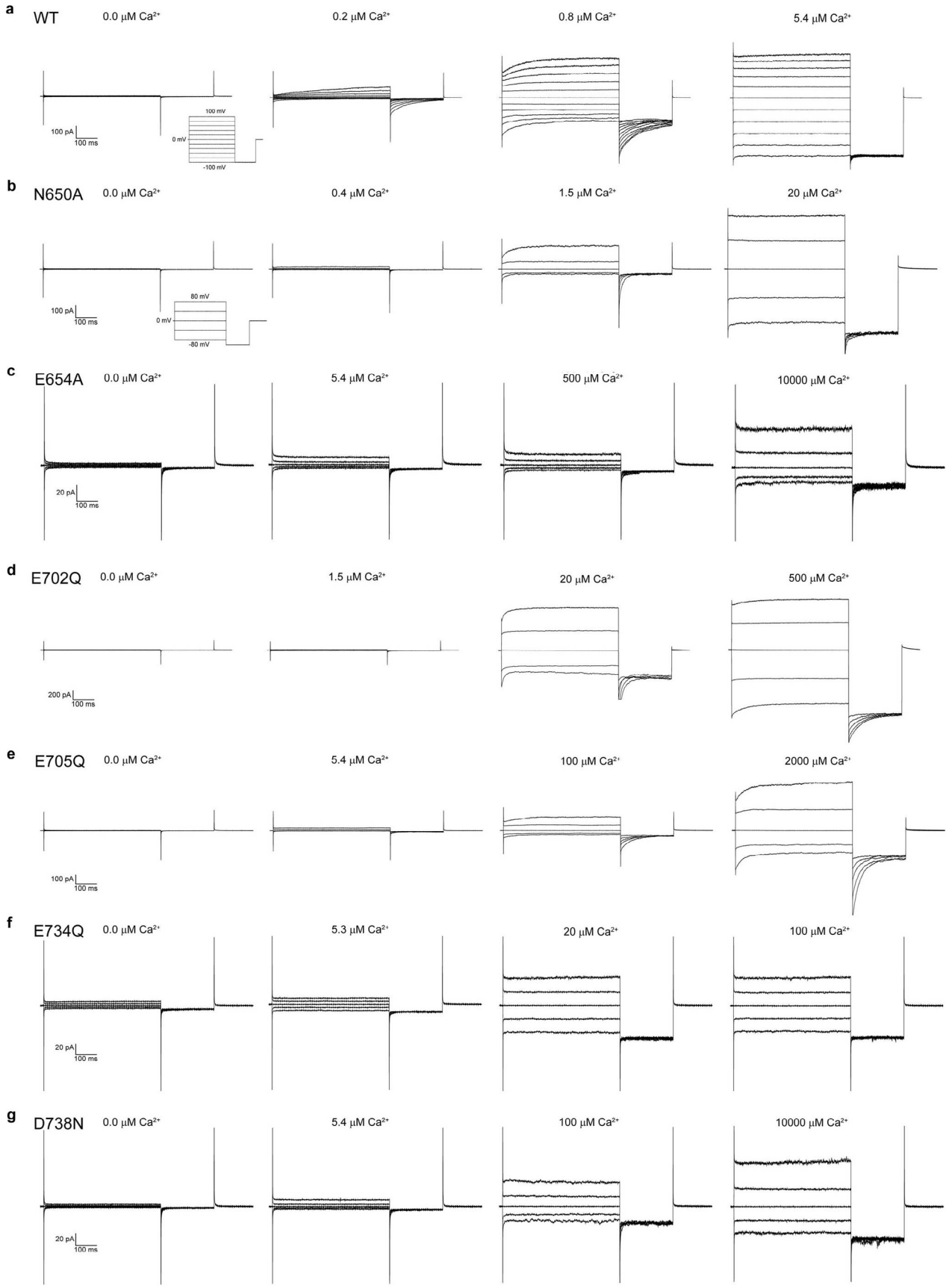

Extended Data Figure 9 | Electrophysiology. Current response in HEK293T cells overexpressing mTMEM16A–YFP and point mutants of the Ca^{2+}-binding site. All recordings were measured from single excised patches in the inside-out configuration after changing to intracellular solutions containing the indicated Ca^{2+} concentrations. **a**, WT, with voltage protocol shown as inset. **b**, Mutant N650A, with the voltage protocol shown as inset. **c**–**g**, Recordings of mutants E654A, **c**, E702Q, **d**, E705Q, **e**, E634Q, **f**, and mutant D738N, **g**.

©2014 Macmillan Publishers Limited. All rights reserved

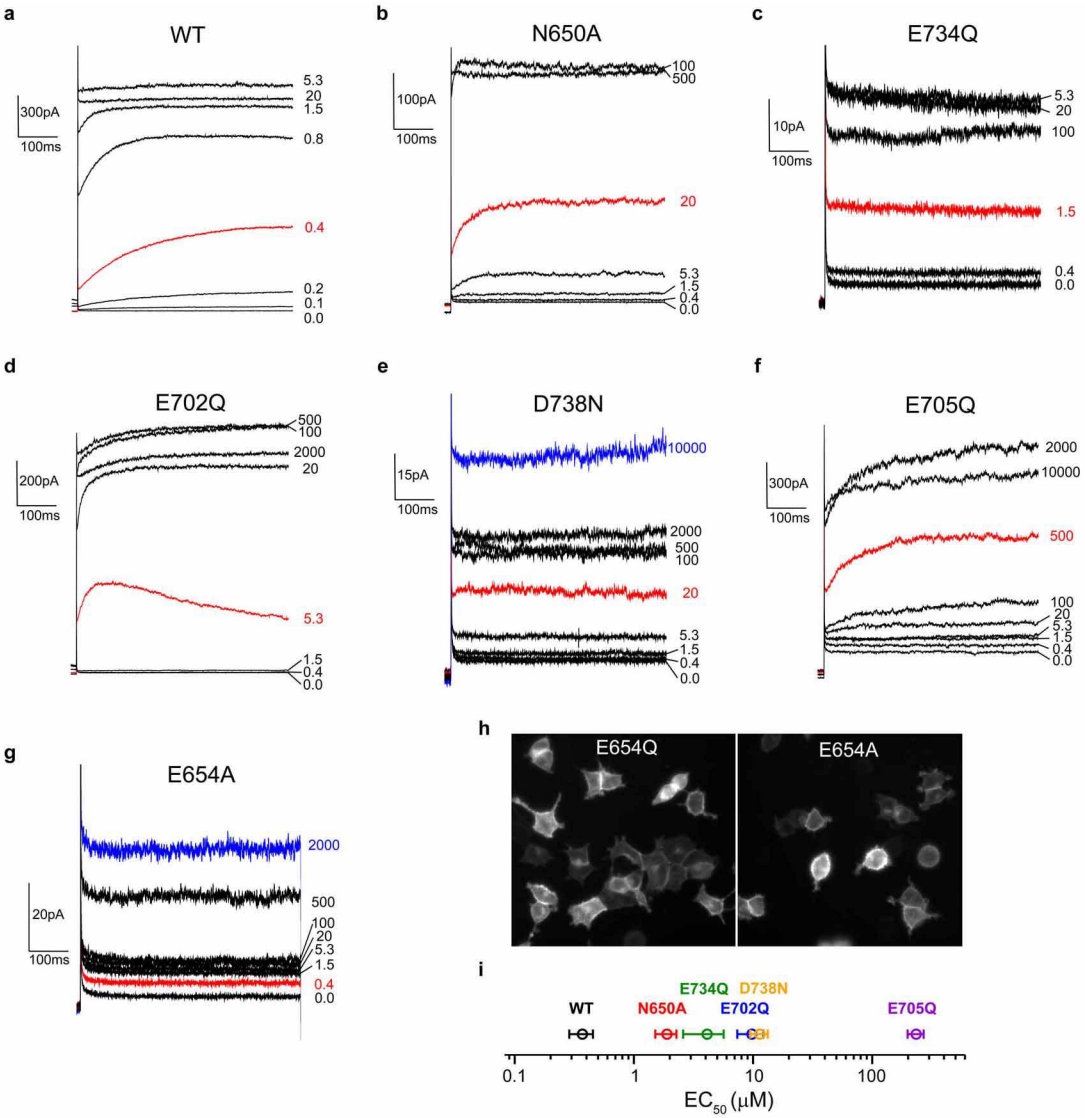

Extended Data Figure 10 | Ca^{2+} activation of mTMEM16A. Representative current traces of mTMEM16A and mutants of the Ca^{2+}-binding site. Currents were measured from excised inside-out patches of HEK293T cells expressing the respective protein at 80 mV. The Ca^{2+} concentration is indicated, selected traces are shown in colour. **a**, WT, **b**, N650A, **c**, E734Q, **d**, E702Q, **e**, D738N **f**, E705Q and **g**, E654A. **h**, Fluorescence microscopy image of mTMEM16A mutants expressed in HEK293T cells. Expression of fluorescently labelled protein is shown for mutants E654Q (left) and E654A (right). **i**, Analysis of the EC_{50} of Ca^{2+} activation for different binding site mutants. The data show averages of fits to 3–4 independent recordings. Errors are s.d.

©2014 Macmillan Publishers Limited. All rights reserved

Published October 17, 2016

Independent activation of ion conduction pores in the double-barreled calcium-activated chloride channel TMEM16A

Novandy K. Lim,* Andy K.M. Lam,* and Raimund Dutzler

Department of Biochemistry, University of Zürich, CH-8057 Zürich, Switzerland

The TMEM16 proteins constitute a family of membrane proteins with unusual functional breadth, including lipid scramblases and Cl^- channels. Members of both these branches are activated by Ca^{2+}, acting from the intracellular side, and probably share a common architecture, which was defined in the recent structure of the lipid scramblase nhTMEM16. The structural features of subunits and the arrangement of Ca^{2+}-binding sites in nhTMEM16 suggest that the dimeric protein harbors two locations for catalysis that are independent with respect to both activation and lipid conduction. Here, we ask whether a similar independence is observed in the Ca^{2+}-activated Cl^- channel TMEM16A. For this purpose, we generated concatenated constructs containing subunits with distinct activation and permeation properties. Our biochemical investigations demonstrate the integrity of concatemers after solubilization and purification. During investigation by patch-clamp electrophysiology, the functional behavior of constructs containing either two wild-type (WT) subunits or one WT subunit paired with a second subunit with compromised activation closely resembles TMEM16A. This resemblance extends to ion selectivity, conductance, and the concentration and voltage dependence of channel activation by Ca^{2+}. Constructs combining subunits with different potencies for Ca^{2+} show a biphasic activation curve that can be described as a linear combination of the properties of its constituents. The functional independence is further supported by mutation of a putative pore-lining residue that changes the conduction properties of the mutated subunit. Our results strongly suggest that TMEM16A contains two ion conduction pores that are independently activated by Ca^{2+} binding to sites that are embedded within the transmembrane part of each subunit.

The Journal of General Physiology

Downloaded from on November 10, 2016

INTRODUCTION

Calcium-activated chloride channels (CaCCs) constitute a heterogeneous family of membrane proteins, which activate an anion-selective pore in response to the increase of the intracellular calcium concentration (Hartzell et al., 2005; Kunzelmann et al., 2009). Although these proteins have been characterized by electrophysiology for decades (Arreola et al., 1996; Qu and Hartzell, 2000), their molecular identity was unknown for a long time. CaCCs are expressed in different tissues where they contribute to epithelial chloride secretion and electrical signaling in smooth muscle and certain neurons (Huang et al., 2012; Pedemonte and Galietta, 2014). About seven years ago, three groups independently identified the protein TMEM16A (for transmembrane protein of unknown function number 16A) as the main constituent of a CaCC (Caputo et al., 2008; Schroeder et al., 2008; Yang et al., 2008). After activation by Ca^{2+} from the intracellular side with an EC_{50} in the submicromolar range, the protein mediates anion-selective currents (Yang et al., 2008). Activation by Ca^{2+} is voltage dependent with a decreased potency of the ligand at negative transmembrane potentials (Arreola et al., 1996; Kuruma and Hartzell, 2000; Yang et al., 2008; Xiao et al., 2011; Ni et al., 2014). TMEM16A is a member of a conserved family of membrane proteins that is only expressed in eukaryotic organisms and encompasses 10 paralogues in humans (Schroeder et al., 2008; Yang et al., 2008). Because of assumed molecular features, the name anoctamin was introduced, synonymous for the putative anion selectivity of family members and the presence of eight transmembrane helices predicted by hydropathy analysis (Yang et al., 2008). It was thus unexpected when TMEM16F, another member of the family, was identified as a calcium-activated lipid scramblase, which catalyzes the diffusion of lipids between the two leaflets of the phospholipid bilayer (Suzuki et al., 2010) and thereby leads to the dissipation of the lipid asymmetry and the exposure of the negatively charged phosphatidyl-serine to the cell exterior. The scramblase function was later also observed for other family members (Suzuki et al., 2013), and it was subsequently confirmed for fungal TMEM16 homologues in vitro, after purification and reconstitution of the proteins (Malvezzi et al., 2013; Brunner et al., 2014). Because the two identified CaCCs, TMEM16A and TMEM16B, do not promote lipid scrambling (Malvezzi et al., 2013; Brunner et al., 2014), a functional division within the family was proposed, with some members either functioning as calcium-activated ion channels or

*N.K. Lim and A.K.M. Lam contributed equally to this paper.
Correspondence to Raimund Dutzler: dutzler@bioc.uzh.ch
Abbreviation used: CaCC, calcium-activated chloride channel.

© 2016 Lim et al. This article is distributed under the terms of an Attribution–Noncommercial–Share Alike–No Mirror Sites license for the first six months after the publication date (see http://www.rupress.org/terms). After six months it is available under a Creative Commons License (Attribution–Noncommercial–Share Alike 3.0 Unported license, as described at http://creativecommons.org/licenses/by-nc-sa/3.0/).

The Rockefeller University Press $30.00
J. Gen. Physiol. 2016 Vol. 148 No. 5 375–392
https://doi.org/10.1085/jgp.201611650

Check for updates

Supplemental Material can be found at:
/content/suppl/2016/10/10/jgp.201611650.DC1.html

Published October 17, 2016

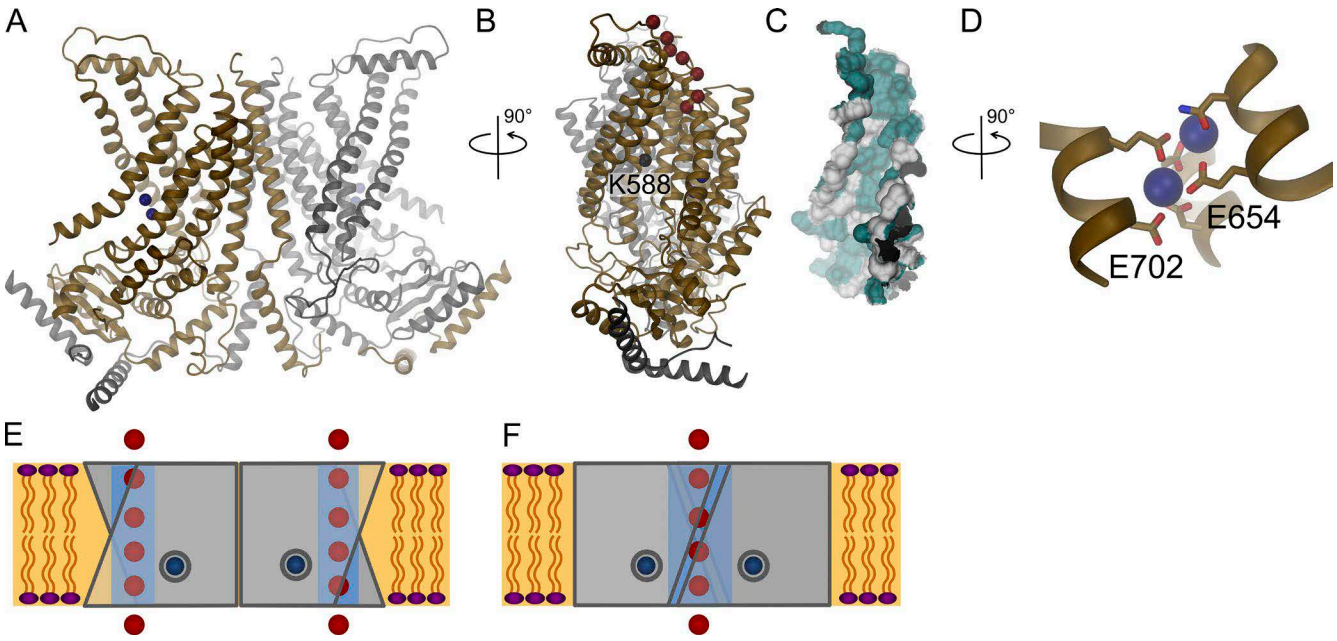

Figure 1. **Structural features of the TMEM16 family.** (A) Ribbon representation of the nhTMEM16 structure. The view is form within the membrane. Bound Ca^{2+} ions are shown as blue spheres. (B) View on the subunit cavity. The relationship to A is indicated. The position of the residue equivalent to Lys588 of mTMEM16 is shown as a black sphere and labeled. Corresponding positions of amino acids that have been shown to change ion conduction in mTMEM16 (Yu et al., 2012) are shown as red spheres. (C) Surface representation of the subunit cavity. The view is as in B. The location of polar and charged residues is shown in cyan. (D) Structure of the Ca^{2+}-binding site. The relation to B is indicated. Ca^{2+} ions are shown as blue spheres, and side chains of interacting residues are shown as sticks. The numbering of selected residues corresponds to mTMEM16A. (E) Schematic representation of TMEM16A containing two pores that are independently regulated by Ca^{2+}. (F) Hypothetical alternative arrangement of subunits resulting in a single pore.

lipid scramblases. Interestingly, some members have also been suggested to possess dual properties (Yang et al., 2012; Picollo et al., 2015). Recently, the architecture of the protein family was revealed by the structure determination of the phospholipid scramblase from the fungus *Nectria haematococca* (termed nhTMEM16; Brunner et al., 2014). Because of the high sequence conservation, it can be assumed that this structure defines the general architecture of both functional branches of the family. The protein forms homodimers, with subunits containing 10 membrane-spanning helices (Fig. 1 A). Each subunit harbors a hydrophilic groove, the "subunit cavity," located at the periphery of the dimer that is exposed to the lipid bilayer (Fig. 1, B and C). This membrane-spanning furrow was proposed to constitute the site for lipid scrambling by offering a hydrophilic path for lipid head groups across the hydrophobic core of the bilayer (Brunner et al., 2014, 2016). The equivalent region in TMEM16 channels is probably involved in ion permeation, as suggested by mutations that affect conduction properties of TMEM16A (Fig. 1 B; Yang et al., 2012; Yu et al., 2012). Each subunit of nhTMEM16 contains a highly conserved calcium-binding site in the vicinity of the subunit cavity, which is embedded within the transmembrane part of the protein (Fig. 1 D; Brunner et al., 2014). The location of this site in the hydrophobic part of the phospholipid bilayer offers a plausible explanation for the observed voltage dependence of calcium activation in TMEM16 channels as these divalent cations have to cross part of the transmembrane electric field to reach their binding site (Yu et al., 2012; Brunner et al., 2014; Tien et al., 2014). Mutations of residues constituting the Ca^{2+}-binding site have been shown to affect the activation of both scramblases and channels, suggesting that both functional branches of the family may share a similar mechanism of activation (Yu et al., 2012; Malvezzi et al., 2013; Terashima et al., 2013; Brunner et al., 2014; Tien et al., 2014). Single mutations of Ca^{2+}-binding residues in TMEM16A decrease the potency of Ca^{2+} to a different extent according to their contribution to Ca^{2+} binding and channel activation (Yu et al., 2012; Brunner et al., 2014; Tien et al., 2014). The nhTMEM16 structure thus suggests that family members acting as scramblases contain two potentially independent sites of catalysis, a feature that might also be shared by TMEM16 channels (Fig. 1 E). However, because of the distinct architecture of the subunit cavity, which forms a half-channel that is exposed to lipids on one side, a potential alternative arrangement of subunits in the ion channels TMEM16A and B was envisioned (Brunner et al., 2014). In this alternative arrangement, the two ex-

Downloaded from on November 10, 2016

Published October 17, 2016

posed half-channels might interact to form a single enclosed aqueous pore that would be completely surrounded by protein residues, akin to other known channel architectures (Fig. 1 F; Doyle et al., 1998; Miyazawa et al., 2003). In such an arrangement, the Ca^{2+}-binding site and the residues lining the ion conduction path would be in close proximity, and it could thus be expected that any change in the pore or the Ca^{2+}-binding site in one of the subunits may affect the activation and conduction properties of the entire protein. In contrast, in the case of two separated ion conduction paths, the same mutation may only affect activation and conduction in one of the two protopores.

We became interested in the question of whether the calcium-activated channel TMEM16A contains two separate ion conduction pores that are independently activated by calcium. In ClC proteins, this question was addressed by the kinetic analysis of single channel recordings (Miller, 1982). However, because the low single-channel conductance of TMEM16A precludes such strategy, we decided to study macroscopic currents of concatenated subunits with one of the two subunits carrying mutations that change the functional properties of the channel. We show that these concatenated proteins are stable and dimeric and that the covalent link between the two subunits does not alter the functional properties of the protein. By introducing mutations that have been shown to shift the potency of Ca^{2+} in nonconcatenated proteins into one subunit, we demonstrate that properties such as the concentration and voltage dependence of activation by Ca^{2+}, as well as the ion selectivity and conductance of the individual protopores are preserved. Our data are thus consistent with functional independence of two ion conduction pores in a double-barreled channel, which resembles the behavior of ion channels of the ClC family.

MATERIALS AND METHODS

Construct generation

The a, c splice variant of mouse TMEM16A (mTMEM16A; Ferrera et al., 2009) was cloned with fragment-exchange (FX) cloning (Geertsma and Dutzler, 2011) into a modified pcDNA3.1 vector (Invitrogen), bearing a 5′ untranslated region (UTR) of hVEGF (from pcDNA4/HisMax; Invitrogen) upstream of the start codon and a 3′ C terminus encoding the Venus YFP, a Myc tag, and a Streptavidin-binding peptide (SBP) tag downstream of the open reading frame. Mutations were made using PCR-based QuikChange mutagenesis (QIAGEN). In the concatemeric constructs, the two monomers were joined by a 31–amino acid–long Gly-Ser linker with sequence GSS GGSGGSGSSGSSGSGSSGGSGGSGSSGS. The two subunits were separately amplified by PCR. The first half of the linker was introduced with the reverse primer of the first subunit and the second half with the forward primer of the second subunit. (Forward primer of the first subunit: 5′-ATATATGCTCTTCTAGTAGGGTCCCCGAGA AGTACTCGACG-3′; reverse primer of the first subunit: 5′-TTATAGCTCTTCATCCACTAGAGCCTGAACTGC CTGATCCACCACTACCTCCGCTCGAGCCCAGCG CGTCCCCATGGTACTCGTA-3′; forward primer of second subunit: 5′-TTATAGCTCTTCAGGAAGTGGTTC GAGTGGAGGTAGTGGTGGATCAGGTTCAAGTGG ATCCAGGGTCCCCGAGAAGTACTCGACG-3′; and reverse primer of the second subunit: 5′-TATATAGCTCTT CATGCCAGCGCGTCCCCATGGTACTCGTA-3′.) The PCR products and the vector were cleaved with SapI (New England Biolabs, Inc.) and subsequently ligated with T4 DNA ligase (New England Biolabs, Inc.). All constructs were confirmed by sequencing.

Protein expression and biochemistry

HEK293T cells were cultured in Dulbecco's modified Eagle's medium (DMEM; Sigma-Aldrich) supplemented with 10 U/ml penicillin, 0.1 mg/ml streptomycin (Sigma-Aldrich), 2 mM L-glutamine (Sigma-Aldrich), and 10% FBS (Sigma-Aldrich) in a humidified atmosphere containing 5% CO_2 at 37°C. For electrophysiology, HEK293T cells were transfected with mTMEM16A constructs at 3 µg DNA per 60-mm culture dish with the calcium phosphate precipitation method (Chen and Okayama, 1987), and medium was changed 4–5 h after transfection. Transfected cells identified by YFP fluorescence were used for patch clamp experiments within 24–72 h of transfection. For biochemical characterization, cells were grown on 10-cm dishes (Corning) to 70–80% cell confluency and transfected with branched polyethylenimine (PEI; Portolano et al., 2014) at a PEI/DNA ratio of 4:1 (wt/wt) for 36–40 h at 37°C and 2.2% CO_2. After expression, cells were resuspended in buffer A (20 mM HEPES, pH 7.4, 150 mM NaCl, 0.2 mM $CaCl_2$, and 5% [wt/vol] glycerol) containing EDTA-free protease inhibitor complete cocktail (Roche). Cells were lysed with 1% (wt/vol) digitonin (A1905; BioChemica) while stirring for 2 h at 4°C. Insoluble material was pelleted by centrifugation at 40,000 *g* for 30 min, and the supernatant was incubated with Streptavidin Plus UltraLink Resin (Thermo Fisher Scientific) while stirring for 3 h at 4°C. The resin was washed with 30 column volumes of buffer B (buffer A with 0.12% [wt/vol] digitonin), and the bound TMEM16A was eluted with buffer B containing 4 mM biotin. The eluate was concentrated and loaded onto a Zorbax GF450 size-exclusion column (Agilent Technologies) that was equilibrated with buffer B. Fluorescence size-exclusion chromatography (FSEC) was performed with an excitation wavelength of 515 nm and an emission wavelength of 530 nm.

Electrophysiology

All recordings were performed in the inside-out configuration (Hamill et al., 1981). Inside-out patches

Downloaded from on November 10, 2016

Published October 17, 2016

were pulled from HEK293T cells expressing the mTMEM16A construct of interest after the formation of a gigaohm seal. Seal resistance was typically 4–8 GΩ or higher. Recording pipettes were pulled from borosilicate glass capillaries (OD 1.5 mm, ID 0.86 mm; Harvard apparatus or Sutter) and were fire-polished using a microforge (Narishige). Pipette resistance was typically 5–8 MΩ when filled with recording solutions. Voltage-clamp recordings were performed using the Axopatch 200B amplifier controlled by the Clampex 10.6 software through Digidata 1550 (Molecular Devices). For general recordings, raw signals were analogue-filtered through the inbuilt low-pass 4-pole Bessel filter at 5 kHz and were sampled at 10 kHz or higher. For noise analysis, raw signals were low-pass analogue-filtered at 10 kHz with the inbuilt Bessel filter and were sampled at 100 kHz. Liquid junction potential was not corrected. Solution exchange was performed using a theta glass pipette mounted on a high-speed piezo switcher (Siskiyou). Step-like solution exchange was elicited by analogue voltage signals delivered through Digidata 1550. All recordings were performed in symmetrical NaCl solutions except for permeability experiments where the NaCl concentration on the intracellular side was varied (see solution composition). Concentration–response and noise analysis experiments were performed at 80 mV unless specified otherwise. Data were background-subtracted before analysis (background current was obtained by recording in the corresponding 0 Ca^{2+} solution). All experiments were performed at 20°C.

Solutions

Stock Ca-EGTA solution contained 150 mM NaCl, 5.99 mM $Ca(OH)_2$, 5 mM EGTA, and 10 mM HEPES, pH 7.40. Stock EGTA solution contained 150 mM NaCl, 5 mM EGTA, and 10 mM HEPES, pH 7.40. The pH was adjusted using 1 M NMDG-OH solution. The stock Ca-EGTA solution contained a free [Ca^{2+}] of 1 mM. Free [Ca^{2+}] was adjusted by mixing stock Ca-EGTA and EGTA solutions at the ratio calculated according to the WEBMAXC calculator (http://web.stanford.edu/~cpatton/webmaxcS.htm). Free [Ca^{2+}] above 1 mM (up to 3 mM) was adjusted by adding $CaCl_2$ from a 1 M stock solution. The pipette solution (extracellular) had the same ionic composition: 150 mM NaCl and 10 mM HEPES, pH 7.40, and a Ca/EGTA ratio corresponding to free [Ca^{2+}] of 1 µM prepared from the same Ca-EGTA stock solutions. For permeability experiments, NaCl concentrations (with and without Ca^{2+}) were adjusted by mixing NaCl stock solutions and $(NMDG)_2SO_4$ stock solutions at the required ratios. Stock NaCl solutions were the same as above. Stock $(NMDG)_2SO_4$ solutions contained 100 mM $(NMDG)_2SO_4$, 5.99 mM $Ca(OH)_2$, 5 mM EGTA, 10 mM HEPES, pH 7.40, and 100 mM $(NMDG)_2SO_4$, 5 mM EGTA, and 10 mM HEPES, pH 7.40. In experiments that compare the effect of substitution with $(NMDG)_2SO_4$ or sucrose, the sucrose-based solution had 15 mM NaCl, 280 mM sucrose, and 10 mM HEPES, pH 7.40, with the corresponding Ca-EGTA ratios. In some permeability experiments, the pipette solution had 1 mM $[Ca^{2+}]_{free}$ instead of 1 µM to improve patch stability. We observed no change in ion selectivity in 1 µM and 1 mM $[Ca^{2+}]_{free}$ pipette solutions.

Rundown correction

Significant rundown of the mTMEM16A current occurs in the excised patch configuration, which affects the proper determination of concentration–response relations if left uncorrected. To correct for this rundown, we used a method akin to Ni et al. (2014). A reference Ca^{2+} pulse, typically at submaximal $[Ca^{2+}]_{free}$ (4 µM, 300 µM, or 1 mM), was applied at a regular time interval (17–20 s) before and after the test pulse as programmed in Clampex. The protocol for a typical Ca^{2+} jump experiment is outlined in Fig. S1 A. The magnitude of the test pulse was then normalized to the linearly interpolated, i.e., averaged, magnitude of the pre- and post-reference pulses to obtain a normalized concentration–response relation. This method also allows the construction of concentration–response relations of concatemeric constructs, which span over five orders of magnitude, by merging concentration–response relations recorded separately in the nanomolar and micromolar ranges.

Data analysis

Ca^{2+} activation. For nonconcatemeric constructs that display monophasic activation, concentration–response data were fitted to the Hill equation:

$$I = I_{max}\frac{1}{1+10^{((\log EC_{50}-\log[Ca^{2+}])h)}},$$

where EC_{50} is the concentration where the activation is 0.5 and h is the Hill slope. I is normalized to the rundown-corrected current measured at the highest or second to highest Ca^{2+} concentration.

For constructs that display biphasic activation and for comparing concatemeric constructs, concentration–response data were fitted to a biphasic Hill equation:

$$I = I_{max}\left[\begin{array}{l}\mathrm{Frac}\dfrac{1}{1+10^{((\log EC_{50(1)}-\log[Ca^{2+}])h_1)}}+\\ (1-\mathrm{Frac})\dfrac{1}{1+10^{((\log EC_{50(2)}-\log[Ca^{2+}])h_2)}}\end{array}\right],$$

where I is normalized to the rundown-corrected current measured at the highest or second to highest Ca^{2+} concentration. Frac is the fractional amplitude of the corresponding activation phase.

For the WT_E702Q concatemer, concentration–response data were fitted to a triphasic Hill equation:

Downloaded from on November 10, 2016

Published October 17, 2016

Table 1. **Fitted parameters from concentration–response experiments**

Construct	Voltage	log $EC_{50(1)}$	$EC_{50(1)}$	h_1	log $EC_{50(2)}$	$EC_{50(2)}$	h_2	I_{max}	Frac
	mV		*μM*			*μM*			
WT	80	−6.50	0.316	1.88	−3.38	417	0.665	1.46	0.666
		(−6.52 to −6.47)		(1.69 to 2.07)	(−3.85 to −2.91)		(0.341 to 0.989)	(1.29 to 1.64)	(0.566 to 0.766)
	−80	−6.09	0.813	2.23	−3.38	417	0.665	1.46	0.666
		(−6.11 to −6.06)		(1.98 to 2.47)	(−3.85 to −2.91)		(0.341 to 0.989)	(1.29 to 1.64)	(0.566 to 0.766)
E702Q	80	−4.41	38.8	1.09				1.03	
		(−4.46 to −4.36)		(0.963 to 1.21)				(0.996 to 1.06)	
	−80	−3.78	167	1.19				1.13	
		(−3.81 to −3.74)		(1.10 to 1.28)				(1.10 to 1.16)	
K588E/E702Q	80	−5.03	9.44	1.01				1.02	
		(−5.08 to −4.97)		(0.910 to 1.11)				(0.987 to 1.06)	
	−80	−4.44	36	1.07				1.11	
		(−4.51 to −4.38)		(0.963 to 1.18)				(1.05 to 1.17)	
WT_WT	80	−6.68	0.209	1.60	−3.14	724	0.511	1.57	0.609
		(−6.71 to −6.65)		(1.39 to 1.81)	(−3.97 to −2.31)		(0.196 to 0.826)	(1.24 to 1.89)	(0.446 to 0.772)
	−80	−6.23	0.589	1.78	−3.14	724	0.511	1.57	0.609
		(−6.26 to −6.20)		(1.57 to 1.98)	(−3.97 to −2.31)		(0.196 to 0.826)	(1.24 to 1.89)	(0.446 to 0.772)
WT_E654Q	80	−6.52	0.302	1.48	−3.76	174	0.765	1.46	0.653
		(−6.59 to −6.44)		(1.18 to 1.77)	(−4.03 to −3.49)		(0.304 to 1.22)	(1.35 to 1.57)	(0.546 to 0.760)
	−80	−6.11	0.772	1.76	−3.76	174	0.765	1.46	0.653
		(−6.16 to −6.05)		(1.43 to 2.08)	(−4.03 to −3.49)		(0.304 to 1.22)	(1.35 to 1.57)	(0.546 to 0.760)
WT_E702Q (biphasic; no constraints)	80	−6.28	0.525	1.78	−4.12	75.9	0.851	1.00	0.312
		(−6.33 to −6.22)		(1.45 to 2.12)	(−4.18 to −4.06)		(0.754 to 0.948)	(0.978 to 1.02)	(0.284 to 0.340)
	−80	−5.89	1.29	1.96	−3.72	191	1.21	1.00	0.312
		(−5.95 to −5.83)		(1.61 to 2.31)	(−3.76 to −3.68)		(1.06 to 1.37)	(0.978 to 1.02)	(0.284 to 0.340)
WT_E702Q (triphasic; A = 0.6, log $EC_{50(3)}$ = −3.14, h_3 = 0.511, h_1 = 1.88, h_2 = 1.09)	80	−6.26	0.548	=1.88	−4.21	61.8	=1.09	1.25	0.517
		(−6.31 to −6.21)			(−4.29 to −4.13)			(1.22 to 1.27)	(0.495 to 0.538)
	−80	−5.92	1.20	=2.23	−3.77	171	=1.19	1.41	0.444
		(−5.97 to −5.87)			(−3.82 to −3.72)			(1.38 to 1.44)	(0.424 to 0.463)
WT_E702Q (triphasic; A = 0.6, log $EC_{50(3)}$ = −3.14, h_3 = 0.511)	80	−6.29	0.514	1.88	−4.24	58	0.921	1.06	0.477
		(−6.34 to −6.23)		(1.52 to 2.24)	(−4.30 to −4.17)		(0.795 to 1.05)	(1.04 to 1.07)	(0.442 to 0.513)
	−80	−5.88	1.32	1.99	−3.75	179	1.36	1.06	0.477
		(−5.94 to −5.82)		(1.63 to 2.36)	(−3.79 to −3.70)		(1.15 to 1.57)	(1.04 to 1.07)	(0.442 to 0.513)
K588E_E702Q (biphasic; log $EC_{50(1)}$ = −6.46, h_1 = 1.42)	80	= −6.46	=0.347	=1.42	−4.28	52.5	1.13	1.16	0.015
					(−4.34 to −4.21)		(1.01 to 1.24)	(1.10 to 1.22)	(0.0055 to 0.024)
	−80				−3.79	163.2	1.49	1.40	
					(−3.80 to −3.77)		(1.44 to 1.55)	(1.39 to 1.42)	
WT_K588E/E702Q (biphasic)	80	−6.29	0.513	1.56	−4.20	63.1	0.616	1.20	0.412
		(−6.41 to −6.17)		(0.811 to 2.30)	(−4.61 to −3.79)		(0.229 to 1.00)	(1.08 to 1.31)	(0.176 to 0.648)
	−80	−5.97	1.07	1.82	−3.82	151	1.11	1.15	0.599
		(−6.05 to −5.88)		(1.39 to 2.24)	(−4.03 to −3.61)		(0.505 to 1.71)	(1.08 to 1.22)	(0.506 to 0.692)

Asymptotic 95% confidence intervals are in parentheses; values preceded by = were constrained during fitting; values that are identical at 80 and −80 mV were constrained to a shared but freely varying value; data at 80 and −80 mV were normalized to their respective I_{max} values before global fitting.

$$I = I_{max}\left\{\begin{array}{l}\text{Frac}\left[\dfrac{A}{1+10^{((\log EC_{50(1)}-\log[Ca^{2+}])h_1)}}+\dfrac{(1-A)}{1+10^{((\log EC_{50(3)}-\log[Ca^{2+}])h_3)}}\right]\\ +(1-\text{Frac})\dfrac{1}{1+10^{((\log EC_{50(2)}-\log[Ca^{2+}])h_2)}}\end{array}\right\},$$

where A is the fractional component of the high-affinity activation and other parameters are the same as above. Fitting concentration data to this equation therefore accounts for the low-affinity activation observed for the WT subunit (Fig. 3 A) in this concatemer. During curve fitting with this triphasic Hill equation, A, log $EC_{50(3)}$, and h_3 were constrained to the corresponding values of the low-affinity phase of the WT_WT concatemer. This leaves the same number of free parameters to be fitted as for the biphasic Hill equation.

We note that in the biphasic and triphasic Hill equations, at least three model parameters (h_1, h_2, I_{max}, and Frac) are interdependent, and thus a rational concern is that the best fit of the parameters may not be accurately estimated. This is of importance, as the second activation often exhibits shallow Hill slope, and hence the plateau of this activation is relatively less well defined than that of nonconcatemeric constructs (see for example Fig. 6 F). More importantly, the interpretation of the relative contribution of the individual subunits in a concatemer requires an accurate estimate of Frac.

Downloaded from on November 10, 2016

Published October 17, 2016

Table 2. **Fitted parameters from nonstationary noise analysis**

Construct	at $[Ca^{2+}]$	i	γ	$P_{O\,max}$
		pA	*pS*	
WT	2 µM	0.21 ± 0.013	2.63 ± 0.16	0.71 ± 0.022
	1 mM	0.22 ± 0.0091	2.75 ± 0.11	0.87 ± 0.025
E702Q	1 mM	0.19 ± 0.0094	2.38 ± 0.12	0.81 ± 0.018
K588E	2 µM	0.084 ± 0.0057	1.05 ± 0.071	0.48 ± 0.055
K588E/E702Q	1 mM	0.16 ± 0.014	2.00 ± 0.18	0.73 ± 0.025
WT_WT	2 µM	0.15 ± 0.0046	1.88 ± 0.058	0.62 ± 0.039
WT_E654Q	2 µM	0.17 ± 0.018	2.13 ± 0.23	0.66 ± 0.015
	1 mM	0.196 ± 0.019	2.45 ± 0.24	0.81 ± 0.024
WT_E702Q	2 µM	0.14 ± 0.0084	1.75 ± 0.11	0.50 ± 0.037

Presented as mean ± SEM calculated from fitted parameters from individual patches.

To improve the quality of the fits, the activation curves obtained at 80 and −80 mV were fitted simultaneously where Frac and I_{max} were constrained, respectively, to a shared but freely varying value whenever possible. For the WT_E702Q concatemer, good estimates of these model parameters can be obtained without imposing specific constraints. The asymptotic 95% confidence intervals of the log EC_{50} of the first and second activation are generally narrow as the log EC_{50} values show little correlation with the other free parameters and are well defined by the data. The asymptotic 95% confidence intervals of the other fitted parameters (h_1, h_2, I_{max}, and Frac) are higher, but still smaller than 20% of the best-fit values. We have also characterized the errors in parameter estimation during curve fitting by basic Monte Carlo simulation using the root mean squared errors (RMSEs) and the best-fit parameters, assuming that the errors follow a Gaussian distribution with a mean of zero (Fig. S2; see legend for details). We found that, given the experimental errors, well-defined distributions in the expected range can be obtained for all six free parameters for both voltages (Fig. S2 A). Similar to the asymptotic 95% confidence interval, which is symmetric, the distributions of all fitted parameters are also approximately symmetric, with that of h_1 being slightly skewed for both voltages. Correlations between Frac and h_1, h_2, and I_{max} are also observed (Fig. S2, B and C), but the values are expected to cluster around the peaks of the distributions. Thus, although the precise values of these parameters cannot be uniquely determined, they represent reliable estimates. For comparison, we have also included the best fit with h_1 and h_2 constrained to the corresponding values of the nonconcatemeric constructs, which yielded very similar best-fit values (Table 1).

For the K588E_E702Q concatemer, the fraction of the first activation is very small compared with that of the second activation, and as a result, the first activation cannot be fitted very well. For this reason, we have constrained both log $EC_{50(1)}$ and h_1 to the best-fit values obtained for WT_E702Q to obtain an acceptable asymptotic 95% confidence interval for the remaining parameters. The constrained log $EC_{50(1)}$ and h_1 were further adjusted manually. For the WT_K588E/E702Q concatemer, the asymptotic 95% confidence intervals of h_1, h_2, I_{max}, and Frac are somewhat wider than that of WT_E702Q when all the parameters are allowed to vary freely. However, the best-fit values, using our simulation results as a guide, also represent reliable estimates in this setting.

For presentation, the data were normalized to the estimated I_{max} and were fitted with I_{max} constrained to 1. Details of the parameters and constraints can be found in Table 1.

Nonstationary noise analysis. Nonstationary noise analysis was performed according to Sigworth (1980). Nonstationary noise analysis requires information on the fluctuation, characterized by its variance, of an activating and/or deactivating current that samples the mean current space available to the channel. The fluctuation is not time dependent per se but appears to be dependent on time only because P_O is time dependent. This information was experimentally obtained by periodically pulsing Ca^{2+} on the intracellular side at saturating concentrations in concentration jump experiments so that the variance of the mean current at each time point could be estimated. For an example, see Fig. S1 B. Digitized data were filtered at 7.5 kHz with a low-pass Gaussian filter (Clampfit; Molecular Devices) and were subsequently decimated fourfold to a final sampling frequency of 25 kHz before analysis. The variance of 50–100 aligned, successive and kinetically identical currents at each time point was computed using the successive difference method proposed by Heinemann and Conti (1992), which allows the calculation of the variance in the presence of current rundown and artifacts arising from step-like solution switching. The computed variance was plotted against the mean current, and the data were fitted to

$$\text{Variance} = i\langle I\rangle - \frac{\langle I\rangle^2}{N} + c,$$

Downloaded from on November 10, 2016

Published October 17, 2016

where <I> is the mean current, i is the single-channel current, N is the number of functional channels that can contribute to the observed fluctuation, and c is the background variance. The background variance that was estimated from the fit was subtracted, and the resulting data were refitted to the same equation without the background term c. With data that display a parabolic shape, it is possible to obtain a meaningful estimate of the maximum P_O as N is well defined. We therefore estimated the maximum P_O from the ratio of the maximal mean current to the nonzero x-intercept, which corresponds to the theoretically achievable maximal mean current if P_O was 1. With data that do not reach a maximum, N cannot be estimated reliably, and thus the estimated maximum P_O, which is <0.5, rather represents an upper limit. The single-channel current i can generally be estimated with higher confidence, as it is the slope at the zero x-intercept, which is usually well defined by the data.

For presentation, the pairs of variance and <I> data points were sorted, reduced, and smoothed using the substitute average method. The variance-<I> plots from individual patches were normalized to the estimated $\langle I \rangle_{max}$ such that the ordinate becomes variance/$\langle I \rangle_{max}$ and the abscissa becomes P_O. The resulting plots from the individual patches were then merged and reduced using the substitute average method.

Data analysis and statistics. Data analysis was performed using Clampfit, Excel (Microsoft), and Prism 5 and/or 6 (GraphPad Software). Curve fitting and statistical analysis were performed in Prism 5 and/or 6. For comparison of two samples, statistical differences were detected using the *t* test and were considered significant when $P < 0.05$. Data are presented as mean ± SEM. Parameters obtained from curve fitting shown in Table 1 are presented as the best-fit value together with the asymptotic 95% confidence intervals, whereas those in Table 2 are presented as mean of the individual fits ± SEM.

Online supplemental material

Fig. S1 shows measurement protocols and reversal potential measurements. Fig. S2 shows errors in parameter estimation during curve fitting to the triphasic Hill equation estimated in a Monte Carlo simulation for the WT_E702Q concatemer at 80 and −80 mV.

RESULTS

Biochemical characterization of concatemeric proteins

To address the question of whether TMEM16A comprises two ion conduction pores that are independently activated by Ca^{2+}, we have generated concatenated constructs that either contained two WT subunits (WT_WT) or a combination of WT and point mutants with altered properties (e.g., WT_E702Q). These constructs were prepared by linking the C terminus of one to the N terminus of another subunit via a 31-residue-long

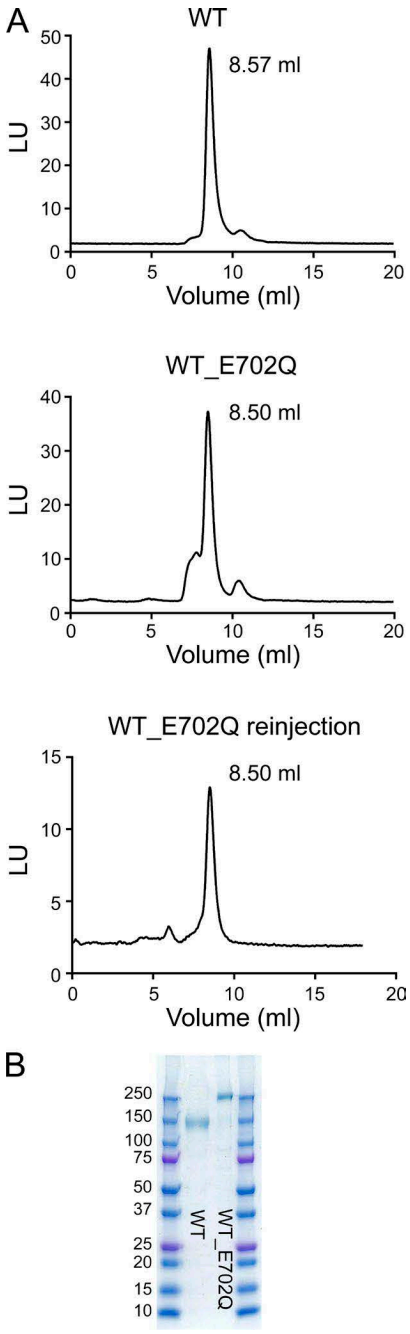

Figure 2. **Purification and biochemical characterization of mTMEM16 constructs.** (A) Gel filtration profiles of WT and the WT_E702Q concatemer. WT (top) and WT_E702Q (center) loaded after purification in digitonin. The protein was detected by the fluorescence of the YFP tag. The bottom graph shows a reinjection of the main peak fraction of WT_E702Q. The elution volume is indicated. LU, luminescence units. (B) SDS-PAGE of the purified proteins. Both proteins (WT and WT_E702Q) run at the expected molecular weight. Molecular weights of the markers (kilodaltons) are indicated.

Downloaded from on November 10, 2016

Published October 17, 2016

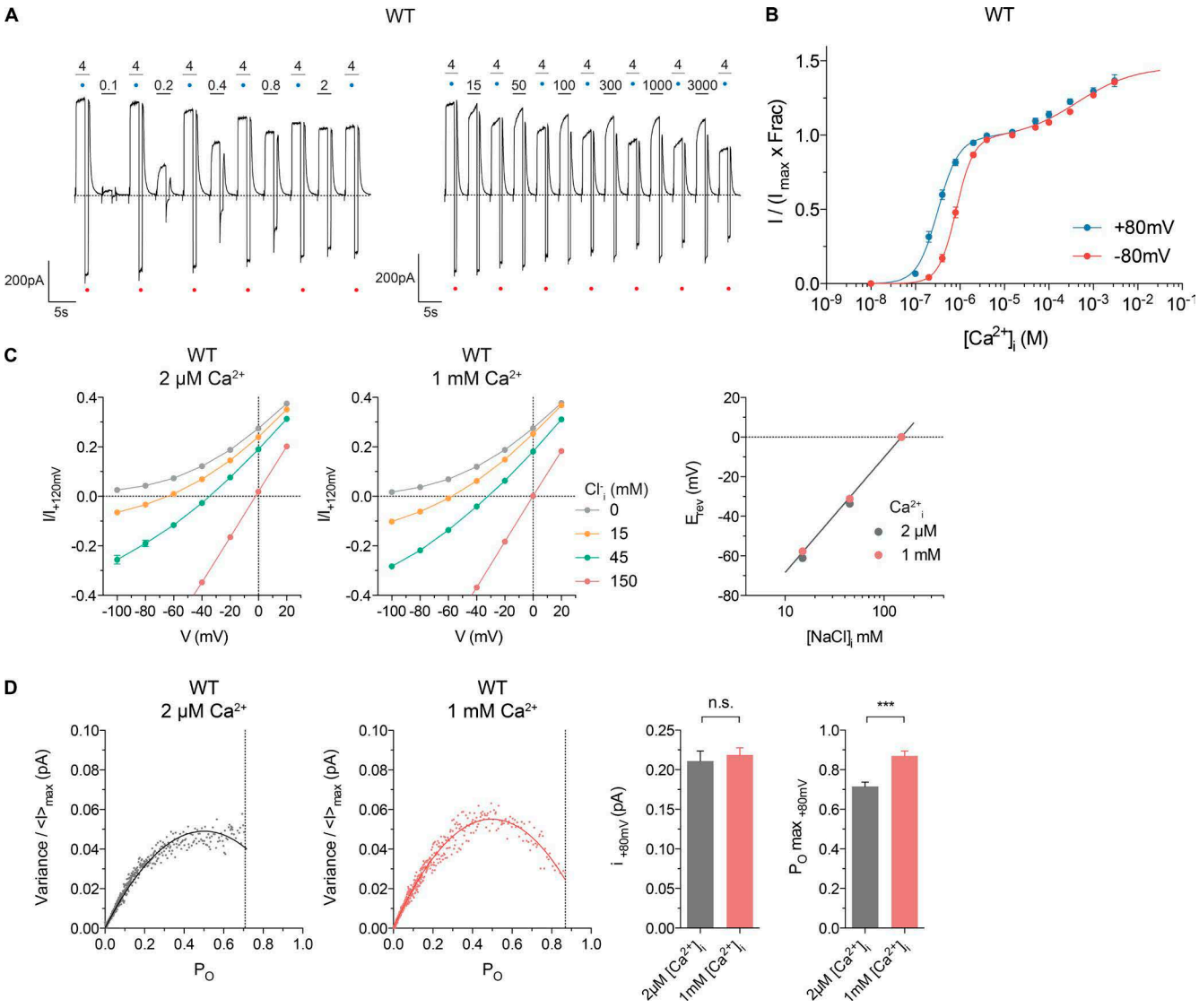

Figure 3. **Functional properties of WT mTMEM16A.** (A) Representative currents of WT mTMEM16A at 80 and −80 mV. Numbers show $[Ca^{2+}]_{free}$ (μM) on the intracellular side of the excised patch. Each sweep was recorded using the voltage and piezo protocol shown in Fig. S1 A. Individual sweeps are separated by a regular time interval (17–20 s, programmed in Clampex) and are concatenated to form a single trace. Blue and red dots indicate the reference pulses used for rundown correction at 80 and −80 mV, respectively (see Materials and methods). Currents at low (left) and high Ca^{2+} (right) were recorded from different patches. (B) Rundown-corrected concentration–response relations of WT mTMEM16A at 80 and −80 mV (n = 4–12 for each data point). Lines are the best fit to a biphasic Hill equation. (C) Na^+ versus Cl^- selectivity of WT mTMEM16A. I-V plots of the instantaneous current in response to the indicated voltage steps at 150 mM extracellular and the indicated intracellular NaCl concentrations at 2 μM (n = 6, left) and 1 mM (n = 6–7, middle) $[Ca^{2+}]_{free}$. Data are mean values of normalized I-V plots from individual patches unless otherwise stated. (right) Relation between intracellular [NaCl] and reversal potential (E_{rev}) at 2 μM (n = 6) and 1 mM (n = 6–7) $[Ca^{2+}]_{free}$. The line indicates the Nernst potential of Cl^-. (D) Merged and averaged variance-<I> plots of WT mTMEM16A obtained at 2 μM (n = 21, left) and 1 mM (n = 10, middle) $[Ca^{2+}]_{free}$ at 80 mV. The solid lines are the best fit to the noise parabola equation. Dotted lines indicate the mean $P_{O\ max}$ across patches. Other variance-<I> plots were constructed in the same way unless otherwise stated. (right) Pooled data of individual i and $P_{O\ max}$ values obtained from individual patches expressing WT mTMEM16A at 2 μM (n = 21) and 1 mM (n = 10) $[Ca^{2+}]_{free}$. n.s., P > 0.05; ***, P ≤ 0.001. In B–D, data are presented as mean and errors as SEM.

linker consisting of alternating Gly and Ser residues. The second subunit in the concatemer is appended by a C-terminal YFP to facilitate the detection of the protein. We have subsequently investigated whether the concatenated proteins are properly folded and assembled and whether their biochemical properties resemble TMEM16A. Both the YFP-tagged WT_E702Q concatemer and a TMEM16A-YFP fusion (WT) used for functional characterization appear to predominately localize at the plasma membrane when expressed in HEK293 cells. When purified in the detergent digitonin and loaded on a gel-filtration column, WT_E702Q

Downloaded from on November 10, 2016

Published October 17, 2016

elutes similarly to WT, at a volume that is compatible with a dimeric organization of the protein (Fig. 2 A). Upon subjection to SDS-PAGE analysis, the concatenated protein migrates at twice the size of a single subunit and no proteolysis is observed, indicative of a stable protein (Fig. 2 B). Collectively, these results suggest that the covalent linkage neither affected the stability of the protein nor did it change its oligomerization behavior, which could have been the case if instead of an intramolecular dimerization, the subunits in the linked concatemer would favor intermolecular interactions, thereby generating assemblies of larger size.

Functional properties of WT

For the functional characterization of TMEM16A constructs, we expressed unlinked and concatenated proteins in HEK293 cells and investigated their properties by electrophysiology in excised patches in the inside-out configuration (Tables 1 and 2). We first studied the properties of WT in a broad range of Ca^{2+} concentrations. At submicromolar concentrations, the protein shows the previously described steep activation that reflects the cooperative opening of the ion conduction pore (Fig. 3, A and B; Arreola et al., 1996; Kuruma and Hartzell, 2000; Yang et al., 2008). In this concentration range, the activation by Ca^{2+} is voltage dependent, with a decreased potency of the ligand at negative potentials (Fig. 3 B). Between 2 and 100 µM Ca^{2+}, the current levels remain constant until, at higher concentrations, a second smaller activation step is observed (Fig. 3, A and B). This biphasic activation is only evident upon a careful correction of the irreversible rundown that becomes more severe at higher Ca^{2+} concentration, and it might thus have escaped previous detection. The second component is shallow, it increases the currents measured in the first plateau by ∼25%, and it saturates with an apparent EC_{50} of 417 µM (Fig. 3 B and Table 1). Unlike the first activation, the second activation step is not voltage dependent (Fig. 3 B). We were interested in whether the activation at high Ca^{2+} concentrations changes the permeation properties of the channel, as it has been suggested previously (Kuruma and Hartzell, 2000; Schroeder et al., 2008; Peters et al., 2015), or whether it reflects an increase in the open probability with similar ion conduction characteristics. We thus studied the ion selectivity of the channel by quantifying reversal potentials (E_{rev}) in asymmetric conditions and its conductance (γ) and open probability (P_O) by nonstationary noise analysis at low and high Ca^{2+} concentrations. The currents measured from channels activated at low (1–2 µM) Ca^{2+} in a 10-fold NaCl gradient (c_{out} 150 mM, c_{in} 15 mM) with an osmotic compensation of the low salt intracellular solution by sucrose reverse at about −45 mV (Fig. S1 C). This value is consistent with a previous study and was attributed to an imperfect selectivity for anions over cations (Qu and Hartzell, 2000). However, when replacing sucrose by NMDG sulfate to minimize junction potential changes (see companion paper by Jeng et al. in this issue) in the same 10-fold NaCl gradient, E_{rev} approaches the Nernst potential of Cl^- (i.e., −58 mV), which indicates that the anion selectivity of the channel might be stronger than anticipated (Fig. 3 C). This was also previously suggested based on data obtained from purified and reconstituted TMEM16A (Terashima et al., 2013). We repeated the selectivity experiments at 1 mM Ca^{2+} and measured a very similar E_{rev}, thus suggesting that the anion over cation selectivity of the channel did not change in conditions where we observed the second activation step (Fig. 3 C). To further characterize the functional properties of the channel, we performed nonstationary noise analysis after the rapid exposure to 2 µM and 1 mM Ca^{2+} (Fig. 3 D and Fig. S1 B). Fitting the variance of the current as a function of the mean current amplitude to the noise parabola equation allows an estimation of γ and P_O of the channel (see Materials and methods). At both Ca^{2+} concentrations, we have observed a parabolic relationship that allowed for a reliable fit of both parameters (Fig. 3 D and Table 2). Interestingly, the estimate of γ of ∼2.7 pS is very similar at both Ca^{2+} concentrations, whereas P_O of the channel is ∼20% higher when measured at 1 mM than at 2 µM Ca^{2+} (Fig. 3 D). This increase in P_O is consistent with the increment observed for macroscopic currents (Fig. 3 B). The fitted values are in general agreement with a previous analysis of TMEM16A (Ta et al., 2016). Our data thus suggest that the increase in current in WT at high Ca^{2+} concentrations might result from an increase in P_O without strongly affecting the permeation properties of the pore.

Functional properties of WT_WT

We next investigated whether the concatenated WT_WT protein has retained a similar functional behavior as WT. We thus repeated the same experiments used to characterize the functional properties of WT for this concatenated construct. The dose–response relationships show a very similar biphasic activation as observed for WT, with a cooperative voltage-dependent opening at low Ca^{2+} concentrations and a shallow voltage-independent second component at high Ca^{2+} concentrations (Fig. 4, A and B; and Table 1). As for WT, the WT_WT currents are highly Cl^- selective at low and high Ca^{2+} concentrations (Fig. 4 C), and both γ and P_O estimated by noise analysis at 2 µM Ca^{2+} closely resemble the values measured for WT (Fig. 4 D and Table 2). Collectively, our data strongly suggest that the covalent linkage of the two subunits in the dimeric protein did not significantly affect the ion permeation and gating characteristics of the protein.

Downloaded from on November 10, 2016

Published October 17, 2016

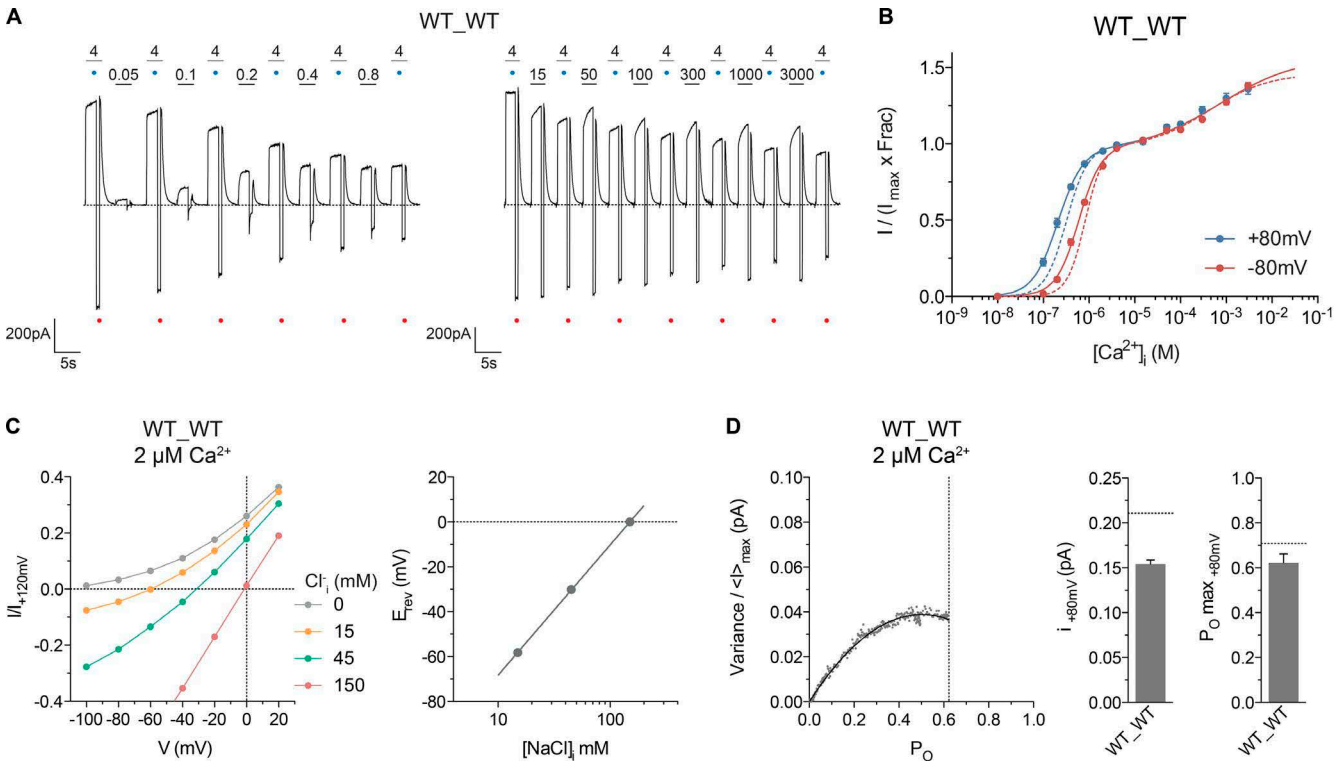

Figure 4. **Functional properties of the WT_WT concatemer.** (A) Representative currents of the WT_WT concatemer at 80 and −80 mV. Blue and red dots indicate the reference pulses used for rundown correction at 80 and −80 mV, respectively (see Materials and methods). (B) Rundown-corrected concentration–response relations of the WT_WT concatemer at 80 and −80 mV (n = 8–11 for each data point). Lines are the best fit to a biphasic Hill equation. Dashed lines indicate the relations of WT mTMEM16A at 80 and −80 mV. (C) Na^+ versus Cl^- selectivity of the WT_WT concatemer. (left) I-V plots recorded at 150 mM extracellular and the indicated intracellular NaCl concentrations at 2 µM (n = 6) $[Ca^{2+}]_{free}$. (right) Relation between intracellular NaCl concentration and E_{rev} at 2 µM (n = 6) $[Ca^{2+}]_{free}$. The line indicates the Nernst potential of Cl^-. (D, left) Merged and averaged variance-<I> plots of the WT_WT concatemer obtained at 2 µM (n = 5) $[Ca^{2+}]_{free}$ at 80 mV. The dotted line indicates the mean $P_{O\,max}$ across patches. (right) Pooled data of individual i and $P_{O\,max}$ values obtained from individual patches expressing the WT_WT concatemer at 2 µM (n = 5) $[Ca^{2+}]_{free}$. Dotted lines indicate the corresponding value of WT mTMEM16A. In B–D, data are presented as mean and errors as SEM.

Downloaded from on November 10, 2016

A concatemer containing a subunit with compromised activation properties

Because the concatenation of two subunits did not strongly affect protein function, we were interested whether the functional phenotype of WT would be preserved in the context of a covalently linked heterodimer, where one of the two subunits contains a mutation that impedes Ca^{2+} activation. This would only be expected in the case of two functionally independent pores in the dimeric protein. For this purpose, we generated a concatenated protein consisting of a WT subunit followed by a second subunit containing the mutation E654Q (WT_E654Q) in the Ca^{2+}-binding site, for which we and others have previously not observed significant activity at Ca^{2+} concentrations up to 1 mM (Brunner et al., 2014; Tien et al., 2014). The Ca^{2+} dose–response relationships show a very similar biphasic activation that was also observed for WT and WT_WT, with a predominant activation at low and a second shallow step at high Ca^{2+} concentrations (Fig. 5, A and B; and Table 1). Because the second component is voltage independent with properties that resemble WT and WT_WT, we assume that any contribution of the subunit containing the E654Q mutant is small. At low Ca^{2+} concentrations, activation proceeds with an EC_{50} that is very close to WT (Fig. 5 B and Table 1). Similarly, the voltage dependence of this Ca^{2+} activation is preserved in this construct (Fig. 5 B). The steep dependence on Ca^{2+} with a Hill coefficient consistently above one indicates that the cooperativity of opening is an intrinsic property of a single subunit (Table 1). Like in WT, the currents are highly anion selective at both low and high Ca^{2+} concentrations (Fig. 5 C). Finally, as suggested by our noise analysis, the channel shows very similar properties as WT with an increase in P_O at high Ca^{2+} concentrations (Fig. 5 D). The results from WT_E645Q, which only contains one functional subunit, are thus consistent with a dimeric protein comprising two ion conduction pores that are independently activated by Ca^{2+}.

Published October 17, 2016

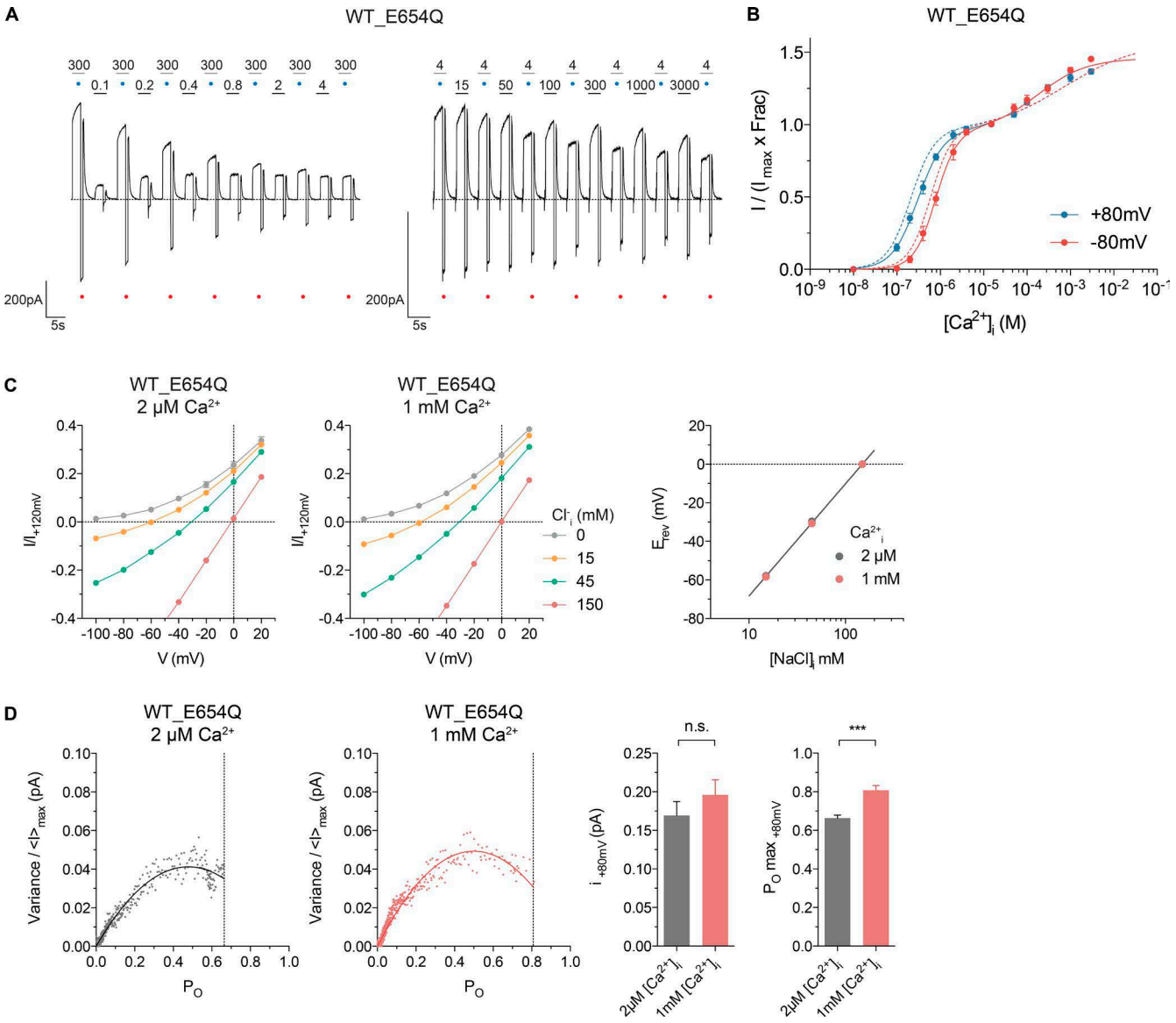

Figure 5. **Functional properties of the WT_E654Q concatemer.** (A) Representative currents of the WT_E654Q concatemer at 80 and −80 mV. Blue and red dots indicate the reference pulses used for rundown correction at 80 and −80 mV, respectively (see Materials and methods). (B) Rundown-corrected concentration–response relations of the WT_E654Q concatemer at 80 and −80 mV (n = 4–10 for each data point). Lines are the best fit to a biphasic Hill equation. Dashed lines indicate the relations of WT_WT at 80 and −80 mV. (C) Na^+ versus Cl^- selectivity of the WT_E654Q concatemer. (left and middle) I-V plots recorded at 150 mM extracellular and the indicated intracellular NaCl concentrations at 2 µM (n = 6) and 1 mM (n = 6–7) $[Ca^{2+}]_{free}$. (right) Relation between intracellular [NaCl] and E_{rev} at 2 µM (n = 6) and 1 mM (n = 6–7) $[Ca^{2+}]_{free}$. The line indicates the Nernst potential of Cl^-. (D, left and middle) Merged and averaged variance-<I> plots of the WT_E654Q concatemer obtained at 2 µM (n = 6) and 1 mM (n = 8) $[Ca^{2+}]_{free}$ at 80 mV. The dotted lines indicate the mean $P_{O\ max}$ across patches. (right) Pooled data of individual i and $P_{O\ max}$ values obtained from individual patches expressing the WT_E654Q concatemer at 2 µM (n = 6) and 1 mM (n = 8) $[Ca^{2+}]_{free}$. n.s., P > 0.05; ***, P ≤ 0.001. In B–D, data are presented as mean and errors as SEM.

A concatemer containing a subunit with decreased potency for Ca^{2+}

In the next step, we wanted to characterize the functional behavior of a concatenated protein containing two functional subunits that are activated at different Ca^{2+} concentrations. We thus combined WT with the mutant E702Q (WT_E702Q), which also removes a negatively charged residue from the Ca^{2+}-binding site. The same construct was used for the biochemical characterization of the concatemeric protein (Fig. 2). E702Q itself mediates robust currents (Fig. 6 A) but has an EC_{50} that is 122-times higher (i.e., from 0.32 µM in WT to 39 µM in E702Q when measured at 80 mV; Yu et al., 2012; Brunner et al., 2014; Tien et al., 2014) and somewhat reduced cooperativity compared with WT (Fig. 6 B and Table 1). As for WT, Ca^{2+} activation is voltage de-

Downloaded from on November 10, 2016

Published October 17, 2016

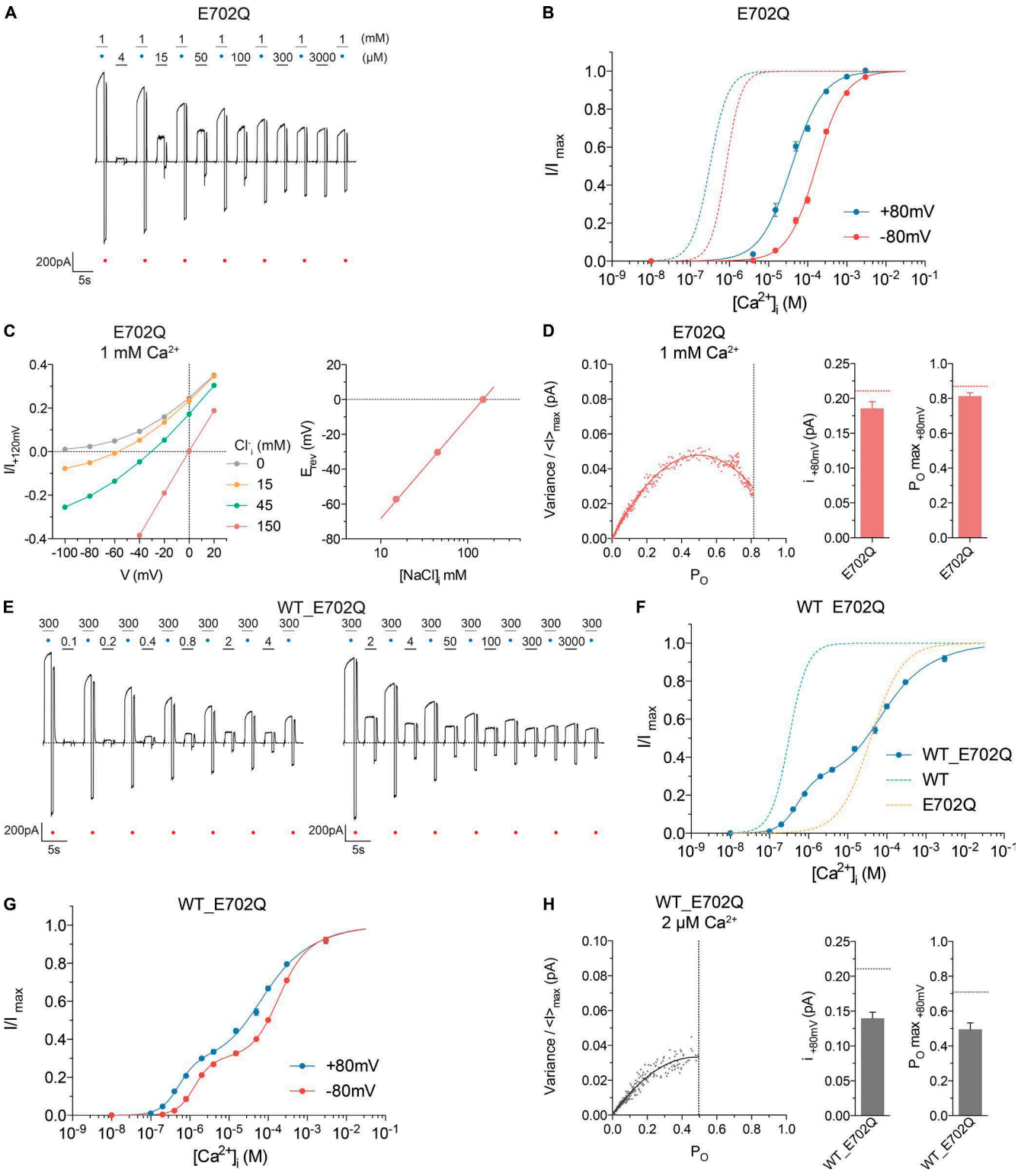

Figure 6. **Functional properties of the WT_E702Q concatemer.** (A) Representative currents of the E702Q mutant at 80 and −80 mV. (B) Rundown-corrected concentration–response relations of the E702Q mutant at 80 and −80 mV (n = 13–14 for each data point). Solid lines are the best fit to the Hill equation. Dashed lines indicate the relations of WT mTMEM16A at 80 and −80 mV. (C) Na^+ versus Cl^- selectivity of the E702Q mutant. (left) I-V plots recorded at 150 mM extracellular and the indicated intracellular NaCl concentrations at 1 mM (n = 5) $[Ca^{2+}]_{free}$. (right) Relation between intracellular [NaCl] and E_{rev} at 1 mM (n = 5) $[Ca^{2+}]_{free}$. The line indicates the Nernst potential of Cl^-. (D) Merged and averaged variance-<I> plot and pooled data (n = 10) of the E702Q mutant obtained at 1 mM $[Ca^{2+}]_{free}$ at 80 mV. (E) Representative currents of the WT_E702Q concatemer at 80 and −80 mV. (A and E) Blue and red dots indicate the reference pulses used for rundown correction at 80 and −80 mV, respectively (see Materials and methods).

Downloaded from on November 10, 2016

Published October 17, 2016

pendent with a decreased potency at negative potentials (Fig. 6 B). Unlike WT, we did not, in this case, observe a biphasic activation, but we cannot exclude that the second component might either be hidden in the main activation step or shifted to very high Ca^{2+} concentrations. Similar to WT, the currents (activated at 1 mM Ca^{2+}) reverse close to the Nernst potential of Cl^-, indicative for a highly anion-selective channel (Fig. 6 C). Because noise analysis of this (nonconcatemeric) mutant suggested a similar γ and P_O as WT (Fig. 6 D), we expected to observe a biphasic activation of the WT_E702Q concatemer with two similar current levels. This behavior should be easily distinguishable from the biphasic activation of WT because, compared with the second component of WT, the activation of the E702Q subunit proceeds at an 11-times-lower Ca^{2+} concentration, contributes about equally to the total currents, and is voltage dependent. Conversely, we anticipate the high Ca^{2+} component of WT to be hidden in the dominant activation of the E702Q subunit. The predicted behavior, with separate transitions at low and high Ca^{2+} concentrations, can readily be observed in the dose–response relationships of this construct (Fig. 6, E and F). As expected, both activation steps are voltage dependent (Fig. 6 G). To account for the biphasic activation of the WT subunit, a sum of three Hill equations was used to fit the WT_E702Q dose–response data (see Materials and methods). We obtained EC_{50} values that are very close to the values of the respective nonconcatenated homomeric proteins (Fig. 6 E and Table 1), either with only four free parameters where h_1 and h_2 were both constrained or six free parameters where h_1 and h_2 were allowed to vary. Consistent with our expectation, we observed in both fits that both transitions contribute about equally to the total currents with a Frac value of ∼0.5 (Fig. 6 E and Table 1). Moreover, when allowed to be further optimized, the values of both h_1 and h_2 remain very similar to their respective nonconcatenated counterparts. In the latter case where six free parameters were to be fitted, we have investigated the interdependence of the parameters by simulations to ensure the reliability of the fit (Fig. S2 and Materials and methods). In addition, we have characterized the ion conduction properties of the first activation step by noise analysis and observed very similar behavior as in the two previously investigated concatemers (Fig. 6 H). Our experiments on WT_E702Q thus provide strong additional evidence for a predominantly independent activation of two separate ion conduction pores in the dimeric mTMEM16A channel. Although we cannot exclude the presence of weak coupling between the two subunits, our data are not detailed enough to permit such analysis.

Effect of a putative pore mutation

Finally, to further support the functional independence of two separate ion conduction pores contained in the dimeric protein, we were interested in changing the ion permeation properties of one subunit by introducing a mutation outside the calcium-binding site. We thus turned our attention toward Lys588, which, upon mutation to Gln, was previously suggested to lower the anion selectivity of mTMEM16A (Yang et al., 2012). In an attempt to enhance the effect of the mutation, we replaced the positively charged lysine with a negatively charged glutamate. Patch-clamp experiments of the single mutant K588E showed very low currents evoked in response to Ca^{2+} at concentrations that fully activate WT (Fig. 7 A). Nonstationary noise analysis indicates that the mutant has likely reduced γ and P_O, but, because the experimental variance–mean current relation has not reached a maximum, these values are, in this case, only a crude estimate (Fig. 7 A). Because of the low magnitude of the calcium-activated currents, we were not able to reliably characterize the ion selectivity of this mutant. In contrast to K588E, the double mutant K588E/E702Q showed robust currents at high Ca^{2+} concentrations, although with a pronounced outward rectification, which probably reflects a change in pore conductance as rectification is instantaneous and the current showed no time dependence in response to voltage jumps (Fig. 7 B). With respect to potency and voltage dependence, the Ca^{2+} dose–response relationships of this double mutant resemble E702Q (Fig. 7 C and Table 1). The characterization of outward currents by nonstationary noise analysis indicates similar properties as WT and E702Q (Fig. 7 D). The current of this double mutant also reverses close to the Nernst potential of Cl^-, indicating that the mutation did not affect the high anion selectivity observed in all investigated constructs (Fig. 7 E). The strong outward rectification but unchanged anion selectivity suggests that the residue may influence the access of anions from the intracellular side presumably by a electrostatic mechanism, akin to a Lys residue identified in the chloride channel CLC-0 (Chen and Chen, 2003). We have subsequently

(F) Rundown-corrected concentration–response relation of the WT_E702Q concatemer at 80 mV (n = 8–18 for each data point). The solid line is the best fit to the triphasic Hill equation. Dashed lines indicate the fist activation of WT (green) and E702Q (orange) at 80 mV. (G) Rundown-corrected concentration–response relations of the WT_E702Q concatemer at 80 and −80 mV (n = 8–18 for each data point). Lines are the best fit to a triphasic Hill equation. (H) Merged and averaged variance-<I> plot and pooled data (n = 9) of the WT_E702Q concatemer obtained at 2 µM $[Ca^{2+}]_{free}$ at 80 mV. (D and H, left) The dotted lines indicate the mean $P_{O\ max}$ across patches. (D and H, right) Dotted lines indicate the corresponding value of WT mTMEM16A. In B–D and F–H, data are presented as mean and errors as SEM.

Downloaded from on November 10, 2016

Published October 17, 2016

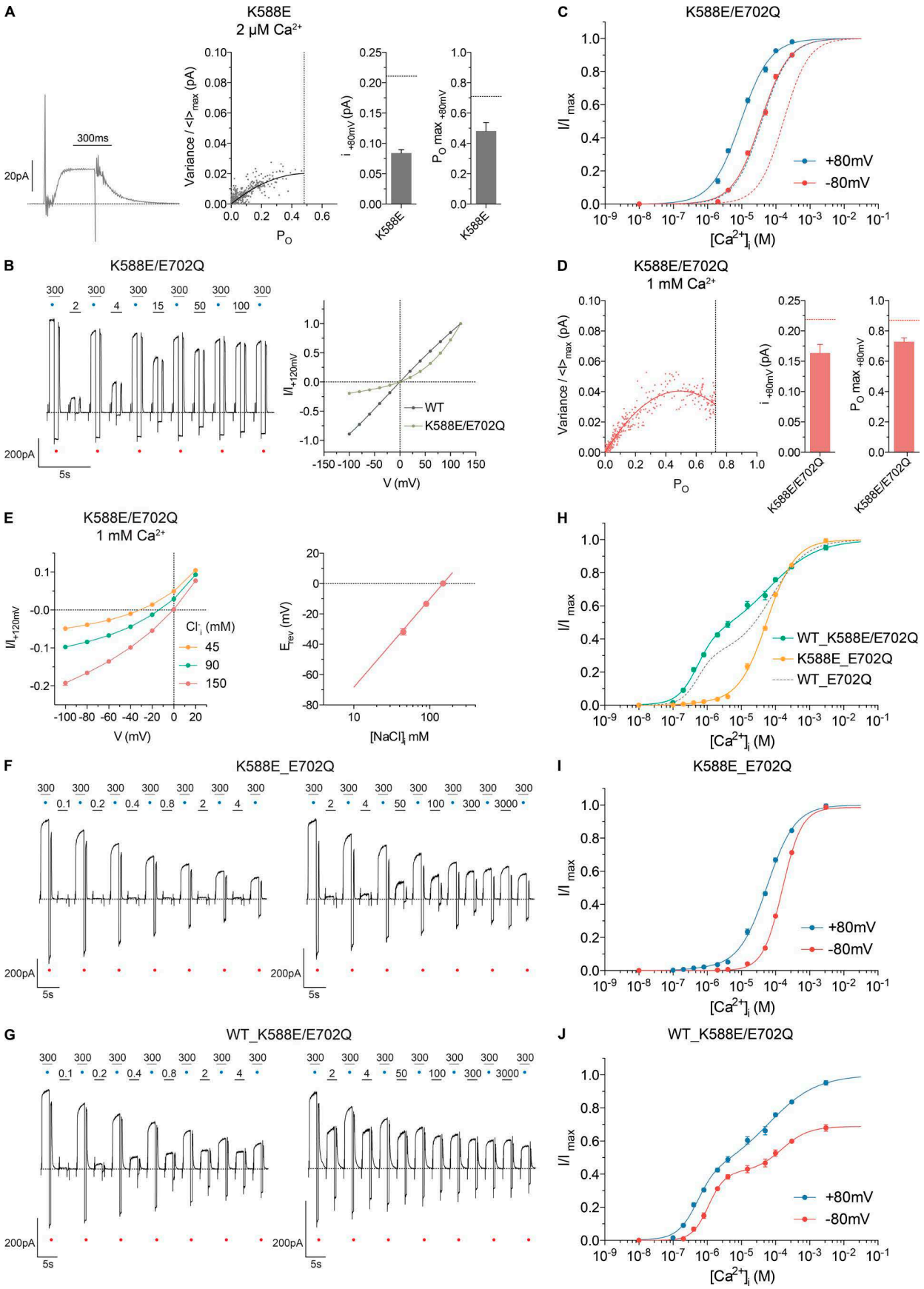

Downloaded from on November 10, 2016

Published October 17, 2016

prepared two chimeric constructs, one where we have introduced the mutation K588E in the WT subunit (K588E_E702Q) and another where we have introduced the mutation in the E702Q subunit (WT_K588E/E702Q). When studying the activation properties of the two concatemers (Fig. 7, F and G), both constructs show a phenotype that is consistent with the behavior of the involved subunits. In K588E_E702Q, the magnitude of the first activation at low Ca^{2+} concentration is small (accounting for 1.5% of the maximum response), consistent with the low currents observed in K588E, whereas the second, much larger activation step proceeds with a similar EC_{50} and Hill slope as expected for E702Q (Fig. 7 G and Table 1). In the mutant WT_K588E/E702Q, activation of both subunits proceeds with the expected Ca^{2+} dependence, but the second activation step in this case accounts for ∼60% of the maximum currents compared with the ∼70% in WT_E702Q when fitted to a biphasic Hill equation (Fig. 7 H and Table 1). This fraction decreases further when taking the biphasic activation of WT into account. In each of the two constructs, both activation steps have retained their voltage dependence, but because of the strong outward rectification of the currents mediated by the subunit containing the K588E mutation, the relative contribution of the K588E-containing subunit to the total current decreases at negative voltages (Fig. 7, I and J; and Table 1). This causes the first component to disappear in K588E_E702Q (Fig. 7 I) and to increase in WT_K588E/E702Q (Fig. 7 J). Our data thus demonstrate that, besides the activation by Ca^{2+}, the functional independence also extends to the conduction properties of the two ion permeation pores.

DISCUSSION

In our study, we have investigated the question of whether TMEM16A contains two separate ion conduction pores that are independently activated by Ca^{2+}. This question was motivated by the structure of nhTMEM16, a family member that works as lipid scramblase and contains two putative sites of catalysis on the opposite ends of a dimeric protein (Fig. 1; Brunner et al., 2014, 2016). We have initially studied the properties of WT in a broad range of Ca^{2+} concentrations and found a biphasic opening with a larger component at submicromolar and a second, smaller component, at low millimolar concentrations. The first activation step was described previously (Arreola et al., 1996; Kuruma and Hartzell, 2000). It is cooperative, voltage dependent, and likely accounts for the binding of Ca^{2+} to a site buried within the membrane domain that was identified in the structure of nhTMEM16 (Fig. 8; Brunner et al., 2014). The second activation lacks any voltage dependence and might thus reflect the interaction of Ca^{2+} with an unknown low-affinity site located at the cytoplasmic part of the channel. Because of its low apparent affinity, it is unlikely that the second activation plays a functional role in the physiological context, but it is important for the investigation of heterodimers with different activation properties described in this study. Our results suggest that exposure to 1 mM Ca^{2+} did not change the high anion over cation selectivity of the channel, nor its conductance, but that it results from an increase in the open probability (Fig. 3, C and D). This argues against a proposed transition into a different conducting conformation at high Ca^{2+} concentrations (Kuruma and Hartzell, 2000; Schroeder et al., 2008).

The investigation of a concatenated channel containing two WT subunits showed very similar properties, underlining that the covalent linkage did not strongly affect channel function (Fig. 4). By investigating the properties of concatenated dimers containing subunits with distinct activation and ion conduction properties, we could demonstrate that both subunits act independently with respect to their ion permeation and gat-

Downloaded from on November 10, 2016

Figure 7. **Functional properties of the K588E_E702Q and the WT_K588E/E702Q concatemers.** (A) Merged and averaged variance-<I> plot and pooled data (n = 5) of the K588E mutant obtained at 2 µM $[Ca^{2+}]_{free}$ at 80 mV. (B, left) Representative currents of the K588E/E702Q double mutant at 80 and −80 mV. (right) I-V plots recorded at symmetrical 150 mM NaCl for WT (n = 8) and the K588E/E702Q double mutant (n = 13) at 1 mM $[Ca^{2+}]_{free}$. (C) Rundown-corrected concentration–response relations of the K588E/E702Q double mutant at 80 and −80 mV (n = 10 for each data point). Solid lines are the best fit to the Hill equation. Dashed lines indicate the relations of E702Q at 80 and −80 mV. (D) Merged and averaged variance-<I> plot and pooled data (n = 9) of the K588E/E702Q double mutant obtained at 1 mM $[Ca^{2+}]_{free}$ at 80 mV. (A [middle] and D [left]) The dotted lines indicate the mean $P_{O\,max}$ across patches. (A and D, right) Dotted lines indicate the corresponding value of WT mTMEM16A. (E) Na^+ versus Cl^- selectivity of the K588E/E702Q double mutant. (left) I-V plots recorded at 150 mM extracellular and the indicated intracellular NaCl concentrations at 1 mM (n = 7–13) $[Ca^{2+}]_{free}$. (right) Relation between intracellular [NaCl] and E_{rev} at 1 mM (n = 7–13) $[Ca^{2+}]_{free}$. The line indicates the Nernst potentials of Cl^-. (F) Representative currents of the K588E_E702Q concatemer at 80 and −80 mV. (G) Representative currents of the WT_K588E/E702Q concatemer at 80 and −80 mV. (B, F, and G) Blue and red dots indicate the reference pulses used for rundown correction at 80 and −80 mV, respectively (see Materials and methods). (H) Rundown-corrected concentration–response relation of the K588E_E702Q (n = 7–19 for each data point) and WT_K588E/E702Q (n = 10–21 for each data point) concatemer at 80 mV. Solid lines are the best fit to a biphasic Hill equation. Dashed line indicates the relation of the WT_E702Q concatemer at 80 mV. (I) Rundown-corrected concentration–response relations of the K588E_E702Q concatemer at 80 and −80 mV (n = 7–19 for each data point). Lines are the best fit to biphasic (80 mV) and monophasic (−80 mV) equations. (J) Rundown-corrected concentration–response relations of the WT_K588E/E702Q concatemer at 80 and −80 mV (n = 10–21 for each data point). Lines are the best fit to a biphasic Hill equation. In A–E and H–J, data are presented as mean and errors as SEM.

Published October 17, 2016

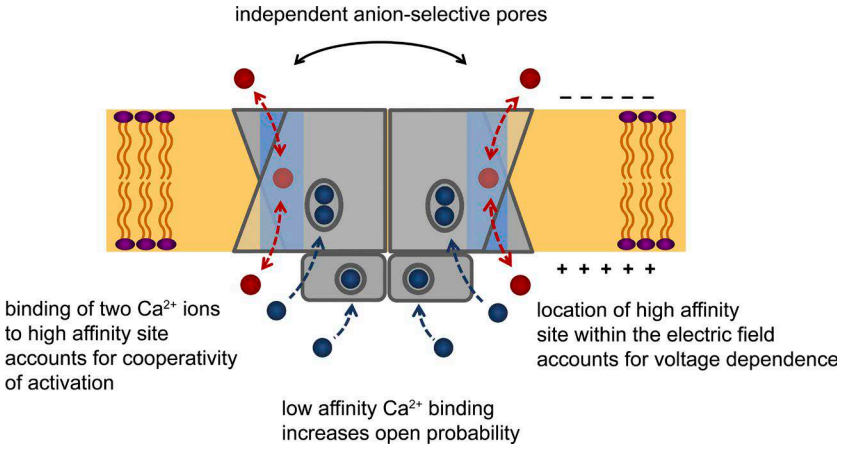

Figure 8. **Properties of TMEM16A.** Scheme summarizing the functional properties of TMEM16A. Ion conduction pores in the dimeric protein are indicated in light blue, Ca^{2+} is displayed as dark blue, and Cl^- is displayed as red spheres.

ing characteristics. We show that Ca^{2+} activates the WT subunit in a concatemer containing a second subunit with strongly impaired activation in a biphasic manner with similar potency and cooperativity as WT (Fig. 5). This implies that the biphasic opening is a property of the single subunit, and it suggests that the mutated subunit does not appreciably contribute to the currents induced at high Ca^{2+} concentrations. The cooperativity of the first transition underlines that the binding of the ligand to sites located within each subunit accounts for pore opening and that this process involves more than a single ion (Fig. 8). Our findings are thus consistent with the structure of nhTMEM16 where each binding site coordinates two Ca^{2+} ions (Brunner et al., 2014). The unchanged voltage dependence of Ca^{2+} activation in this construct supports the hypothesis that this phenomenon originates from the localization of the binding site within the transmembrane electric field (Brunner et al., 2014). Finally, the unaltered anion selectivity and conductance of the construct containing only a single activatable subunit provides additional evidence for the spatial separation of both pores. Functional independence is also supported by experiments on constructs where two subunits show different potency of activation and where each activation step retains the signature of the nonconcatenated counterparts. This is the case for a concatenated channel containing a mutation in the Ca^{2+}-binding site of one subunit that results in a more than 100-fold decrease in potency, and it extends to similar constructs containing an additional mutation that affects the ion conduction properties of the channel. Our data thus strongly suggest that, similar to the ClC family (Ludewig et al., 1996; Middleton et al., 1996; Dutzler et al., 2002, 2003), the dimeric TMEM16A channel contains two separate ion conduction pores. Similar to the fast gating of the channel CLC-0, the activation of a single pore is to a large degree independent, although we cannot exclude weak cross-talk between subunits, which might have escaped our detection.

The functional independence of both pores underlines the assumption that the nhTMEM16 structure displays the general architecture for both functional branches of the family (Fig. 1). In this respect, questions addressing the molecular features that distinguish scramblases from channels become even more important. Recently, it was shown that lipid scrambling could be conferred to TMEM16A by replacing a short stretch of amino acids of the protein lining the intracellular entrance of the subunit cavity by its equivalent sequence of the scramblase TMEM16F (Yu et al., 2015). This implies that the CaCCs of the TMEM16 family might have evolved from ancestral scramblases and that, different from other ion channel families, part of the ion conduction pore of TMEM16A may be lined by lipids (Whitlock and Hartzell, 2016). It is thus remarkable that such an unconventional ion channel has gained a central role in many physiologically relevant processes, which are otherwise mediated by proteins that have evolved for conducting ions from the outset of their functional emergence.

ACKNOWLEDGMENTS

We thank Janine D. Brunner and S. Schenck for advice in the generation of the concatemeric construct and protein expression and all members of the Dutzler laboratory for help in all stages of the project.

The research was supported by a grant from the European Research Council (no. 339116, AnoBest).

The authors declare no competing financial interests.

Author contributions: N.K. Lim initiated the project, constructed the chimeric constructs, and performed biochemistry experiments. N.K. Lim and A.K.M. Lam jointly recorded the data. A.K.M. Lam performed noise analysis. N.K. Lim, A.K.M. Lam, and R. Dutzler analyzed the data and wrote the manuscript.

Merritt Maduke served as editor.

Submitted: 21 June 2016
Accepted: 28 September 2016

REFERENCES

Arreola, J., J.E. Melvin, and T. Begenisich. 1996. Activation of calcium-dependent chloride channels in rat parotid acinar cells. *J. Gen. Physiol.* 108:35–47. http://dx.doi.org/10.1085/jgp.108.1.35

Downloaded from on November 10, 2016

Published October 17, 2016

Brunner, J.D., N.K. Lim, S. Schenck, A. Duerst, and R. Dutzler. 2014. X-ray structure of a calcium-activated TMEM16 lipid scramblase. *Nature.* 516:207–212. http://dx.doi.org/10.1038/nature13984

Brunner, J.D., S. Schenck, and R. Dutzler. 2016. Structural basis for phospholipid scrambling in the TMEM16 family. *Curr. Opin. Struct. Biol.* 39:61–70. http://dx.doi.org/10.1016/j.sbi.2016.05.020

Caputo, A., E. Caci, L. Ferrera, N. Pedemonte, C. Barsanti, E. Sondo, U. Pfeffer, R. Ravazzolo, O. Zegarra-Moran, and L.J. Galietta. 2008. TMEM16A, a membrane protein associated with calcium-dependent chloride channel activity. *Science.* 322:590–594. http://dx.doi.org/10.1126/science.1163518

Chen, C., and H. Okayama. 1987. High-efficiency transformation of mammalian cells by plasmid DNA. *Mol. Cell. Biol.* 7:2745–2752. http://dx.doi.org/10.1128/MCB.7.8.2745

Chen, M.F., and T.Y. Chen. 2003. Side-chain charge effects and conductance determinants in the pore of ClC-0 chloride channels. *J. Gen. Physiol.* 122:133–145. http://dx.doi.org/10.1085/jgp.200308844

Doyle, D.A., J. Morais Cabral, R.A. Pfuetzner, A. Kuo, J.M. Gulbis, S.L. Cohen, B.T. Chait, and R. MacKinnon. 1998. The structure of the potassium channel: molecular basis of K^+ conduction and selectivity. *Science.* 280:69–77. http://dx.doi.org/10.1126/science.280.5360.69

Dutzler, R., E.B. Campbell, M. Cadene, B.T. Chait, and R. MacKinnon. 2002. X-ray structure of a ClC chloride channel at 3.0 Å reveals the molecular basis of anion selectivity. *Nature.* 415:287–294. http://dx.doi.org/10.1038/415287a

Dutzler, R., E.B. Campbell, and R. MacKinnon. 2003. Gating the selectivity filter in ClC chloride channels. *Science.* 300:108–112. http://dx.doi.org/10.1126/science.1082708

Ferrera, L., A. Caputo, I. Ubby, E. Bussani, O. Zegarra-Moran, R. Ravazzolo, F. Pagani, and L.J. Galietta. 2009. Regulation of TMEM16A chloride channel properties by alternative splicing. *J. Biol. Chem.* 284:33360–33368. http://dx.doi.org/10.1074/jbc.M109.046607

Geertsma, E.R., and R. Dutzler. 2011. A versatile and efficient high-throughput cloning tool for structural biology. *Biochemistry.* 50:3272–3278. http://dx.doi.org/10.1021/bi200178z

Hamill, O.P., A. Marty, E. Neher, B. Sakmann, and F.J. Sigworth. 1981. Improved patch-clamp techniques for high-resolution current recording from cells and cell-free membrane patches. *Pflugers Arch.* 391:85–100. http://dx.doi.org/10.1007/BF00656997

Hartzell, C., I. Putzier, and J. Arreola. 2005. Calcium-activated chloride channels. *Annu. Rev. Physiol.* 67:719–758. http://dx.doi.org/10.1146/annurev.physiol.67.032003.154341

Heinemann, S.H., and F. Conti. 1992. Nonstationary noise analysis and application to patch clamp recordings. *Methods Enzymol.* 207:131–148. http://dx.doi.org/10.1016/0076-6879(92)07009-D

Huang, F., X. Wong, and L.Y. Jan. 2012. International Union of Basic and Clinical Pharmacology. LXXXV: Calcium-activated chloride channels. *Pharmacol. Rev.* 64:1–15. http://dx.doi.org/10.1124/pr.111.005009

Jeng, G., M. Aggarwal, W.-P. Yu, and T.-Y. Chen. 2016. Independent activation of distinct pores in dimeric TMEM16A channels. *J. Gen. Physiol.* http://dx.doi.org/10.1085/jgp.201611651

Kunzelmann, K., P. Kongsuphol, F. Aldehni, Y. Tian, J. Ousingsawat, R. Warth, and R. Schreiber. 2009. Bestrophin and TMEM16-Ca^{2+} activated Cl^- channels with different functions. *Cell Calcium.* 46:233–241. http://dx.doi.org/10.1016/j.ceca.2009.09.003

Kuruma, A., and H.C. Hartzell. 2000. Bimodal control of a Ca^{2+}-activated Cl^- channel by different Ca^{2+} signals. *J. Gen. Physiol.* 115:59–80. http://dx.doi.org/10.1085/jgp.115.1.59

Ludewig, U., M. Pusch, and T.J. Jentsch. 1996. Two physically distinct pores in the dimeric ClC-0 chloride channel. *Nature.* 383:340–343. http://dx.doi.org/10.1038/383340a0

Malvezzi, M., M. Chalat, R. Janjusevic, A. Picollo, H. Terashima, A.K. Menon, and A. Accardi. 2013. Ca^{2+}-dependent phospholipid scrambling by a reconstituted TMEM16 ion channel. *Nat. Commun.* 4:2367. http://dx.doi.org/10.1038/ncomms3367

Middleton, R.E., D.J. Pheasant, and C. Miller. 1996. Homodimeric architecture of a ClC-type chloride ion channel. *Nature.* 383:337–340. http://dx.doi.org/10.1038/383337a0

Miller, C. 1982. Open-state substructure of single chloride channels from Torpedo electroplax. *Philos. Trans. R. Soc. Lond. B Biol. Sci.* 299:401–411. http://dx.doi.org/10.1098/rstb.1982.0140

Miyazawa, A., Y. Fujiyoshi, and N. Unwin. 2003. Structure and gating mechanism of the acetylcholine receptor pore. *Nature.* 423:949–955. http://dx.doi.org/10.1038/nature01748

Ni, Y.L., A.S. Kuan, and T.Y. Chen. 2014. Activation and inhibition of TMEM16A calcium-activated chloride channels. *PLoS One.* 9:e86734. http://dx.doi.org/10.1371/journal.pone.0086734

Pedemonte, N., and L.J. Galietta. 2014. Structure and function of TMEM16 proteins (anoctamins). *Physiol. Rev.* 94:419–459. http://dx.doi.org/10.1152/physrev.00039.2011

Peters, C.J., H. Yu, J. Tien, Y.N. Jan, M. Li, and L.Y. Jan. 2015. Four basic residues critical for the ion selectivity and pore blocker sensitivity of TMEM16A calcium-activated chloride channels. *Proc. Natl. Acad. Sci. USA.* 112:3547–3552. http://dx.doi.org/10.1073/pnas.1502291112

Picollo, A., M. Malvezzi, and A. Accardi. 2015. TMEM16 proteins: unknown structure and confusing functions. *J. Mol. Biol.* 427:94–105. http://dx.doi.org/10.1016/j.jmb.2014.09.028

Portolano, N., P.J. Watson, L. Fairall, C.J. Millard, C.P. Milano, Y. Song, S.M. Cowley, and J.W. Schwabe. 2014. Recombinant protein expression for structural biology in HEK 293F suspension cells: a novel and accessible approach. *J. Vis. Exp.* (92):e51897.

Qu, Z., and H.C. Hartzell. 2000. Anion permeation in Ca^{2+}-activated Cl^- channels. *J. Gen. Physiol.* 116:825–844. http://dx.doi.org/10.1085/jgp.116.6.825

Schroeder, B.C., T. Cheng, Y.N. Jan, and L.Y. Jan. 2008. Expression cloning of TMEM16A as a calcium-activated chloride channel subunit. *Cell.* 134:1019–1029. http://dx.doi.org/10.1016/j.cell.2008.09.003

Sigworth, F.J. 1980. The variance of sodium current fluctuations at the node of Ranvier. *J. Physiol.* 307:97–129. http://dx.doi.org/10.1113/jphysiol.1980.sp013426

Suzuki, J., M. Umeda, P.J. Sims, and S. Nagata. 2010. Calcium-dependent phospholipid scrambling by TMEM16F. *Nature.* 468:834–838. http://dx.doi.org/10.1038/nature09583

Suzuki, J., T. Fujii, T. Imao, K. Ishihara, H. Kuba, and S. Nagata. 2013. Calcium-dependent phospholipid scramblase activity of TMEM16 protein family members. *J. Biol. Chem.* 288:13305–13316. http://dx.doi.org/10.1074/jbc.M113.457937

Ta, C.M., A. Adomaviciene, N.J. Rorsman, H. Garnett, and P. Tammaro. 2016. Mechanism of allosteric activation of TMEM16A/ANO1 channels by a commonly used chloride channel blocker. *Br. J. Pharmacol.* 173:511–528. http://dx.doi.org/10.1111/bph.13381

Terashima, H., A. Picollo, and A. Accardi. 2013. Purified TMEM16A is sufficient to form Ca^{2+}-activated Cl^- channels. *Proc. Natl. Acad. Sci. USA.* 110:19354–19359. http://dx.doi.org/10.1073/pnas.1312014110

Tien, J., C.J. Peters, X.M. Wong, T. Cheng, Y.N. Jan, L.Y. Jan, and H. Yang. 2014. A comprehensive search for calcium binding sites critical for TMEM16A calcium-activated chloride channel activity. *eLife.* 3:e02772. http://dx.doi.org/10.7554/eLife.02772

Whitlock, J.M., and H.C. Hartzell. 2016. A Pore Idea: the ion conduction pathway of TMEM16/ANO proteins is composed partly of lipid. *Pflugers Arch.* 468:455–473. http://dx.doi.org/10.1007/s00424-015-1777-2

Downloaded from on November 10, 2016

Published October 17, 2016

Xiao, Q., K. Yu, P. Perez-Cornejo, Y. Cui, J. Arreola, and H.C. Hartzell. 2011. Voltage- and calcium-dependent gating of TMEM16A/Ano1 chloride channels are physically coupled by the first intracellular loop. *Proc. Natl. Acad. Sci. USA*. 108:8891–8896. http://dx.doi.org/10.1073/pnas.1102147108

Yang, H., A. Kim, T. David, D. Palmer, T. Jin, J. Tien, F. Huang, T. Cheng, S.R. Coughlin, Y.N. Jan, and L.Y. Jan. 2012. TMEM16F forms a Ca^{2+}-activated cation channel required for lipid scrambling in platelets during blood coagulation. *Cell*. 151:111–122. http://dx.doi.org/10.1016/j.cell.2012.07.036

Yang, Y.D., H. Cho, J.Y. Koo, M.H. Tak, Y. Cho, W.S. Shim, S.P. Park, J. Lee, B. Lee, B.M. Kim, et al. 2008. TMEM16A confers receptor-activated calcium-dependent chloride conductance. *Nature*. 455:1210–1215. http://dx.doi.org/10.1038/nature07313

Yu, K., C. Duran, Z. Qu, Y.Y. Cui, and H.C. Hartzell. 2012. Explaining calcium-dependent gating of anoctamin-1 chloride channels requires a revised topology. *Circ. Res.* 110:990–999. http://dx.doi.org/10.1161/CIRCRESAHA.112.264440

Yu, K., J.M. Whitlock, K. Lee, E.A. Ortlund, Y.Y. Cui, and H.C. Hartzell. 2015. Identification of a lipid scrambling domain in ANO6/TMEM16F. *eLife*. 4:e06901. http://dx.doi.org/10.7554/eLife.06901

Downloaded from on November 10, 2016

3. Method

Blast Search

The murine TMEM16A protein (mTMEM16A) sequence obtained from the Uniprot K database was used as a query in the basic local alignment tool (104)(Blastp, http://blast.ncbi.nlm.nih.gov/Blast.cgi) applying standard settings to identify homologous genes from different eukaryotic kingdoms. Around 60 genes were thereafter obtained as cDNAs (from ImaGenes) or as synthetic genes (from GenScript).

Cloning

Genes that were available as cDNA clones were purchased from Imagene.com (now Source Bioscience) or Origene. Genes that did not contain any introns were cloned by Stephan Schenck from genomic DNA if the organism was available from DSMZ, the German Collection of Microorganisms and Cell Cultures (*Aspergillus nidulans, Kluyveromyces lactis, Lachancea thermotolerans, Neurospora crassa, Pichia pastoris*, *Saccharomyces cerevisiae*, *Schizosaccharomyces pombe* and *Ustilago maydis*). Any othergenes were synthesized by GenScript without codon optimization.

The genes were modified by standard PCR procedure recommended for Phusion polymerase (Thermo Scientific Finnzymes or NEB) with addition of 3% DMSO (v/v). The PCR products were separated on a 1% agarose gel. DNA bands of the expected size were cut out and purified with High Pure PCR Product Purification Kit (Roche). PCR primers were designed to contain flanking *SapI* sites upstream (5'TATATAGCTCTTCTAGT3') and downstream (5'GCATGAAGAGCTAATA3') of the coding sequence to make them compatible for *SapI*-dependent FX sub-cloning method (111). The expression vectors were modified to be compatible with FX-cloning. PCR products were cloned into the intermediate sequencing vector, pINITIAL. In brief, 50 ng vector was mixed with purified PCR product at a molar ratio of 1:5 and digested with SapI for 1 h at 37 °C. The reaction was incubated for 20 min at 65 °C to heat-inactivate the restriction enzyme. For ligation ATP and T4 ligase were added to the reaction and incubated for 1h at RT. Prior to transformation into chemo-competent *E.coli* MC1061 (112). The ligase was heat inactivated by a 20 min incubation step at 65 °C. Gene in pINITIAL could be subcloned into any FX-compatible expression vector with similar protocol.

For expression in *S. cerevisiae*, the genes were subcloned into a modified pYES2/CT plasmid (Life technologies) as N –terminal and C-terminal fusion to a cassette encoding enhanced GFP (eGFP), preceded by a His10-tag and followed by a HRV-3C cleavage site. For expression and electrophysiology in HEK tsA201 cells, the a, c splice variant of mTMEM16A (113) was cloned into a modified pcDNA3.1 vector (Invitrogen), bearing a 5' UTR of hVEGF (from pcDNA4/HisMax, Invitrogen) bearing a 5' untranslated region (UTR) of hVEGF (from pcDNA4/HisMax, Invitrogen) upstream of the start codon and a 3' C-terminus encoding a Venus-yellow fluorescent protein (YFP) (114), a Myc-tag and a Streptavidin Binding Peptide (SBP) tag downstream of the open reading frame. Mutations were made using PCR-based Quikchange mutagenesis (Qiagen).

In the concatemeric constructs, the two monomers were joined by a 31 amino-acid long Gly-Ser linker with sequence GSSGGSGGSGSSGSSGSGSSGGSGGSGSSGS. The two subunits were separately amplified

by PCR. The first half of the linker was introduced with the reverse primer of the first subunit and the second half with the forward primer of the second subunit. (Forward primer of the first subunit: ATATATGCTCTTCTAGTAGGGTCCCCGAGAAGTACTCGACG; reversed primer of the first subunit: TTATAGCTCTTCATCCACTAGAGCCTGAACTGCCTGATCCACCACTAC
CTCCGCTCGAGCCCAGCGCGTCCCCATGGTACTCGTA; Forward primer of second subunit: TTATAGCTCTTCAGGAAGTGGTTCGAGTGGAGGTAGTGGTGGATCAGGTT
CAAGTGGATCCAGGGTCCCCGAGAAGTACTCGACG; reversed primer of the second subunit: TATATAGCTCTTCATGCCAGCGCGTCCCCATGGTACTCGTA). All constructs were confirmed by sequencing.

Protein expression

For expression in mammalian cells, tsA201 cells (Cat # 96121229, Sigma-Aldrich) with a confluency of 40-60% were transfected with plasmid DNA containing the respective genes as described [322], except that the transfection buffer was prepared with 2.8 mM Na2HPO4. Expression was carried out in 10 cm dishes (10 ml, Corning) at 37 °C and 2.2% CO2 for 1–2 days. For small scale expression screening only 1-2 dishes per construct were needed. The expression level and the cellular localization of Venus-YFP tagged proteins was monitored by fluorescence microscopy.

Expression in yeast

The pYES2/CT vectors carrying the respective full-length genes were transformed into *S. cerevisiae* FGY217 cells carrying an URA deletion for positive selection as described in Gietz et al. (115). The Expression screening in yeast was adapted from Drew 2008 (106). The culture medium is composed of 6.7 g/l yeast nitrogen base without amino acids (Sigma) supplemented with 1.92 g/l Synthetic Complete drop-out medium without URA (Formedium) and 10 mg/l Ampicilin.

For small-scale expression screening, 5 ml inoculum cultures containing 2% glucose were grown overnight at 30°C in shaking incubator and used the following day to inoculate 50 ml expression media containing 0.1% glucose to starting OD600 of 0.12. The expression culture were grown at 30 °C until OD600 0.8-1.0. Protein expression was induced with 2% galactose for 40 h at 25 °C.

For medium scale expression, 5-10 l of culture were grown in 2 l baffled flasks containing 600 ml expression media. 50 ml inocolum culture were grown overnight and added into expression media to OD600 of 0.12. For large scale expression of over 10 l, culture is grown in 19 l or 30 l fermenter (Bioengineering). Appropriate volume of distilled water was previously autoclaved before 10 x concentrated expression media was added. The media was inoculated to starting OD600 of 0.15. Stirring was set to 350rpm with 1 bar, 5l/min aeration. Induction condition is identical to that for small-scale expression.

Homologue screening

Cells were harvested at an OD600 of 4.5-6 and resuspended to an OD600 of 60 in resuspension buffer A (20 mM HEPES pH7.4, 150 mM NaCl) containing 0.5 mM $CaCl_2$, , 1x protease inhibitors cocktail (Complete, Roche). 100 µl sample was taken for fluorescence measurement (excitation 480 nm, emission 515 nm). 2 x 550 µl per construct were transferred into Eppendorf 2ml conical bottomed tubes that were loaded with approximately 500 mg glass beads (425-600 µm size, Sigma). The cells

were lysed in a FastPrep-24 (MP Biomedicals) with the settings 5 x 40 s at 6 M/s. A 30 s spin at 10,000 g separated the glass beads and cell debris from the supernatant containing the membranes. 700 µl of the combined supernatant were transferred into a Snap-On Cap tube (Beckman Coulter) and centrifuged at 150,000 g for 45 mins in TLA-100.3 rotor (Beckman Coulter). The Supernatant was removed and the membrane were frozen in liquid nitrogen for storage at -80 °C.

Membranes were resuspended in 140 µl buffer A and solubilized with 2% 1% *n*-dodecyl-β-d-maltopyranoside (DDM) at 4 °C for 90 mins. 100 µl of post-solubilization sample were measured for fluorescence as total fluorescence reading and repooled. 30 µl sample were taken for SDS PAGE. 130 µl sample was centrifuged at 150,000 g for 30 min (TLA-100 rotor) to remove unsolubilised material. 100ul supernatant were measured for fluorescence again as the fluorescence reading of solubilized fraction. 30 µl SDS PAGE sample was collected to analyse the solubilized fraction. 50 µl were run on a size exclusion column Zorbax GF 450 (Agilent) on Agilent 1200 Series HPLC (Agilent) in buffer A containing 0.03% DDM (w/v). FSEC was performed by measuring GFP fluorescence.

In-gel fluorescence

Directly after SDS-PAGE, in-gel fluorescence was detected for GFP-fusion proteins with a Fujifilm LAS-3000 imaging system (Fujifilm Super CCD camera, 460 nm EPI blue light, Y515AttoPhos Filter, Iris F2.8).

Western blotting

Proteins from SDS gel were transferred onto a PVDF membrane (PVDF membranes were pre-soaked in methanol) by semi-dry electrophoretic transfer (BioRad Transblot SD, 50 min, 15 V). The filter paper was pre-soaked for 10 minutes in pre-chilled transfer buffer (25 mM Tris, 192 mM glycine, pH 8.3, 20% methanol). After transfer, PVDF membranes were blocked for 1h at RT with 5% (w/v) milk powder in phosphate buffered saline with 0.1% Tween (v/v) (PBST) and then incubated with an anti-polyhistidine antibody (Roche 11965985001, 1:1000 (v/v)) in PBST containing 1% milk powder. The blots were developed with Immobilion Western chemiluminescent HRP substrate (Millipore) and imaged with a Fujifilm LAS-3000 imaging system (Fujifilm Super CCD camera).

Membrane isolation and Protein purification from medium/large scale expression

After 40 hour of induction, cells were harvested by centrifugation and resuspended in buffer A (50 mM HEPES pH 7.4, 150 mM NaCl) containing 0.5 mM $CaCl_2$, protease inhibitors (Complete, Roche), DNase I, and 1 mM $MgCl_2$ and lysed in a custom-made pressure-based cell disruptor at 40,000 p.s.i. Cell debris was removed by low-spin centrifugation. Membranes were harvested by ultracentrifugation with a 45 TI rotor (Beckmann) at 40,000 r.p.m. for 1.5 h. All steps were carried out on ice or at 4 °C. Protein was extracted in buffer A containing 0.5 mM $CaCl_2$, 1% *n*-dodecyl-β-d-maltopyranoside (DDM, Anatrace) and protease inhibitors (Roche) for 1.5 h. Insoluble parts were removed by centrifugation for 30 min at 40,000 rpm. with a 45 TI rotor (Beckmann). After addition of 15 mM imidazole the protein was bound in batch to NiNTA for 1.5 h, washed with buffer B (10 mM HEPES pH 7.6, 150 mM NaCl, 5% glycerol, 0.025% DDM) containing 5 mM $CaCl_2$ and 50 mM imidazole and eluted in buffer B containing 5 mM $CaCl_2$ and 400 mM imidazole. The eluted fraction was cleaved with HRV 3C protease for 2 h and dialysed against buffer B containing 5 mM $CaCl_2$. The GFP–10xHis fragment was removed by binding to NiNTA resin, the flow-through was concentrated with 100 kDa molecular weight cutoff (MWCO) (Amicon) and applied to a Superdex 200 column (GE healthcare) equilibrated in buffer C (5 mM HEPES

pH 7.6, 150 mM NaCl, 0.025% DDM) containing 3 mM $CaCl_2$. Fractions from the eluted peak corresponding to the elution volume of dimeric protein were pooled and concentrated with 100 kDa MWCO concentrator to 5-10 mg/ml for crystallization trials.

SEC-MALS

Purified nhTMEM16 samples were subjected to size exclusion chromatography on Superdex 200 10/300 GL column and ÄKTA Explorer purification system (GE Healthcare) coupled with a tri-angle light scattering detector (miniDAWN Tristar, Wyatt Technology) and a differential refractometer (Optilab, Wyatt Technology). The running buffer contained 10 mM HEPES pH 7.4, 150 mM NaCl, 2 mM $CaCl_2$, 0.03% DDM (w/v). In order to match the exact composition of the running buffer and the sample buffer, an excess of the running buffer was prepared earlier and the same batch was used during the gel filtration purification step of the protein.

The sample was injected at 1 mg/ml concentration at a flow rate of 0.5 ml/min. 1 mg/ml bovine serum albumin (Sigma-Aldrich) filtered through a 0.22 µm filter was used as a standard. The data were recorded and processed with ASTRA V software (Wyatt Technology). A specific refractive index increment (dn/dc) value of 0.186 ml/g for the protein and 0.1435 ml/g for the DDM detergent were used in the analysis.

Solutions for electrophysiology

Stock Ca-EGTA solution contained 150 mM NaCl, 5.99 mM $Ca(OH)_2$, 5 mM EGTA, and 10 mM HEPES, pH 7.40. Stock EGTA solution contained 150 mM NaCl, 5 mM EGTA, and 10 mM HEPES, pH 7.40. The pH was adjusted using 1 M NMDG-OH solution. The stock Ca-EGTA solution contained a free $[Ca^{2+}]$ of 1 mM. Free $[Ca^{2+}]$ was adjusted by mixing stock Ca-EGTA and EGTA solutions at the ratio calculated according to the WEBMAXC calculator (http://web.stanford.edu/~cpatton/webmaxcS.htm). Free $[Ca^{2+}]$ above 1 mM (up to 3 mM) was adjusted by adding $CaCl_2$ from a 1 M stock solution. The pipette solution (extracellular) had the same ionic composition: 150 mM NaCl and 10 mM HEPES, pH 7.40, and a Ca/EGTA ratio corresponding to free $[Ca^{2+}]$ of 1 µM prepared from the same Ca-EGTA stock solutions. For permeability experiments, NaCl concentrations (with and without Ca^{2+}) were adjusted by mixing NaCl stock solutions and $(NMDG)_2SO_4$ stock solutions at the required ratios. Stock NaCl solutions were the same as above. Stock $(NMDG)_2SO_4$ solutions contained 100 mM $(NMDG)_2SO_4$, 5.99 mM $Ca(OH)_2$, 5 mM EGTA, 10 mM HEPES, pH 7.40, and 100 mM $(NMDG)_2SO_4$, 5 mM EGTA, and 10 mM HEPES, pH 7.40. In experiments that compare the effect of substitution with $(NMDG)_2SO_4$ or sucrose, the sucrose-based solution had 15 mM NaCl, 280 mM sucrose, and 10 mM HEPES, pH 7.40, with the corresponding Ca-EGTA ratios. In some permeability experiments, the pipette solution had 1 mM $[Ca^{2+}]_{free}$ instead of 1 µM to improve patch stability. We observed no change in ion selectivity in 1 µM and 1 mM $[Ca^{2+}]_{free}$ pipette solutions.

Electrophysiology

All recordings were performed in the inside-out configuration (116). Inside-out patches were pulled from HEK293T cells expressing the mTMEM16A construct of interest after the formation of a gigaohm seal. Seal resistance was typically 4–8 GΩ or higher. Recording pipettes were pulled from borosilicate glass capillaries (OD 1.5 mm, ID 0.86 mm; Harvard apparatus or Sutter) and were fire-polished using a microforge (Narishige). Pipette resistance was typically 5–8 MΩ when filled with recording solutions. Voltage-clamp recordings were performed using the Axopatch 200B amplifier controlled by the

Clampex 10.6 software through Digidata 1550 (Molecular Devices). For general recordings, raw signals were analogue-filtered through the inbuilt low-pass 4-pole Bessel filter at 5 kHz and were sampled at 10 kHz or higher. For noise analysis, raw signals were low-pass analogue-filtered at 10 kHz with the inbuilt Bessel filter and were sampled at 100 kHz. Liquid junction potential was not corrected. Solution exchange was performed using a theta glass pipette mounted on a high-speed piezo switcher (Siskiyou). Step-like solution exchange was elicited by analogue voltage signals delivered through Digidata 1550. All recordings were performed in symmetrical NaCl solutions except for permeability experiments where the NaCl concentration on the intracellular side was varied (see solution composition). Concentration–response and noise analysis experiments were performed at 80 mV unless specified otherwise. Data were background-subtracted before analysis (background current was obtained by recording in the corresponding 0 Ca^{2+} solution). All experiments were performed at 20°C.

4. Discussion

Although the central roles of CaCCs in various physiological processes have been well documented, very little was known about the molecular mechanisms underlying its regulation and activation due to the unknown molecular identity until almost a decade ago. When I started on this project in late 2010, the discovery of TMEM16 as the protein family coding for CaCCs has just opened up many avenues of research and plenty of novel insights were gained in the following couple of years. However, the unexpected discovery in 2012 that some TMEM16 family members could function as scramblases emphasized the fact that much is still unknown about this protein family. A big bottleneck was the lack of structural information, which hampered detailed investigations of the molecular function of TMEM16 members. A big focus of our research was thus initially put on structure determination.

The extensive homologue expression screen performed in our lab has led to discovery of nhTMEM16 as potential crystallization candidate and eventually led to its structure determination. The crystal structure revealed that nhTMEM16 forms a homodimer, with each subunit containing 10 TMHs. While the dimeric nature has been described previously (72, 73), the structure uncovered the topology of the transmembrane domain and showed that each subunit consists of 10 transmembrane helices instead of 8 helices predicted by hydropathy analysis and epitope mapping. More importantly, the structure revealed presence of Ca^{2+}-binding sites within the transmembrane region and of a hydrophilic groove, the subunit cavity, which is exposed to the lipid bilayer. This discovery provided a glimpse on the mode of Ca^{2+}-binding in TMEM16 proteins and it allowed the proposal of mechanisms on how TMEM16 scramblases facilitate lipid flipping.

The high sequence similarity of around 30% in the transmembrane region of nhTMEM16 compared to mammalian homologues suggested that TMEM16 proteins share a similar structural organisation. Thus, despite the fact that nhTMEM16 does not function as an ion channel, its architecture provides an invaluable framework for many functional properties of the CaCC TMEM16A. These features will be discussed in the next sub chapters.

4.1. Ca^{2+}-binding site

The crystal structure of nhTMEM16 revealed the presence of a Ca^{2+}-binding site embedded in each subunit of a dimeric protein. The location of this binding site within the membrane provides a plausible explanation for the voltage-dependence of Ca^{2+} activation observed in TMEM16A, 16B and 16F, as the ion needs to cross approximately a third of the transmembrane electric field to reach the binding site. This is in agreement with several studies, which suggested that Ca^{2+} binding site might reside within the transmembrane region (76, 86). The presence of Ca^{2+} bound to the protein defined by X-ray crystallography strengthens the hypothesis that the channel is activated directly by Ca^{2+} and not indirectly through the binding of calmodulin (88, 89).

The binding site is highly conserved in all members of TMEM16 family. In mTMEM16A, it consists of four glutamates, one aspartate and one asparagine. In my studies, I have shown that mutations of each of the 6 residues in mTMEM16A shifts the EC_{50} to higher Ca^{2+} concentrations, with Glu654 exhibiting the strongest effect. The results were in agreement with recent studies, which collectively identified the five acidic residues in the absence of a structure (71, 89). They have, however, been misinterpreted to be located at the cytoplasmic side due to an incorrect topology prediction.

In the crystal structure, two Ca^{2+} ions were observed in the binding site as accounted by two strong peaks in the anomalous difference map. Although from our data, we cannot tell with certainty whether one or two Ca^{2+} ions are bound at the same time, simultaneous occupancy seems possible owing to the high density of negative charge in this region. The electrophysiological data from my study on TMEM16A also provide further indications that there are at least two Ca^{2+} involved in channel activation. In TMEM16A, the Hill coefficient of activation by Ca^{2+} around 2 implies that there is cooperativity of activation, suggesting that there are at least two Ca^{2+} ions binding to the protein. Furthermore, the mutation of individual residues in the Ca^{2+} binding site of TMEM16A decreased the Hill coefficient of activation to various degrees, suggesting that the binding of the second Ca^{2+} could be compromised. In D738N mutant, a biphasic activation was observed, which could indicate a low affinity to bind the second ion. Lastly, in experiments using concatenated mTMEM16A showed cooperative binding in constructs where only one of the two subunits is activated.

The spatial arrangement of the six coordinating residues in TMEM16 suggest that simultaneous occupancy of two Ca^{2+} is plausible (Figure 35a). The two Ca^{2+} ions are 4.2 Å apart and each is within the expected coordination distance of 2.1-3.5 Å of oxygens of the sidechains of several of the involved residues. Estimations based on the proximity of Ca^{2+} to the coordinating oxygens and under the assumption that there is no indirect coordination through a water molecule, the Ca^{2+} coordination number would be 5 and 6 for each of the two Ca^{2+} (117). According to a statistical analysis study on different Ca^{2+} binding sites of available protein structures, the average Ca^{2+} coordination number in non-EF-hand proteins is 4 ± 2 for oxygens from protein ligands and 2 ± 2 for oxygens from water. Due to the comparably low resolution our data, does not permit to estimate the coordination contribution by water.

The arrangement of non-EF hand binding sites coordinating two Ca^{2+} in close proximity have been observed in several proteins. In the structure of metalloprotease thermolysin (1FJ3) (118), two Ca^{2+} ions, which are 3.8 Å apart, are coordinated by two asparagines and four glutamates (one of which is coordinated by a backbone oxygen) (Figure 35b). The high resolution structure also revealed that one Ca^{2+} is additionally coordinated by two water molecules, hence resulting in coordination number of 6 and 7 for the two Ca^{2+} ions. In the context of membrane proteins, a similar example was observed in the crystal structure of rabbit SERCA1a (1SU4) (119), the fast-twitch skeletal muscle P-type Ca^{2+}-ATPase of the sarcoplasmic reticulum

(Figure 35c). The Ca^{2+} binding site is found just below the cytoplasmic side and shows two bound Ca^{2+} that are 5.9 A apart. One of the Ca^{2+} is coordinated by two water molecules. The coordination numbers for the two Ca^{2+} are 6 and 7.

Due to the comparable ion coordination of TMEM16 to the two described examples, the simultaneous occupancy of the site by two Ca^{2+} in TMEM16 appears likely. However, since the coordination numbers of interacting ligands are comparably low, it is possible that additional coordination is facilitated by a structured water molecule, which could not be observed at the current resolution of the data.

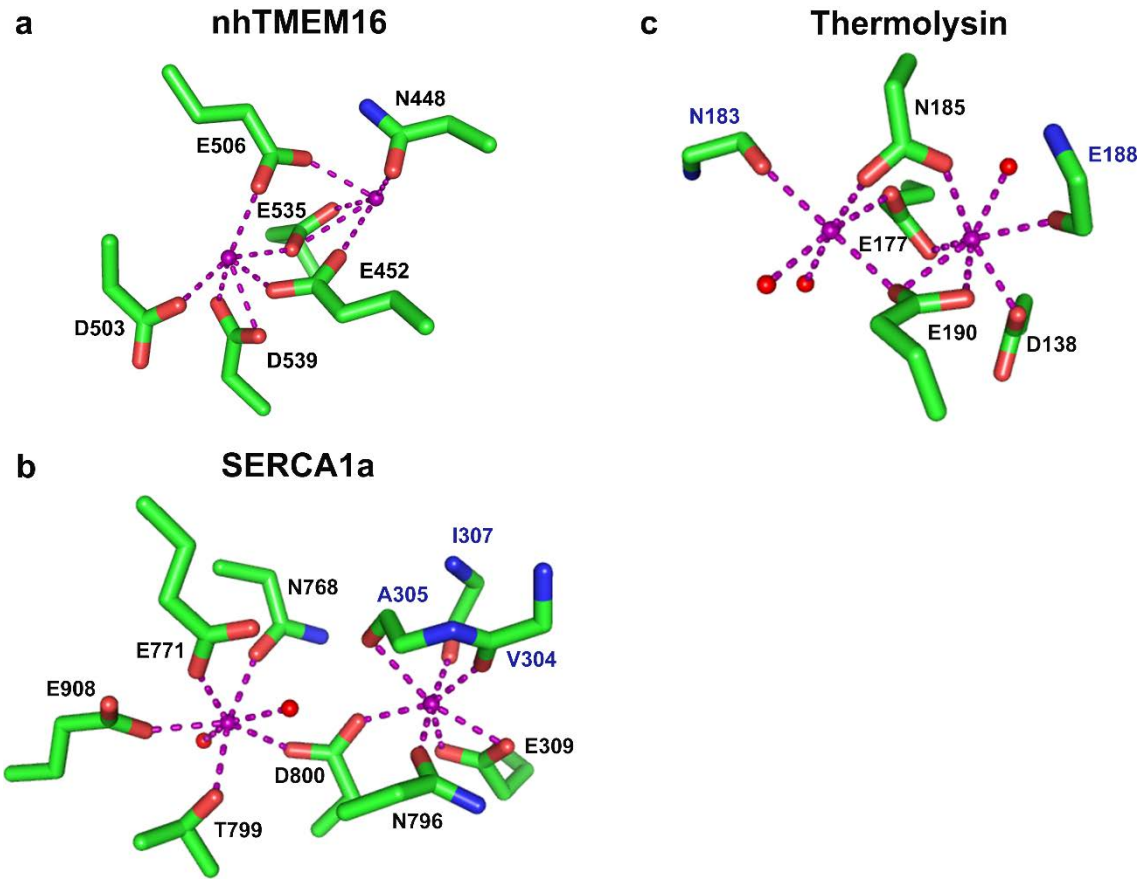

Figure 35 Comparison of 'two Ca^{2+}'-binding sites.

Ca^{2+} binding site of **a**, nhTMEM16. **b**, thermolysin (Ca1,2)and **c**, Serca1a. labeled residues coordinate Ca^{2+} via backbone oxygens. Red spheres represent coordinating water molecules. Ca^{2+} is shown as purple spheres.

4.2 Transport pathway in TMEM16 proteins

The structure of nhTMEM16 revealed two membrane spanning hydrophilic furrows that are laterally exposed to the lipid bilayer. These sites provide a favourable surface for facilitated diffusion of the polar lipid headgroups, while the alkyl group of the lipids remain embedded in the hydrophobic environment. In this process the energy barrier for lipid flipping is reduced, thereby enhancing the rate of movement between the two leaflets. A residue in TMEM16F at the lateral edge of the subunit cavity was shown to be involved in phospholipid scrambling (120), further suggesting that the subunit cavity is the site of lipid scrambling.

While the pathway for lipid flip-flop along the subunit cavity appears plausible, the location of the ion conduction pathway in TMEM16A is less straightforward. Although the large central pore at the dimeric interface could provide a passage across the membrane, it is partly exposed to the membrane and mainly lined by hydrophobic residues, thus making it energetically unfavourable path for ion conduction. The subunit cavity, on the other hand, is exposed to the lipid bilayer and the hydrophobic alkyl groups of lipids lining the pore could render the site and unlikely path for ion permeation at first sight as there is *no precedent* in the literature of such pore architecture. However, there are number of observations that collectively suggest that the subunit cavity is the pore of TMEM16A. Firstly, the Ca^{2+}-binding site is situated next to the subunit cavity, hence allowing rapid gating of the pore. Secondly, several mutational studies have identified residues around the extracellular entrance of the subunit cavity to influence ion conduction (71, 121). Moreover, mutation of the cavity residue Lys 588 to Gln was shown to alter the ion selectivities of TMEM16A and TMEM16 (19). In our study, described in the manuscript that is part of this thesis (122), the mutant K588E was constructed as an attempt to enhance the change in selectivity. Although the resulting currents were too small to characterize the selectivity of the mutant, noise analysis showed a decrease of the conductance of the channel, thus suggesting that the mutated residue might line the pore and influence ion permeation (110).

In this study and the attached publication (122), I have also investigated whether TMEM16A consists of two separate ion conduction pores that are independently activated by Ca^{2+}. The study was motivated by the hypothesis of a potential alternative arrangement in CaCCs whereby the two half-channels of the subunit cavity rearrange to form a central pore (108). By concatenating two TMEM16A subunits, mutations that alter the Ca^{2+}-binding affinity and conductance could be selectively introduced to a single subunit. Constructs containing subunits with different Ca^{2+} affinities show a biphasic activation curve that can be described as a sum of the activation properties of its constituents. The results thus suggest that TMEM16A contains two ion conduction pores that are independently activated by Ca^{2+}.

Several TMEM16 proteins such as afTMEM16 and TMEM16F were shown to both conduct ions and scramble lipids. In my study, I was not able to show the presence of ion conduction in the scramblase nhTMEM16. A possible explanation was the lipid mixture of Phosphatidylethanolamine (PE) and Phosphatidylglycerol (PG) used in the lipid bilayer might inhibit ion conduction. In a study by Malvezzi et al. (103), the activity of afTMEM16 reconstituted in PE:PG bilayer were very low compared to the robust activity of the protein reconstituted in PE/egg PC (Phosphatidylcholine) observed in Cl^- efflux assays. It was suggested that the requirement for certain lipids to observe ion conduction is a consequence for interactions of the protein with specific lipids (95). In other words, certain lipids could block the ion conduction path for the lipid headgroup and hence preventing permeation.

Regardless of the lipid dependence on ion permeation but not lipid scrambling observed in afTMEM16, it is likely that both substrates, utilize the subunit cavity for translocation. Recently, a study identified a scrambling domain (SCRD) of 35 aminoacids in TMEM16F at the cytoplasmic entrance of the subunit cavity, which appears to play a role for scrambling in TMEM16F (123) . Upon activation by high Ca^{2+} concentrations, the TMEM16A chimera containing the SCRD of TMEM16F showed lipid scrambling activity and furthermore, exhibited the non-selective currents that have been associated with TMEM16F. The study further showed that the TMEM16F currents coincide with lipid scrambling and is in fact a leak from lipid scrambling that is concurrent with lipid movement. The current observed in afTMEM16 could thus potentially be a byproduct of lipid scrambling. The varying ion conduction properties of TMEM16F observed in various studies might be due to different lipids being scrambled, which in turn determines the nature of the ion slipping alongside the lipid (123). From these findings, Whitlock and Hartzell (95) hypothesised that the lipid head groups of the bilayer may form part of the Cl^- conductance pathway in TMEM16A. In this case the pore would be made up of protein residues on one side and lined by lipids on the opposite side (Figure 36a). A potential explanation for the difference in conduction seen in TMEM16A and TMEM16F might be a slight difference in the architecture of the subunit cavity in these two proteins. The Location of the SCRD domain being at the edge of one side of the groove suggests that it might play a role in scaffolding. The helices conferred by the equivalent residues in TMEM16A could adopt a different tertiary structure. As illustrated in Figure 36b, the two edges of the subunit cavity of each TMEM16A subunit could be stronger curved, resulting in an almost full enclosure of the cavity thus resembling conventional channel pores. A structural study by either X-ray crystallography or electron microscopy will be required to test this hypothesis.

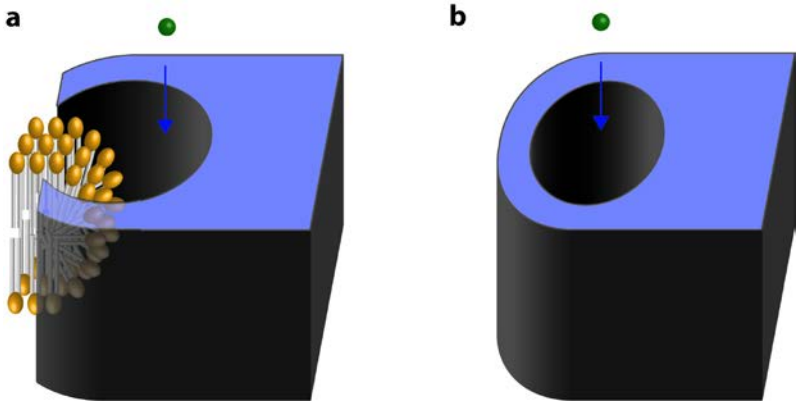

Figure 36 Potential model for the pore of TMEM16A

a, A pore model where the subunit cavity is lined by lipid on one side. **b,** a pore model where the edges of the subunit cavitiy fold towards one another to form a fully enclosed pore.

4.3 Potential mechanisms of channel activation

TMEM16A is gated by both Ca^{2+} and voltage. In my studies I have provided evidence that the voltage dependence of channel activation was due to the binding of Ca^{2+} in a site located within the membrane electrical field. Apart from that, there are other factors influencing the voltage-dependence gating. The occupancy of the pore by the permeant anions influence the voltage sensitivity. Substituting Cl^- with NO_3^- reduces outward rectification and increases the fraction of current activated instantaneously by depolarization in the absence of Ca^{2+}, thus suggesting that the voltage dependent gating is altered. This could be explained by NO_3^- having a lower hydration energy and higher relative permeability than Cl^-. Additionally, the replacement of the sequence EEEEEAVK within the first intracellular loop was shown to modulate the interplay between activation by Ca^{2+} and voltage. Although it is possible that the stretch of 5 acidic residues is acting as a weak Ca^{2+} site prior to entering the main Ca^{2+} binding site within the membrane, it remains unclear how the deletion of the EAVK motif would render the channel more sensititve to the activation by voltage in the absence of Ca^{2+}.

It is also still unknown how the binding of Ca^{2+} could lead to the opening of the channel and whether the full occupancy of the two Ca^{2+} sites are a requirement for this process. It is conceivable that upon Ca^{2+} binding, a local conformational change at the vicinity of the site could open a pore that is blocked by an obstructing helix (124). Alternatively, the Ca^{2+} binding site might play a direct role in gating without the need of conformational changes. In the absence of Ca^{2+}, the negative charges from the five acidic residues in the binding site might serve as a repulsive electrostatic gate for permeant anions passing through the cavity. Binding of Ca^{2+} would therefore reduce or neutralize the negative charges, hence permitting ions to pass through.

4.4 Outlook

The structure of nhTMEM16 has provided first insight into the architecture of a protein family for which little was known previously. This crystal structure has suggested potential mechanisms of how TMEM16 scramblase could catalyse lipid scrambling and, in combination with the results described in this thesis, it has revealed how TMEM16s functioning as CaCCs may be gated by Ca^{2+} and voltage. Despite this breakthrough, there are still many open questions with regards to the molecular mechanisms underlying CaCC function.

Despite the described advances, the molecular mechanism of channel opening by the binding of Ca^{2+} remains unknown. As mentioned in the discussion, plausible mechanisms of gating could involve electrostatic repulsion or occlusion of the ion conduction path by residues of the protein. The hypothesis of gating through electrostatic repulsion by the cluster of negatively charged residues could be explored by mutagenesis and a functional characterization by electrophysiology. By employing a combination of charge reversal or neutralizing mutations of all residues in vicinity of the binding site, the appearance of constitutive channel activity could reflect a decrease of the electrostatic barrier. The mechanism of channel opening through conformational changes could be probed by a series of distance measurements. For that purpose, spin-label pairs could be introduced through selective labelling on several locations across the subunit cavity for DEER EPR spectroscopy. The concatemeric construct used in our recent study could be used as a template for selective labelling in a single subunit of the dimer to avoid multi-spin systems. Any conformational changes in the presence of Ca^{2+} leading to a widening of the pore could be monitored by changes in the measured distance between the labels.

Ultimately, the unanswered questions concenring the architecture of TMEM16A could be answered through determination of high resolution structures of TMEM16A. This will conclusively show whether TMEM16A would adopt a similar open arrangement of helices forming the subunit cavity as seen in nhTMEM16 or adopt a more enclosed architecture expected for a conventional ion conduction pore. Obtaining the crystal structures of the protein in the presence and absence of Ca^{2+} would also elucidate the mechanisms behind channel activation. TMEM16A has been successfully expressed in HEK cells and purified in our lab but the low yield of the protein has prevented crystallization screening. Further effort could be invested in improving the yield for crystallization studies. Alternatively, cryo-electron microscopy could be employed to determine the structures, hence circumventing the requirement of high amounts of protein for crystallization.

CURRICULUM VITAE

LIM Novandy Karunia

Date of Birth: 02.11.1985

Place of Birth: Pontianak, Indonesia

Nationality: Indonesian

Address: Kirchensteig 6, 8152 Opfikon

Email: n.lim@bioc.uzh.ch

Education

Oct 2010 – Nov 2016	**PhD thesis in the group of Prof. Raimund Dutzler** Department of Biochemistry, University of Zurich, Switzerland Member of the Biomolecular Structure and Mechanism PhD Program of UZH and ETHZ
2009-2010	**Master of Research in Structural Molecular Biology** Imperial College London Thesis in the group of Prof. David Drew and Prof. So Iwata Thesis in the group of Prof. Kurt Drickamer
2005-2009	**Bachelor of Science in Biochemistry with a year in Industry** Imperial College London One year industrial placement in AstraZeneca, Alderley Park, UK
2004-2005	**GCE A Level** Cambridge Tutors College, Croydon, UK
2000-2003	**Secondary school and GCE O Level** St. Joseph Institution, Singapore

Professional Development

2015 Activation of Ca^{2+}-Activated Chloride Channel TMEM16A

Biophysical Society Annual Meeting, Baltimore, Maryland, USA (Poster)

Publication List

2016 **Independent activation of ion conduction pores in the double-barreled calcium-activated chloride channel TMEM16A**

Lim NK, Lam AKM, Dutzler R

The Journal of general physiology. 2016;148(5): 375-92.

2014 **X-ray structure of a calcium-activated TMEM16 lipid scramblase**

Brunner JD, Lim NK, Schenck S, Duerst A, Dutzler R

Nature. 2014;516(7530):207-12

References

Reference

1. Ben-Ari Y, Gaiarsa JL, Tyzio R, Khazipov R. GABA: a pioneer transmitter that excites immature neurons and generates primitive oscillations. Physiological reviews. 2007;87(4):1215-84.
2. Rivera C, Voipio J, Payne JA, Ruusuvuori E, Lahtinen H, Lamsa K, et al. The K+/Cl- co-transporter KCC2 renders GABA hyperpolarizing during neuronal maturation. Nature. 1999;397(6716):251-5.
3. Duran C, Thompson CH, Xiao Q, Hartzell HC. Chloride channels: often enigmatic, rarely predictable. Annual review of physiology. 2010;72:95-121.
4. Nauntofte B. Regulation of electrolyte and fluid secretion in salivary acinar cells. The American journal of physiology. 1992;263(6 Pt 1):G823-37.
5. Melvin JE. Chloride channels and salivary gland function. Critical reviews in oral biology and medicine : an official publication of the American Association of Oral Biologists. 1999;10(2):199-209.
6. Barrett KE, Keely SJ. Chloride secretion by the intestinal epithelium: molecular basis and regulatory aspects. Annual review of physiology. 2000;62:535-72.
7. Devor DC, Singh AK, Lambert LC, DeLuca A, Frizzell RA, Bridges RJ. Bicarbonate and chloride secretion in Calu-3 human airway epithelial cells. The Journal of general physiology. 1999;113(5):743-60.
8. Quinton PM. Physiological basis of cystic fibrosis: a historical perspective. Physiological reviews. 1999;79(1 Suppl):S3-S22.
9. Pusch M, Steinmeyer K, Koch MC, Jentsch TJ. Mutations in dominant human myotonia congenita drastically alter the voltage dependence of the CIC-1 chloride channel. Neuron. 1995;15(6):1455-63.
10. Dutzler R, Campbell EB, Cadene M, Chait BT, MacKinnon R. X-ray structure of a ClC chloride channel at 3.0 A reveals the molecular basis of anion selectivity. Nature. 2002;415(6869):287-94.
11. Zhou Y, Morais-Cabral JH, Kaufman A, MacKinnon R. Chemistry of ion coordination and hydration revealed by a K+ channel-Fab complex at 2.0 A resolution. Nature. 2001;414(6859):43-8.
12. Jentsch TJ, Neagoe I, Scheel O. CLC chloride channels and transporters. Current opinion in neurobiology. 2005;15(3):319-25.
13. Jentsch TJ, Stein V, Weinreich F, Zdebik AA. Molecular structure and physiological function of chloride channels. Physiological reviews. 2002;82(2):503-68.
14. Nilius B, Eggermont J, Voets T, Buyse G, Manolopoulos V, Droogmans G. Properties of volume-regulated anion channels in mammalian cells. Progress in biophysics and molecular biology. 1997;68(1):69-119.
15. Voss FK, Ullrich F, Munch J, Lazarow K, Lutter D, Mah N, et al. Identification of LRRC8 heteromers as an essential component of the volume-regulated anion channel VRAC. Science. 2014;344(6184):634-8.
16. Hartzell C, Putzier I, Arreola J. Calcium-activated chloride channels. Annual review of physiology. 2005;67:719-58.
17. Caputo A, Caci E, Ferrera L, Pedemonte N, Barsanti C, Sondo E, et al. TMEM16A, a membrane protein associated with calcium-dependent chloride channel activity. Science. 2008;322(5901):590-4.
18. Schroeder BC, Cheng T, Jan YN, Jan LY. Expression cloning of TMEM16A as a calcium-activated chloride channel subunit. Cell. 2008;134(6):1019-29.
19. Yang H, Kim A, David T, Palmer D, Jin T, Tien J, et al. TMEM16F forms a Ca2+-activated cation channel required for lipid scrambling in platelets during blood coagulation. Cell. 2012;151(1):111-22.
20. Papazian DM, Timpe LC, Jan YN, Jan LY. Alteration of voltage-dependence of Shaker potassium channel by mutations in the S4 sequence. Nature. 1991;349(6307):305-10.
21. Moroni M, Biro I, Giugliano M, Vijayan R, Biggin PC, Beato M, et al. Chloride ions in the pore of glycine and GABA channels shape the time course and voltage dependence of agonist currents.

The Journal of neuroscience : the official journal of the Society for Neuroscience. 2011;31(40):14095-106.
22. Pusch M, Ludewig U, Rehfeldt A, Jentsch TJ. Gating of the voltage-dependent chloride channel CIC-0 by the permeant anion. Nature. 1995;373(6514):527-31.
23. Maduke M, Pheasant DJ, Miller C. High-level expression, functional reconstitution, and quaternary structure of a prokaryotic ClC-type chloride channel. The Journal of general physiology. 1999;114(5):713-22.
24. Hwang TC, Sheppard DN. Gating of the CFTR Cl- channel by ATP-driven nucleotide-binding domain dimerisation. The Journal of physiology. 2009;587(Pt 10):2151-61.
25. Xiao Q, Yu K, Perez-Cornejo P, Cui Y, Arreola J, Hartzell HC. Voltage- and calcium-dependent gating of TMEM16A/Ano1 chloride channels are physically coupled by the first intracellular loop. Proceedings of the National Academy of Sciences of the United States of America. 2011;108(21):8891-6.
26. Barish ME. A transient calcium-dependent chloride current in the immature Xenopus oocyte. The Journal of physiology. 1983;342:309-25.
27. Miledi R. A calcium-dependent transient outward current in Xenopus laevis oocytes. Proceedings of the Royal Society of London Series B, Biological sciences. 1982;215(1201):491-7.
28. Angermann JE, Sanguinetti AR, Kenyon JL, Leblanc N, Greenwood IA. Mechanism of the inhibition of Ca2+-activated Cl- currents by phosphorylation in pulmonary arterial smooth muscle cells. The Journal of general physiology. 2006;128(1):73-87.
29. Large WA, Wang Q. Characteristics and physiological role of the Ca(2+)-activated Cl- conductance in smooth muscle. The American journal of physiology. 1996;271(2 Pt 1):C435-54.
30. Pacaud P, Loirand G, Mironneau C, Mironneau J. Noradrenaline activates a calcium-activated chloride conductance and increases the voltage-dependent calcium current in cultured single cells of rat portal vein. British journal of pharmacology. 1989;97(1):139-46.
31. von der Weid PY, Rahman M, Imtiaz MS, van Helden DF. Spontaneous transient depolarizations in lymphatic vessels of the guinea pig mesentery: pharmacology and implication for spontaneous contractility. American journal of physiology Heart and circulatory physiology. 2008;295(5):H1989-2000.
32. ZhuGe R, Sims SM, Tuft RA, Fogarty KE, Walsh JV, Jr. Ca2+ sparks activate K+ and Cl- channels, resulting in spontaneous transient currents in guinea-pig tracheal myocytes. The Journal of physiology. 1998;513 (Pt 3):711-8.
33. Davis MJ, Hill MA. Signaling mechanisms underlying the vascular myogenic response. Physiological reviews. 1999;79(2):387-423.
34. Bao R, Lifshitz LM, Tuft RA, Bellve K, Fogarty KE, ZhuGe R. A close association of RyRs with highly dense clusters of Ca2+-activated Cl- channels underlies the activation of STICs by Ca2+ sparks in mouse airway smooth muscle. The Journal of general physiology. 2008;132(1):145-60.
35. Leblanc N, Forrest AS, Ayon RJ, Wiwchar M, Angermann JE, Pritchard HA, et al. Molecular and functional significance of Ca(2+)-activated Cl(-) channels in pulmonary arterial smooth muscle. Pulmonary circulation. 2015;5(2):244-68.
36. Llano I, Leresche N, Marty A. Calcium entry increases the sensitivity of cerebellar Purkinje cells to applied GABA and decreases inhibitory synaptic currents. Neuron. 1991;6(4):565-74.
37. Achilles K, Okabe A, Ikeda M, Shimizu-Okabe C, Yamada J, Fukuda A, et al. Kinetic properties of Cl uptake mediated by Na+-dependent K+-2Cl cotransport in immature rat neocortical neurons. The Journal of neuroscience : the official journal of the Society for Neuroscience. 2007;27(32):8616-27.
38. Gamba G. Molecular physiology and pathophysiology of electroneutral cation-chloride cotransporters. Physiological reviews. 2005;85(2):423-93.
39. Gilbert D, Franjic-Wurtz C, Funk K, Gensch T, Frings S, Mohrlen F. Differential maturation of chloride homeostasis in primary afferent neurons of the somatosensory system. International journal of developmental neuroscience : the official journal of the International Society for Developmental Neuroscience. 2007;25(7):479-89.

40. Lu J, Karadsheh M, Delpire E. Developmental regulation of the neuronal-specific isoform of K-Cl cotransporter KCC2 in postnatal rat brains. Journal of neurobiology. 1999;39(4):558-68.
41. Stein V, Hermans-Borgmeyer I, Jentsch TJ, Hubner CA. Expression of the KCl cotransporter KCC2 parallels neuronal maturation and the emergence of low intracellular chloride. The Journal of comparative neurology. 2004;468(1):57-64.
42. Alvarez-Leefmans FJ, Leon-Olea M, Mendoza-Sotelo J, Alvarez FJ, Anton B, Garduno R. Immunolocalization of the Na(+)-K(+)-2Cl(-) cotransporter in peripheral nervous tissue of vertebrates. Neuroscience. 2001;104(2):569-82.
43. Rocha-Gonzalez HI, Mao S, Alvarez-Leefmans FJ. Na+,K+,2Cl- cotransport and intracellular chloride regulation in rat primary sensory neurons: thermodynamic and kinetic aspects. Journal of neurophysiology. 2008;100(1):169-84.
44. Schobel N, Radtke D, Lubbert M, Gisselmann G, Lehmann R, Cichy A, et al. Trigeminal ganglion neurons of mice show intracellular chloride accumulation and chloride-dependent amplification of capsaicin-induced responses. PloS one. 2012;7(11):e48005.
45. Kleene SJ, Gesteland RC. Calcium-activated chloride conductance in frog olfactory cilia. The Journal of neuroscience : the official journal of the Society for Neuroscience. 1991;11(11):3624-9.
46. Lalonde MR, Kelly ME, Barnes S. Calcium-activated chloride channels in the retina. Channels. 2008;2(4):252-60.
47. Maricq AV, Korenbrot JI. Calcium and calcium-dependent chloride currents generate action potentials in solitary cone photoreceptors. Neuron. 1988;1(6):503-15.
48. Hengl T, Kaneko H, Dauner K, Vocke K, Frings S, Mohrlen F. Molecular components of signal amplification in olfactory sensory cilia. Proceedings of the National Academy of Sciences of the United States of America. 2010;107(13):6052-7.
49. Ponissery Saidu S, Dibattista M, Matthews HR, Reisert J. Odorant-induced responses recorded from olfactory receptor neurons using the suction pipette technique. Journal of visualized experiments : JoVE. 2012(62):e3862.
50. Melvin JE, Koek L, Zhang GH. A capacitative Ca2+ influx is required for sustained fluid secretion in sublingual mucous acini. The American journal of physiology. 1991;261(6 Pt 1):G1043-50.
51. Fischer H, Illek B, Sachs L, Finkbeiner WE, Widdicombe JH. CFTR and calcium-activated chloride channels in primary cultures of human airway gland cells of serous or mucous phenotype. American journal of physiology Lung cellular and molecular physiology. 2010;299(4):L585-94.
52. Huang F, Rock JR, Harfe BD, Cheng T, Huang X, Jan YN, et al. Studies on expression and function of the TMEM16A calcium-activated chloride channel. Proceedings of the National Academy of Sciences of the United States of America. 2009;106(50):21413-8.
53. Puchelle E, Bajolet O, Abely M. Airway mucus in cystic fibrosis. Paediatric respiratory reviews. 2002;3(2):115-9.
54. Ratjen F, Durham T, Navratil T, Schaberg A, Accurso FJ, Wainwright C, et al. Long term effects of denufosol tetrasodium in patients with cystic fibrosis. Journal of cystic fibrosis : official journal of the European Cystic Fibrosis Society. 2012;11(6):539-49.
55. Yang YD, Cho H, Koo JY, Tak MH, Cho Y, Shim WS, et al. TMEM16A confers receptor-activated calcium-dependent chloride conductance. Nature. 2008;455(7217):1210-5.
56. Ferrera L, Caputo A, Ubby I, Bussani E, Zegarra-Moran O, Ravazzolo R, et al. Regulation of TMEM16A chloride channel properties by alternative splicing. The Journal of biological chemistry. 2009;284(48):33360-8.
57. Britschgi A, Bill A, Brinkhaus H, Rothwell C, Clay I, Duss S, et al. Calcium-activated chloride channel ANO1 promotes breast cancer progression by activating EGFR and CAMK signaling. Proceedings of the National Academy of Sciences of the United States of America. 2013;110(11):E1026-34.
58. Simon S, Grabellus F, Ferrera L, Galietta L, Schwindenhammer B, Muhlenberg T, et al. DOG1 regulates growth and IGFBP5 in gastrointestinal stromal tumors. Cancer research. 2013;73(12):3661-70.

59. Huang F, Zhang H, Wu M, Yang H, Kudo M, Peters CJ, et al. Calcium-activated chloride channel TMEM16A modulates mucin secretion and airway smooth muscle contraction. Proceedings of the National Academy of Sciences of the United States of America. 2012;109(40):16354-9.
60. Huang F, Wang X, Ostertag EM, Nuwal T, Huang B, Jan YN, et al. TMEM16C facilitates Na(+)-activated K+ currents in rat sensory neurons and regulates pain processing. Nature neuroscience. 2013;16(9):1284-90.
61. Charlesworth G, Plagnol V, Holmstrom KM, Bras J, Sheerin UM, Preza E, et al. Mutations in ANO3 cause dominant craniocervical dystonia: ion channel implicated in pathogenesis. American journal of human genetics. 2012;91(6):1041-50.
62. Maniero C, Zhou J, Shaikh LH, Azizan EA, McFarlane I, Neogi S, et al. Role of ANO4 in regulation of aldosterone secretion in the zona glomerulosa of the human adrenal gland. Lancet. 2015;385 Suppl 1:S62.
63. Bolduc V, Marlow G, Boycott KM, Saleki K, Inoue H, Kroon J, et al. Recessive mutations in the putative calcium-activated chloride channel Anoctamin 5 cause proximal LGMD2L and distal MMD3 muscular dystrophies. American journal of human genetics. 2010;86(2):213-21.
64. Hicks D, Sarkozy A, Muelas N, Koehler K, Huebner A, Hudson G, et al. A founder mutation in Anoctamin 5 is a major cause of limb-girdle muscular dystrophy. Brain : a journal of neurology. 2011;134(Pt 1):171-82.
65. Mahjneh I, Jaiswal J, Lamminen A, Somer M, Marlow G, Kiuru-Enari S, et al. A new distal myopathy with mutation in anoctamin 5. Neuromuscular disorders : NMD. 2010;20(12):791-5.
66. Tsutsumi S, Kamata N, Vokes TJ, Maruoka Y, Nakakuki K, Enomoto S, et al. The novel gene encoding a putative transmembrane protein is mutated in gnathodiaphyseal dysplasia (GDD). American journal of human genetics. 2004;74(6):1255-61.
67. Suzuki J, Umeda M, Sims PJ, Nagata S. Calcium-dependent phospholipid scrambling by TMEM16F. Nature. 2010;468(7325):834-8.
68. Bera TK, Das S, Maeda H, Beers R, Wolfgang CD, Kumar V, et al. NGEP, a gene encoding a membrane protein detected only in prostate cancer and normal prostate. Proceedings of the National Academy of Sciences of the United States of America. 2004;101(9):3059-64.
69. Vermeer S, Hoischen A, Meijer RP, Gilissen C, Neveling K, Wieskamp N, et al. Targeted next-generation sequencing of a 12.5 Mb homozygous region reveals ANO10 mutations in patients with autosomal-recessive cerebellar ataxia. American journal of human genetics. 2010;87(6):813-9.
70. Das S, Hahn Y, Walker DA, Nagata S, Willingham MC, Peehl DM, et al. Topology of NGEP, a prostate-specific cell:cell junction protein widely expressed in many cancers of different grade level. Cancer research. 2008;68(15):6306-12.
71. Yu K, Duran C, Qu Z, Cui YY, Hartzell HC. Explaining calcium-dependent gating of anoctamin-1 chloride channels requires a revised topology. Circulation research. 2012;110(7):990-9.
72. Fallah G, Romer T, Detro-Dassen S, Braam U, Markwardt F, Schmalzing G. TMEM16A(a)/anoctamin-1 shares a homodimeric architecture with CLC chloride channels. Molecular & cellular proteomics : MCP. 2011;10(2):M110 004697.
73. Sheridan JT, Worthington EN, Yu K, Gabriel SE, Hartzell HC, Tarran R. Characterization of the oligomeric structure of the Ca(2+)-activated Cl- channel Ano1/TMEM16A. The Journal of biological chemistry. 2011;286(2):1381-8.
74. Tien J, Lee HY, Minor DL, Jr., Jan YN, Jan LY. Identification of a dimerization domain in the TMEM16A calcium-activated chloride channel (CaCC). Proceedings of the National Academy of Sciences of the United States of America. 2013;110(16):6352-7.
75. Nilius B, Prenen J, Voets T, Van den Bremt K, Eggermont J, Droogmans G. Kinetic and pharmacological properties of the calcium-activated chloride-current in macrovascular endothelial cells. Cell calcium. 1997;22(1):53-63.
76. Kuruma A, Hartzell HC. Bimodal control of a Ca(2+)-activated Cl(-) channel by different Ca(2+) signals. The Journal of general physiology. 2000;115(1):59-80.

77. Fuller CM, Ismailov, II, Keeton DA, Benos DJ. Phosphorylation and activation of a bovine tracheal anion channel by Ca2+/calmodulin-dependent protein kinase II. The Journal of biological chemistry. 1994;269(43):26642-50.
78. Pifferi S, Dibattista M, Sagheddu C, Boccaccio A, Al Qteishat A, Ghirardi F, et al. Calcium-activated chloride currents in olfactory sensory neurons from mice lacking bestrophin-2. The Journal of physiology. 2009;587(Pt 17):4265-79.
79. Stohr H, Heisig JB, Benz PM, Schoberl S, Milenkovic VM, Strauss O, et al. TMEM16B, a novel protein with calcium-dependent chloride channel activity, associates with a presynaptic protein complex in photoreceptor terminals. The Journal of neuroscience : the official journal of the Society for Neuroscience. 2009;29(21):6809-18.
80. Stephan AB, Shum EY, Hirsh S, Cygnar KD, Reisert J, Zhao H. ANO2 is the cilial calcium-activated chloride channel that may mediate olfactory amplification. Proceedings of the National Academy of Sciences of the United States of America. 2009;106(28):11776-81.
81. Gajewski C, Dagcan A, Roux B, Deutsch C. Biogenesis of the pore architecture of a voltage-gated potassium channel. Proceedings of the National Academy of Sciences of the United States of America. 2011;108(8):3240-5.
82. Takahashi T, Neher E, Sakmann B. Rat brain serotonin receptors in Xenopus oocytes are coupled by intracellular calcium to endogenous channels. Proceedings of the National Academy of Sciences of the United States of America. 1987;84(14):5063-7.
83. Pifferi S, Dibattista M, Menini A. TMEM16B induces chloride currents activated by calcium in mammalian cells. Pflugers Archiv : European journal of physiology. 2009;458(6):1023-38.
84. Cenedese V, Betto G, Celsi F, Cherian OL, Pifferi S, Menini A. The voltage dependence of the TMEM16B/anoctamin2 calcium-activated chloride channel is modified by mutations in the first putative intracellular loop. The Journal of general physiology. 2012;139(4):285-94.
85. Tian Y, Kongsuphol P, Hug M, Ousingsawat J, Witzgall R, Schreiber R, et al. Calmodulin-dependent activation of the epithelial calcium-dependent chloride channel TMEM16A. FASEB journal : official publication of the Federation of American Societies for Experimental Biology. 2011;25(3):1058-68.
86. Arreola J, Melvin JE, Begenisich T. Activation of calcium-dependent chloride channels in rat parotid acinar cells. The Journal of general physiology. 1996;108(1):35-47.
87. Kaneko H, Mohrlen F, Frings S. Calmodulin contributes to gating control in olfactory calcium-activated chloride channels. The Journal of general physiology. 2006;127(6):737-48.
88. Terashima H, Picollo A, Accardi A. Purified TMEM16A is sufficient to form Ca2+-activated Cl- channels. Proceedings of the National Academy of Sciences of the United States of America. 2013;110(48):19354-9.
89. Tien J, Peters CJ, Wong XM, Cheng T, Jan YN, Jan LY, et al. A comprehensive search for calcium binding sites critical for TMEM16A calcium-activated chloride channel activity. eLife. 2014;3.
90. Adomaviciene A, Smith KJ, Garnett H, Tammaro P. Putative pore-loops of TMEM16/anoctamin channels affect channel density in cell membranes. The Journal of physiology. 2013;591(14):3487-505.
91. Almaca J, Tian Y, Aldehni F, Ousingsawat J, Kongsuphol P, Rock JR, et al. TMEM16 proteins produce volume-regulated chloride currents that are reduced in mice lacking TMEM16A. The Journal of biological chemistry. 2009;284(42):28571-8.
92. Juul CA, Grubb S, Poulsen KA, Kyed T, Hashem N, Lambert IH, et al. Anoctamin 6 differs from VRAC and VSOAC but is involved in apoptosis and supports volume regulation in the presence of Ca2+. Pflugers Archiv : European journal of physiology. 2014;466(10):1899-910.
93. Shimizu T, Iehara T, Sato K, Fujii T, Sakai H, Okada Y. TMEM16F is a component of a Ca2+-activated Cl- channel but not a volume-sensitive outwardly rectifying Cl- channel. American journal of physiology Cell physiology. 2013;304(8):C748-59.
94. Szteyn K, Schmid E, Nurbaeva MK, Yang W, Munzer P, Kunzelmann K, et al. Expression and functional significance of the Ca(2+)-activated Cl(-) channel ANO6 in dendritic cells. Cellular

physiology and biochemistry : international journal of experimental cellular physiology, biochemistry, and pharmacology. 2012;30(5):1319-32.
95. Whitlock JM, Hartzell HC. A Pore Idea: the ion conduction pathway of TMEM16/ANO proteins is composed partly of lipid. Pflugers Archiv : European journal of physiology. 2016;468(3):455-73.
96. Schreiber R, Uliyakina I, Kongsuphol P, Warth R, Mirza M, Martins JR, et al. Expression and function of epithelial anoctamins. The Journal of biological chemistry. 2010;285(10):7838-45.
97. Manford AG, Stefan CJ, Yuan HL, Macgurn JA, Emr SD. ER-to-plasma membrane tethering proteins regulate cell signaling and ER morphology. Developmental cell. 2012;23(6):1129-40.
98. Liou J, Kim ML, Heo WD, Jones JT, Myers JW, Ferrell JE, Jr., et al. STIM is a Ca2+ sensor essential for Ca2+-store-depletion-triggered Ca2+ influx. Current biology : CB. 2005;15(13):1235-41.
99. Mesmin B, Bigay J, Moser von Filseck J, Lacas-Gervais S, Drin G, Antonny B. A four-step cycle driven by PI(4)P hydrolysis directs sterol/PI(4)P exchange by the ER-Golgi tether OSBP. Cell. 2013;155(4):830-43.
100. West M, Zurek N, Hoenger A, Voeltz GK. A 3D analysis of yeast ER structure reveals how ER domains are organized by membrane curvature. The Journal of cell biology. 2011;193(2):333-46.
101. Fischer MA, Temmerman K, Ercan E, Nickel W, Seedorf M. Binding of plasma membrane lipids recruits the yeast integral membrane protein Ist2 to the cortical ER. Traffic. 2009;10(8):1084-97.
102. Juschke C, Wachter A, Schwappach B, Seedorf M. SEC18/NSF-independent, protein-sorting pathway from the yeast cortical ER to the plasma membrane. The Journal of cell biology. 2005;169(4):613-22.
103. Malvezzi M, Chalat M, Janjusevic R, Picollo A, Terashima H, Menon AK, et al. Ca2+-dependent phospholipid scrambling by a reconstituted TMEM16 ion channel. Nature communications. 2013;4:2367.
104. Altschul SF, Gish W, Miller W, Myers EW, Lipman DJ. Basic local alignment search tool. Journal of molecular biology. 1990;215(3):403-10.
105. States DJ, Gish W. Combined use of sequence similarity and codon bias for coding region identification. Journal of computational biology : a journal of computational molecular cell biology. 1994;1(1):39-50.
106. Drew D, Newstead S, Sonoda Y, Kim H, von Heijne G, Iwata S. GFP-based optimization scheme for the overexpression and purification of eukaryotic membrane proteins in Saccharomyces cerevisiae. Nature protocols. 2008;3(5):784-98.
107. Kantardjieff KA, Rupp B. Matthews coefficient probabilities: Improved estimates for unit cell contents of proteins, DNA, and protein-nucleic acid complex crystals. Protein science : a publication of the Protein Society. 2003;12(9):1865-71.
108. Brunner JD, Lim NK, Schenck S, Duerst A, Dutzler R. X-ray structure of a calcium-activated TMEM16 lipid scramblase. Nature. 2014;516(7530):207-12.
109. Ni YL, Kuan AS, Chen TY. Activation and inhibition of TMEM16A calcium-activated chloride channels. PloS one. 2014;9(1):e86734.
110. Lim NK, Lam KMA, Dutzler R. Independent activation of ion conduction pores in the double-barreled calcium-activated chloride channel TMEM16A. Journal of General Physiology. 2016.
111. Geertsma ER, Dutzler R. A versatile and efficient high-throughput cloning tool for structural biology. Biochemistry. 2011;50(15):3272-8.
112. Casadaban MJ, Cohen SN. Analysis of gene control signals by DNA fusion and cloning in Escherichia coli. Journal of molecular biology. 1980;138(2):179-207.
113. Ferrera L, Caputo A, Ubby I, Bussani E, Zegarra-Moran O, Ravazzolo R, et al. Regulation of TMEM16A chloride channel properties by alternative splicing. The Journal of biological chemistry. 2009;284(48):33360-8.
114. Nagai T, Ibata K, Park ES, Kubota M, Mikoshiba K, Miyawaki A. A variant of yellow fluorescent protein with fast and efficient maturation for cell-biological applications. Nature biotechnology. 2002;20(1):87-90.
115. Gietz RD, Schiestl RH. High-efficiency yeast transformation using the LiAc/SS carrier DNA/PEG method. Nature protocols. 2007;2(1):31-4.

116. Hamill OP, Marty A, Neher E, Sakmann B, Sigworth FJ. Improved patch-clamp techniques for high-resolution current recording from cells and cell-free membrane patches. Pflugers Archiv : European journal of physiology. 1981;391(2):85-100.
117. Wang X, Kirberger M, Qiu F, Chen G, Yang JJ. Towards predicting Ca2+-binding sites with different coordination numbers in proteins with atomic resolution. Proteins. 2009;75(4):787-98.
118. English AC, Groom CR, Hubbard RE. Experimental and computational mapping of the binding surface of a crystalline protein. Protein engineering. 2001;14(1):47-59.
119. Toyoshima C, Nakasako M, Nomura H, Ogawa H. Crystal structure of the calcium pump of sarcoplasmic reticulum at 2.6 A resolution. Nature. 2000;405(6787):647-55.
120. Suzuki T, Suzuki J, Nagata S. Functional swapping between transmembrane proteins TMEM16A and TMEM16F. The Journal of biological chemistry. 2014;289(11):7438-47.
121. Peters CJ, Yu H, Tien J, Jan YN, Li M, Jan LY. Four basic residues critical for the ion selectivity and pore blocker sensitivity of TMEM16A calcium-activated chloride channels. Proceedings of the National Academy of Sciences of the United States of America. 2015;112(11):3547-52.
122. Lim NK, Lam AK, Dutzler R. Independent activation of ion conduction pores in the double-barreled calcium-activated chloride channel TMEM16A. The Journal of general physiology. 2016;148(5):375-92.
123. Yu K, Whitlock JM, Lee K, Ortlund EA, Cui YY, Hartzell HC. Identification of a lipid scrambling domain in ANO6/TMEM16F. eLife. 2015;4:e06901.
124. Brunner JD, Schenck S, Dutzler R. Structural basis for phospholipid scrambling in the TMEM16 family. Current opinion in structural biology. 2016;39:61-70.